Effect of alkaline conditions on near-field processes of a spent nuclear fuel geological repository

Doctoral Thesis – 2014

Author: Albert Martínez Torrents

Directors: Joan de Pablo Ribas, Ignasi Casas Pons

Department of Chemical Engineering

Universitat Politècnica de Catalunya-Barcelona Tech

Acknowledgements

Són moltes les persones que m'han ajudat a desenvolupar aquesta tesis i per tant en aquest apartat voldria agrair el suport que he rebut. Soc despistat de mena, així que si em deixo algú que sapigueu que no és per malicia sinó per error.

Voldria començar agraint a la gent del CTM el seu suport. Encara recordo els partits de basquet de la lliga tecnològica amb en Raul, el Dani Casellas, en Quim, en Palmi, etc... Els companys de despatx en Sebas i en Martin. I sobretot la meva àrea, l'àrea de tecnologia Ambiental. Moltes gràcies, Miquel, Xevi, Isabel, Frederic, Irene, Ramon, Mireia, Montse, Sandra, Jose, Cristina, Neus, Laura, Laia, Gemma, David, Vicenç. Hem compartit molts moments tant a la feina, com a la riera salada, en sopars, concerts, cates de cervesa... Se us troba molt a faltar! També moltes gràcies a la Eli, la Carolina, al Christoph i a la Maria Rosa. De tots ells haig d'agrair especialment a la persona que em va convèncer per ficar-me en aquesta aventura que ha estat la tesis... Moltes gràcies Sandra! Estic molt content d'haver-te fet cas! I moltes gràcies per la ajuda i suport que sempre m'has donat!

La meva altra casa durant aquesta aventura ha estat la UPC de Barcelona. Haig d'agrair a la Carme Gauchia, la Adriana Farran i la Irene Pérez el suport que sempre m'ha donat. Aquesta tesis no hauria pogut tirar endavant sense el suport del grup de persones que es dediquen des de fa anys i amb molt èxit al mon dels actínids a la planta 4 de la UPC. Moltes gràcies Javi i Sandra. Moltes gràcies Joan i Ignasi, perdoneu per tot el que heu patit per ser els meus directors de tesis. Moltíssimes gràcies per tot el vostre esforç, suport i paciència durant aquesta tesis.

Per realitzar aquesta tesis m'he bellugat una mica i la meva primera estança va ser en el Helmholtz Zentrum Dresden Rossendorf. I want to specially thank my supervisor during this three month stay for all his effort and help. Without him it would have been very difficult to obtain such good results. Thank you very much Dr. Nils Baumann! I also want to thank the staff from the HZDR – Institute of resource ecology, specially Dr. Thuro Arnold, Dr. Gerhard Geipel, Dr. Andrea Cherkouk and Dr. Sonja Seleska-Pobell. También me gustaría agradecer a los Dresdenitas todos los buenos momentos, muchas gracias, Marta, Dayana, Fran y Marga. Agradezco su gran recibimiento, los cocteles a tres euros y la gran excursión a Moritzburg.

La segona estada va ser també a Alemanya, al Karlsruhe Intitute of Technology. In the Institute of Nuclear Waste Disposal. From this stay I would like to especially thank Dr.Volker Metz, Dr. Ernesto Gonzalez-Robles and Dr.Elke Bohnert for her patience, collaboration and support. Sorry Elke for the Gas-Maus!! A Ernesto le agradezco también que me hiciera de guía de Karlsruhe en los días que estuve allí! I also remember the good moments in the cantine, making coffee in the "David way" or in the Kapp. Thanks for all this moments, David, Xavi, Michel, Florian, Teresa, Vanessa, Ezgi, Katia, Yuri, etc…

I also have good memories from my short stay in the far west, the rainy Carlsbad. I would like to thank the personnel from the LANL and CEMRC, Dr. Don Reed, Danielle, Marian and Barbara Borkowski, Jullie, Punam, Michael, etc… But I would like to specially thank Jean Francois and Kae Lucchini for letting me stay in their house, for all the help I received and definitively for being such good friends!

Many thanks also to the external reviewers of this thesis that have contributed to the improvement of this work with their comments and suggestions. Thanks Dr. Nils Baumann and Dr. Daniel Serrano-Purroy. I appreciate also the interest of Dr. Laura Aldave de las Heras in the reviewing of this Thesis.

Me gustaría agradecer a ENRESA y más concretamente a Aurora Martínez-Esparza su colaboración y su apoyo en el desarrollo de esta Tesis.

También quiero agradecer al ministerio de Economia y Competitividad por el apoyo económico que he recibido a través de la beca FPI y las becas adicionales que ofrece el programa para realizar estancias breves.

Per acabar m'agradaria agrair a la meva família tot el recolzament que m'han donat sempre i a la Sara per la seva companyia, valentia i suport en els moments mes durs, i la seva alegria i felicitat en els bons moments, gràcies per viure amb mi aquesta aventura.

Moltes gràcies a tots!

Albert.

Table of contents

List of acronyms

AGP	Almacenamiento Geológico Profundo
BET	Brunauer Emmett Teller
BSE	BackScattered Electron
CC	Charge Compensation
CCD	Charge Coupled Device
CNG	Combustible Nuclear Gastado / Combustible Nuclear Gastat
Cryo-TRLFS	Time-Resolved Laser-induced Fluorescence Spectroscopy at low temperature
DGR	Deep Geologic Repository
ENRESA	Empresa Nacional Residuos Radioactivos S.A.
ENUSA	Empresa Nacional del Uranio S.A.
ESEM	Environmental Scanning Electron Microscopes
fs-TRLFS	Ultra-short laser pulse induced time-resolved spectroscopy
GC	Gas Chromatography
HLNW	High Level Nuclear Waste
HLNWR	High Level Nuclear Waste Repository
HLW	High Level Waste
HOMO	Highest Occupied Molecular Orbital
HZDR	Helmholtz-Zentrum Dresden-Rossendorf
ICCD	Intensified Charge Coupled Device
ICP	Inductively Coupled Plasma
ICP-MS	Inductively Coupled Plasma Mass Spectrometry
IE	Ionization Energy
INE	Institute Nuclear Waste Disposal
IR	Infra Red
LC	Liquid Chromatography

LET	Linear Energy Transfer
LIBD	Laser-Induced BreakDown Spectroscopy
LIBS	Laser-Induced BreakDown Spectroscopy
LIPAS	Laser Induced PhotoAcoustic Spectroscopy
MDA	Minimum Detectable Activities
MGP	Magatzem Geològic Profund
MOX	Mixed OXide fuel
NEA	Nuclear Energy Agency
PIPS	Passivated Implanted Planar Silicon
PWR	Pressurized Water Reactor
pzc	Point of Zero Charge
RF	Radio Frequency
SEM	Scanning Electron Microscopy
SEV	Sekundär Elektronen Vervielfacher ; Secondary Electron Multiplier
SFM	Scanning Force Microscope
SNF	Spent Nuclear fuel
STAR	STability constants by Absorbance Reading
SWNIR	Short Wavelength Near Infra Red
TMACl	TetraMethylAmmonium Chloride
TMAH	TetraMethylAmmonium Hydroxide
TRLFS	Time-Resolved Laser-induced Fluorescence Spectroscopy
USA	United States of America
UV	Ultra Violet
UV-Vis	Ultra Violet Visible
WIPP	Waste Isolation Pilot Plant
XRD	X-Ray Difraction

Summary

The nuclear waste produced in the nuclear industry is one of the most complex materials known and one of the major disadvantages in the use of nuclear energy. The most accepted solution for the final treatment of this waste is the deep geologic repository (DGR). The DGR is designed in a way that the waste will be protected by different barriers for hundreds of thousands of years. Nevertheless in the DGR safety assessment, very conservative but still reasonable suppositions must be assumed. For example, the contact of the spent nuclear fuel (SNF) with water due to a failure in the canister would be a conservative but still plausible hypothesis. Concrete and cementitious materials will be part of the DGR structure. Water in contact with those materials will have a very alkaline pH. Once the water gets in contact with the SNF the following 4 stages may take place: Radiolysis, Oxidation, Dissolution and Secondary Phase Formation.

The formation of uranyl-peroxide complexes was studied at alkaline media by using UV-Visible spectrophotometry and the STAR code. Two different complexes were found at a H_2O_2/U(VI) ratio lower than 2. A graphical method was used in order to obtain the formation constants of such complexes and the STAR program was used to refine the formation constants values because of its capacity to treat multiwavelength absorbance data and refining equilibrium constants. The values obtained for the two equilibrium constants were: $\log \beta^{\circ}_{1,1,4} = 28.1 \pm 0.1$ and $\log \beta^{\circ}_{1,2,6} = 36.8 \pm 0.2$.

$$UO_2^{2+} + H_2O_2 + 4OH^- \leftrightarrows UO_2(O_2)(OH)_2^{2-} + 2H_2O: \beta^{\circ}_{1,1,4}$$

$$UO_2^{2+} + 2H_2O_2 + 6OH^- \leftrightarrows UO_2(O_2)_2(OH)_2^{4-} + 4H_2O: \beta^{\circ}_{1,2,6}$$

At hydrogen peroxide concentrations higher than 10^{-5} mol dm^{-3}, and in the absence of carbonate, the $UO_2(O_2)_2(OH)_2^{4-}$ complex is predominant in solution, indicating the significant affinity of peroxide ions for uranium and the strong complexes of uranium(VI) with peroxide.

Time-resolved laser-induced fluorescence spectroscopy (TRLFS) was used to study the speciation of uranium(VI) at very alkaline pH (11–13.5), at room temperature and in the absence of CO_2. In this case, at pH = 11, two different fluorescence lifetimes appeared, which were attributed to the species $UO_2(OH)_3^-$ and $(UO_2)_3(OH)_7^-$. At pH = 13, no fluorescence was detected, indicating that the predominant species,$UO_2(OH)_4^{2-}$, is not fluorescent. At pH = 12, the lifetime obtained is attributed to the predominant species $UO_2(OH)_3^-$.

Because of the absence of fluorescence of the $UO_2(OH)_4^{2-}$ species at room temperature, measurements at 10 K were made, obtaining two different lifetimes in the pH range between 12 and 13.5, indicating the presence of two different species: $UO_2(OH)_3^-$ and $UO_2(OH)_4^{2-}$. The difference between the lifetimes allowed the calculation of the contribution of each species to the total fluorescence signal intensity.

From the experiments carried out in the presence of hydrogen peroxide, it was observed that hydrogen peroxide produces a quenching effect to the fluorescence of the uranium species. At pH 12 the quenching is static, which points to the formation of a non-fluorescent complex between U(VI) and hydrogen peroxide.

Using the Stern–Volmer equation for static quenching, the equilibrium formation constant of the first species, $UO_2O_2(OH)_2^{2-}$, was calculated to be $\log K_0 = 28.7 \pm 0.4$, which is similar to the one determined using UV–Visible spectrometry.

A flow-through experimental reactor has been designed in order to perform studies at both high pressure and high temperature conditions. A chromatographic pump is used to impulse the leachant throughout the reactor in order to work at very low flows but high pressures. Therefore, high surface solid to volume leachant ratios, similar to the ones predicted in the final repository, can be obtained. The reactor allows working at different atmospheres at pressures up to 50 bars. The temperature inside the reactor can be set using a jacket.

Using this new reactor the evolution of uranium concentrations released from an UO_2 sample was studied at different conditions. The dissolution rates were higher in the solution with $1 \cdot 10^{-3}$ mol·dm^{-3} HCO_3^- and $19 \cdot 10^{-3}$ mol·dm^{-3} $NaClO_4$ than with pore water, due to the

effect of carbonates. At hydrogen pressures between 5 and 7 bars, hydrogen was only capable to partially reduce the effect of hydrogen peroxide on the dissolution rate of uranium. It was concluded that, under hydrogen atmosphere, the presence of hydrogen peroxide increases the dissolution rate of uranium by several orders of magnitude with or without carbonates.

The effects of alpha-radiolysis were determined, on one hand, through the generation of radiolytic products: H_2, O_2, HClO and H_2O_2, and on the other hand from the dissolution of both U and Pu. The studies were focused on the effect produced by different dose rates, different ionic strength as well as varying the location of the alpha-emitters (either into the pellets or dissolved in solution) The experiments were performed at pH 12.

Regarding the O_2 and H_2 production neither the location of the alpha-emitters nor the ionic strength had any effect on the gas formation. The ionic strength is a key factor for the formation of HClO or H_2O_2. At high ionic strength only the HClO formation is observed, while at low ionic strength only the H_2O_2 formation is observed. Higher dose rates increases the formation of radiolysis products and the dissolution of U and Pu.

The experimental data regarding the formation of O_2 and H_2 was fitted using Macksima-Chemist software, obtaining a good simulation in the studied accumulated dose range in the formation of O_2, an especially at accumulated doses higher than 40 kGy in the formation of H_2. The model proved to be sensitive to the changes in most of the G-values but robust to the changes in the kinetic constants.

The sorption of Se(IV) and Se(VI) on uranium peroxide has been studied considering the sorption kinetics, the sorption isotherms and the effect of pH. Selenium sorption on studtite is fitted with a pseudosecond order reaction model; in addition, two different mechanisms seem to influence the sorption process: micropore diffusion and intra-particle diffusion. Both selenium(IV) and selenium(VI) are sorbed on studtite through a monolayer coverage. Sorption is higher at acidic pH than at alkaline pH. This behaviour is consistent with the chemical speciation of selenium in solution and with the acid-base properties of the solid.

Sumario

Los residuos nucleares producidos por la industria nuclear son uno de los materiales conocidos más complejos y una de las mayores desventajas en el uso de la energía nuclear. La solución más aceptada para el tratamiento final de residuos nucleares es el almacenamiento geológico profundo (AGP). El AGP está diseñado de manera que el residuo estará protegido por diferentes barreras a lo largo de cientos de miles de años. No obstante en el informe de evaluación de la seguridad de un AGP, se deben considerar hipótesis muy conservadoras aunque razonables. Por ejemplo el contacto del combustible nuclear gastado (CNG) con agua debido a un fallo en la cápsula de protección es una hipótesis conservadora pero plausible. Hormigón y cemento estarán presentes en la estructura del AGP. El agua en contacto con estos materiales tendrá un pH muy alcalino. El agua que entre en contacto con el CNG puede sufrir 4 procesos diferentes: Radiólisis, Oxidación, Disolución y Formación de Fases Secundarias.

La formación de complejos uranilo-peróxido se estudió en medio alcalino usando espectrofotometría UV-Visible y el código STAR. Se encontraron dos complejos diferentes en un ratio H_2O_2/U(VI) más bajo de 2. Se usó un método gráfico para obtener información de dichos complejos y el programa STAR para refinar los valores de las constantes de formación debido a su capacidad para tratar datos de absorbancia en múltiples longitudes de onda y para refinar constantes de equilibrio. Los valores obtenidos para las dos contantes de equilibrio fueron: $\log \beta^{\circ}_{1,1,4} = 28.1 \pm 0.1$ y $\log \beta^{\circ}_{1,2,6}=36.8 \pm 0.2$.

$$UO_2^{2+} + H_2O_2 + 4OH^- \leftrightarrows UO_2(O_2)(OH)_2^{2-} + 2H_2O: \beta^{\circ}_{1,1,4}$$

$$UO_2^{2+} + 2H_2O_2 + 6OH^- \leftrightarrows UO_2(O_2)_2(OH)_2^{4-} + 4H_2O: \beta^{\circ}_{1,2,6}$$

A concentraciones de peróxido de hidrogeno más altas de 10^{-5} mol dm^{-3}, y en ausencia de carbonatos, el complejo $UO_2(O_2)_2(OH)_2^{4-}$ es predominante en solución, indicando la significativa afinidad de los iones peróxido por el uranio y los fuertes complejos del uranio (VI) con el peróxido.

La espectroscopia de fluorescencia inducida por láser resuelta en el tiempo (TRLFS) se usó para estudiar la especiación del uranio (VI) a pHs muy alcalinos (11-13.5), a temperatura ambiente y en ausencia de CO_2. A pH=11, aparecieron dos tiempos de vida que fueron atribuidos a las especies $UO_2(OH)_3^-$ y $(UO_2)_3(OH)_7^-$. A pH=13 no se detectó ningún tipo de fluorescencia, indicando que la especie predominante $UO_2(OH)_4^{2-}$ no es fluorescente. A pH=12 el tiempo de vida obtenido se atribuyó a la especie predominante $UO_2(OH)_3^-$.

Debido a la ausencia de fluorescencia de la especie $UO_2(OH)_4^{2-}$ a temperatura ambiente, se hicieron medidas a 10 K, obteniendo dos tiempos de vida diferentes en un rango de pH entre 12 y 13.5. Esto indicó la presencia de dos especies $UO_2(OH)_3^-$ y $UO_2(OH)_4^{2-}$. La diferencia entre tiempos de vida permitió el cálculo de la contribución de cada especie a la intensidad de la señal de fluorescencia total.

En los experimentos llevados a cabo en presencia de peróxido de hidrogeno, se observó que el peróxido de hidrogeno produce un efecto de extinción (quenching) de la fluorescencia de las especies de uranio. A pH 12 la extinción era estática, cosa que apunta a la formación de un complejo no-fluorescente entre el U(VI) y el peróxido de hidrogeno.

Usando la ecuación de Stern-Volmer para la extinción estática se calculó la constante de equilibrio de la especie $UO_2O_2(OH)_2^{2-}$ obteniendo un valor similar al obtenido por espectrofotometría UV-Visible.

Se diseñó un reactor experimental de flujo para hacer estudios tanto a altas presiones como a elevadas temperaturas. Se usó una bomba de cromatografía para impulsar el lixiviante a través del reactor de manera que trabaje a alta presión pero a un caudal muy reducido. De esa manera la relación superficie del solido volumen de lixiviante es muy alta y similar a la que se predice en un AGP. El reactor permite trabajar con diferentes atmosferas hasta 50 bares de presión. La temperatura dentro del reactor se puede ajustar usando una camisa.

Usando este nuevo reactor se estudió la evolución de la concentración de uranio liberado de una muestra de UO_2, en diferentes condiciones. Las velocidades de disolución fueron más altas en la solución con $1 \cdot 10^{-3}$ mol·dm^{-3} de HCO_3^- y $19 \cdot 10^{-3}$ mol·dm^{-3} de $NaClO_4$ que con agua de poro debido al efecto de los carbonatos. A presiones de hidrogeno entre 5 y

7 bares, el hidrogeno solo fue capaz de reducir parcialmente el efecto del peróxido de hidrogeno en la velocidad de disolución del uranio. Se concluyó que en atmosfera de hidrogeno, la presencia de peróxido de hidrogeno aumenta en varios ordenes de magnitud la velocidad de disolución del uranio con o sin carbonatos.

Se determinaron los efectos de la alfa-radiólisis, por un lado a través de la generación de productos radiolíticos: H_2, O_2, HClO y H_2O_2 y por otro lado a partir de la disolución de U y Pu. Los estudios se centraron en el efecto producido por diferentes tasas de dosis, diferentes fuerzas iónicas, así como también modificando la localización de los emisores alfa (dentro de la pastilla o disueltos en la solución). Los experimentos se realizaron a pH 12.

En cuanto a la producción de O_2 y H_2, ni la localización de los emisores alfa ni la fuerza iónica tienen ningún efecto en la formación de gas. La fuerza iónica es un factor clave en la formación de HClO y H_2O_2. A elevadas fuerzas iónicas se observa solo formación de HClO, mientras que a baja fuerza iónica solo se observa formación de H_2O_2. Tasas de dosis altas incrementan la formación de productos radiolíticos y la disolución de U y Pu.

Los datos experimentales referentes a la formación de O_2 y H_2 fueron ajustados usando el software Macksima-Chemist, consiguiendo una buena simulación de la formación de O_2 en el rango de dosis acumulada estudiado y de la formación de hidrogeno, especialmente para dosis acumuladas superiores a 40 kGy. El modelo demostró ser sensible a cambios producidos en la mayoría de los valores G, pero robusto frente a cambios en el valor de las constantes cinéticas.

Se ha estudiado la sorción de Se(IV) y Se(VI) en el peróxido de uranio considerando la cinética de sorción, la isoterma de sorción y el efecto del pH. La sorción de Selenio en Studtita se ajusta a un modelo de reacción de pseudo-segundo orden. Además hay dos mecanismos diferentes que parecen influenciar el proceso de sorción: difusión por microporos y difusión intra-particular. Ambos Se(IV) y Se(VI) se sorben en la Studtita a través de una cobertura monocapa. La sorción es más alta a pH ácido que a pH básico. Este comportamiento es consistente con la especiación química del Selenio en solución y con las propiedades ácido-base del sólido.

Sumari

Els residus nuclears produïts per la industria nuclear són un dels materials coneguts més complexes i un dels majors inconvenients de l'ús de l'energia nuclear. La solució més acceptada per al tractament final de residus nuclears és el magatzem geològic profund (MGP). El MGP esta dissenyat de manera que el residu estarà protegit per diferents barreres al llarg de centenars de milers d'anys. No obstant en l'informe de l'avaluació de seguretat de un MGP, s'han de considerar hipòtesi molt conservadores tot i que raonables. Per exemple el contacte del combustible nuclear gastat (CNG) amb l'aigua degut a una fallada en la càpsula de protecció és una hipòtesis conservadora però plausible. Formigó i ciment seran presents en l'estructura del MGP. L'aigua en contacte amb aquests materials tindrà un pH molt alcalí. L'aigua que entri en contacte amb el CNG pot patir 4 processos diferents: Radiòlisi, Oxidació, Dissolució i Formació de Fases Secundàries.

La formació de complexes uranil-peròxid va ser estudiada en medi alcalí utilitzant espectrofotometria UV-Visible i el codi STAR. Es van trobar dos complexes diferents en una ràtio H_2O_2/U(VI) per sota de 2. Es va usar un mètode gràfic per obtenir informació dels complexes esmentats i s'utilitzà el programa STAR per a refinar els valors de les constants de formació degut a la seva capacitat per a tractar dades d'absorbància en múltiples longituds d'ona i per refinar constants d'equilibri. Els valors obtinguts per a les dues constants de equilibri van ser: $\log \beta^{\circ}_{1,1,4} = 28.1 \pm 0.1$ i $\log \beta^{\circ}_{1,2,6} = 36.8 \pm 0.2$.

$$UO_2^{2+} + H_2O_2 + 4OH^- \leftrightarrows UO_2(O_2)(OH)_2^{2-} + 2H_2O: \beta^{\circ}_{1,1,4}$$

$$UO_2^{2+} + 2H_2O_2 + 6OH^- \leftrightarrows UO_2(O_2)_2(OH)_2^{4-} + 4H_2O: \beta^{\circ}_{1,2,6}$$

A concentracions de peròxid d'hidrogen més altes de 10^{-5} mol dm^{-3}, i en absència de carbonats, el complex $UO_2(O_2)_2(OH)_2^{4-}$ és predominant en solució, indicant la significativa afinitat dels ions peròxid per l'urani i els forts complexos d'urani(VI) amb el peròxid.

L'espectroscòpia de fluorescència induïda per làser resolta en el temps (TRLFS) s'utilitzà per estudiar l'especiació de l'urani (VI) a pHs molt alcalins (11-13.5), a temperatura ambient i en absència de CO_2. En aquest cas, a pH=11, aparegueren dos temps de vida que van ser atribuïts a les espècies $UO_2(OH)_3^-$ i $(UO_2)_3(OH)_7^-$. A pH=13 no es detectà cap tipus de fluorescència, indicant que l'espècie predominant $UO_2(OH)_4^{2-}$ no és fluorescent. A pH=12 el temps de vida obtingut s'atribuí a l'espècie predominant $UO_2(OH)_3^-$.

Degut a l'absència de fluorescència de l'espècie $UO_2(OH)_4^{2-}$ a temperatura ambient, es varen fer mesures a 10 K, obtenint dos temps de vida diferents en un rang de pH entre 12 i 13.5. Això indicà la presència de dos espècies $UO_2(OH)_3^-$ i $UO_2(OH)_4^{2-}$. La diferència entre temps de vida va permetre el càlcul de la contribució de cada espècie a la intensitat del senyal de fluorescència total.

En els experiments que es van dur a terme en presència de peròxid d'hidrogen, s'observà com el peròxid d'hidrogen produeix un efecte de extinció (quenching) de la fluorescència de les espècies d'urani. A pH 12 l'extinció era estàtica, cosa que va apuntar a la formació de un complex no fluorescent entre el U(VI) i el peròxid d'hidrogen.

Utilitzant l'equació de Stern-Volmer per a l'extinció estàtica es va calcular la constant d'equilibri de l'espècie $UO_2O_2(OH)_2^{2-}$ obtenint un valor similar a l'obtingut per espectrofotometria UV-Visible.

Es va dissenyar un reactor experimental de flux per fer estudis tant a altes pressions com a elevades temperatures. Es va usar una bomba de cromatografia per impulsar el lixiviant a través del reactor de forma que treballés a alta pressió però a un cabal molt reduït. D'aquesta manera la relació entre la superfície del sòlid i el volum de lixiviant és molt alta i similar a la que es preveu en un MGP. El reactor permet treballar amb diferents atmosferes fins a 50 bars de pressió. La temperatura de dins del reactor es pot ajustar mitjançant una camisa.

Utilitzant aquest nou reactor es va estudiar l'evolució de la concentració d'urani alliberat d'una mostra de UO_2, en diferents condicions. Les velocitats de dissolució van ser mes altes en la solució amb $1 \cdot 10^{-3}$ mol·dm^{-3} de HCO_3^- i $19 \cdot 10^{-3}$ mol·dm^{-3} de $NaClO_4$ que amb

aigua de por degut a l'efecte dels carbonats. A pressions d'hidrogen entre 5 i 7 bars, l'hidrogen només va ser capaç de reduir parcialment l'efecte del peròxid d'hidrogen en la velocitat de dissolució de l'urani. Es va concloure que en atmosfera d'hidrogen, la presencia de peròxid d'hidrogen augmenta en diversos ordres de magnitud la velocitat de dissolució de l'urani amb o sense carbonats.

Es determinaren els efectes de l'alfa-radiòlisi, d'un cantó a través de la generació de productes radiolítics: H_2, O_2, HClO i H_2O_2 i de l'altre a partir de la dissolució de U i Pu. Els estudis es centraren en l'efecte produït per diferents taxes de dosi, diferents forces iòniques, així com també modificant la localització dels emissors alfa (dins de la pastilla o dissolts en la solució). Els experiments es realitzaren a pH 12.

Pel que fa a la producció de O_2 i H_2, ni la localització dels emissors alfa ni la força iònica tenen cap efecte en la formació de gas. La força iònica és un factor clau en la formació de HClO i H_2O_2. A elevada força iònica s'observa només formació de HClO, mentre que a baixa força iònica tan sols es veu formació de H_2O_2. Taxes de dosi altes augmenten la formació de productes radiolítics i la dissolució de U i Pu.

Les dades experimentals referents a la formació de O_2 i H_2, es van ajustar utilitzant el software Macksima-Chemist, aconseguint una bona simulació de la formació de O_2 en el rang de dosis acumulada estudiat i de la formació d'hidrogen, especialment per a dosis acumulades superiors a 40 kGy. El model va demostrar ser sensible a canvis en la majoria de valors G, però robust davant de canvis en el valor de les constants cinètiques.

S'ha estudiat la sorció de Se(IV) i Se(VI) en el peròxid d'urani considerant la cinètica de sorció, la isoterma de sorció i l'efecte del pH. La sorció de Seleni en Studtita s'ajusta a un model de reacció de pseudo-segon ordre. A més a més hi ha dos mecanismes diferents que semblen influenciar el procés de sorció: difusió per microporus i difusió intra-particular. Ambdós Se(IV) i Se(VI) es sorveixen en la Studtita a través d'una cobertura monocapa. La sorció és més alta a pH àcid que a pH bàsic. Aquest comportament és consistent amb l'especiació química del Seleni en solució i amb les propietats àcid-base del sòlid.

1 Introduction

1 Introduction

1.1. Uranium as a waste

Every year in the world tons of nuclear wastes are generated. Most of them come as by-products of nuclear power generation or from nuclear weapons decommissioning. A small percentage of the total is generated by hospitals, pharmaceutical industries, research centers, etc...

Spain has 6 nuclear power plants and a total of 8 nuclear reactors. It has also some uranium mines, uranium factories and some reprocessed spent fuel in France and England (Figure 1.1).

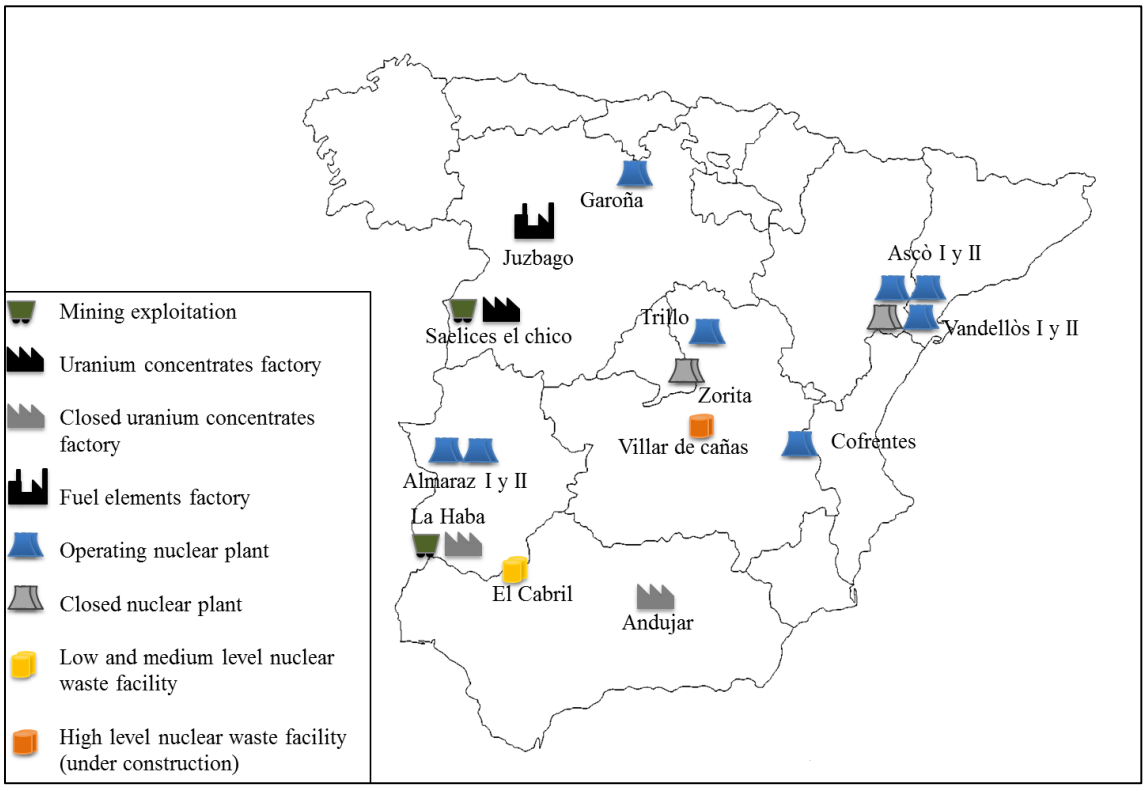

Figure 1.1. Spanish map of radioactive installations (Baró et al. [1]).

The fuel for nuclear power plants in Spain is composed mainly of oxides of U^{238} with a variable enrichment of U^{235} up to 5%. Once inside the reactor the nuclear fuel is submitted to various processes that causes the appearance of several secondary

products, with representation in nearly the entire periodic table. These secondary products are generally classified as activation products, fission products, minor actinides and Pu. The transuranides (Pu and minor actinides) are generated due to successive reactions of the neutron layer of U^{238}. Those reactions are mainly neutron capture and alpha, beta and gamma decay. In neutron capture a neutron is caught by an atom core, increasing the atom mass. In the alpha decay case an Helium nucleus (alpha particle) is expulsed from the core in order to become more stable. The resulting atom has less atomic mass and a lower atomic number. In decay beta reactions a neutron is transformed into a proton generating and electron and an electron antineutrino. The resulting atom has increased the atomic number. Sometimes the opposite can occur, a proton is converted into a neutron emitting a positron and an electron neutrino. Depending on the energy levels photons (gamma rays) can also be emitted.(Figure 1.2).

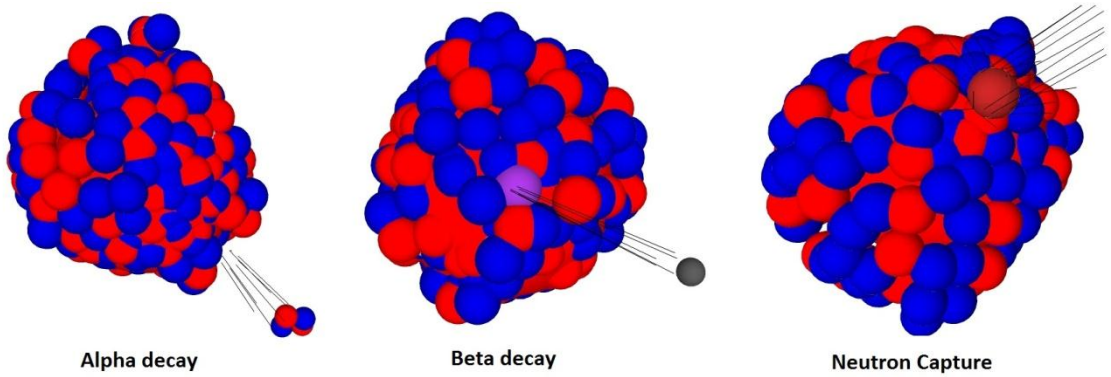

Figure 1.2. Alpha decay, beta decay and neutron capture.

The fission products are generated due to the fission of the fuel, and the activation products are produced by neutron activation of the in-core structure materials, the control rods, the reactor coolant and the fuel impurities. Depending on the time the fuel spends in the reactor, we can talk of various degrees of burn-up, which are a measure of the energy produced in megawatt days per ton of initial uranium. The final burn-up grade of the uranium pellets has increased over the years because of the interest in maximizing the fuel efficiency.

Most radionuclides are distributed heterogeneously inside the matrix of UO_2, according to the fission yield, which changes from the center to the periphery of the

fuel. The burning of the fuel depends not only on the position in the pin but also inside the pellets, the periphery of the fuel is submitted to higher neutron capture and fission yield and therefore, more fission products and less uranium than in the center are expected to be found. These radionuclides react and behave in different ways, either forming precipitates, oxidizing themselves, in gaseous fraction form or in solid solutions.

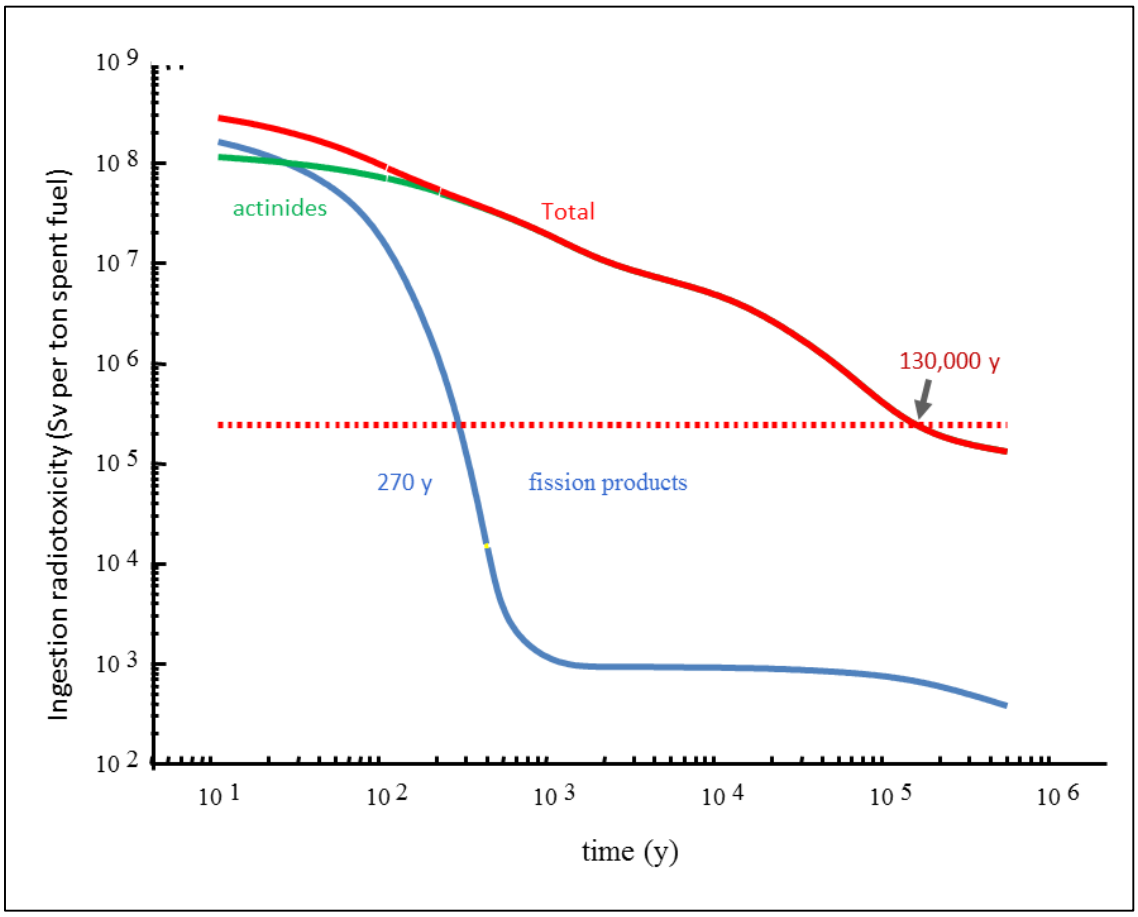

Figure 1.3. Radiotoxicity curves of the fission products and actinides for one tone of spent fuel in dependence of time. The horizontal dot line, is the radio toxic level of 7.83 tons of natural uranium, in equilibrium with its daughters, needed to produce 1 ton of enriched uranium (Magill [2]).

The life of radionuclides varies depending on their typology. After 270 years the radiotoxicity of the fission products will be lower than the radiotoxicity of the amount of natural uranium needed to produce 1 ton of enriched uranium. After 270 years the actinides will be the main responsible for the radiotoxicity of the spent nuclear fuel. Only after 130000 years the radiotoxicity of the actinides will reach the same radiotoxic

level. Fission products are mainly generators of β and γ radiation, and actinides emit mostly α radiation. After 270 years the radiotoxicity is predominantly due to α particles generated mainly from actinide elements (Figure 1.3).

1.2. Spent fuel in deep geological repository

Currently the most widely accepted solution for the nuclear waste, by the international scientific community, is the deep geological repository (DGR).

Some countries like Sweden and Finland have this option very advanced while others like Spain still do not have a clear resolution.

The DGR is based on a multibarrier concept. It is designed to last the time needed for most of the nuclear waste to decay into harmless substances. It is not necessary to contain the nuclear waste forever, but the DGR needs to be designed in a way that the multiple barriers guarantee that the waste that reaches the biosphere is in quantities that don't have any significant impact.

We will talk about engineered barriers, geological barrier and biospherical barriers.

The engineered barriers are the fuel matrix itself, the cladding, the storage capsules and the compacted clay barrier (bentonite). Its function is to isolate the capsule from water, to dissipate heat and to give mechanical protection.

The geological barrier will vary depending on the lithological characteristics of the site chosen to hold the repository. In any case, the chosen site has to be a seismically stable place, lithologically homogeneous, where water has difficulty to reach the waste and then transport it to the biosphere, and that protects the engineered barriers. Accidental human intrusion has to be avoided, although in some cases DGR are designed thinking about a hypothetical future option of reopening the repository for reuse or retreat of the waste.

Regarding the geological barrier three kinds of lithologies are the most studied to host a deep geologic repository: Clay lithology, salt lithology and granite lithology.

The different characteristics of each lithology are shown in Table 1.

Table 1. Characteristics of the different lithologies.

Characteristics	**Clay**	**Salt**	**Granite**
Permeability	Very low	Very low	Low
Radionuclide retention capacity	High	Very low	Variable
Plasticity	Variable	-	-
Thermal conductivity	Low	High	Moderated
Corrosivity	Low	High	-
Erosionability	High	High	Low
Radionuclide transport	Diffusive	Diffusive	Diffusive (matrix) Dispersive (fractures)
Supporting Systems	Required	-	-
Pore water salinity	High	-	-
Fracturing	-	Very low	-
Solubility	-	High	Low
Excavation	-	Easy	-
Self-sealing property	-	Yes	-
Red-Ox capacity	-	-	High
Tectonic stability	-	-	Yes
Resistance	-	-	High

The biospherical barrier is the final receptor of the radionuclides, and the ability of dispersion and dilution to the biosphere is considered as the last barrier (Astudillo [3]).

1.3. Processes that affect the UO_2 matrix

In a DGR water is considered as the most likely media through which the transport of radionuclides can occur.

The most conservative projections consider that it may take 1000 years until a defective canister breaks and water comes into contact with the fuel. At this situation there will be a series of steps or reactions between the fuel and water (Cera et al. [4]).

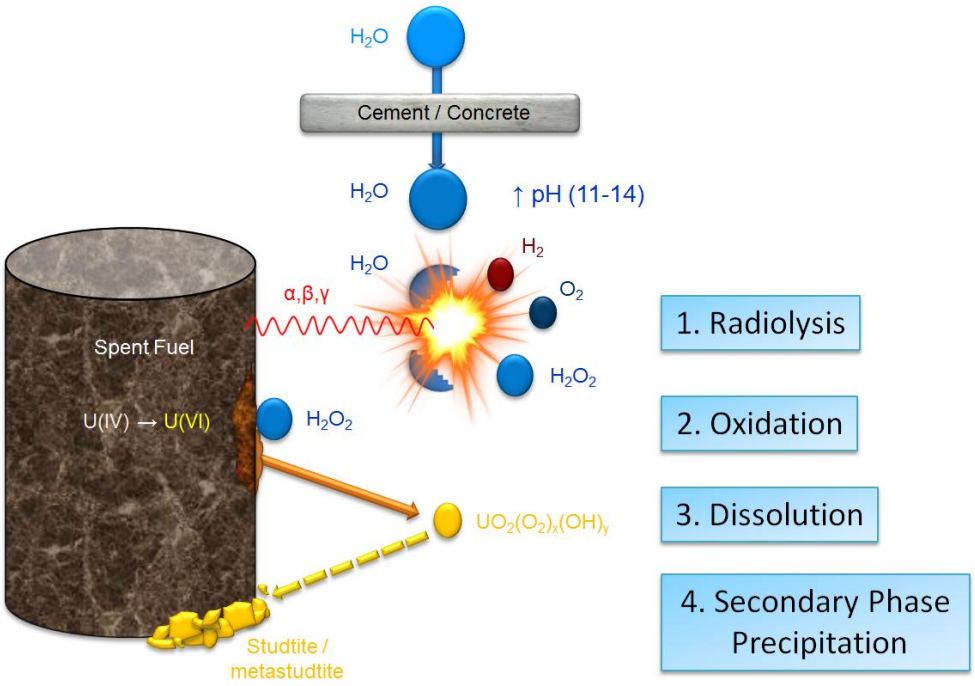

Figure 1.4. Processes affecting the Spent fuel matrix

1. Water radiolysis.

   α, β and γ particles emitted by the spent fuel will generate O_2, H_2 and H_2O_2 from the radiolysis of the water molecules.

2. Fuel oxidation.

   The oxidants generated by water radiolysis oxidize the surface of the fuel matrix, where the U (IV) will be oxidized to U (VI).

3. Fuel dissolution.

   The previous oxidation will enhance the dissolution of UO_2 releasing some of the radionuclides stuck in the matrix of the fuel. At this stage the carbonates present in water play an important role since they form very stable complexes with U(VI).

4. Precipitation of secondary phases.

   The expected liquid/solid volume ratio will be very low. Then saturation conditions will be reached very soon and therefore precipitation of uranium secondary phases will take place.

Each stage may differ depending on various parameters such as pH, temperature, composition of water etc. ... Because of that, several studies have been done, including the effect of temperature on the mechanisms of dissolution of UO_2 (De Pablo et al. [5] Serrano et al. [6]), the effect of radiation (Eriksen et al. [7], Jégou et al. [8]) or the formation of a secondary phase as Studtite ($UO_4 \cdot 4H_2O$) (Clarens et al. [9], Rey et al. [10]).

There are some articles and publications that try to collect all the studies on this subject such as the Fuel corrosion processes under waste disposal conditions (Shoesmith, [11]) or the Modelling spent Fuel and HLW Behaviour in Repository Conditions (ENRESA, [12]).

However most of the studies performed are at acid, neutral or low alkaline pH conditions, being difficult to find data at pH conditions higher than 10 (hyperalkaline). This pH conditions are reached easily if the water flows through cement or concrete materials that could be present in the deep geologic repository as structural or sealing materials. Reducing this lack of data is one of the main objectives of this thesis together with the studies of one of the main oxidants produced by radiolysis at low ionic strength, the hydrogen peroxide. Due to that, most of the experiments performed in this thesis are performed at hyperlalkaline pH with hydrogen peroxide species.

The radiolysis experiments performed in chapter 7, at pH 12, quantified for the first time, the formation of radiolysis gases O_2 and H_2 at low ionic strength in the presence of hydrogen peroxide formed by radiolysis. The speciation of UO_2 at hyperlalkaline pH is rather unknown; therefore in chapter 5, Time Resolved Laser Induced Fluorescence Spectroscopy (TRLFS) analyses were made at pH higher than 11, determining the predominant species at hyperalkaline pH. Also in chapter 5 but especially in chapter 4 the interactions with H_2O_2 and UO_2 at pH 12 were analyzed, determining the formation constants of two uranium hydroxoperoxocomplexes. Experiments at the deep geologic repository conditions are a challenge due to its complexity. In chapter 6 experiments to study the dissolution of UO_2 at high pressures and anoxic and reducing conditions with a very low flow of hyperalkaline leachant were made using H_2O_2 as oxidant. The sorption capacities of the main uranium secondary phase of hydrogen peroxide: Studtite, were studied in chapter 8.

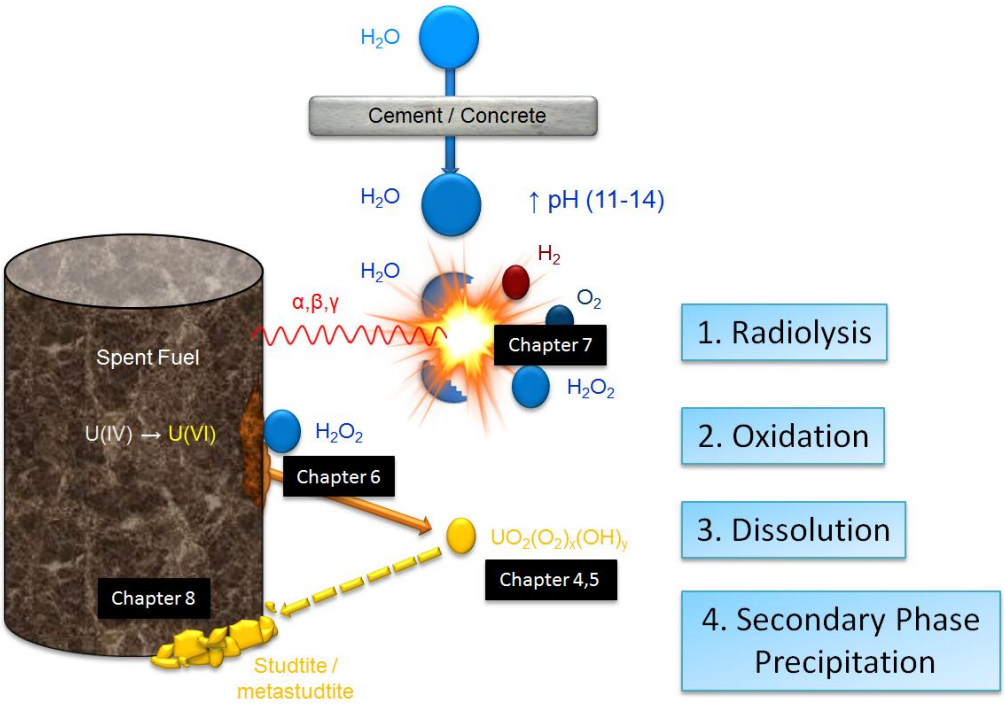

Figure 1.5. Scheme of the chapters of the thesis related to the processes affecting the Spent fuel matrix

1.4. Water radiolyis

Radiation alpha, beta and gamma, interacts with molecules producing new species. Reducing species like Hydrogen [13], and oxidizing species like Hydrogen peroxide or oxohalogenides such as HClO [14] may form depending on water chemistry.

In order to study the effects of radiation, different approaches are possible:

- Direct addition of radiolysis products: With this method it is possible to work in non-rad laboratories.[15-19]
- Addition of a short-lived isotope: This method is more complex but it is possible to analyze the results in a non-rad laboratory, and the radiolysis products are formed in situ [20-21].
- Use of cyclotron radiation: Much more costly and complex, but it has the advantage that nothing needs to be added to the system [22,23].
- Doped pellets with a radioactive element: It is necessary to work in a rad laboratory but the experimental set-up is the closer to the expected scenario, in a deep geologic repository [24-28.]

Most of these approaches were used to study the radiolysis at acid media or neutral-alkaline media but there is a lack of data at high pH. In the Institute of Nuclear Waste Disposal, the group of Kelm, Bohnert, Metz and Gonzalez-Robles [14,29] have performed some studies of the effects of the formation of radiolysis products at pH 12. These studies were focused mainly at high ionic strength conditions were no hydrogen peroxide is formed. However, the groundwater of some lithologies like granite does not have a high ionic strength, and therefore it is also important to know if the production of radiolysis products is affected by the presence of hydrogen peroxide in solution instead of oxo-halogenides at high pH.

1.5. Matrix fuel oxidation

Because of the possible spent fuel matrix oxidation, many studies have been carried out and are being carried out on the behavior of uranium in contact with oxidants.

Oxidation of UO_2 can be favored by adding chlorides or sulfates of alkaline earth elements or by generating superoxides in the solution. In the first case oxidation increases as decreases the atomic radius of the cation. For example it will be most favored by Lithium than by Cesium.

It has been observed experimentally that in the presence of these compounds, UO_2 needs much less temperature to oxidize itself, and in the case of superoxide generation in solution, it has been found that if it is combined with the addition of nitrate, the rate of oxidation increases (Volkovich et al. [30]).

Peper et al [31] studied the dissolution of UO_2 with various oxidants, and saw how the hydrogen peroxide was the one with the faster initial dissolution. This result is due in part to the ability of peroxide to act both as oxidizing and as ligand in alkaline conditions.

On the other hand Sunder et al. [32] studied the corrosion of hydrogen peroxide at different concentrations, and they found that it behaved differently depending on the range of concentration. Specifically for lower concentrations than 10^{-4} $mol \cdot dm^{-3}$ corrosion of UO_2 is directly proportional to the concentration of H_2O_2. For concentrations between 10^{-4} and 10^{-2} $mol \cdot dm^{-3}$ decomposition of the peroxide seems to buffer the redox potential of the surface of UO_2. Finally, for concentrations higher than 10^{-2} $mol \cdot dm^{-3}$ the accumulation of products caused by the corrosion of U(VI) creates a layer that can block the decomposition of the peroxide.

But if carbonates are present in the solution, they will prevent the formation of deposits of corrosion products and the decomposition of the peroxide will continue.

Apart from carbonates another factor that influences the UO_2 dissolution is the pH, by lowering the pH, the dissolution of UO_2 accelerates.

Corbel et al. [33] observed differences in the effects of hydrogen peroxide when it is added to the solution and when it occurred due to water radiolysis. If it is added, and in concentrations high enough, it can be observed that a precipitate is forming after some time and the thickness of the layer of precipitate increases with time continuously. But in the case of hydrogen peroxide produced by radiolysis, the growth rate of the layer of precipitates decreases as the thickness increases, until it reaches a point where stops growing.

The combination of hydrogen peroxide and carbonates has been studied in other works, such as the one of Goldik et al. [34] or the one of Goff et al. [35]. In the article by Goff et al. [35], performed in alkali and carbonate media, they observed replacement of one carbonate of the tris-carbonate complex of uranyl by a peroxide, forming a peroxo-carbonate complex. This complex has a great stability in the environment, and thus facilitates the transport of uranium. The effect of temperature and pH in peroxocarbonate media is the motivation of the study in papers from De Pablo et al. [5] and Clarens et al. [18].

Nowadays there is an interest in taking advantage of the dissolution ability of carbonates and hydrogen peroxide to replace the use of nitric acid at high temperature in the process of leaching and recovery of uranium from the spent fuel. The method of carbonates has the advantage that can be done at room temperature, at pH between 8 and 9, which does not generate nitrogen oxides or volatile radionuclides (I, Br, Ru) and does not attack many of the noble metals fission products (Mo, Tc, Ru, Rh, Pd). For some actinides and fission products the reprecipitation leaves the uranium solution with only few other elements. (Soderquist et al. [36], Chung et al. [37] and Stepanov et al. [38]).

The fuel matrix oxidation is not the unique redox process that occurs in the area between the fuel matrix and the cladding. α, β and γ particles emitted by the fuel can also generate hydrogen from water radiolysis. This hydrogen can attack the wall of the

cladding, corroding the steel and generating various iron precipitates such as magnetite. This process can inhibit the oxidation of U(IV) (Ferriss et al. [39]).

The hydrogen peroxide is not only important in the fuel matrix oxidation but also in the uranium complexes formation (Moskvin et al. [40]), uranium secondary phases formation (Clarens et al. [9]) and different crystals and nanoclusters formation (Sigmon et al. [41,42], Unruh et al. [43]).

Merino et al. [44] proposed a model for the mechanism of oxidative dissolution of spent fuel, obtaining results that are in accordance with experimental results obtained for several conditions of pH, carbonate and oxidant concentration.

1.6. Matrix fuel solubility

Another very important step linked to oxidation state is the stage of solubility. As happened in the oxidation processes the solubility is also affected by the presence of carbonates in solution.

There are studies of the solubility of uranium in real contaminated media. Elless et al. [45] studied the solubility of uranium in a contaminated media rich in carbonates such as the environment of Fernald Site (State of Ohio, USA), an old atomic weapons industry. In that study they have seen how there is mainly an anionic uranyl carbonate species, which is not adsorbed in soil and therefore it is very mobile. In fact it has contaminated the groundwater in the area. Other soluble elements such as calcium and magnesium favor the solubility of several uranium minerals too [45].

Other studies of real contaminated media are those of Lind et al. [46], which studied the contamination of the environment due to the use of depleted uranium ammunition and weapons in Kuwait and Kosovo. It has been seen in this case that uranium had high solubility as well as high mobility.

Uranium can be found also as a side product of the phosphate ores used in the fertilizing industries. Decades of waste dumping into the Ebre river (Spain) have caused an accumulation of wastes and sediments in the Flix water reservoir (Catalonia – Spain). Meca et al. [47] were the first to study the uranium speciation in the Flix sediments, determining that uranium was mainly present as meta-autunite [$Ca(UO_2)_2(PO_4)_2 \cdot 10\text{-}12H_2O$], an uranium phase with low solubility that will reduce the mobility of uranium to the river.

Casas et al. [48] determined the dissolution kinetics of UO_2 in oxidizing conditions proposing a first mechanism of oxidation-dissolution of UO_2. Casas et al.[49] also studied the role of pe, pH and carbonate on the solubility of UO_2 at reducing conditions. Reducing conditions in the final repository are possible mainly due to the formation of Hydrogen. Hydrogen can be formed due to anoxic corrosion of iron present on the engineered barriers and also in a small amount due to the radiolysis of water. When the experiments are performed at reducing conditions the dissolution rate decreases in some cases even 4 order of magnitude less than for oxidizing conditions [50,51].

The oxidative dissolution mechanism was improved in De Pablo et al. [5,52] by adding the effect of temperature, pH and oxygen partial pressure. A mechanism of the dissolution of UO_2 due to the uranium-carbonate complexation was proposed. This mechanism was improved at low concentrations of carbonate in the later work of Giménez et al. [53]. Due to the radiolysis of water not only hydrogen is formed, but also another species like O_2 and H_2O_2. Hydrogen peroxide is a very strong oxidant. Giménez et al. [54] performed various experiments in order to determine the kinetics of the hydrogen peroxide consumption due to the hydrogen presence. They found a k of 0.029 ± 0.009 $dm^3\ mol^{-1}\ s^{-1}$ for the reaction between hydrogen and hydrogen peroxide. Nilsson et al. [55] studied also the reaction between H_2O_2 and H_2 observing that the UO_2 surface does not have any catalytic effect on the reaction. Palladium on the contrary does have catalytic effects but his presence on the spent fuel is much lower, only due to impurities and as a fission product. Clarens et al. [18] added the concentration of hydrogen peroxide as a new parameter to the oxidative dissolution mechanism studies. They studied the effect of the pH in the dissolution on UO_2 in H_2O_2 solutions. Precipitation of the uranium peroxide Studtite was observed at high

concentrations of hydrogen peroxide adding complexity to the dissolution mechanism. Casas et al. [56] added a new parameter to the dissolution experiments, pressure. They designed a reactor in order to perform experiments up to 100 bars, with temperatures up to 100°C. The reactor was continuosly stirred and they determined UO_2(s) dissolution rates in a hydrogen peroxide and carbonate media as a function of pressure and temperature. Lately Casas et al. [19] improved the knowledge in the effect of carbonate and hydrogen peroxide concentration in UO_2 dissolution observing and increase in the dissolution when both the concentration of carbonate and hydrogen peroxide increased. Sureda et al. [57] studied the kinetics of UO_2 dissolution by an oxidant formed by radiolysis like hydrogen peroxide but stronger, hypochlorite. In solutions with high concentrations of chloride based salts, like the ones present in the saline repository safety assessment models [14], the hydrogen peroxide formed due to alpha radiolysis is rapidly decomposed and on the contrary hypochlorite, chlorite and chlorate are formed. Sureda et al. [57] observed a higher dissolution rate for hypochlorite than for previous works in hydrogen peroxide and oxygen. On the other hand they did not observe any effect of chlorite or chlorate.

All this experiments have something in common. In all of them the rate volume of solid versus volume of liquid was very low. There was a lot of liquid volume for a few grams of UO_2 powder or a small pellet. This low S/V ratio does not reproduce what it is expected in a deep geologic repository where is predicted that only small drops of water could interact with the spent nuclear fuel in the case where all the engineered barriers fail. Wronkiewicz et al. [58] take this fact in consideration and used an experimental set-up with a very low flow of leaching solution during 10 years at 90ºC. In this experiment the ratio S/V was very high. They observe a decrease in the release rate after the first two years produced by a dense mat of alteration phases that trap the loose particles of UO_2. They also observe precipitation of secondary uranium phases, reducing the concentration of UO_2 in solution. The S/V ratio is also important in the alpha-radiation experiments due to the short range of the alpha particles in solution [59]. Summarizing, experiments with a high S/V ratio are more realistic when compared to the future repository conditions and therefore future experiments on the dissolution rate, the solubility and the secondary phase formation of the spent fuel matrix should take this parameter into account.

The works from Ryan et al. [60] and Fujiwara et al. [61] coincide in the study of Uranium (IV) solubility at very alkaline pH and reducing conditions. In some of the waste surface disposal and also waste final repositories there is a huge amount of cement and concrete. When the groundwater flows through those materials the pH increases. There is a range of materials derived from the cement that meet various functions in a deep geological storage, such as sealing cracks in the rock or set different materials in the rock. Concrete is used as a support material in the tunnels and galleries to seal part of the repository in the closing phase. Concrete also will be used to build auxiliary structures in the operational phase of the repository (Huertas et al. [62]).

The water from the cement will have high alkalinity and carry in solution many cations such as Ca^{2+}, Na^{+}, K^{+}, silicates, or Al, which interacting with the matrix of UO_2, may react differently, giving precipitates, forming superficial complexes, etc...

This complexity in the cement water chemistry needs to be studied and investigated in order to implement the predictive models of the behavior of spent fuel in a deep geological repository. Berner [63] studied the degradation of cement in an environment similar to the one that might be found in a deep geological repository. He observed how the composition of ground water was the key parameter for the lifetime of the cement.

The work done by Stegemann et al. [64] showed how affects the pH, the presence of several metals. They found that the presence of copper increases pH, while Zn and NO^{3-} decreases it. Other metals like Ba, Cd, Cr (III), Ni, etc., do not have any acid neutralizing capacity, and therefore they do not affect the pH.

More recent studies like the one of Huertas et al. [62] have studied the interaction of bentonite and concrete supercarbonated. It can be observed that with enough time the pH stabilizes between 9 and 10, for all types tested, being 13 the highest initial pH. This buffering is due in one hand to the presence of carbonates, and in the other to the bentonite itself. Montmorillonite from the bentonite is dissolved and secondary phases such as smectite precipitate maintaining the pH between 9 and 10.

Blanc et al. [65] have characterized the system $CaO\text{-}SiO_2\text{-}H_2O$ (CSH) depending on the temperature, finding thermodynamic constants of Mg bearing phases, Fe bearing phases, and the systems $CaO–Al2O_3–SiO_2–H_2O$ and $CaO–Al_2O_3–SO_3–CO_2–Cl–H_2O$. The work also suggests a possible influence of impurities from the solid phases in the system requirements. Nowadays the cement industry is developing new products with better features than the previous ones, which could be used in a deep geological repository. One example is the work of Guerrero et al. [66] on the class C concrete, of volatile ashes of Belita (Ca_2SiO_4).

1.7. Mobility of uranium and radionuclides in the environment

As mentioned earlier, the DGR is designed with the aim of preventing the transport of radionuclides to the biosphere, or if it exists to make it as slow as possible. To ensure this case we need to know the mobility of the matrix and radionuclides in different environments and lithologies.

In order to study the long-term effect of a DGR several natural analogues have been used over the years[67,68]. For example the natural nuclear fission reactor in Oklo (Gabon) is one of the most studied formations due to its unique characteristics. It is the only known formation in the world where a self-sustained chained reaction has occurred naturally [69-71]. Cigar Lake in Canada is also a very interesting natural analogue. It is considered the world's second largest uranium deposit but it has remained intact during at least the last 10000 years. Moreover there is no trace of uranium in the surface, meaning that the natural barriers have prevented the transport of uranium to the surface. The uranium mineralization is located at 450 m surrounded by clay, like some of the possible options for a DGR, where the SNF will be surrounded by a bentonitic clay and buffered by several meters of host rock[72,73]. Poços de Caldas in Brasil is a natural analogue with two particular anomalies: the Osamu Utsumi mine and the Morro de Ferro Thorium and Rare Earth Elements deposit. Morro de Ferro is considered the most naturally radioactive place on earth and in the Osamu Utsumi mine is possible to observe Redox fronts like the ones that will be present in a DGR, between the oxidant zone created during the construction of the repository and the reducing medium of the

geologic site[72,74,75]. Another sites studied are the Palmottu (fractured crystalline bedrock) formation in Finland[76,77], the El Berrocal granite system in Spain[78,79] and the Maqarin limestone in Jordan, where natural cements are produced, increasing the pH of the groundwater to hyperalkaline (12.3 - 12.9)[72,80,81]. Basically the natural analogues studies are divided in different stages, first a groundwater flow and chemical evolution study, second identify and quantify the processes related to the radionuclide migration and finally modellization of the data acquired. For example, Curtis et al. [82] have used the location of Naturita Site (Colorado, USA), for simulation and analysis of what would be the contamination of aquifers by uranium. The Naturita zone has had in the past uranium and vanadium mines, which residues have been moved to a controlled waste storage facility. Mathematical models have been used to predict the transport of uranium in the environment and they have been compared to in situ experiments with tracers.

Contaminated zones with depleted uranium were used in their studies by Crançon et al. [83]. In their superficial transport of uranium experiments, they have seen how complexes formed with humic acid control the mobility. These complexes can be adsorbed on different minerals, but it is a reversible sorption that depends on both pH and ionic strength of the medium. They also studied how the rain water or a sudden rise of the water level in the aquifer can help the uranium mobilization.

Another long studied location is Hanford (Washington State, USA). Um et al. [84] have studied the field contaminated by an accident, taking soil samples at different depths. They observed how part of the uranium has migrated into deeper areas, and therefore part of the uranium has some mobility. Using advanced techniques of analysis they have determined that the dominant oxidation state is the U(VI), and most of the uranium appears in the form of silicates or phosphates. This study provides a model of migration of uranium through several lithologies, each with a specific hydraulic capacity.

Clarens et al. [18] studied the oxidative dissolution of the UO_2 as function of pH and the hydrogen peroxide concentration. They observed an increase in the dissolution rate, increasing the hydrogen peroxide concentration until a threshold value of H_2O_2 concentration where the dissolution rate decreases. This phenomenon was thought to be

due to the precipitation of Studtite, a secondary phase of uranium and H_2O_2. They also observe an increase of the dissolution rate at pHs higher than 10, and at first they suggested that it was due to the predominance of the specie HO_2^- at this pH. Nevertheless another option came into their mind, the possibility of a complex formation between UO_2 and H_2O_2 that enhances the dissolution and also the mobility of UO_2 in the medium. Moskvin et al. [40] already suggested this possibility in their work, where they dissolved Studtite to obtain a series of complexes between UO_2 and H_2O_2. Unfortunately the constants obtained in this work were not accepted by the NEA (Nuclear Energy Agency) and were not included in the uranium thermodynamic databases [85].

Also most recently, Goff et al. determined the apparent formation constants of the ternary complex $UO_2(O_2)(CO_3)_2^{4-}$ using UV-Vis Spectroscopy [35]. It is clear then the need of studying the speciation of UO_2 at hyperalkaline pH in the presence of hydrogen peroxide. Moreover since the speciation of UO_2 has been focused in the acid, neutral and low alkaline pH, the speciation of UO_2 at high pH is not well known and more studies at this medium are required.

The mobility will also be affected by the precipitation of secondary phases of uranium. When studying the uranium secondary phases several authors have tried to simulate the conditions that will be found in the deep geological repository.

Rey et al.[86] have used a flow through reactor in their studies obtaining chernikovite in a phosphate media. The ratio between volume of solid and volume of liquid is a very important parameter in the secondary phases studies [87]. Higher solid to volume ratios mean more possibilities to find secondary phases.

The importance of the S/V ratio has been taken in account in the works of Trocellier et al.[88], Amme et al.[89] and Wronkiewicz et al. [58], where the presence of secondary uranium phases like Schoepite, Ekanite, Coffinite or Uranophane has been observed.

Other parameters that can affect the formation of secondary phases are the composition of the solution, pH and temperature. Kim et al[90] have studied the precipitation of uranium for a wide range of pH and different carbonate and hydrogen peroxide concentrations, finding secondary phases like the uranium peroxide $UO_4(H_2O)_4$ and clarkeite. The temperature determines which complex would be formed as it could be seen in the work with uranium peroxide complexes of Rey et al. [10].

In some works natural uranium secondary phases have been used. Reyes-Cortés et al. [91] have studied the uranium secondary phases of Sierra San Marcos, and Schindler et al. [92] have used the uranophane of Shinkolobwe mine of the Democratic Republic of Congo, in their experiments.

Studtite and metastudtite are the only peroxide containing minerals found in nature [93]. Hydrogen peroxide is formed by the radiolysis of water. If some water gets trapped in contact to a mineral phase of uranium the hydrogen peroxide would accumulate in this water. Deep in the ground the sun light would not be able to reach the water and degrade the hydrogen peroxide. H_2 and O_2 that are also significant radiolysis products could escape through the cracks of the mineral since they are gases. In some years the concentration of hydrogen peroxide in solution would be high enough to form, together with the UO_2 dissolved, the uranium peroxide Studtite [94].

Studtite is also found where nuclear accidents have occurred, in the Chernobyl lava [95] and in Fukushima [96]. Being the SNF more radioactive than the natural uranium minerals, Studtite will easily form in the surface of the fuel when water contacts it. This is very important for the safety assessment of a DGR. Clarens et al. studied the formation of Studtite during the oxidative dissolution of UO_2 by hydrogen peroxide using an ex-situ scanning force microscope (SFM) [9]. The sorption capacities of Studtite were studied by the same group against two different cations Cs and Sr [97,98]. Those cations are two very important radionuclides due to its mobility and large half-life. However the sorption capacities of Studtite against anions are still unknown. In sorption studies it is also useful to know the pH at which some mineral has the same number of positive charges and negative charges, known as the point of zero charge (pzc). In the case of Studtite the pzc still needs to be determined.

Most of the fission products are in the matrix of Uranium dioxide. However, due to their physical and chemical characteristics some of them are present in grain boundaries, in cracks, in bubbles formed in the fuel matrix and in the gap, the space between the fuel pellet and the cladding. In the case of an accidental failure of all the barriers and intrusion of groundwater through the pellet, most of these radionuclides will dissolve faster than the uranium matrix. This is called instant release fraction, or fast release fraction. Cs, Sr and Se are typically found in Instant Release fraction experiments [99-101].

Selenium is an element of special concern in the nuclear fuel cycle and it is one of the main radionuclides considered in the safety analysis of a High Level Nuclear Waste Repository (HLNWR), because of the long half-life ^{79}Se isotope, which is chemically and radiologically toxic [102,103]. In addition to the toxicity of the ^{79}Se isotope, selenium is a highly mobile element in oxidizing geochemical environments and may have a high impact on the cumulative radioactive dose if there is not a mechanism that might retard its transport through the geosphere [104].

Uranium(VI) forms complexes with selenium species in solution in the form ML, ML_2, being M the uranium(VI) and L the selenium specie (SeO_3^-, SeO_4^{2-}) [105,106]. This phenomenon will help the mobility both of uranium (VI) and radioselenium. Moreover, another kind of interaction has been studied by Krivovichev et al. They had managed to synthesize nanoscale tubules in uranyl selenates [107].

Due to its interest in the safety assessment of a waste repository and its reactivity with uranium, Selenium would be a very good anion to study the sorption capacities of Studtite.

1.8. Spectroscopic techniques

To study the chemistry of uranium many kinds of spectrophotometric techniques are used. They serve either to know the formation of uranium complexes, or to study red-ox potentials, adsorption phenomena, precipitation of secondary phases, superficial complexations, etc. From all of them, the spectroscopic laser-induced techniques are particularly interesting to study the speciation of actinides (Geipel [108]).

In the field of laser-induced spectroscopy, mainly 4 methods are used: LIPAS (Laser Induced PhotoAcoustic Spectroscopy), TRLFS (Time Resolved Laser-induced Fluorescence Spectroscopy), fs-TRLFS (ultra-short laser pulse induced time-resolved spectroscopy) and LIBD or LIBS (Laser-Induced BreakDown Spectroscopy). In recent decades these methods have been developed intensively, and have become a powerful tool to study the interactions that occur in solution or in solid-liquid interface. These techniques are not invasive or intrusive and allow for in situ qualitative and quantitative determinations. Compared to conventional spectroscopic methods such as UV-Visible spectroscopy, the detection limit can be up to 2 orders of magnitude lower.

In many cases a particular study may combine several techniques.

In some studies, for example, IR spectrometry and Raman spectrometry are combined, in the work of Frost et al. and Cejka et al. [109-112], on uranium minerals such as Rutherfordine, natrouranospinite, metauranospinite and Jaquimovite.

In other studies spectrophotometry in the UV-Visible region has been used. It has been used for organic ligands, for example the study of the complexation of the uranyl-oxalate (Havel et al. [113]), and for inorganic ligands in studies of the interaction of the uranium (VI) with ortosilicic acid (Yusov et al. [114]). It has also been used to study the equilibrium of oxidation / reduction pair U_2^{2+} / U_2^{+} in a solution of NaCl-2CsCl (Nagai et al. [115]).

The interaction of selenium with uranyl (Sladkov et al. [116]) has been observed through the UV-Visible spectrophotometer, and TRLFS (Time Resolved Laser Fluorescence Spectroscopy).

As mentioned above, laser fluorescence spectroscopy resolved in time, is a technique that can work at very low detection limits, such as the complexation of uranium (IV) with hydrofluoric acid, which worked at concentrations of $5 \cdot 10^{-7}$ $mol \cdot dm^{-3}$ (Lehmann et al. [117]).

TRLFS has been used in projects where the objective was to determine the complexation of uranyl with inorganic ligands like phosphates (Lehmann et al. [118]), silicates (Moll et al. [119]) and sulfates (Vercouter et al. [120]), and organic ligands such as phospholipids (Koban [121]). It is also a very useful technique to study the speciation of Uranium even in mediums as complex as biofilms [122].

Fs-TRLFS technique has been used in combination with TRLFS to determine the interaction of uranyl ligands with nitrogen-bearing molecules such as nicotinic acid and antranilic acid. (Raditzky et al. [123]).

It is currently possible to perform TRLFS measures at very low temperature, thanks to the use of a cryostat in the experimental system. This usually minimizes the quenching and allows seeing some spectra that are undetectable at room temperature. This technique has been used in the study of uranium (VI) complexation with glucose (Steudtner et al. [124]) and in the determination of uranium (V) complexes with carbonates (Grossmann et al. [125]).

TRLFS techniques can also be used to study solid-liquid interactions. It has been used in studies of sorption of uranium (VI) in muscovite (Arnold et al. [126]), Gibbsite (Baumann [127]) and Calcite (Wang et al. [128]), in the last case in combination with TRLFS at low temperatures and XRD (X-Ray Difraction).

1.9. References

1 J. Baró, G. Echagüe, E. González, R. Herranz, S. Marcos, M. Martínez, P. Olivares, M. Cruz, J. M. Rodríguez. (2000). Origen y gestión de residuos radiactivos. *Ilustre Colegio Oficial de Físicos*.

2 J. Magill. Nuclides.net. An integrated environment for computations on radionuclides and their radiation. (2003). *Springer*.

3 J. Astudillo (2001). El almacenamiento geológico profundo de los residuos radiactivos de alta actividad. Principios básicos y tecnología. *ENRESA*.

4 E. Cera, J. Merino and J. Bruno. (2000).Liberación de los radionucleidos e isótopos estables contenidos en la matriz del combustible. Modelo conceptual y modelo matemático del comportamiento del residuo. *ENRESA Publicación Técnica 03/2000*.

5 J. de Pablo, I. Casas, J. Giménez, M. Molera, M. Rovira, L. Duro and J. Bruno. (1999). The oxidative dissolution mechanism of uranium dioxide. I. The effect of temperature in hydrogen carbonate medium. *Geochimica et Cosmochimica Acta*, **63**, (19-20), 3097-3103.

6 J.A. Serrano, J. P. Glatz, E.H. Toscano, D. Papaioannou, J. Barrero, and M. Coquerelle. (1998). Influence of low-temperature air oxidation on the dissolution behaviour of high burn-up LWR spent fuel. *J. Alloys Comp.*, **271-273**, 573-576.

7 T.E. Eriksen, U. Eklund, L. Werme, and J. Bruno. (1995). Dissolution of irradiated fuel: a radiolytic mass balance study. *J. Nucl. Mater.*, **227**, 76-82

8 C. Jégou, B. Muzeau, V. Broudic, S. Peuget, A. Poulesquen, D. Roudil and C. Corbel. (2005). Effect of external gamma irradiation on dissolution of the spent UO_2 fuel matrix. *J. Nucl. Mater.*, **341**, 62-82

9 F. Clarens, J. de Pablo, I. Díez-Perez, I. Casas, J. Gimènez, and M. Rovira. (2004). Formation of studtite during the oxidative dissolution of UO_2 by hydrogen peroxide: A SFM study. *Environmental Science & Technology* **38**, 6656-6661.

10 A. Rey, I. Casas, J. Giménez, J. Quiñones and J. de Pablo. (2009) Effect of temperature on studtite stability: Thermogravimetry and differential scanning calorimetry investigations. *J. Nucl. Mater.*, **385**, 467-473.

11 D.W. Shoesmith. (2000). Fuel corrosion processes under waste disposal conditions. *J. Nucl. Mater.*, **282**(1), 1-31.

12 A. Martínez-Esparza, J.A. Esteban, J. Quiñones, J. de Pablo, I. Casas, J. Giménez, F. Clarens, M. Rovira, J. Merino, E. Cera, J. Bruno and S. Ripoll. (2002). Modelling spent fuel and HLW behaviour in repository conditions. *ENRESA Publicación Técnica 08/2002*.

13 T.A. Hu. (2012) Improved model for hydrogen generation rate of radioactive waste at the Hanford site. *Nuclear Technology*, **178** (1), 39-54.

14 M. Kelm. and E. Bohnert. (2004). A kinetic model for the radiolysis of chloride brine, its sensitivity against model parameters and a comparison with experiments. *Forschungszentrum Karlsruhe Wissenschaftliche Berichte FZKA*, 6977, 60.

15 M.M. Hossain and M. Jonsson. (2008). Effects of ionic strength on the kinetics for UO_2 oxidation. *J. Nucl. Mater.*, **373**, 190-193.

16 O. Roth, H. Hasselberg and M. Jonsson. (2009). Radiation chemical synthesis and characterization of UO_2 nanoparticles. *J. Nucl. Mater.*, **383**, 231-236.

17 J. Giménez, E. Baraj, M.E. Torrero, I. Casas and J. de Pablo. (1996). Effect of H_2O_2, NaClO and Fe on the dissolution of unirradiated UO_2 in NaCl 5 mol kg^{-1}. Comparison with spent fuel dissolution experiments. *J. Nucl. Mater.*, **238**, 64-69.

18 F. Clarens, J. de Pablo, I. Casas, J. Giménez, M. Rovira, J. Merino, E. Cera, J. Bruno, J. Quiñones and A. Martínez-Esparza. (2005). The oxidative dissolution of unirradiated UO_2 by hydrogen peroxide as a function of pH. *J. Nucl. Mater.*, **345**, 225-231.

19 I. Casas, J. de Pablo, F. Clarens, J. Giménez, J. Merino, J. Bruno and A. Martínez-Esparza. (2009). Combined effect of H_2O_2 and HCO_3^- on UO_2(s) dissolution rates under anoxic conditions. *Radiochim. Acta*, **97**, 485-490.

20 F.N. Smith, S.I. Sinkov, C.Z. Soderquist, R.S. Wittman, A.R. Geanes, B.K. McNamara and E.C. Buck. (2013). Spectroscopic detection of hydrogen peroxide generated by alpha radiolysis in solution.14th International High-Level Radioactive Waste Management Conference, IHLRWMC 2013: Integrating Storage, Transportation, and Disposal, **2**, 679-684.

21 C. Ekberg, E. Aneheim, A. Fermvik and G. Skarnemark. (2010). Using At-211 as internal alpha radiolysis source allowing for simple detection of radiolysis products. *Radiation Physics and Chemistry* **79** 454-456.

22 G. Guimbretière, A. Cañizares, P. Simon, Y. A. Tobon-Correa, M.R. Ammar, C. Corbel and M.F. Barthe. (2011). In-Situ Raman observation of the first step of uranium dioxide weathering exposed to water radiolysis. *Spectroscopy Letters*, **44** (7-8) 570-573.

23 F. Crumière, J. Vandenborre, R. Essehli, G. Blain, J. Barbet and M. Fattahi. (2013). LET effects on the hydrogen production induced by the radiolysis of pure water. *Radiation Physics and Chemistry* **82** 74-79.

24 B. Muzeau, C. Jégou, F. Delaunay, V. Broudic, A. Brevet, H. Catalette, E. Simoni and C. Corbel. (2009). Radiolytic oxidation of UO_2 pellets doped with alpha-emitters ($^{238/239}$Pu). *J. Alloys Comp.*, **467**, 578-589.

25 D. Cui, E. Ekeroth, P. Fors and K. Spahiu. (2008). Surface mediated processes in the interaction of spent fuel or alpha-doped UO_2 with H-2. *Materials Research Society Symposium Proceedings*, **1104**, 87-99.

26 M. Kelm. and E. Bohnert. (2005). Gamma radiolysis of NaCl brine: Effect of dissolved radiolysis gases on the radiolytic yield of long-lived products. *J. Nucl. Mater.*, **346**, 1-4.

27 V. Metz, E. Bohnert, M. Kelm, D. Schild, J. Reinhardt, B. Kienzler and M.R. Buchmeiser. (2007). Gamma-radiolysis of NaCl brine in the presence of UO_2 (s): effects of hydrogen and bromide. *Materials Research Society Symposium Proceedings* **985** 33-40.

28 V. Metz, A. Loida, E. Bohnert, D. Schild and K. Dardenne. (2008). Effects of hydrogen and bromide on the corrosion of spent nuclear fuel and γ-irradiated UO_2(s) in NaCl brine. *Radiochim. Acta* **96** (9-11) 637-648.

29 M. Kelm and E. Bohnert. (2002). Radiolysis and corrosion of ^{238}Pu-doped UO2 pellets in chloride brine. *Proc. Indian Acad. Sci. (Chem. Sci.)*, **114**, 6, 697-704.

30 V.A. Volkovich, T.R. Griffiths, D.J. Fray and M. Fields. (1997). Increased oxidation of UO_2 in molten alkali-metal carbonate based mixtures by increasing oxygen solubility and by controlled generation of superoxide ions, and evidence for a new sodium uranate. *J. Chem. Soc., Trans.*, **93**(21), 3819-3826.

31 S.M. Peper, L.F. Brodnax, S.E. Field, R.A. Zehnder, S.N. Valdez and W.H. Runde. (2004). Kinetic Study of the Oxidative Dissolution of UO_2 in Aqueous Carbonate Media. *Ind. Eng. Chem. Res.* **43**, 8188-8193.

32 S. Sunder, N.H. Miller and D.W. Shoesmith. (2004). Corrosion of uranium dioxide in hydrogen peroxide solutions. *Corrosion Sci.*, **46**, 1095-1111.

33 C. Corbel, G. Sattonay, S. Guilbert, F. Garrido, M. Barthe and C. Jegou. (2006). Addition versus radiolytic production effects of hydrogen peroxide on aqueous corrosion of UO_2. *J. Nucl. Mater.*, **348**, 1-17.

34 Goldik, J.S. ; Noël, J.J. and Shoesmith, D.W. (2006). Surface electrochemistry of UO_2 in dilute alkaline hydrogen peroxide solutions. Part II. Effects of carbonate ions. *Electrochim. Acta*, **51**, 3278-3286.

35 G.S. Goff, L.F. Brodnax, M.R. Cisneros, S.M. Peper, S.E. Field, B.L. Scott and W.H. Runde. (2008). First identification and thermodynamic characterization of the ternary U(VI) species, $UO_2(O_2)(CO_3)_2^{4-}$, in UO_2-H_2O_2-K_2CO_3 solutions. *Inorg. Chem.*, **47**, 1984-1990.

36 C. Soderquist and B. Hanson. (2010). Dissolution of spent nuclear fuel in carbonate-peroxide solution. *J. Nucl. Mater.*, **396**, 159-162.

37 D. Chung, H. Seo, J. Lee, H. Yang, E. Lee and K. Kim. (2010). Oxidative leaching of uranium from SIMFUEL using Na_2CO_3-H_2O_2 solution. *J. Radioanal. Nucl. Chem.*, **284**, 123-129.

38 S.I. Stepanov, A.V. Boyarintsev and A.M. Chekmarev. (2009). Physicochemical foundations of spent nuclear fuel leaching in carbonate solutions. *Doklady Akademii Nauk*, **427** (6), 793-797.

39 E.D.A. Ferriss, K.B. Helean, C.R. Bryan, P.V. Brady and R.C. Ewing. (2009). UO_2 corrosion in an iron waste package. *J. Nucl. Mater.*, **384**, 130-139.

40 A.I. Moskvin. (1968). Complexing of uranium(VI) and neptunium(IV) with hydrogen peroxide and of neptunium(IV) in oxalate solutions. *Radiokhimiya* **10**(1), 13-21.

41 G.E. Sigmon, B. Weaver, K. Kubatko and P.C. Burns. (2009). Crown and bowl-shaped clusters of uranyl polyhedra. *Inorg. Chem.*, **48**, 10907-10909.

42 G.E. Sigmon, J. Ling, D.K. Unruh, L. Moore-Shay, M. Ward, B. Weaver and P.C. Burns. (2009). Uranyl-Peroxide interactions favor nanocluster self-assembly. *J. Am. Chem. Soc.*, **131**, 16648-16649.

43 D.K. Unruh, A. Burtner and P.C. Burns. (2009). Expanding the crystal chemistry of actynil peroxides: μ-η^2:η^1 Peroxide coordination in trimers of U^{6+} polyhedra. *Inorg. Chem.*, **48**, 2346-2348.

44 J. Merino, E. Cera, J. Bruno, J. Quiñones, I. Casas, F. Clarens, J. Giménez, J. de Pablo, M. Rovira and A. Martínez-Esparza. (2005). Radiolytic modelling of spent fuel oxidative dissolution mechanism. Calibration against UO_2 dynamic leaching experiments. *J. Nucl. Mater.*, **346**, 40-47.

45 M.P. Elless and S.Y. Lee. (1998). Uranium solubility of carbonate-rich uranium-contaminated soils. *Water, Air and Soil Pollution*, **107**, 147-162.

46 O.C. Lind, B. Salbu, L. Skipperud, K. Janssens, J. Jaroszewicz and W. De Nolf. (2009). Solid state speciation and potential bioavailability of depleted uranium particles from Kosovo and Kuwait. *J. Environ. Radioact.*, **100**, 301-307.

47 S. Meca, J. Giménez, I. Casas, V. Martí and J. de Pablo. (2012). Uranium speciation in river sediments contaminated by phosphates ores. *Environ. Chem. Lett.*, **10**, 49-53.

48 I. Casas, J. Giménez, V. Martí, M.E. Torrero and J. de Pablo. (1994). Kinetic studies of unirradiated UO_2 dissolution under oxidizing conditions in batch and flow experiments. *Radiochim. Acta*, **66/67**, 23-27.

49 I. Casas, J. de Pablo, J. Giménez, M.E. Torrero, J. Bruno, E. Cera, R.J. Finch and R.C. Ewing. (1998). The role of pe, pH, and carbonate on the solubility of UO_2 and uraninite under nominally reducing conditions. *Geochim. Cosmochim. Acta*, **62**, 13, 2223-2231.

50 S.Röllin, K.Spahiu and U.-B. Eklund. (2001). Determination of dissolution rates of spent fuel in carbonate solutions under different redox conditions with a flow-through experiment. *J. Nucl. Mater.*, **297**, 231-243.

51 K. Spahiu, L. Werme and U.-B. Eklund. (2000). The influence of near field hydrogen on actinide solubilities and spent fuel leaching. *Radiochim. Acta*, **88**, 507-511.

52 J. de Pablo, I. Casas, J. Giménez, F. Clarens, L. Duro and J. Bruno. (2003). The Oxidative Dissolution Mechanism of Uranium Dioxide. The Effect of pH and Oxygen Partial Pressure. *MRS Proceed.*, **807**, 83.

53 J. Giménez, F. Clarens, I. Casas, M. Rovira, J. de Pablo and J. Bruno. (2005). Oxidation and dissolution of UO2 in bicarbonate media: Implications for the spent nuclear fuel oxidative dissolution mechanism. *J. Nucl. Mater.*, **345**, 232-238.

54 J. Giménez, I. Casas, R. Sureda and J. de Pablo. (2012). Kinetics of hydrogen peroxide consumption in aqueous phase at different hydrogen partial pressures. *Radiochim. Acta*, **100**, 445-448.

55 S. Nilsson and M. Jonsson. (2008). On the catalytic effects of UO_2(s) and Pd(s) on the reaction between H_2O_2 and H_2 in aqueous solution. *J. Nucl. Mater.*, **372**, 160-163.

56 I. Casas, M. Borrell, L. Sánchez, J. de Pablo, J. Giménez and F. Clarens. (2008). Determination of UO2(s) dissolution rates in a hydrogen peroxide medium as a function of pressure and temperature. *J. Nucl. Mater.*, **375**, 151-156.

57 R. Sureda, I. Casas, J. Giménez and J. de Pablo. (2008). Kinetics of UO_2 (s) dissolution in the presence of hypochlorite, chlorite, and chlorate solutions. *MRS Proceed.*, **1107**, 599-604.

58 D.J. Wronkiewicz, J.K. Bates, S.F. Wolf and E.C. Buck. (1996). Ten-year results from unsaturated drip tests with UO_2 at 90 ºC: Implications for the corrosion of spent nuclear fuel. *J. Nucl. Mater.*, **238**, 1, 78-95.

59 A. Loida, B. Grambow and H. Geckeis. (1996). Anoxic corrosion of various high burnup spent fuel samples. *J. Nucl. Mater.*, **238**, 1, 1-22.

60 J.L. Ryan and D. Rai. (1983). The solubility of uranium(IV) hydrous oxide in sodium-hydroxide solutions under reducing conditions. *Polyhedron*, **2**, 9, 947-952.

61 K. Fujiwara, H. Yamana, T. Fujii, K. Kawamoto, T. Sasaki and H. Moriyama. (2005). Solubility of uranium(IV) hydrous oxide in high pH solution under reducing condition. *Radiochim. Acta*, **93**, 347-350.

62 F.J. Huertas, A. Hidalgo, M.L. Rozalén, S. Pellicione, C. Domingo, C.A. García-González, C. Andrade and C. Alonso. (2009). Interaction of bentonite with supercritically carbonated concrete. *Applied Clay Science*, **42**, 488-496.

63 U.R. Berner. (1992). Evolution of pore water chemistry during degradation of cement in a radioactive waste repository environment. *Waste Management*, **12,** 201-219.

64 J.A. Stegemann and N.R. Buenfeld. (2002). Prediction of leachate pH for cement paste containing pure metal compounds. *J. Hazard. Mater.*, **B90**, 169-188

65 Ph. Blanc, X. Bourbon, A. Lassin and E.C. Gaucher. (2010). Chemical model for cement-based materials: Temperature dependence of thermodynamic functions for nanocrystalline and crystalline C-S-H phases. *Cement and Concrete Research*, **40**, 851-866.

66 A. Guerrero, S. Goñi and V.R. Allegro. (2009). Resistance of class C fly ash belite cement t simulated sodium radioactive liquid waste attack. *J. Hazard. Mater.*, **161**, 1250-1254.

67 J. Smellie. (2010). Analogue evidence from uranium ore bodies. *Nuclear Decommissioning Authority Version 2009-12-01*.

68 N.P. Laverov, V.A. Petrov, S.I. Shchukin and J. Hammer. (2009). Underground laboratory and natural analogue of an SNF storage facility in granite: An example of the Antei deposit. *The IAEA Contact Experts Group (CEG) Workshop on Disposal of Radioactive Waste and Spent Nuclear Fuel - Experience and Plans. Bommersvik-Oskarshamn, Sweden, 23-27 February 2009*.

69 J. Salas and C. Ayora. (2004). Goundwater chemistry of the Okélobondo uraninite deposit area (Oklo, Gabon): two-dimensional reactive transport modelling. *J. Contam. Hydrol.*, **69**, 115-137.

70 S-E. Bentridi, B. Gall, F. Gauthier-Lafaye, A. Seghour and D-E. Medjadi. (2011) Inception and evolution of Oklo natural nuclear reactors. *C. R. Geoscience*, **343** 738-748.

71 D. Louvat. (1998). Oklo, natural analogue of the radionuclides migration through the geological barrier. *Orstom Ed.*

72 J. Bruno, L. Duro and M. Grivé. (2002). The applicability and limitations of thermodynamic geochemical models to simulate trace element behaviour in natural waters. Lessons learned from natural analogue studies. *Chem. Geol.*, **190**, 371-393.

73 J. Cramer and J. Smellie. (1994). Final report of the AECL/SKB Cigar Lake analog study. *SKB Technical Report 94-04*.

74 N.A. Chapman, I.G. McKinley, M.E. Shea and J.A.T. Smellie. (1991). The Poços de Caldas project: Summary and implications for radioactive waste management. *SKB Technical Report 90-24*.

75 J. Bruno, L. Duro, S. Jordana and E. Cera. (1996). Revisiting Poços de Caldas. Application of the co-precipitation approach to establish realistic solubility limits for performance assessment. *SKB Technical Report 96-04*.

76 A. Blyth, S. Frape, T. Ruskeeniemi and R. Blomqvist. (2004). Origins, closed system formation and preservation of calcites in glaciated crystalline bedrock: evidence from the Palmottu natural analogue site, Finland. *Appl. Geochem.*, **19**, 675-686.

77 J. Kaija, R. Blomqvist, J. Suksi and K. Rasilainen. (2000). The Palmottu natural analogue project. Summary Report 1996-1999. Report YST-102. *Geological survey of finland*.

78 L. Pérez del Villar, E. Reyes, A. Delgado, R. Núñez, M. Pelayo and J.S. Cózar. (2003). Argillization processes at the El Berrocal analogue granitic system (Spain): mineralogy, isotopic study and implications for the performance assessment of radwaste geological disposal. *Chem. Geol.*, **193**, 273-293.

79 L. Pérez del Villar, M. Pelayo, J.S. Cózar, B. De la Cruz, J. Pardillo, E. Reyes, E. Caballero, A. Delgado, R. Núñez, M. Ivanovich and S.E. Hasler. (1997). Mineralogical and geochemical evidence of the migration/retention processes of U and Th in fracture fillings from the El Berrocal granitic site (Spain). *J. contam. Hydrol.*, **26**, (1-4) 45-60.

80 C. Linklater, I. Albisson, W.R. Alexander, I. Casas, I. McKinley and P. Sellin. (1996). A natural analogue of high-pH cement pore waters from the Maqarin area of northern Jordan: Comparison of predicted and observed trace-element chemistry of uranium and selenium. *J. Contam. Hydrol.*, **21**, 59-69.

81 J.A.T. Smellie. (1998). Maqarin natural analogue study: Phase III. *SKB Technical Report 98-04*.

82 G.P. Curtis, M. Kohler and J.A. Davis. (2009). Comparing approaches for simulating the reactive transport of U(VI) in ground water. *Mine Water Environ.*, **28**, 84-93.

83 P. Crançon, E. Pili and L. Charlet. (2010). Uranium facilitated transport by water-dispersible colloids in field and soil columns. *Sci. . total environ.*, **408**, 2118-2128.

84 W. Um, J.P. Icenhower, C.F. Brown, R.J. Serne, Z. Wang, C.J. Dodge and A.J. Francis. (2010). Characterization of uranium-contaminated sediments from beneath a nuclear waste storage tank from Hanford, Washington: Implications for contaminant transport and fate. *Geochim. Cosmochim. Acta*, **74**, 1363-1380.

85 R. Guillaumont, T. Fanghänel, V. Neck, J. Fuger, D.A. Palmer, I. Grenthe and M.H. Rand. (2003). In Chemical Thermodynamics 5. Update on the chemical thermodynamics of Uranium, Neptunium, Plutonium, Americium and Technetium. *Elsevier, Amsterdam*.

86 A. Rey, J. Giménez, I. Casas, F. Clarens and J. de Pablo. (2008). Secondary phase formation on UO_2 in phosphate media. *Appl. Geochem.*, **23**, 2249-2255.

87 A. Loida, B. Grambow and H. Geckeis. (1996). Anoxic corrosion of various high burnup spent fuel samples. *J. Nucl. Mater.*, **238**, 11-22.

88 P. Trocellier, C. Cachoir and S. Guilbert. (1998). A simple thermodynamical model to describe the control of the dissolution of uranium dioxide in granitic groundwater by secondary phase formation. *J. Nucl. Mater.*, **256** 197-206.

89 M. Amme, T. Wiss, H. Thiele, P. Boulet and H. Lang. (2005). Uranium secondary phase formation during anoxic hydrothermal leaching processes of UO_2 nuclear fuel. *J. Nucl. Mater.*, **341**, 209-223.

90 K.-W. Kim, Y.-H. Kim, S.-Y. Lee, J.-W. Lee, K.-S. Joe, E.-H. Lee, J.-S. Kim, K. Song and K.-C. Song. (2009). Precipitation characteristics of uranyl ions at different pHs depending on the presence of carbonate ions and hydrogen peroxide. *Environ. Sci. Technol.*, **43**, 2355-2361.

91 M. Reyes-Cortés, L. Fuentes-Cobas, E. Torres-Moye, H. Esparza-Ponce and M.E. Montero-Cabrera. (2010). Uranium minerals from the San Marcos District, Chihuahua, Mexico. *Miner Petrol.*, **99**, 121-132.

92 M. Schindler, M. Freund, F.C. Hawthorne, P.C. Burns and P.A. Maurice. (2009). Dissolution of uranophane: An AFM, XPS, SEM and ICP study. *Geochim. Cosmochim. acta*, **73**, 2510-2533.

93 P.C. Burns and K.-A. Hughes. (2003). Studtite, $[(UO_2)(O_2)(H_2O)_2](H_2O)_2$: The first structure of a peroxide mineral. *Amer. Mineral.*, **88**, 1165-1168.

94 K.-A.H. Kubatko, K.B. Helean, A. Navrotsky and P.C. Burns. (2003). Stability of peroxide-containing uranyl minerals. *Science*, **302**, 1191.

95 B.E. Burakov, E.E. Strykanova and E.B. Anderson. (1996). Secondary uranium minerals on the surface of Chernobyl "Lava". *MRS Proceedings*, 465.

96 P.C. Burns, R.C. Ewing and A. Navrotsky. (2012). Nuclear fuel in a reactor accident. *Science*, **335**, 1184.

97 J. Giménez, X. Martínez-Lladó, M. Rovira, J. de Pablo, I. Casas, R. Sureda and A. Martínez-Esparza. (2010). Cesium sorption on studtite ($UO_2O_2 \cdot 4H_2O$). *Radiochim. Acta*, **98**, 479-483.

98 R. Sureda, X. Martínez-Lladó, M. Rovira, J. de Pablo, I. Casas and J. Giménez. (2010). Sorption of strontium on uranyl peroxide: Implications for a high-level nuclear waste repository. *J. Hazard. Mater.*, **181**, 881-885.

99 D. Serrano-Purroy, I. Casas, E. González-Robles, J.P. Glatz, D.H. Wegen, F. Clarens, J. Giménez, J. de Pablo and A. Martínez-Esparza. (2013). Dynamic leaching studies of 48 MWd/kgU UO_2 commercial spent nuclear fuel under oxic conditions. *J. Nucl. Mater.*, **434**, 451–460.

100 D. Serrano-Purroy, F. Clarens, E. González-Robles, J.P. Glatz, D.H. Wegen, J. de Pablo, I. Casas, J. Giménez and A. Martínez-Esparza. (2012). Instant release fraction and matrix release of high burn-up UO_2 spent nuclear fuel: Effect of high burn-up structure and leaching solution composition. *J. Nucl. Mater.*, **427**, 249–258.

101 T. Fanghänel, V.V. Rondinella, J.-P. Glatz, T. Wiss, D.H. Wegen, T. Gouder, P. Carbol, D. Serrano-Purroy, and D. Papaioannou. (2013). Reducing Uncertainties Affecting the Assessment of the Long-Term Corrosion Behavior of Spent Nuclear Fuel. *Inorg. Chem.*, **52**, 3491−3509.

102 F. Chen, P.C. Burns, R.C. Ewing. (1999). ^{79}Se: geochemical and crystallo-chemical retardation mechanisms. *J. Nucl. Mater.*, **275**, 81-94.

103 ENRESA, (1997), Evaluación del comportamiento y la seguridad de un almacenamiento profundo en granito. Documento de Síntesis. *Report 48-1P-M-OOG-21, Madrid, Spain.*

104 F. Séby, M. Potin-Gautier, E. Giffaut and O. Donard. (1998). Assessing the speciation and the biogeochemical processes affecting the mobility of selenium from a geological repository of radioactive wastes to the biosphere. *Analysis*, **26**, 193-198.

105 P. Lubal and J. Havel. (1997). The study of complex equilibria of uranium (VI) with selenate. *Talanta*, **44**, 457-466.

106 R. Djogić, I. Pižeta and M. Zelić. (2000). Voltamnnetric study of uranyl-selenium interactions. *Anal. Chim. Acta*, **404**, 159-166.

107 S.V. Krivovichev, V. Kahlenberg, R. Kaindl, E. Mersdorf, I.G. Tananaev and B.F. Myasoedov. (2005). Nanoscale tubules in uranyl selenates. *Chem.Int.Ed.*, **44**, 1134-1136.

108 G. Geipel. (2006). Some aspects of actinide speciation by laser-induced spectroscopy. *Coord. Chem. Rev.*, **250**, 844-854.

109 R.L. Frost and J. Čejka. (2009). A Raman spectroscopic study of the uranyl mineral rutherfordine – revisited. *J. Raman Spectrosc.*, **40**, 1096-1103.

110 J. Čejka, J. Sejkora, R.L. Frost and E.C. Keeffe. (2009). Raman spectroscopic study of the uranyl mineral natrouranospinite $(Na_2,Ca)[(UO_2)(AsO_4)]_2 \cdot 5H_2O$. *Raman Spectrosc.*, **40**, 1521-1526.

111 J. Čejka, J. Sejkora, R.L. Frost and E.C. Keeffe. (2009). Raman spectroscopic study of the uranyl mineral metauranospinite $Ca[(UO_2)(AsO_4)]_2 \cdot 8H_2O$. *Raman Spectrosc.*, **40**, 1786-1790.

112 J. Čejka, J. Sejkora, R.L. Frost and E.C. Keeffe. (2009). Raman spectroscopic study of the uranyl sulphate mineral jáchymovite $(UO_2)_8(SO_4)(OH)_{14} \cdot 13H_2O$. *Raman Spectrosc.*, **40**,1464-1468.

113 J. Havel, J. Soto-Guerrero and P. Lubal. (2002). Spectrophotometric study of uranyl-oxalate complexation in solution. *Polyhedron*, **21**, 1411-1420.

114 A.B. Yusov and A.M. Fedossev. (2005). A spectrophotometric study of the interaction of uranyl ions with orthosilicic acid and polymeric silicic acids in aqueous solutions. *Radiochemistry*, **47** (4), 345-351.

115 T. Nagai, T. Fujii, O. Shirai and H. Yamana. (2004). Study on Redox Equilibrium of UO_2^{2+}/UO_2^{+} in Molten NaCl-2CsCl by UV-Vis Spectrophotometry. *J. nucl. sci. technol.*, **41** (6), 690-695.

116 V. Sladkov, B. Fourest and F. Mercier. (2009). Uranyl-Se(IV) interaction in aqueous acid solutions studied by time-resolved laser-induced fluorescence spectroscopy (TRLFS) and UV-Vis spectrophotometry. *Dalton Trans.*, **37**, 7734-7740.

117 S. Lehmann, G. Geipel, G. Grambole and G. Bernhard. (2009). A novel time-resolved laser fluorescence spectroscopy system for research on complexation of uranium (IV). *Spectrochim. Acta Part A*, **73**, 902-908.

118 S. Lehmann, G. Geipel, G. Grambole and G. Bernhard. (2010). Complexation of aqueous uranium (IV) with phosphate investigated using time-resolved laser-induced fluorescence spectroscopy. *J. Radioanal. Nucl. Chem.*, **283**, 395-401.

119 H. Moll, G. Geipel, V. Brendler, G. Bernhard and H. Nitsche. (1998). Interaction of uranium(VI) with silicic acid in aqueous solutions studied by time-resolved laser-induced fluorescence spectroscopy (TRLFS). *J. alloys comp.*, **271-273**, 765-768.

120 T. Vercouter, P. Vitorge, B. Amekraz and C. Moulin. (2008). Stoichiometries and thermodynamic stabilities for aqueous sulfate complexes of U(VI). *Inorg. Chem.*, **47**, 2180-2189.

121 A. Koban and G. Bernhard. (2007). Uranium(VI) complexes with phospholipid model compounds – A laser spectroscopic study. *J. Inorg. Biochem.*, **101**, 750-757.

122 T. Arnold, K. Grobmann and N. Baumann. (2010). Uranium speciation in biofilms studied by laser fluorescence techniques. *Anal. Bioanal. Chem.*, **396**, 1641.

123 B. Raditzky, K. Schmeide, S. Sachs, G. Geipel and G. Bernhard. (2010). Interaction of uranium (VI) with nitrogen containing model ligands studied by laser-induced fluorescence spectroscopy. *Polyhedron*, **29**, 620-626.

124 R. Steudtner, T. Arnold, G. Geipel and G. Bernhard. (2010). Fluorescence spectroscopic study on complexation of uranium (VI) by glucose: a comparison of room and low temperature measurements. *J Radioanal. Nucl. Chem.*, **284**, 421-429.

125 K. Grossmann, T. Arnold, A. Ikeda-Ohno, R. Steudtner, G. Geipel and G. Bernhard. (2009). Fluorescence properties of a uranyl(V)-carbonate species $[U(V)O_2(CO_3)_3]^{5-}$ at low temperature. *Spectrochim. Acta Part A*, **72**, 449-453.

126 T. Arnold, S. Utsunomiya, G. Geipel, R.C. Ewing, N. Baumann and V. Brendler. (2006). Adsorbed U(VI) Surface Species on Muscovite Identified by Laser Fluorescence Spectroscopy and Transmission Electron Microscopy. *Environ. Sci. Technol.*, **40**, 4646-4652.

127 N. Baumann, V. Brendler, T. Arnold, G. Geipel and G. Bernhard. (2005). Uranyl sorption onto gibbsite studied by time-resolved laser-induced fluorescence spectroscopy (TRLFS). *J. Colloid Interf. Sci.*, **290**, 318-324.

128 Z. Wang, J.M. Zachara, J.P. McKinley and S.C. Smith. (2005). Cryogenic Laser Induced U(VI) Fluorescence Studies of a U(VI) substituted natural calcite: Implications to U(VI) speciation in contaminated Hanford sediments. *Environ. Sci. Technol.* , **39**, 2651-2659.

2. Objectives

2. Objectives

This thesis is focused in the near field processes that may take place in radiolytic conditions at alkaline pH.

In this sense the following objectives were proposed:

- Study of the formation of complexes in the UO_2-H_2O_2 system in the absence of carbonate by UV-vis spectrophotometry at a constant pH = 12.

- Speciation study of uranium (VI) at very alkaline pH (11–13) and the quenching effect produced by hydrogen peroxide on the fluorescence of the uranium hydroxocomplex $UO_2(OH)_3^-$, using Time-Resolved Laser-induced Fluorescence Spectroscopy (TRLFS).

- Design of a flow-through experimental reactor in order to perform dissolution rate studies of UO_2 under both anoxic and reducing conditions at alkaline pH.

- Effect of α-radiolysis at alkaline conditions at low and high ionic strength.

- Study of the studtite sorption capacity for selenium (IV) and selenium (VI) by means of kinetic and equilibrium experiments. Determination of the point of zero charge of studtite.

3 Analytical Techniques

3 Analytical Techniques

3.1. MASS SPECTROMETRY

Mass spectrometry identifies a compound from the molecular or atomic mass(es) of its constituents. This identification is based in the generation of ions, the separation of these ions by their mass-to-charge ratio (m/z) and their qualitatively and quantitatively detection by their respective m/z and abundance.

Mass Spectrometry is broadly used in many fields, from the food chemistry, to space missions and military applications. In the field of radiochemistry is used for elemental identification and isotopic abundance measurement of both short-lived and stable species. It can be also coupled to separation methods such as gas chromatography (GC) and liquid chromatography (LC).

One of the disadvantages of the mass spectrometry is the total consumption of the analyte, compared to other techniques like UV-Visible spectroscopy or laser fluorescence spectroscopy where it is possible to recover the sample. On the other hand, the extremely low sample consumption of mass spectrometry makes it the method of choice when most other analytical techniques fail because they are not able to yield analytical information from nanogram amounts of sample. Moreover, the limit detection of mass spectrometry use to be lower than most other techniques and it is also fast and easily quantifiable.

The structure of a spectrometer (Figure 3.1) is quite simple. A mass spectrometer is formed by an ion source, a mass analyzer and a detector, all of them working under high vacuum conditions.

Figure 3.1. General scheme of any mass spectrometer.

The sample will be injected to the ion source, where most of the atoms and molecules will be ionized. The mass analyzer will disperse the ions in relation by their mass/charge (m/z) relation and will be converted in an electrical signal by the detector. The software data system will evaluate the data from detector transforming it in something easy to understand and to work with [1].

A quadropole gass mass spectrometer GAM 400 from InProcess Instruments (Bremen, Germany) was used to analyze O_2 and H_2. The gas mass spectrometer was provided with a cross-beam ion source, Faraday and SEV (SekundärElektronenVervielfacher = secondary electron multiplier) detectors and a batch inlet system.

The calibration was performed in the same pressure range as the sample measurements. The gas samples were measured 10 times and the mean value was specified. Measurements were performed with the SEV-detector.

The gas samples were collected in a glass single-ended device (also known as gas-maus) that could be connected to the experimental set-up and to the gas mass spectrometer (Figure. 3.2).

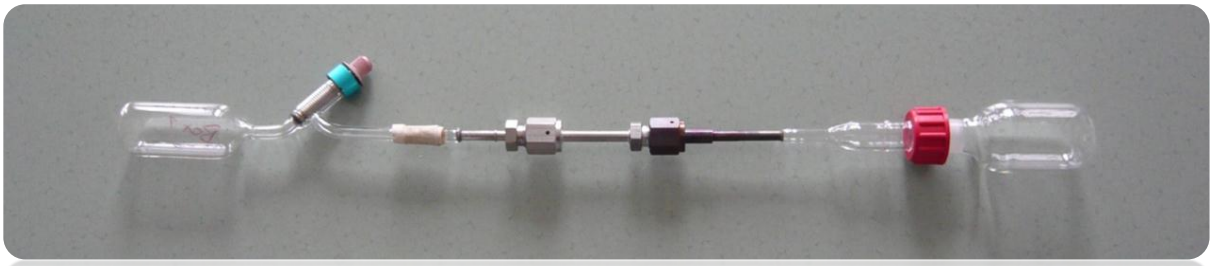

Figure. 3.2. Gas sampling device made from glass, connected to an experimental flask.

The volume of the whole set-up was of approximately 50 ml. The gas was collected during the experiment and when the sample had to be analyzed the valve was closed and the gas sampling device was connected directly to the gas mass spectrometer (Figure 3.3.).

Figure. 3.3. Metallic gas sampling device connected directly to the gas mass spectrometer.

3.1.1. Inductively Coupled Plasma Mass Spectrometry (ICP-MS)

In inductively coupled plasma mass spectrometry (ICP-MS), atomization and ionization are achieved in radiofrequency argon plasma at atmospheric pressure. The ICP-MS is one of the most used methods. The wide acceptance of the ICP-MS is thanks to its robustness, versatility and speed when determining trace levels. Moreover, its high sensitivity, low detection limit and the ability to analyze most elements and isotopes in the periodic table have turned ICP-MS, an essential technique in most laboratories, universities and technology centers. ICP-MS offers not only high ionization efficiency for low ionization energy (IE) elements, but is also applicable to non-metals such as P and even Cl.

The nucleus of an ICP source is formed by the so-called plasma torch. It consists of three coaxially aligned quartz tubes inserted along the central axis of a water cooled radiofrequency (RF) coil. After ignition caused by an electrical spark discharge, coil feeds the plasma produced by coupling of electrical energy in the gas, due to the fluctuation of the magnetic field that causes ion motion that in turn heats the gas and maintains the plasma flowing continuously. The outer quartz tube is about 20 mm in diameter and has its walls cooled by a gas flow of argon (12-20 dm^3 min^{-1}). The middle tube provides another stream of argon (1-2 dm^3 min^{-1}), called auxiliary gas flow that is fueling the plasma. Then the sample is introduced into the center of the toroidal plasma by an argon carrier gas flow (1-1.5 dm^3 min^{-1}). The carrier gas passes through a nebulizer and leads to the dissipation and

transfer of a fluid sample in the form of micrometer-sized droplets , which can be vaporized , atomized and ionized within the ICP. The typical consumption of the sample is in the order of 0.02 to 1 ml min^{-1} (Figure. 3.4.).

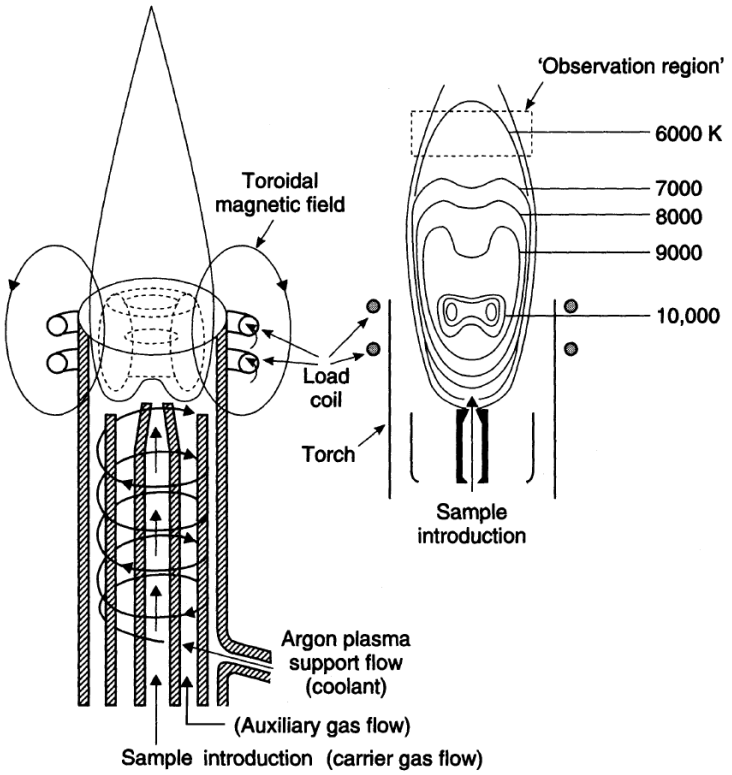

Figure 3.4.ICP plasma torch and the temperature distribution inside the plasma [1].

The ICP approaches a temperature of 10000 K in the area of induction close to the coil, and in the center where the evaporation and atomization occur, it is around 8000 K. While the plasma flows away from the coil, the excitation of the neutrals takes place at 7500 K (Figure. 3.5.).

The transfer of ions into the mass analyzer is accomplished through a differential pumping interface. A small part of the plasma enters the first stage of pumping through a hole in the center of the cone sampling. Cooling water of the sampling cone preserves its surface from its rapid destruction due to exposure to hot plasma. Then the ions are guided through the entrance of the skimmer by applying an electric potential (Figure. 3.5.).

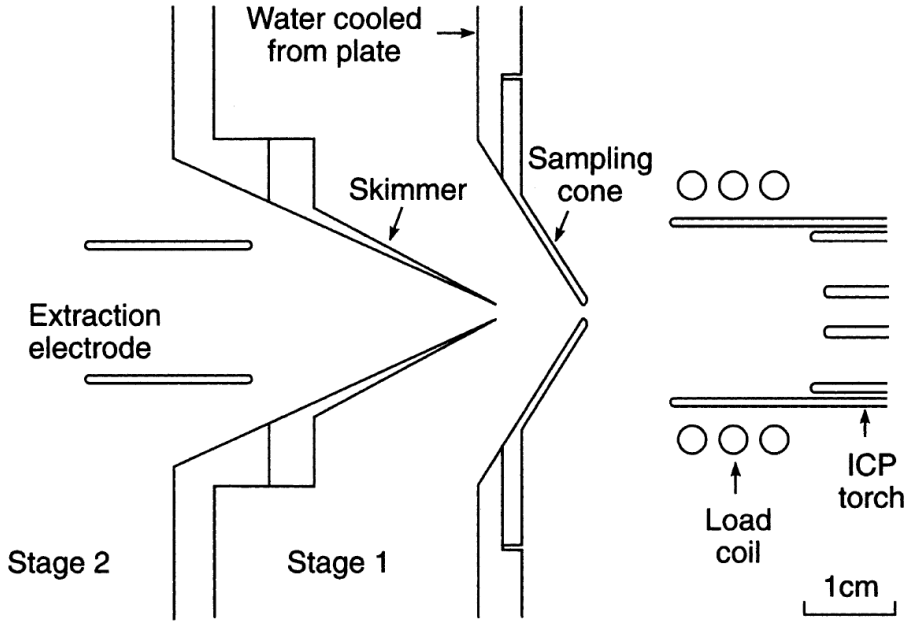

Figure 3.5. Ion extraction interface for ICP-MS [1].

A quadrupole analyzer is connected to the ICP, because of its moderate acceptance of the vacuum conditions. Moreover quadrupoles have several advantages. They have a high transmission and light weight. They are compact and relatively cheap. They also have low ion acceleration voltages, and allow scanning at high speeds, since the procedure is performed solely seeping electric potentials [1].

Two different ICP-MS spectrometers were used during this thesis, an ELAN 6100, from Perkin Elmer Inc (Waltham, USA) and an Agilent 7500cx (USA). This technique was used to analyze uranium, plutonium, cesium and selenium.

In order to avoid matrix interferences, calibration curve was prepared using an internal standard. An internal standard is an element similar to the analyte with a known concentration that is not present in the sample. Then corrections could be made regarding the signal and the concentration. Apart from the internal standard, external standards were also used. The external standard was a dilution of an analyte standard from a different batch that the one used in the calibration curve.

Interference by isotopes with a similar relation weight/charge has been taken into account in all the measurements, especially in samples with U and Pu.

3.2. ULTRAVIOLET VISIBLE SPECTROSCOPY

Every species absorb a determinate spectrum of light. Thanks to that is possible to identify species using spectroscopic techniques. Moreover, it is also possible to quantify the amount of the species using the Lambert-Beer law. These two facts have made that techniques like Ultraviolet Visible Spectroscopy are being used in laboratories all over the world. It is also a non-destructive technique, meaning that it is possible to reuse the sample analyzed, with the exception of photosensitive species.

Tungsten or tungsten-iodine filament lamps are usually the conventional sources in the region of visible light, while for the near-ultraviolet region, the deuterium discharge lamp is usually the most used. The high-pressure xenon arc lamp is a more intense source for both regions. In this lamp an arc struck between the two tungsten poles that can be separated between 1 mm and 1 cm in an atmosphere of xenon gas at 20 atmospheres, contained in a quartz envelope. This lamp is capable of emitting radiation below 200 nm.

Pyrex glass type is commonly used for lenses and cell windows in the visible region and fused quartz both in the visible and the near ultraviolet region.

Glass prism or mostly diffraction gratings are used as elements of dispersion.

Photomultipliers are often used as detectors, in which the photons fall on a metal surface, such as cesium, and then the surface reacts emitting electrons. These electrons are under an accelerating voltage and fall on a second surface releasing secondary electrons. This process is repeated several times in order to amplify the current. Photographic plates and photodiode arrays are also used and they have the advantage of detecting a wide range of wavelengths all the time [2].

In Figure 3.6 the optical system of the spectrometer used in this thesis is shown. It was a Hewlett-Packard 8453 (USA) spectrophotometer with temperature cell HP 89090A (USA). A deuterium-discharge lamp combined with a tungsten lamp form the necessary radiation source to embrace a range from the short-wavelength near-infrared (SWNIR) to the ultraviolet wavelengths. The image of the tungsten filament light is concentrated in an

opening in the back of the deuterium lamp, allowing a combination of the two light sources and obtaining a single axis in the sources lens. The sources lens produces a single collimated beam of light. The beam passes through the shutter / stray-light correction filter area and after that through the sample and to the spectrograph lens and slit. The light is dispersed by a holographic grating in the diode array, once inside the spectrograph. Thus permits accessing to all the information, simultaneously. This instrument provides a fundamental increase in the rate of acquisition of spectra.

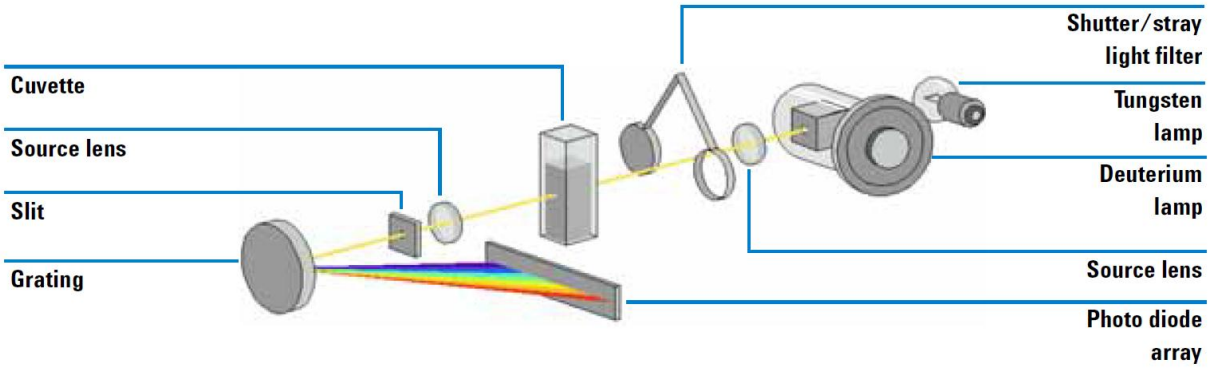

Figure 3.6. Optical system of Spectrophotometer [3].

Lamps

For the ultraviolet region, the light source is a deuterium lamp with a range between 190 and 800 nm. For the area of the visible spectra and the near infrared a tungsten lamp with a range between 370 nm and 1100 nm is used.

Source lens

The function of the lens is to collimate the two light beams from the lamps and turn it into a single beam that passes through the sample.

Shutter

The shutter is closed between measurements in order to limit the exposure of the sample to light.

Stray - Light Correction Filter

The stray- light filter is a filter with 50 % blocking at 420 nm. With this filter in place, any light below 400 nm is only stray light. The intensity of stray light is subtracted from the measured spectrum without the filter, to give a corrected spectrum respect the stray light.

Spectrograph

The spectrograph housing material is ceramic to reduce thermal effects to a minimum. The main components of the spectrograph are lens, slit, the grating and the photodiode array with front-end electronics. The average sampling interval of the diode array is approximately 0.9 nm over the wavelengths from 190 nm to 1100 nm. The nominal spectral slit width is 1 nm.

Spectrograph Lens

The spectrograph lens is mounted on the housing of the spectrograph. The spectrograph lens refocuses the collimated beam after passing through the sample.

Slit

The slit is a narrow opening in a plate located in the focus of the spectrograph lens. It is exactly the size of one of the photodiodes. By limiting the size of the light beam, ensures that each band of wavelengths is projected onto only the desired photodiode.

Grating

The combination of dispersion and spectral imaging is carried out using a concave holographic diffraction grating. The grating disperses the light onto the diode array at a linear angle proportional to the wavelength.

Diode Array

It is a series of 1024 individual photodiodes and control circuits etched on a semiconductor chip [3].

The sample cell material recommended to work with UV-Visible spectrophotometer used in this thesis, are the quartz sample cells, or the good quality glass cells if only the range between 350 and 1100 nm is used. The cell path length was the one recommended by Agilent Technologies (USA), 10 mm.

In every sample measurement a blank was used. The blank had the same matrix composition than the sample but without the analyte. For long duration measurements, the blank was measured several times to avoid thermal interferences.

Before measuring the sample, the cell was rinsed previously with the sample itself. Enough volume of sample to rinse the cell and make the measurements was foreseen. They were made by triplicate and the experiments were made twice.

3.2.1. Photometric analysis of H_2O_2

A photometer is an instrument that works in a similar way than visible spectroscopy, but is simpler. It only uses the loss of intensity of a determined light source to quantify the analyte. In this work a Photometer PF-12 Macherey Nagel (Germany) was used to quantify the H_2O_2 present in solution. This technique uses different chemicals depending on the analyte. In this case, the determination of peroxide, was by catalytic oxidation of an indicator using peroxidase. The wavelength used was 620 nm, and the concentration range was between 0.03 $mg \cdot dm^{-3}$ and 2.00 $mg \cdot dm^{-3}$. The quantity of sample used was 4 ml. A calibration curve at different H_2O_2 concentrations was performed before each analysis.

3.3. TIME RESOLVED LASER FLUORESCENCE SPECTROSCOPY

Time Resolved Laser Fluorescence Spectroscopy is based in the emission spectroscopy. The laser beam excites the molecules, specifically the electrons. The excited electron returns to the ground state emitting a photon. The time between the excitation and the return to the ground state is characteristic of the species. The emitted photons are captured by the spectrometer that transforms the emitted light into an electronic signal, that is sent to the computer where the signal is treated by specific software.

The spectrum obtained is characteristic of each element. The light is emitted at different wavelengths depending on the element.

A wide variety of processes may affect the intensity of fluorescence. A decrease in the fluorescence is known as fluorescence quenching. There exist different kinds of quenching. The deactivation of the excited state of the fluorophore by the interaction of another molecule is known as collisional or dynamic quenching. The Stern-Volmer equation describes this phenomenon:

$$\frac{F_0}{F} = 1 + K[Q] = 1 + k_q \tau_0 [Q] \quad (1)$$

Where F_0 is the fluorescence without the quencher (molecule that produces quenching), F is the fluorescence with the quencher, K is the Stern-Volmer quenching constant, k_q is the bimolecular quenching constant, τ_0 is the unquenched lifetime and $[Q]$ is the quencher concentration.

In dynamic quenching the following ratio is preserved:

$$\frac{F_0}{F} = \frac{\tau_0}{\tau} \quad (2)$$

When a non-fluorescent complex is formed between the fluorophore and some other molecule, this kind of quenching is known as static quenching. In this case the ratio τ_0/τ is always 1. Static quenching doesn't affect the species lifetime.

Quenching can also occur for other reasons such as attenuation of the incident light by the fluorophore itself or other absorbing species [4].

In some cases of quenching like dynamic quenching, the quenching effect could be attenuated by decreasing the temperature. Cryo-TRLFS is a very useful technique that allows the determination of species that normal TRLFS techniques could not analyze. The main difference in the experimental set-up of this technique is that the sample is in a cryostat at very low temperatures.

In this work Origin program has been used to adjust the experimental lifetime to exponential decays in order to identify the number of species and the species itself. It also has been used to deconvolute the main spectra in the spectra of each species.

A Nd:YAG laser (20 Hz, 4–6 ns pulse duration, k = 266 nm, Emax = 5 mJ, Polaris II, New Wave Research, USA) was used for the TRLFS analysis performed in the Fundació CTM Manresa. The uranium(VI) samples were introduced in a 1 cm path-length quartz cuvette, which was inside a dark sample compartment (SampleMax, JobinYvon, France). The fluorescence signal was measured perpendicular to the excitation laser beam. Both the laser beam and the uranyl emitted fluorescence were focalized using quartz lenses. The focused fluorescence was directed to a monochromator (TRIAX 320, JobinYvon, France, grating groove density:600 lines/mm, k range = 470–590 nm). The monochromator was connected to a Charge Coupled Device (CCD) (JobinYvon, France). The signal acquisition was performed using the LABSPEC5.0 for Windows (JobinYvon, France) program.

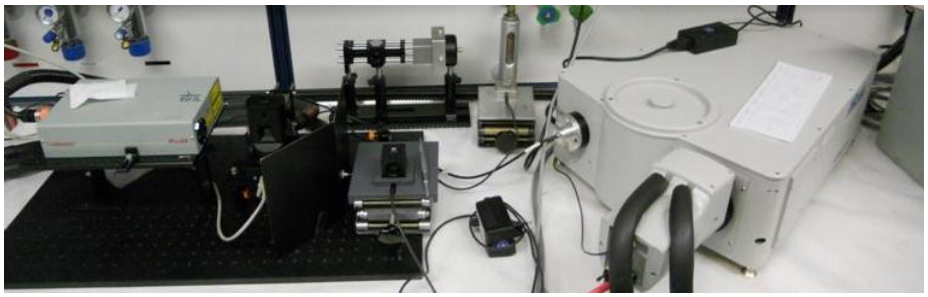

Figure 3.7. TRLFS set-up in the Helmholtz-Zentrum Dresden-Rossendorf.

At the Helmholtz-Zentrum Dresden-Rossendorf (HZDR), the laserfluorescence system for room temperature measurements consisted of a ‘‘Minilite II’’ (Continuum) laser, an ‘‘iHR 550’’spectrometer (Horiba JobinYvon, France) and an Intensified CCD (ICCD)camera (Horiba JobinYvon, France) (Figure 3.7). The fluorescence measuring system for the low temperature experiments consisted of an ‘‘Inlite’’ (Continuum) laser, a 1235 Digital Triple Grating Spectrograph spectrometer (EG&G Princeton Applied Research, USA), and an ICCD camera (Princeton Instruments, inc., belonging to Roper Scientific, USA).The sample was cooled with a closed He-cycle, consisting of aRDK10-320 He-cryostat (OerlikonLeybold Vacuum, Germany), a ‘‘Coolpak2000 A’’ compressor unit (Oerlikon Leybold Vacuum, Germany) and a ‘‘D 25B’’ oil vacuum pump (Leybold Vacuum GmbH, Germany) (Figure 3.8).

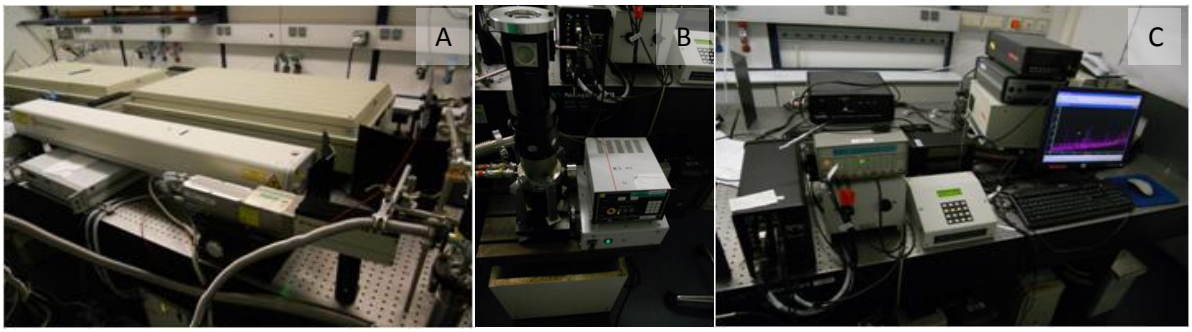

Figure 3.8. A. Laser system; B. Cryostat; C. Spetrometer.

FLURAN ®[5] was used in some experiments of this work to enhance the fluorescence of the uranium. FLURAN ®was used only to quantify the uranium on solution but never was used if the interest was in the speciation.

3.4. ALPHA SPECTROSCOPY

Most of the transuranium elements emit alpha-particles. Alpha-particles are heavy charged particles, large and slow, and they lose energy readily in materials. That makes their detection quite difficult. Most of the particles emitted are absorbed by the material itself, and the ones that are released can be stopped by a single sheet of paper. Any physical medium between the sample and the detector will absorb part of the alpha particle energy.

The energy of the alpha particles produced by the alpha-emitters is between 4 and 7 MeV, with a difference between them as little as 10 keV, which is close to the detectors resolution.

To solve this problem two different techniques are commonly used. Liquid Scintillation and measurements in an aqueous medium using high resolution passivated implanted planar silicon (PIPS) detectors.

Liquid scintillation is the faster option but the resolution is lower and the possibility of reducing interferences is limited. In this work the measurements has been made using PIPs detectors. This technique allows the identification of the alpha energies of the different radionuclides with almost no interferences. Thanks to that very low minimum detectable

activities (MDA) can be reached. The handicap of this technique is that requires long analysis times [6].

In this work α-spectrometry was used to determine the amount of ^{238}Pu, ^{239}Pu and ^{240}Pu using a analysis chamber with a S100 field channel analysator (^{238}Pu, $^{239/240}$Pu) and passivated implanted planar silicon (PIPS) detectors (Canberra 74/01, Canberra Industries Inc, Meriden, USA). PIPS detectors increase the resolution of the spectra, which is necessary to deconvolute the $^{239/240}$Pu peak in order to obtain a precise ^{239}Pu/^{240}Pu ratio.

3.5. BET

In 1938 Brunauer , Emmett and Teller (BET) published a new theory based on the theory of Langmuir gas adsorption in a solid [7]. A technique based on this theory was used in this work in the surface area measurements of Studtite and uranium dioxide samples.

The BET adsorption method is widely used in surface science to calculate the surface area of porous materials by physical adsorption of gas molecules.

In most cases nitrogen is used as gas to be adsorbed but in specific cases, such as activated carbon, is more common to use the adsorption of argon or carbon dioxide. Samples with low surface area can also be characterized by krypton gas adsorption.

Langmuir adsorption theory is a theory for monolayer molecular adsorption. BET theory expands this theory for multilayer adsorption cases as long as they meet three hypotheses:

H1 : That the gas molecules physically adsorbed on a solid in layers infinitely.
H2 : That there is no interaction between the layers of adsorption .
H3 : That the Langmuir theory can be applied to each layer .

BET adsorption isotherm is indicated in the following equation:

$$\frac{1}{\vartheta[(P_0/P)-1]} = \frac{c-1}{\vartheta_m}\left(\frac{P}{P_0}\right) + \frac{1}{\vartheta_m c} \quad (3)$$

Where P and P_0 are the equilibrium and the saturation pressure of adsorbates at the temperature of adsorption, v is the amount of gas adsorbed, and v_m is the amount of monolayer adsorbed gas. c is the BET constant:

$$c = exp\left(\frac{E_1 - E_L}{RT}\right) \quad (4)$$

E_1 is the heat of adsorption for the first layer, and E_L is that for the second and higher layers and is equal to the heat of liquefaction.

The determination of the surface area is made in the range that meets the linearity of the BET adsorption isotherm equation. The linearity is maintained only for *P/Po* between 0.05 and 0.35 [8].

The value of the surface area is the one where the measure of adsorption is equal to the desorption measurement. By dividing this value by the amount of sample used, the specific surface area is obtained.

In this study a Micromeritics Flowsorb II 2300 (USA) was used. The adsorbed gas was N_2 from a mixture of 30% N_2 and the rest of Helium.

3.6. SCANNING ELECTRON MICROSCOPY

The Scanning Electron Microscopy (SEM) is a technique that uses electrons instead of light to obtain images from a sample. It was developed at the beginning of the fifth decade of the twentieth century and now is used in a wide variety of research from biology to material science.

It has a much higher resolution than optical microscopes, allowing the observation of nanoparticles. SEM also has a large depth of field that allows more of a specimen to be in focus at one time and creates a 3D sensation.

A Scanning Electron Microscope is based in an electron gun that emits an electron beam through different electromagnetic fields and lenses to the sample. The sample is in vacuum in order to create a vertical electron flow through the microscope. Once the electron beam hits the sample, primary, secondary and auger electrons plus X-rays are ejected (Figure3.9).

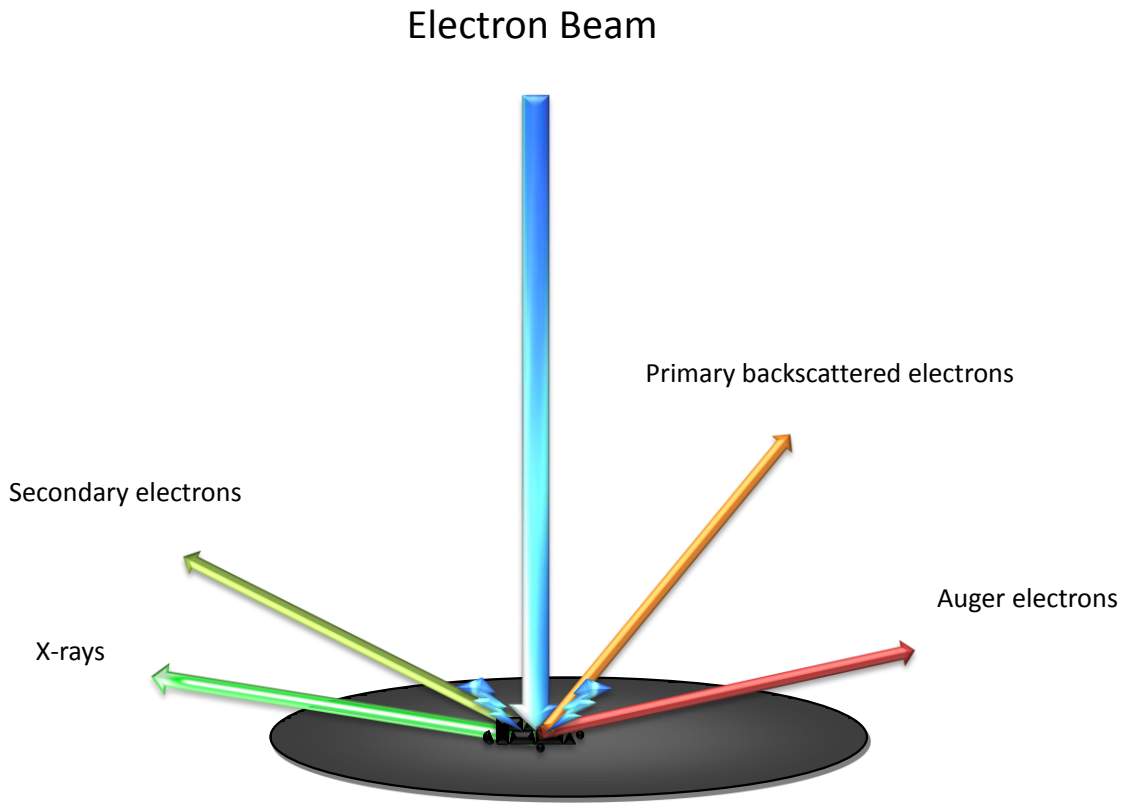

Figure 3.9. Effects of the electron beam on a SEM sample.

X-rays, backscattered electrons, and secondary electrons are captured in the SEM by the secondary electron detector, the backscattered electron detector and the scanning coils. These detectors sent a signal to a screen that produces the final image.

As mentioned before, the sample is in vacuum inside the SEM. Due to that, the sample must be dry in order to avoid vapour formation inside the microscope (Except for the Environmental Scanning Electron Microscopes, ESEM, that operate at higher pressures,

allowing the analysis of wet samples). The use of electrons instead of light, carries some inconvenience for the non-metallic samples. The metallic samples are conductive and don't require any preparation but the non-metallic samples need to be made conductive by attaching to them some conductive element forming a layer.

In this work a Scanning Electron Microscope from the brand ZEISS (Germany) a model ULTRA PLUS has been used. The ULTRA series by Carl Zeiss have two different detectors, the In-lens SE detector GEMINI that is capable of clear topographic imaging and also the EsB detector for compositional contrast imaging that enables simultaneous real time imaging and mixing of both signals. The EsB incorporates filtering technology which enables high resolution energy selective backscattered electron (BSE) imaging at low voltages revealing previously unseen image details.

The ULTRA PLUS combines the detection capabilities of the ULTRA series plus a revolutionary charge compensation (CC) system for imaging of most critical non-conducting samples [9].

3.7. REFERENCES

1 J.H. Gross. (2011) Mass Spectrometry, a text book. 2d Edition, *Springer*.

2 J.M. Hollas. (2004) Modern Spectroscopy. 4th Edition, *Wiley*.

3 Agilent 8453 UV-visible Spectroscopy System Operator's Manual. (2007), *Agilent Technologies*.

4 J.R. Lakowicz. (2006). Principles of Fluorescence Spectroscopy. *3d Edition Springer*.

5 K.W. Jung, J.M. Kim, C.J. Kim and J.M. Lee. (1987). *J. Korean Nucl. Soc.*,**19**, 4, 242-248.

6 B. de Celis, V. del Canto, R. de la Fuente, J.M. Lumbreras, J. Mundo and B. de Celis Alonso. (2011). Determination of Actinides Using Digital Pulse Processing Analysis, Radioisotopes - *Applications in Physical Sciences*, Prof. Nirmal Singh (Ed.). ISBN: 978-953-307-510-5

7 S. Brunauer, P. H. Emmett, and E. Teller. (1938). Adsorption of Gases in Multimolecular Layers. *J. Am.Chem. Soc.*, **60**, (2), 309–319.

8 Micromeritics Flowsorb II 2300 Manual. (1989). *Micromeritics Instrument Corporation*.

9 FESEM ULTRA PLUS Manual. *Carl Zeiss Microscopy GmbH*.

4 Determination Of The Equilibrium Formation Constants Of Two U(VI)-Peroxide Complexes At Alkaline pH

4 Determination Of The Equilibrium Formation Constants Of Two U(VI)-Peroxide Complexes At Alkaline pH

4.1. INTRODUCTION

The dissolution of UO_2(s) under oxidizing conditions controls the uranium mobility in the environment from natural deposits and nuclear waste repositories, such as spent nuclear fuel (SNF) and transuranic wastes. The radiolysis of water in contact with the SNF in a repository for high level nuclear waste (HLNW) can lead to the formation of oxidizing species [1-3] . In particular, hydrogen peroxide has been shown to be produced by radiolysis of water, either by radiation alpha, beta or gamma [4-6]. In addition, hydrogen peroxide strongly affects the oxidative dissolution of UO_2 and SNF, by oxidizing the U(IV) of the solid to more soluble U (VI) species [7-9]. Thus, different experiments have shown the increase of the dissolution rates in the presence of hydrogen peroxide in a wide pH range [8,10], and the mechanism of oxidative dissolution of UO_2 in hydrogen peroxide has been described [9,10]. These results indicate that in a hypothetical future repository of HLNW the evolution of the waste could be strongly affected by the interaction of uranium with H_2O_2.

Moreover, hydrogen peroxide can also affect the release of uranium from SNF by the formation of solid phases and/or uranyl-peroxide soluble complexes. The uranium peroxides studtite ($UO_2O_2{\cdot}4H_2O$) and metastuditte ($UO_2O_2{\cdot}2H_2O$) have been identified as uranyl secondary solid phases in UO_2 leaching experiments under different experimental conditions and irradiations [5,6,11-13] as well as in SNF dissolution experiments [14,15]; actually, the only effective source for providing a high enough hydrogen peroxide concentration for the formation of studtite is the radiolysis of water [16]. The solubility product of studtite [16] was determined to be $1.3{\cdot}10^{-3}$, and studtite has been demonstrated to precipitate at bulk hydrogen peroxide concentrations between 10^{-5} and 10^{-4} mol dm^{-3} on the UO_2 surface [5,11].

The solution chemistry of the uranyl-peroxide system is still relatively unknown. In order to improve the knowledge in this system, a scientific effort has been made in recent

years towards the identification and thermodynamic characterization of the complexes between U(VI) and H_2O_2 in solution. Moskvin [17] determined, from studtite dissolution experiments, the formation constants of three uranyl-peroxide complexes, but they were not considered reliable by the Nuclear Energy Agency (NEA) and have not been included in the uranium thermodynamic databases [18].

$$UO_2O_2{\cdot}4H_2O(s) \leftrightarrows UO_2O_2^{0} + 4H_2O \quad (1)$$

$$UO_2O_2{\cdot}4H_2O(s) + H_2O_2 \leftrightarrows UO_2(O_2)_2^{2-} + 2H^{+} + 4H_2O \quad (2)$$

$$UO_2O{\cdot}\ 4H2O\ (s) + 2H_2O_2 \leftrightarrows UO_2(O_2)_3^{4-} + 4H^{+} + 4H_2O \quad (3)$$

Goff et al. [19] have identified by UV-vis spectroscopy the ternary complex $UO_2(O_2)(CO_3)_2^{4-}$ and they have determined its apparent formation constant, log*K'*= 4.70 ± 0.02 relative to $UO_2(CO_3)_3^{4-}$.

$$UO_2(CO_3)_3^{4-} + HO_2^{-} \leftrightarrows UO_2O_2(CO_3)_2^{4-} + CO_3^{2-} + H^{+} \quad (4)$$

A. Meca in her PhD Thesis "Processos que afecten la mobilitat de l'urani en entorns hiperalcalins oxidants i sediments contaminants" [20] studied the formation of complexes in the UO_2-H_2O_2 system in the absence of carbonate using UV-vis spectrophotometry at a constant pH = 12, which may be reached after the interaction of groundwater with concrete materials of the repository [21-23]. In her Thesis she pointed out the existence of two urano-peroxo complexes. Using graphical methods she obtained the value of the formation constant for the complex $[UO_2(HO_2)(OH)_2]^{-}$: logβ=25.4 ± 0.2.

The work presented in this chapter has its origins in the work from A. Meca, and continues the research from there. The experimental data was increased from the original 42 spectra to 150 spectra, enhancing the reliability in the graphical methods. Moreover, in order to increase the accuracy and reliability of the constants determination the program STAR (STability constants by Absorbance Reading)[24] was used and the constants of the two U(VI)-peroxo complexes were determined. Finally this new constants were used in the MEDUSA software in order to model the impact of these new complexes in the speciation of uranium at high alkaline pH.

Months after the publication of the work described in this section [25] appeared the paper of Zanonato et al. [26] which proposed the formation of two uranyl-peroxide complexes $[UO_2(OH)(O_2)]^-$ and $[(UO_2)_2(OH)(O_2)_2]^-$. The first was the predominant species at pHs between 9.5 and 11.5 while the second was present at pHs below 10.5 in their experimental conditions. In their paper lamented that the work described in this section was performed at a fixed pH. There are several reasons to work at a fixed pH = 12, and are explained in the section of materials and methods. Moreover, in a later work [27, chapter 5], using a completely different technique as Time Resolved Laser Fluorescence Spectroscopy (TRLFS), the value for the first constant complex $[UO_2O_2OH_2^{2-}]$ was calculated, and it was very similar to determined using UV-Visible spectrophotometry. This coincidence in the values of the constants increases the confidence in the data presented in this work.

4.2. MATERIALS AND METHODS

The experiments were carried out at pH = 12. The pH was buffered using a 0.01 mol dm^{-3} tetramethylammonium hydroxide (TMAH) solution (Fluka), because of the capacity of TMAH to prevent uranate precipitation [28] by avoiding the presence of high concentrations of alkaline ions. The ionic strength was 0.01 mol dm^{-3}. Stock solutions of uranyl nitrate (Panreac) and hydrogen peroxide (Merck) were prepared. Uranium content was determined by ICP-MS and the stock H_2O_2 was periodically standardized with $Na_2S_2O_3$ (Scharlau) in H_2SO_4.

Two different series of experiments were carried out. In the first series, hydrogen peroxide was kept constant ($[H_2O_2]_{tot} = 1 \cdot 10^{-3}$ mol dm^{-3}) and uranium(VI) concentration was varied between $5 \cdot 10^{-6}$ and $2 \cdot 10^{-4}$ mol dm^{-3}. In the second series, uranium(VI) concentration was constant ($2 \cdot 10^{-4}$ mol dm^{-3}) and total hydrogen peroxide concentration was varied between $1 \cdot 10^{-5}$ and $1 \cdot 10^{-3}$ mol dm^{-3}.

The range of uranium and hydrogen peroxide concentrations as well as the constant pH used in these experiments were chosen considering that some analytical problems are involved when studying the uranium(VI)–peroxide system. The use of the TMAH buffer avoids the precipitation of uranates. However, some other uranyl-containing solid phases are likely to precipitate if the total uranium concentration in solution, or even the total hydrogen

peroxide concentration increases. In particular, the uranyl peroxide studtite ($UO_2O_2 \cdot 4H_2O$) [11,16] has been demonstrated to precipitate even at relatively low hydrogen peroxide concentrations ($\log K_{s0(studtite)}$ between -2.88 and -2.86 [16]). Avoiding the precipitation of uranyl peroxide phases as well as the uranyl hydroxide schoepite ($UO_2(OH)_2$) limited the range of experimental uranium and hydrogen peroxide concentrations ($\log K_{s0(schoepite)}$ = 4.93 [18]). In this sense, the saturation indexes for these two solid phases in the experiments with the highest uranium concentration in solution ($1 \cdot 10^{-4}$ mol dm^{-3}) were determined to be -0.10 and -0.99 for studtite and schoepite, respectively.

On the other hand, the experiments have been carried out at a constant pH due to the variation of the uranium(VI) speciation with pH in the neutral to alkaline pH even in the absence of complexing agents. A constant pH was also necessary in order to keep in all the experiments a constant H_2O_2/HO_2^- ratio (pK_a for hydrogen peroxide is 11.6).

The experiments were carried out at 25.0 ± 0.1 °C in a N_2 glove-box, in order to avoid CO_2 intrusion and to prevent the formation of uranyl–carbonate complexes. All the samples were closed in tubes and measured immediately after taking them out of the glovebox. A Hewlett-Packard 8453 spectrophotometer with temperature cell HP 89090A was used for the UV-vis measurements (1 cm length cell). The measurements were made by triplicate and the experiments were made twice.

4.3. RESULTS

The UV-vis spectra recorded from solutions with a constant hydrogen peroxide concentration and variable total uranium concentration are shown in Figure 4.1. Uranium(VI) solutions at the same pH and TMAH concentration showed no absorbance in the absence of hydrogen peroxide in the range studied: 300–600 nm. The same occurred with solutions with H_2O_2 and TMAH. The uranium–H_2O_2 solutions exhibit similar spectra with an absorbance maximum at around 350 nm, pointing to the formation of a U(VI)–H_2O_2 complex; in addition, there is an increase of the absorbance with the total uranium concentration in solution.

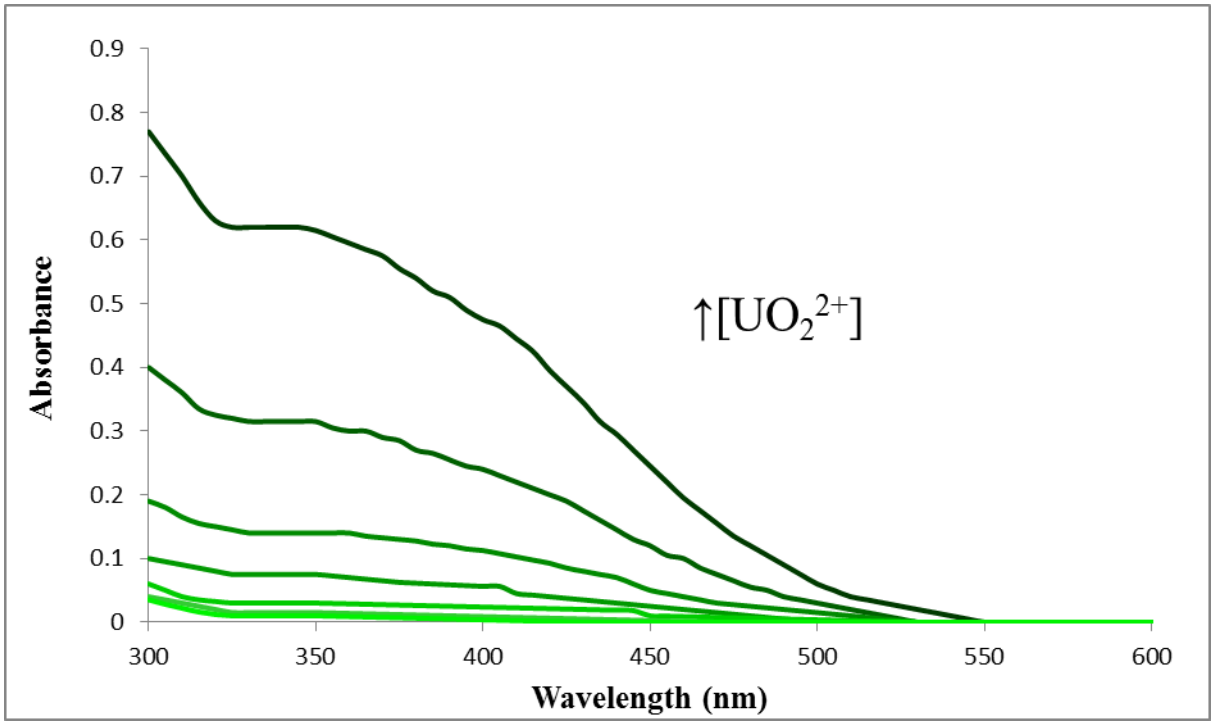

Figure 4.1 Spectra recorded for the solutions with a constant hydrogen peroxide concentration ($1 \cdot 10^{-3}$ mol dm^{-3}) and a variable uranium concentration ($5 \cdot 10^{-6}$ to $2 \cdot 10^{-4}$ mol dm^{-3}; pH = 12).

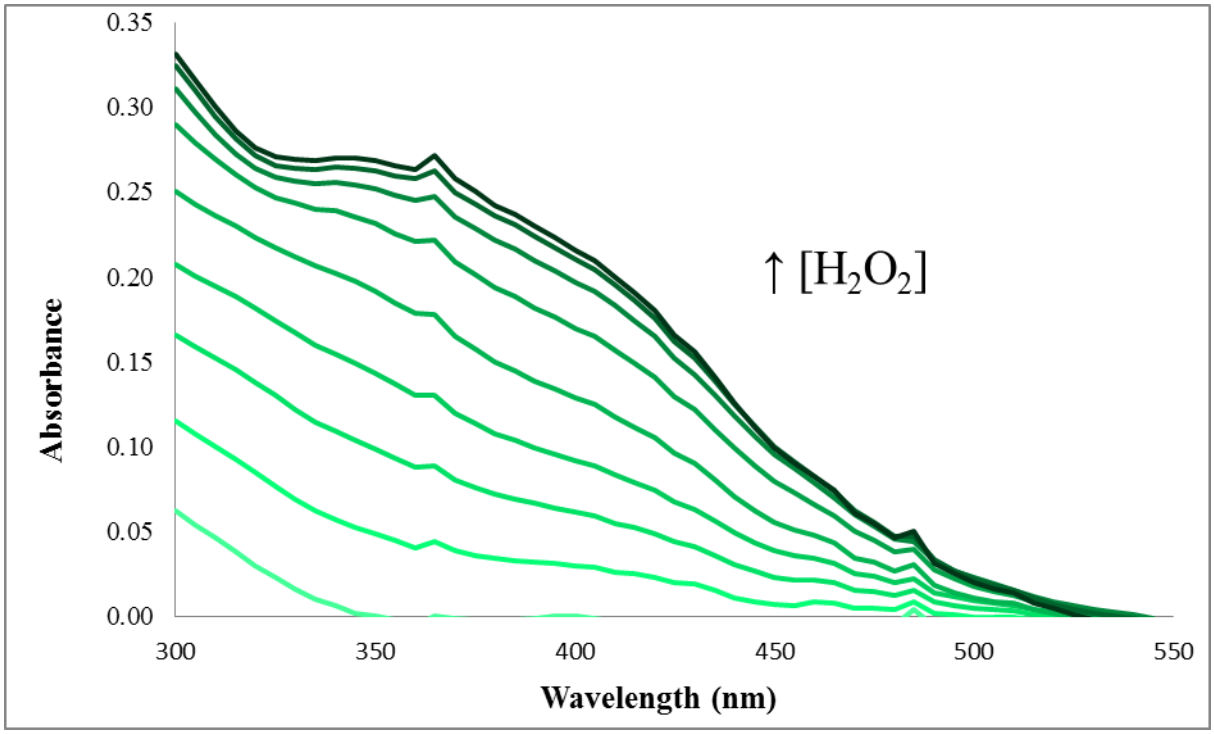

Figure 4.2 Spectra recorded for the solutions with a constant uranium concentration and a variable initial hydrogen peroxide concentration (hydrogen peroxide concentration between $1 \cdot 10^{-5}$ and $1 \cdot 10^{-3}$ mol dm^{-3}, and uranium concentration of $2 \cdot 10^{-4}$ mol dm^{-3}; pH= 12).

The spectra recorded for the solutions with a constant uranium concentration ($2 \cdot 10^{-4}$ mol dm^{-3}) and a variable initial hydrogen peroxide concentration are shown in Figure 4.2. Interestingly, the solutions with hydrogen peroxide concentrations higher than total uranium concentration (this means with a $[H_2O_2]_0/[U(VI)]_0$ ratio higher than 1) present a change in the shape of the spectra. Assuming that the shape of the first spectra is due to a 1:1 U(VI):H_2O_2 complex, this second shape could be attributed to a 1:2 complex.

These changes might also be seen in Figure 4.3, that shows the variation of the absorbance with the $\{H_2O_2\}_0/\{U(VI)\}_0$ ratio. The slope of the curve changes at $\{H_2O_2\}/\{U(VI)\}_0 = 1$ and it is very low at $\{H_2O_2\}/\{U(VI)\}_0 > 2$. As above, these changes in the slope are assumed to be due to the formation of two complexes of different stoichiometry.

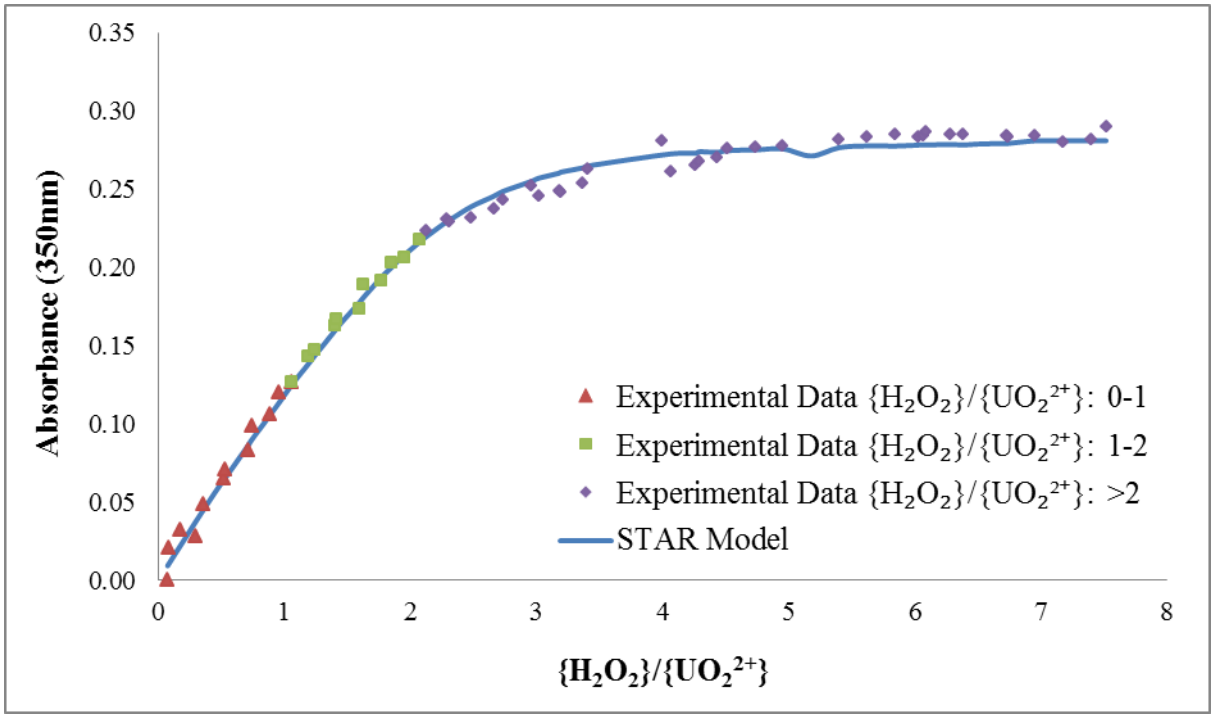

Figure 4.3. Variation of the absorbance with the ratio of activities ($[H_2O_2]_0 = 1 \cdot 10^{-5}$ to $1 \cdot 10^{-3}$ mol dm^{-3}, $[U(VI)]_0 = 2 \cdot 10^{-4}$ mol dm^{-3}, pH= 12). The line represents the fitting of the data considering the equilibrium constants determined with the STAR program.

4.3.1. Graphical determination of the formation equilibrium constant of the first U(VI)–H_2O_2 complex

A graphical method was used to determine the equilibrium constant of the first U(VI)–peroxide complex. This value was afterwards used as an input to be refined with the STAR program (see below).

At the experimental conditions of $[H_2O_2]_0/[U(VI)]_0 < 2$ and pH = 12, hydroxyl concentration (about 10^{-2} mol dm^{-3}) is two orders of magnitude higher than both uranium and hydrogen peroxide concentrations, and it can be supposed to be constant. Under the experimental conditions of this work, the equilibria involving uranium(VI) that have to be considered can be expressed in a general reaction:

$$m UO_2^{2+} + n H_2O_2 + p OH^- \leftrightarrows (UO_2)_m(O_2)_n(OH)_{p-2n}^{(2m-p)+} + 2n H_2O: \log\beta_{m,n,p} \quad (5)$$

and are [18,29]:

$$UO_2^{2+} + H_2O_2 + 4OH^- \leftrightarrows UO_2(O_2)(OH)_2^{2-} + 2H_2O: \log\beta_{1,1,4} \quad (6)$$

$$UO_2^{2+} + 3OH^- \leftrightarrows UO_2(OH)_3^-: \log\beta_{1,0,3} = 21.75 \quad (7)$$

$$UO_2^{2+} + 4OH^- \leftrightarrows UO_2(OH)_4^{2-}: \log\beta_{1,0,4} = 23.6 \quad (8)$$

The concentration of the complexes in solution at equilibrium will be:

$$[UO_2(OH)_3^-] = \beta_{1,0,3}[UO_2^{2+}][OH^-]^3 \quad (9)$$

$$[UO_2(OH)_4^{2-}] = \beta_{1,0,4}[UO_2^{2+}][OH^-]^4 \quad (10)$$

$$[UO_2(O_2)(OH)_2^{2-}] = \beta_{1,1,4}[UO_2^{2+}][H_2O_2][OH^-]^4 \quad (11)$$

Considering the mass-balances of uranium(VI) and hydrogen peroxide in solution:

$$[UO_2^{2+}] = [UO_2^{2+}]_o - [UO_2(O_2)(OH)_2^{2-}] - [UO_2(OH)_3^-] - [UO_2(OH)_4^{2-}] \quad (12)$$

$$[H_2O_2] = [H_2O_2]_o - [UO_2(O_2)(OH)_2^{2-}] \quad (13)$$

The addition of eqn (9) and (10) gives the total concentration of the uranyl hydroxo-complexes, as a function of free uranyl concentration, which has been obtained from eqn (12). This gives:

$$[UO_2(OH)_3^-] + [UO_2(OH)_4^{2-}] = \frac{(\beta_{1,0,3}+\beta_{1,0,4}[OH^-])\left([UO_2^{2+}]_0 - [UO_2O_2(OH)_2^{2-}]\right)[OH^-]^3}{1+(\beta_{1,0,3}+\beta_{1,0,4}[OH^-])[OH^-]^3} \quad (14)$$

The concentration of the uranyl–peroxide complex is given by the combination of eqn (11) and (13) and the addition of the concentrations of the uranyl–hydroxide complexes by eqn (12). The expression obtained is:

$$\frac{1}{[UO_2(O_2)(OH)_2^{2-}]} = \frac{1}{[UO_2^{2+}]_0} + \frac{1+(\beta_{1,0,3}+\beta_{1,0,4}[OH^-]+\beta_{1,1,4}[UO_2^{2+}]_0[OH^-])[OH^-]^3}{\beta_{1,1,4}[OH]^4[UO_2^{2+}]_0} \cdot \frac{1}{[H_2O_2]_0} \quad (15)$$

According to the Lambert–Beer equation, the absorbance is proportional to the concentration of the uranyl–peroxide complex:

$$A = \varepsilon l [UO_2(O_2)(OH)_2^{2-}] \quad (16)$$

where A is the absorbance, ε is the molar extinction coefficient and l is the cuvette length. Combining eqn (15) and (16):

$$\frac{1}{A} = \frac{1}{\varepsilon \cdot \ell \cdot [UO_2^{2+}]_0} + \frac{1+(\beta_{1,0,3}+\beta_{1,0,4}[OH^-]+\beta_{1,1,4}[UO_2^{2+}]_0[OH^-])[OH^-]^3}{\varepsilon \cdot \ell \cdot \beta_{1,1,4} \cdot [OH]^4 \cdot [UO_2^{2+}]_0} \cdot \frac{1}{[H_2O_2]_0} \quad (17)$$

The representation of *1/A* vs. $1/[H_2O_2]_0$ is shown in Figure 4.4. The lineal regression of the data allowed to determine the molar extinction coefficient, $(1.7 \pm 0.9)\cdot 10^3$ mol^{-1} dm^3 cm^{-1}, as well as the value of the formation constant of the complex: $\log\beta_{1,1,4} = 27.1 \pm 0.5$.

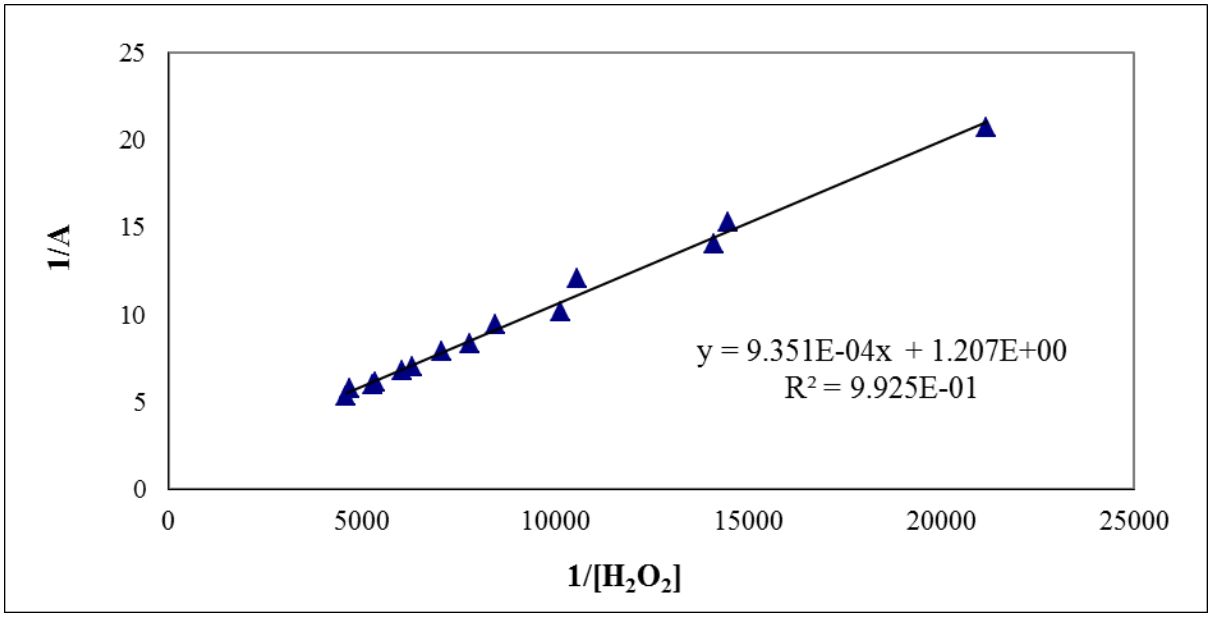

Figure 4.4 Representation of 1/Absorbance vs. $1/[H_2O_2]_0$, for $[H_2O_2]/[UO_2^{2+}]$ ratio < 1.

The equilibrium constant obtained was corrected considering the ionic strength of the solution by using the Debye–Hückel approximation [18], the value obtained was: $\log\beta°_{1,1,4}$ = 27.2 ± 0.5. This value is higher than the one from the work of Meca [20]: $\log\beta°$=25.4± 0.2.

Uncertainties have been estimated in order to make a propagation of error analysis on the experimental data. Uncertainties from the origin ordinate and the slope have been estimated considering the equations related to the regression line [30].

$$\Delta a = \left[\frac{\sum_{i=1}^{N} (y_i - a x_i - b)^2}{(N-2)\sum_{i=1}^{N} (x_i - \bar{x})^2} \right]^{\frac{1}{2}} \tag{18}$$

$$\Delta b = \left[\left(\frac{1}{N} + \frac{\bar{x}^2}{\sum_{i=1}^{N} [(x_i - \bar{x})^2]} \right) \left(\frac{\sum_{i=1}^{N} (y_i - a x_i - b)^2}{N-2} \right) \right]^{\frac{1}{2}} \tag{19}$$

where Δa is the slope error, Δb is the origin ordinate error, $\bar{x}$ is the mean value of x, and N is the number of values.

The absolute errors estimated for the origin ordinate and the slope are 1.5 and $5.6 \cdot 10^{-4}$, respectively.

The error of the initial concentration of uranium has been estimated measuring six samples of uranium with the same concentration ($2\cdot10^{-4}$ mol dm^{-3}), the standard deviation was $5.5\cdot10^{-6}$. The error in the measurement of the hydroxyl concentration was estimated from seven pH measurements, which gave a standard deviation of $4.3\cdot10^{-4}$. The uncertainties of the $\beta°_{1,0,3}$ and $\beta°_{1,0,4}$ constants have been obtained from the literature [29].

With those estimated uncertainties, propagation of error analysis was made, using the following equation:

$$e_F = \sqrt{\left(\frac{\partial F}{\partial x}\right)^2 e_x{}^2 + \left(\frac{\partial F}{\partial y}\right)^2 e_y{}^2 + \left(\frac{\partial F}{\partial z}\right)^2 e_z{}^2 + \cdots} \tag{20}$$

where F is the equation used to find the value of its uncertainty, $x,y, z, \ldots$ are the parameters of this equation and e_i is the uncertainty of the parameter.

For example in the case of the molar extinction coefficient (ε):

$$\varepsilon = \frac{1}{O.O.\cdot [UO_2^{2+}]_0} \tag{21}$$

where *O.O.* is the origin ordinate and $[UO_2{}^{2+}]_0$ is the initial concentration of $UO_2{}^{2+}$.

$$e_\varepsilon = \sqrt{\left(\frac{\partial \varepsilon}{\partial O.O.}\right)^2 e_{o.o.}^2 + \left(\frac{\partial \varepsilon}{\partial [UO_2^{2+}]_0.}\right)^2 e_{[UO_2^{2+}]_0}^2} \tag{22}$$

$$e_\varepsilon = \sqrt{\left(\frac{-1}{O.O.{}^2[UO_2^{2+}]_0}\right)^2 e_{o.o.}^2 + \left(\frac{-1}{O.O.[UO_2^{2+}]_0^2}\right)^2 e_{[UO_2^{2+}]_0}^2} \tag{23}$$

Finally the uncertainty value for $\log\beta°_{1,1,4}$ is 0.5.

4.3.2. Determination of the formation constants of the two UO_2^{2+}–H_2O_2 complexes by using the STAR program

The graphical method described above did not allow the determination of the formation constant of the second complex. Numerical methods are more reliable and accurate than most of the graphical methods and in this work the program STAR (STability constants by Absorbance Reading) [24] was used. While in the graphical method [18] experimental points were used to fit the model, in the STAR program 2500 experimental points have been used, minimizing the effect from experimental data uncertainties in the model. The STAR program also allows the refinement of up to ten constants at the same time and, in addition, the program tries different models and wavelengths ranges and allows finding the best chemical model for a given system. In addition to the experimental spectra, the STAR program needs an input data file with information of the components and species assumed to be in solution at equilibrium as well as the equilibrium formation constants of such species [29]. The program calculates a model to represent the theoretical spectra and the residuals.

The refinement of equilibrium constants is done by the procedure REFINE, using the Gauss–Newton non-linear least-squares algorithm [30] by numerical differentiation, until a minimum in the sum of squares residuals (U) is attained. This function is defined as

$$U = \sum_{i=1}^{n_S} \sum_{j=1}^{n_W} r_{i,j}^{\ 2} = \sum_{i=1}^{n_S} \sum_{j=1}^{n_W} (A_{i,j,\mathrm{exp}} - A_{i,j,\mathrm{calc}})^2 \qquad (24)$$

where n_s and n_w are the number of solutions and the number of wavelengths, respectively. The minimization process is repeated until the relative change of U between two iterations is less than 0.01%. In the case of divergence in the refinement procedure, the method is modified to optimize the “shifts” of the constants [29].

Table 4.1. Species in the chemical equilibrium. Constants are referenced to zero ionic strength at 25 °C, but before their incorporation to the STAR code database, the equilibrium constants were extrapolated to the experimental ionic strength, using the Debbye-Hückel approximation[18].

Species	logK°	Reaction
$\mathbf{UO_2(OH)_3^-}$	-20.25 ± 0.42	$3H_2O(l) + UO_2^{2+} \leftrightarrows 3H^+ + UO_2(OH)_3^-$
$\mathbf{UO_2(OH)_4^{2-}}$	-32.40 ± 0.68	$4H_2O(l) + UO_2^{2+} \leftrightarrows 4H^+ + UO_2(OH)_4^{2-}$
$\mathbf{UO_2OH^+}$	-5.25 ± 0.24	$H_2O(l) + UO_2^{2+} \leftrightarrows H^+ + UO_2OH^+$
$\mathbf{UO_2(OH)_2}$	-12.15 ± 0.07	$2H_2O(l) + UO_2^{2+} \leftrightarrows 2H^+ + UO_2(OH)_2$
$\mathbf{(UO_2)_2OH^{3+}}$	-2.70 ± 1.00	$H_2O(l) + 2UO_2^{2+} \leftrightarrows H^+ + (UO_2)_2OH^{3+}$
$\mathbf{(UO_2)_2(OH)_2^{2+}}$	-5.62 ± 0.04	$2H_2O(l) + 2UO_2^{2+} \leftrightarrows 2H^+ + (UO_2)_2OH_2^{2+}$
$\mathbf{(UO_2)_3(OH)_4^{2+}}$	-11.90 ± 0.30	$4H_2O(l) + 3UO_2^{2+} \leftrightarrows 4H^+ + (UO_2)_3OH_4^{2+}$
$\mathbf{(UO_2)_3(OH)_5^+}$	-15.55 ± 0.12	$5H_2O(l) + 3UO_2^{2+} \leftrightarrows 5H^+ + (UO_2)_3OH_5^+$
$\mathbf{(UO_2)_3(OH)_7^-}$	-32.20 ± 0.80	$7H_2O(l) + 3UO_2^{2+} \leftrightarrows 7H^+ + (UO_2)_3OH_7^-$
$\mathbf{(UO_2)_4(OH)_7^+}$	-21.90 ± 1.00	$7H_2O(l) + 4UO_2^{2+} \leftrightarrows 7H^+ + (UO_2)_4OH_7^+$
$\mathbf{HO_2^-}$	-11.60	$HO_2^- + H^+ \leftrightarrows H_2O_2$
$\mathbf{O_2^{2-}}$	-36.60	$O_2^{2-} + 2H^+ \leftrightarrows H_2O_2$
$\mathbf{UO_2(O_2)(OH)_2^{2-}}$	Unknown	$2H_2O(l) + UO_2^{2+} + H_2O_2 \leftrightarrows 4H^+ + UO_2(O_2)(OH)_2^{2-}$
$\mathbf{UO_2(O_2)_2(OH)_2^{4-}}$	Unknown	$2H_2O(l) + UO_2^{2+} + 2H_2O_2 \leftrightarrows 6H^+ + UO_2(O_2)_2(OH)_2^{4-}$

The values of A_{calc} are obtained by Beer's law in the procedure CALCABS, from the calculated concentrations of each species and their molar absorptivities. For the species which have unknown spectra, these are calculated by multilinear regression, damped to avoid negative values. The mass balance equations of the system are solved in the COMPLEX procedure, from the given model, the total concentrations of the components and the pH of the solution. In this procedure, the COGS routine of the COMICS program [31] and a damped Newton non-linear method [32] are used alternatively. This approach has been applied successfully to the simulation of complex equilibria in multi-metal-multi-ligand systems [32].

With the chemical species postulated for the model of the chemical equilibrium (shown in Table 4.1), the values of the formation constants obtained with the STAR program are log ${}^{*}\beta_{1,1,4}$ = -28.10 ± 0.14 and log ${}^{*}\beta_{1,2,6}$ = -46.9 ± 0.2 (the STAR program calculates formation constants referred to the formation or consumption of H+, instead of OH-, even at alkaline pH). By using the water dissociation constant, the values obtained are: log $\beta_{1,1,4}$ = 27.9 ± 0.1 and log $\beta_{1,2,6}$ = 37.1 ± 0.2. The extrapolation of these equilibrium constants to zero ionic strength, using the Debye–Hückel approximation, resulted in:

$\log \beta^{\circ}_{1,1,4} = 28.1 \pm 0.1$

$\log \beta^{\circ}_{1,2,6} = 36.8 \pm 0.2$

The value of the first constant is similar to the one found using a graphical method, $\log\beta^{\circ}_{1,1,4}$ = 27.2 ± 0.5 and higher than the one from the work of Meca [20]: $\log\beta^{\circ}$=25.4± 0.2.

The variation of the absorbance with the $[H_2O_2]/[U(VI)]$ ratio has been modeled considering the values of the equilibrium constants obtained with the STAR program, the fitting of the model to the absorbance data is shown in Figure 4.3.

Table 4.2 shows the statistic parameters obtained. The most important parameters are the sum of squared residuals, the standard deviation of residuals, and the residual mean. A fit is considered good when the standard deviation of residuals is lower than 0.005. The perfect fit will have a residual mean and a sum of squared residuals equal to 0. In our case all are optimal values. These parameters give information about the fitting of the model while skewness, kurtosis and Pearson's χ^2 tests evaluate the distribution of the residuals. Skewness, kurtosis and Pearson's χ^2 test optimal values for a Gaussian distribution with six degrees of freedom and 95% of confidence level are 0, 3 and 12, respectively.

Skewness and kurtosis are very close to the optimal value, while Pearson's χ^2 test is a little bit higher than the optimal value but it is also statistically acceptable.

Table 4.2 Statistic parameters from the STAR calculations for the H_2O_2–UO_2 system

	Value
Sum of squared residuals	0.0044761
Standard d. of residuals	0.002936743
Mean residual	0.002220761
Residual mean	-0.000215541
Chi-squared test	19.0000000
Skewness	0.1655885
Kurtosis	2.9626457

The STAR program includes the STARFA utility, which determines the number of absorbing species by a factor analysis of the absorbance data matrix [24].The rank of this absorbance matrix gives the minimum number of absorbing species in solution. In the plot $s_k(A)$ *vs.* k, the rank of our matrix corresponds to the greater k with $s_k(A) > s_{inst}(A)$. $s_k(A)$ is the calculated standard deviation of absorbance as estimated by factor analysis of the absorbance matrix (A), k is the rank of the matrix and $s_{inst}(A)$ is the instrumental error. We have taken as instrumental error the maximum value of absorbance (0.00112) in the range between 300 and 500 nm, for a TMAH solution without uranium and hydrogen peroxide. The results obtained are shown in Figure 4.5 and confirm the likely existence of two different U(VI)–hydrogen peroxide complexes.

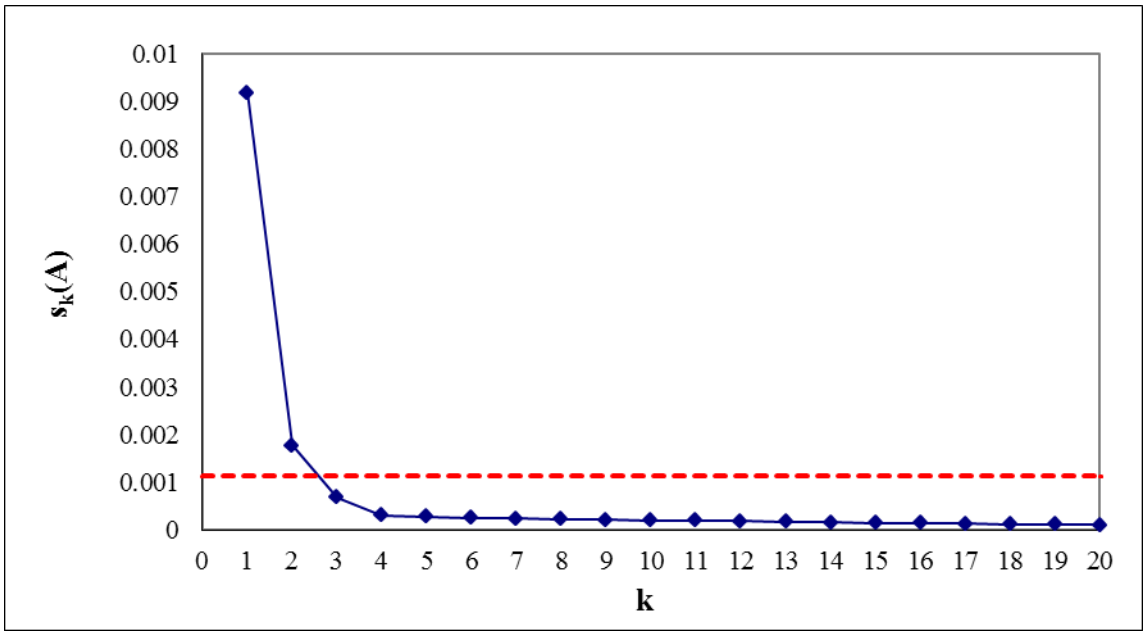

Figure 4.5 Standard deviation of the absorbance vs. rank of the absorbance matrix. The dotted line represents instrumental error (see text).

4.3.3. Impact of the existence of U(VI)–H_2O_2 complexes on the uranium(VI) chemical speciation in solution

In order to know the relative strength of the uranyl–H_2O_2–OH complexes described in this work, a theoretical study of the influence of these complexes on the chemical speciation of uranium(VI) at alkaline pH has been done, using specific software to simulate the speciation at different conditions.

Figure 4.6 shows the predominance diagram at pH = 12 which is found to depend on both total carbonate concentration and total hydrogen peroxide concentration. The predominance diagram was made by using the MEDUSA code [33], including the species shown in Table 4.1 and the formation constant of the $UO_2O_2(CO_3)_2^{4-}$ complex [19]. Solid species have not been included, in order to evaluate only the chemical speciation in solution.

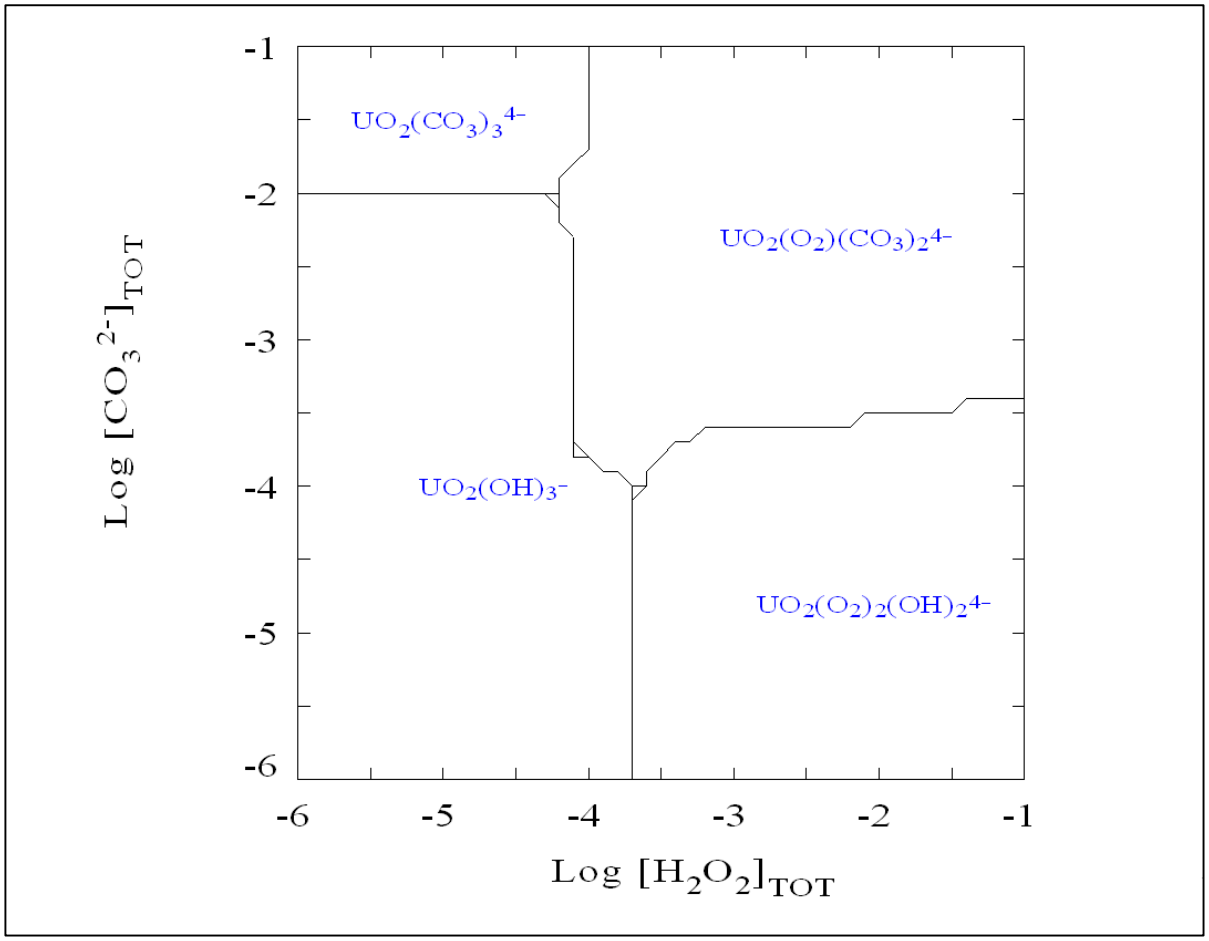

Figure 4.6 Predominance diagram of the uranium(VI) species in solution at pH = 12 and 0.01 mol dm^{-3} ionic strength.

It can be seen that the $UO_2(O_2)_2(OH)_2^{4-}$ complex predominates at hydrogen peroxide concentrations higher than 10^{-4} mol dm^{-3} at total carbonate concentrations lower than $5 \cdot 10^{-4}$ mol dm^{-3}. Peroxide easily replaces the hydroxyl ion in the complexes to form the U(VI)–H_2O_2–OH^- ternary complexes in a similar way that it replaces the carbonate ion to form mixed complexes with uranium [19] and plutonium [34]. The final picture is that at hydrogen peroxide concentrations higher than 10^{-4} mol dm^{-3}, the mixed complexes predominate, and the predominant ternary complex depends on carbonate concentration in solution.

On the other hand, a fraction diagram corroborates the importance of the mixed complexes on the U(VI) speciation in the presence of H_2O_2, because it allows the elucidation of not only the predominant complexes but all the complexes present at equilibrium in solution. Figure 4.7 shows the uranium(VI) fraction diagram at pH = 12 and a 10^{-4} mol dm^{-3} carbonate concentration. As can be seen, at hydrogen peroxide concentrations higher than 10^{-5} mol dm^{-3}, the complexes with peroxide (both the two complexes described in this work and the ternary complex identified by Goff et al.) are present in solution; these complexes account for almost all the uranium in solution at $[H_2O_2]_{tot} > 10^{-3}$ mol dm^{-3}.

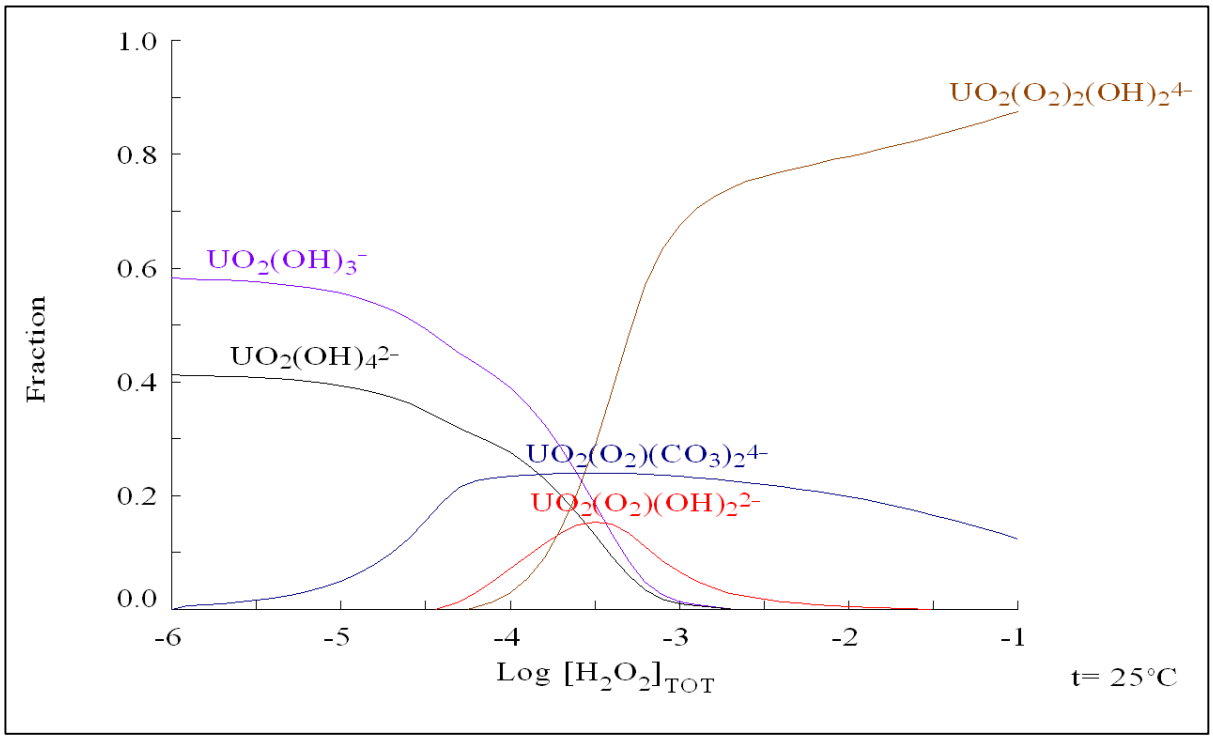

Figure 4.7 Fraction diagram of the uranium(VI) species in solution at $[CO_3^{2-}] = 10^{-4}$ mol dm^{-3}, pH= 12 and 0.01 mol dm^{-3} ionic strength.

This theoretical study on the uranium(VI) speciation in solution corroborates the high affinity of peroxide ion for actinides, in particular for uranium. The strong UO_2^{2+}–H_2O_2–OH- complexes, which would increase the solubility of the UO_2 and the uranium secondary solid phases (specially studtite, whose solubility could increase an order of magnitude at pH = 13 and hydrogen peroxide concentrations between 10^{-5} and 10^{-4} mol dm^{-3}), would have a significant impact on the migration of uranium in a deep geological repository for SNF.

4.4. CONCLUSIONS

The speciation of uranium(VI) in the presence of hydrogen peroxide was studied in alkaline conditions and in the absence of carbonates. Two UO_2^{2+}–H_2O_2–OH- complexes were considered at pH12 according to UV-vis spectrophotometric data on uranium solutions titrated with H_2O_2. The proposed formation reactions are:

$$UO_2^{2+} + H_2O_2 + 4OH^- \leftrightarrows UO_2(O_2)(OH)_2^{2-} + 2H_2O: \beta^\circ_{1,1,4} \quad (25)$$

$$UO_2^{2+} + 2H_2O_2 + 6OH^- \leftrightarrows UO_2(O_2)_2(OH)_2^{4-} + 4H_2O: \beta^\circ_{1,2,6} \quad (26)$$

The equilibrium constants for both reactions were determined by using the STAR program: $\log \beta^\circ_{1,1,4} = 28.1 \pm 0.1$ and $\log \beta^\circ_{1,2,6} = 36.8 \pm 0.2$.

Considering their formation constants, the ternary complexes $UO_2(O_2)(OH)_2^{2-}$ and $UO_2(O_2)_2(OH)_2^{4-}$ would have a significant impact on the uranium(VI) migration in solution, which is especially important in a High-Level Nuclear Waste Repository.

4.5. REFERENCES

1 D. W. Shoesmith. (2000). Fuel corrosion processes under waste disposal conditions. *J. Nucl. Mater.*, **282**, 1.

2 J. Bruno, E. Cera, M.Grivé, U. B. Eklund and T. Eriksen. (1999). Experimental determination and chemical modeling of radiolytic processes at spent fuel/water interface. *Report SKB TR-99-26*, Stockholm, Sweden.

3 T. Eriksen, U. B. Eklund, L. Werme and J. Bruno, J. (1995). Dissolution of irradiated fuel: A radiolytic mass balance study. *J. Nucl. Mater.*, **227**, 76.

4 C. Corbel, G. Sattonnay, S. Guilbert, F. Garrido, M. F. Barthe and C. Jégou. (2006). Addition versus radiolytic production effects of hydrogen peroxide on aqueous corrosion of UO_2. *J. Nucl. Mater.*, **348**, 1.

5 F. Clarens, J. Giménez, J. de Pablo, I. Casas, M. Rovira, J. Dies, J. Quiñones and A. Martínez-Esparza. (2005). Influence of β radiation on UO_2 dissolution at different pH values. *Radiochim. Acta*, **93**,533.

6 C. Jégou, B. Muzeau, V. Broudic, S. Peuget, A. Poulesquen, D. Roudil and C. Corbel. (2005). Effect of external gamma irradiation on dissolution of the spent fuel UO_2 fuel matrix. *J. Nucl. Mater.*, **341**, 62.

7 S. Sunder, N. H. Miller and D. W. Shoesmith. (2004). Corrosion of uranium dioxide in hydrogen peroxide solutions . *Corros. Sci.*, **46**,1095.

8 F. Clarens, J. de Pablo, I. Casas, J. Giménez, M. Rovira, J. Merino, E. Cera, J. Bruno, J. Quiñones and A.Martínez-Esparza. (2005). The oxidative dissolution of unirradiated UO_2 by hydrogen peroxide as a function of pH. *J. Nucl. Mater.*, **345**, 225.

9 J. Merino, E. Cera, J. Bruno, J. Quiñones, I. Casas, F. Clarens, J. Giménez, J. de Pablo, M. Rovira and A. Martínez-Esparza. (2005). Radiolytic modelling of spent fuel oxidative dissolution mechanism. Calibration against UO_2 dynamic leaching experiments. *J. Nucl.Mater.*, **346**, 40.

10 I. Casas, J. de Pablo, F. Clarens, J. Giménez, J.Merino, J. Bruno and A. Martínez-Esparza. (2009). Combined effect of H_2O_2 and HCO_3^- on UO_2(s) dissolution rates under anoxic conditions. *Radiochim. Acta*, **97**, 485.

11 F. Clarens, J. de Pablo, I. Díez, I. Casas, J. Giménez and M. Rovira. (2004). Formation of studtite during the oxidative dissolution of UO_2 by hydrogen peroxide: A SFM study. *Environ. Sci. Technol.*, **38**, 6656.

12 J. Cobos, T. Wiss, T. Gouder and V. V. Rondinella. (2003). XPS and SEM studies on the corrosion of UO_2 containing plutonium in demineralized and carbonate water. *Materials Research Society Symposium Proceedings,Scientific Basis for NuclearWaste Management XXVI*, **757**, 365–376.

13 G. Sattonnay, C. Ardois, C. Corbel, J. F. Lucchini, M. F. Barthe, F. Garrido and D. Gosset. (2001). Alpha-radiolysis effects on UO_2 alteration in water. *J. Nucl. Mater.*, **288**, 11.

14 B. McNamara, E. C. Buck and B. Hanson. (2003). Observation of studtite and metastudtite on spent fuel. *Materials Research Society Symposium Proceedings, Scientific Basis for Nuclear Waste Management XXVI*, **757**, 401–406.

15 B. Hanson, B. McNamara, E. C. Buck, J. Friese, E. Jenson, K. Krupka and B. Arey. (2005). Corrosion of commercial spent nuclear fuel. 1. Formation of studtite and metastudtite. *Radiochim. Acta*, **93**, 159.

16 K. A. Hughes-Kubatko, K. B. Helean, A. Navrotsky and P. C. Burns. (2003). Stability of peroxide-containing uranyl minerals. *Science,* **302**, 1191.

17 A. I. Moskvin. (1968). The question of the complex formation of U(VI) and Np(IV) with hydrogen peroxide and of Np(IV) in oxalate solutions. *Radiokhimiya*, **10**, 13.

18 I. Grenthe, J. Fuger, R. J. M. Konings, R. J. Lemire, A. B. Muller, C. Nguyen-Trung and H. Wanner. (1992). Chemical Thermodynamics of Uranium. *Elsevier, Amsterdam.*

19 G. S. Goff, L. F. Brodnax, M. R. Cisneros, S. M. Peper, S. E. Field, B. L. Scott and W. H. Runde. (2008). First Identification and Thermodynamic Characterization of the Ternary U(VI) Species, $UO_2(O_2)(CO_3)_2^{4-}$, in $UO_2{-}H_2O_2{-}K_2CO_3$ Solutions. *Inorg. Chem.*, **47**, 1984.

20 A. Meca. (2009). PhD Thesis: Processos que afecten la mobilitat de l'urani en entorns hiperalcalins oxidants i sediments contaminats. *Universitat Politècnica de Catalunya*.

21 J. A. Stegemann and N. R. Buenfeld. (2002). Prediction of leachate pH for cement paste containing pure metal compounds. *J. Hazard. Mater.*, **90**, 169.

22 U. R. Berner. (1992). Evolution of pore water chemistry during degradation of cement in a radioactive waste repository environment. *Waste Manage.*, **12**, 201.

23 B. Kienzler, P. Vejmelka, H. J. Herbert, H. Meyer and C. Altenhein-Haese. (2000). Long-Term Leaching Experiments of Full-Scale Cemented Waste Forms: Experiments and Modeling. *Nucl. Technol.*, **129**, 101.

24 J. L. Beltran, R. Codony and M. D. Prat. (1993). Evaluation of stability constants from multi-wavelength absorbance data: program STAR. *Anal. Chim. Acta*, **276**,441.

25 S. Meca, A. Martínez-Torrents, V. Martí, J. Giménez, I. Casas, J. de Pablo. (2011). Determination of the equilibrium formation constants of two U(VI)-peroxide complexes at alkaline pH. *Dalton Trans.*, **40**, 7976.

26 L. Zanonato, P. Di Bernardo, I. Grenthe. (2012). Chemical equilibria in the binary and ternary uranyl(VI)-hydroxide-peroxide systems. *Dalton Trans.*, **41,** 3380.

27 A. Martínez-Torrents, S. Meca, N. Baumann, V. Martí, J. Giménez, J. de Pablo and I. Casas. (2013). Uranium speciation studies at alkaline pH and in the presence of hydrogen peroxide using time-resolved laser-induced fluorescence spectroscopy. *Polyhedron*, **55**, 92–101.

28 C. L. Clark, S. D. Conradson, R. J. Donohoe, D. W. Keogh, D. E. Morris, P. D. Palmer, R. D. Rogers and C. D. Tait. (1999). Chemical Speciation of the Uranyl Ion under Highly Alkaline Condition. Synthesis, Structures, and Oxo Ligand Exchange Dynamics. *Inorg. Chem.*, **38**, 1456.

29 R. Guillamont, T. Fanghänel, V. Neck, J. Fuger, D. A. Palmer, I. Grenthe and M. H. Rand. (2003). Chemical Thermodynamics 5. Update on the chemical Thermodynamics of Uranium, Neptunium, Plutonium, Americium and Technetium. *Elsevier, Amsterdam*.

30 J. N. Miller and J. C. Miller. (2000). Statistics and Chemometrics for Analytical Chemistry, *4th edn, Prentice Hall, NJ*.

31 E. Durand. (1972). Solutions Numeriques des Equations Algébriques. Tome II: Systèmes de Plusiers Equations, Masson, Paris.

32 W. E. Wentworth. (1965). Rigorous least squares adjustment: Application to some non-linear equations, I. *J. Chem. Educ.*, **42**, 96.

33 D. D. Perrin and I. G. Sayce. (1967). Computer calculation of equilibrium concentrations in mixtures of metal ions and complexing species. *Talanta*, **14**, 833.

34 A. Izquierdo and J. L. Beltrán. (2005). SOL1: A program for the simulation of complex equilibria using a personal computer. *J. Chemom.*, **3**, 209.

35 I. Puigdomenech. (2004). MEDUSA, Sweden; http://w1.156.telia.com/~u15651596/.

36 W. Runde, L. F. Brodnax, G. S. Goff, S. M. Peper, F. L. Taw and B. L. Scott. (2007). Synthesis and structural characterization of a molecular plutonium(IV) compound constructed from dimeric building blocks. *Chem. Commun.*, **1728**. 7982

5 Uranium speciation studies at alkaline pH and in the presence of hydrogen peroxide using time-resolved laser-induced fluorescence spectroscopy

5 Uranium speciation studies at alkaline pH and in the presence of hydrogen peroxide using time-resolved laser-induced fluorescence spectroscopy

5.1. INTRODUCTION

The most predominant states of oxidation of uranium are U(IV) and U(VI). Being U(VI) much more soluble than U(IV) its speciation in solution is critical to understand the mobility of uranium though the different barriers of the deep geological repository. Concrete has been proposed to be used in the building of the deep geologic repository due to its structural properties and also its capacity to retain radionuclides[1-3]. In the presence of concrete the groundwater could reach a pH higher than 11 [4-7], and precisely the speciation of uranium(VI) in high alkaline pHs is not very well known since most of the past speciation studies of uranium(VI) are focused in acid or neutral pH.

Time-Resolved Laser-induced Fluorescence Spectroscopy is an analytical technique widely used in the study of Uranium(VI) complex formation [8-15]. However this technique could be applied only to fluorescent species and at room temperature and at high alkaline pH the fluorescence of the predominant uranyl species is very low or even inexistent [16-19]. To avoid this problem, fluorescence measurements were made at temperatures below freezing point (at 77 K using liquid nitrogen and at 4.2 K using liquid helium), because fluorescence depends on temperature, and at low temperatures the dynamic quenching effects may decrease [8,17,20]. This effect was observed in some uranyl carbonates that due to the quenching effect of the carbonate ion, they are non-fluorescent at room temperature, but fluorescent at low temperatures [8,21].

The fluorescence dependence on temperature has been known since 1959 [22,23]. Lowering the temperature changes the behavior of the mechanisms and processes that affects the fluorescence enhancing the signal and the spectra resolution.

The main differences of working at low temperature are [24-29]:

- The interference in the fluorescence signal produced by phonons and different molecules, like solvent water molecules, is reduced.
- Fluorescence signals due to thermally populated vibrational levels that can be present at room temperature are not observed.
- Minimizes the energy loss due to vibrations, enhancing the signal intensity.
- Increases the signal intensity because of the reduction of quenching effects caused by proton and electron transfers.

In the present work, the formation of uranyl–peroxide complexes at pH values higher than 11 are studied by TRLFS, and the formation of uranyl-hydroxo complexes at pH values between 12 and 13.5 are determined using the Cryo-TRLFS technique.

The radiation emitted by the SNF is capable of breaking the water molecules creating new species. One of the most oxidant species formed by water radiolysis is hydrogen peroxide[30-32]. Hydrogen peroxide is capable of oxidizing U(IV) to a more soluble Uranium (VI), affecting the oxidative dissolution of the fuel[33-35]. In this sense, different experiments demonstrated the increase of the uranium dissolution rates in the presence of hydrogen peroxide over a wide range of pH [34,36], and the mechanism of the UO_2 oxidative dissolution in hydrogen peroxide has been described [35,36].

Hydrogen peroxide might also affect the release of uranium from spent fuel by the formation of solid phases and/or uranyl–peroxide soluble complexes. Moskvin [37], based on studtite ($[(UO_2)(O_2)(H_2O)_2](H_2O)_2$) dissolution experiments, determined the formation constants of three uranyl–peroxide complexes (namely $UO_2O_2(aq)$, $UO_2(O_2)_2^{2-}$ and $UO_2(O_2)_3^{4-}$), but the constant values were not found to be reliable by the reviewers and have not been included in thermodynamic databases. Kim et al. have studied the influence of temperature and pH on the precipitation and stability of several uranyl peroxocarbonate complexes at different concentrations of carbonate and hydrogen peroxide [38–40]. In a carbonate solution of 0.5 mol dm^3 Na_2CO_3, the uranyl peroxocarbonate is decomposed at pH values higher than 12. Faster decomposition rates were achieved when the temperature was increased. Also in carbonate media, using UV–Visible spectrometry, Goff et al.[41] identified and determined the formation constant of the ternary complex $UO_2(O_2)(CO_3)_2^{4-}$, formed

through the reaction of the $UO_2(CO_3)_3^{4-}$ complex with hydrogen peroxide. It is important to point out that according to Goff et al. [41], there is an exceedingly high affinity of peroxide ions for actinide ions, as is deduced from the very high apparent formation constant of the $UO_2(O_2)(CO_3)_2^{4-}$ complex, which indicates that peroxide is able to compete with the carbonate ion for uranyl, even in concentrated carbonate solutions. Lately, a new study from Meca et al. [42,43] determined the formation of uranyl–peroxide complexes in the absence of carbonates, in alkaline media, by using UV–Visible spectrophotometry. Two different complexes were found at a H_2O_2/U(VI) ratio lower than 2. The values obtained for the equilibrium constants were 28.1 ± 0.1 for the $UO_2O_2(OH)_2^{2-}$ complex and 36.8 ± 0.2 for the $UO_2(O_2)_2(OH)_2^{4-}$ complex. However, in a recent work of Zanonato et al. [44], the article of Meca et al. was criticized for performing the study at only one pH value. Potentiometric and spectrometric titrations were used in their experiments over a wide range of pH values to study the chemical equilibria in the binary and ternary uranyl(VI)-hydroxide-peroxide systems. Two complexes were identified, $[UO_2(OH)(O_2)]^-$ and $(UO_2)_2(OH)(O_2)_2]^-$, the first was predominant at pH 9.5–11.5, while the second was found at pH < 10.5, under their experimental conditions. In addition to solid phases and complex studies, in recent years a lot of work has been done in the field of uranyl peroxide based nanoclusters. Taking as a reference studtite and metastudtite, it was found that the peroxide bridges between uranium atoms in the mineralogical structure were bent, and therefore the formation of uranium clusters based on uranium–peroxide–uranium interactions was possible [45]. Taking advantage of this phenomenon, several uranium-based nanoclusters have been synthesized [46–48]. Burns synthesized 26 nanoclusters and all of them were formed spontaneously under ambient conditions [48]. Some of these nanoclusters could be used in a separation process due to their low solubility and rapid formation [49]. The recent Fukushima–Daiichi disaster made Armstrong et al. [50] perform studies in seawater, where the formation of nanoclusters was observed. Apart from uranium, other actinides like neptunium are capable of forming nanoclusters [51].

Like in chapter 4, this work is a continuation of the work presented in the PhD. thesis of A. Meca [43]. The amount of experiments was substantially increased specially at low temperature. Also some experiments were repeated in order to improve the quality of the experimental data. New data treatment allowed the determination of the individual spectra of each species and new results were obtained. The work presented in this chapter was published in Martinez-Torrents et al. [52].

5.2. MATERIALS AND METHODS

The experiments were carried out in a glovebox, in order to prevent CO_2 intrusion, and at 25 ± 1 ºC. U(VI) stock solution was prepared from uranyl nitrate (Panreac). It was dissolved, precipitated at pH 7–8, filtered with 0.2 μm cellulose acetate filters, recrystallized, repurified by precipitation from aqueous solution and dried for two days. Finally a stock concentration was prepared and its concentration ($2.9 \cdot 10^{-3} \pm 2.5 \cdot 10^{-5}$ mol dm^{-3}) was determined by ICP-MS. This same technique was also used to determine the uranium in the sample solutions. The ionic strength was either 0.01 or 0.1 mol dm^{-3} using tetramethylammonium chloride (TMACl, Flucka) solution, because of the capacity of TMACl to prevent uranate precipitation [53]. Tetramethylammonium hydroxide (TMAH, Flucka) was used to adjust the pH for the same reason. Although it is known that chloride produces quenching in TRLFS measurements, it was experimentally assured that neither TMACl nor TMAH had any interaction or secondary effect with hydrogen peroxide or uranium(VI) under the experimental conditions of the present work. Two solutions of U(VI) of $4.5 \cdot 10^{-6} \pm 6.8 \cdot 10^{-7}$ mol dm^{-3} were prepared. The ionic strength was fixed at 0.1 mol dm^{-3}, using $NaClO_4$ in one case and using TMACl for the other. In the same way the pH was adjusted to 12, using NaOH in one case and TMAH in the other. TRLFS analyses were made and both solutions presented the same spectra, proving that in our case the use of TMAH and TMACl did not have any effect. The hydrogen peroxide solutions were obtained from the same initial solution (Merck) and the concentration was periodically standardized with thiosulfate (Scharlau) in H_2SO_4.

For the TRLFS measurements, a Nd:YAG laser (20 Hz, 4–6 ns pulse duration, k = 266 nm, Emax = 5 mJ, Polaris II, New Wave Research) was used. The uranium(VI) samples were introduced in a 1 cm path-length quartz cuvette, which was inside a dark sample compartment (SampleMax, JobinYvon). The fluorescence signal was measured perpendicular to the excitation laser beam. Both the laser beam and the uranyl emitted fluorescence were focalized using quartz lenses. The focused fluorescence was directed to a monochromator (TRIAX 320, JobinYvon, grating groove density: 600 lines/mm, k range = 470–590 nm). The monochromator was connected to a Charge Coupled Device (CCD) (JobinYvon). The signal acquisition was performed using the LABSPEC5.0 for Windows (JobinYvon) program.

At the Helmholtz-Zentrum Dresden-Rossendorf (HZDR), the laser fluorescence system for room temperature measurements consisted of a ‘‘Minilite II’’ (Continuum) laser, an ‘‘iHR 550’’ spectrometer (Horiba Jobin Yvon) and an Intensified CCD (ICCD) camera (Horiba Jobin Yvon). The fluorescence measuring system for the low temperature experiments consisted of an ‘‘Inlite’’ (Continuum) laser, a 1235 Digital Triple Grating Spectrograph spectrometer (EG&G Princeton Applied Research), and an ICCD camera (Princeton Instruments, inc., belonging to Roper Scientific). The sample was cooled with a closed He-cycle, consisting of a RDK10-320 He-cryostat (OerlikonLeybold Vacuum), a ‘‘Coolpak 2000 A’’ compressor unit (OerlikonLeybold Vacuum) and a ‘‘D 25 B’’ oil vacuum pump (Leybold Vacuum GmbH).

The spectra were recorded in the range 400–650 nm. The acquisition parameters were optimized for different time domains (see Tables 5.1 and 5.2) with respect to the laser pulse, thus allowing for a more reliable determination of the shortest and the longest lifetimes [13]. As has already been said above, the temperature affects the fluorescence. For this reason, all the spectral measurements for each uranium concentration were made on the same day and each measurement was repeated three times. The time dependencies of the spectra were calculated with the ORIGINPRO7 (OriginLab Corporation) program. A more detailed data processing procedure is described in previous works [13,54].

Table 5.1 Acquisition parameters used for the experiments carried out at pH: 11,12,13 at room temperature.

Parameter	**Experiment 1**		**Experiments 2-4**	
	Spectra	**Time Resolved**	**Spectra**	**Time Resolved**
Pulse width (ns)	100	100	100	100
Slit (μm)	200	200	200	200
Gain	150	150	150	150
Accumulations	250	250	250	250
Wavelength (nm)	525	525	525	525
ΔT(ns)	-	100	-	50
Grating	600(300)	600(300)	600(300)	600(300)

Table 5.2 Acquisition parameters used for the experiments with U(VI) and H_2O_2 at room temperature.

Parameter	Experiment 8		Experiments 9-11		Experiments 12-20	
	Spectra	Time Resolved	Spectra	Time Resolved	Spectra	Time Resolved
Pulse width (ns)	500	25	500	25	50	50
Slit (μm)	500	1000	1000	1000	200	200
Gain	150	150	150	150	128	128
Accumulations	250	250	250	250	150	50
Wavelength (nm)	400-650	525	400-650	525	520	520
ΔT(ns)	-	50	-	50	-	75
Grating	600(300)	600(300)	600(300)	600(300)	100(450)	100(450)

5.3. RESULTS

5.3.1. Speciation studies at alkaline pH

TRLFS studies were made at three different pH values, at room temperature in the absence of CO_2 (Tables 5.1 and 5.3). At alkaline pH uranium has very low fluorescence and a short lifetime. The spectra obtained at pH 11 and 12 are quite similar, but at pH 13 fluorescence was not observed, indicating that the predominating species, $UO_2(OH)_4^{2-}$, is not fluorescent.

Table 5.3 Experiments carried out at pH: 11, 12, 13 at room temperature.

Experiment	pH	Ionic strength ($mol \cdot dm^{-3}$)	[U(VI)] ($mol \cdot dm^{-3}$)
1	11	0.1	$6.6 \cdot 10^{-5}$
2	12	0.1	$6.6 \cdot 10^{-5}$
3	12	0.1	$1.5 \cdot 10^{-5}$
4	13	0.1	$6.6 \cdot 10^{-5}$

At pH 11 the function with the best fit is obtained by using a biexponential decay. That means that there are two different uranium species, one of them with a shorter lifetime than the other. However at pH 12 a monoexponential decay fits perfectly the fluorescence

decay, meaning that there is only one fluorescent species. The lifetime of the species at pH 12 is similar to the shorter lifetime from the two lifetimes at pH 11. This lifetime was assigned to the species $UO_2(OH)_3^-$. At pH 11, at a relatively high concentration of U(VI), the polynuclear species $(UO_2)_3(OH)_7^-$ is formed. As was already deduced by Eliet et al. [16], the larger lifetime was assigned to this species (Table 5.4).

Table 5.4 Lifetime measurements at room temperature (pH: 11, 12, 13).

pH	**Ionic strength ($mol \cdot dm^{-3}$)**	**[U(VI)] ($mol \cdot dm^{-3}$)**	τ_1 (ns)	τ_2 (ns)
11	0.1	$6.6 \cdot 10^{-5}$	129±6	1100±20
12	0.1	$1.5 \cdot 10^{-5}$	276±3	-
13	0.1	$6.6 \cdot 10^{-5}$	-	-

Because of the absence of fluorescence of the $UO_2(OH)_4^{2-}$ species at room temperature, measurements at 10 K were made, obtaining two different lifetimes in the pH range between 12 and 13.5 and a ionic strength of approximately 0.1 $mol \cdot dm^{-3}$, indicating the presence of two different species (Table 5.5). It was considered that the species with the shorter lifetime is $UO_2(OH)_4^{2-}$, since it is not fluorescent at room temperature, and the one with the larger lifetime corresponds to the species $UO_2(OH)_3^-$.

Table 5.5 Lifetime measurements at low temperature (10 K).

Experiment	**pH**	**[U(VI)] ($mol \cdot dm^{-3}$)**	τ_1 (μs)	τ_2 (μs)
5	12	$5 \cdot 10^{-6}$	198.2±7.8	11.2±0.4
6	13	$5 \cdot 10^{-6}$	150.1±7.0	8.3±0.3
7	13.5	$5 \cdot 10^{-6}$	194.9±5.0	10.0±0.6

The lifetime of the species $(UO_2)_3(OH)_7^-$ is one order of magnitude higher than the lifetime of the species $UO_2(OH)_3^-$ at room temperature. At 10K the lifetime of the species $UO_2(OH)_3^-$ is one order of magnitude higher than the species $UO_2(OH)_4^{2-}$. It seems that as the pH values increase, the lifetime of the uranium species decrease, perhaps due to the effect of the OH ion on the stability of the excited species [17]. The values of the lifetimes are similar to the ones found in the bibliography (Table 5.6), taking into account that Kitamura fits the exponential decay to the predominant species only, $UO_2(OH)_3^-$ at pH 12.3 and $UO_2(OH)_4^{2-}$ at pH 14.

Table 5.6 Lifetime measurements and maximum peaks found in the bibliography.

Species	T (K)	pH	I.S. ($mol \cdot dm^{-3}$)	[U] ($mol \cdot dm^{-3}$)	λ (nm)	τ (μs)	Reference
$UO_2(OH)_3^-$	77	12.3	1	$1 \cdot 10^{-5}$	492-511-534-556-581[a]	110	(Kitamura et al. [17])
$UO_2(OH)_4^{2-}$	77	14	1	$1 \cdot 10^{-4}$	495-515-536-559-585[a]	85	(Kitamura et al. [17])
$UO_2(OH)_3^-$	~40	12	0.01	$1 \cdot 10^{-5}$	495-514-534-556	51	(Meca [43])
$UO_2(OH)_4^{2-}$	~40	12	0.01	$1 \cdot 10^{-5}$	495-514-534-556	5.9	(Meca [43])
$UO_2(OH)_3^-$	10	12	0.1	$5 \cdot 10^{-6}$	485-503-521-534-550-569	198.2±7.8	This work
$UO_2(OH)_4^{2-}$	10	12	0.1	$5 \cdot 10^{-6}$	488-504-519-533-549-569	11.2±0.4	This work
$UO_2(OH)_3^-$	10	13	0.1	$5 \cdot 10^{-6}$	487-501-517-532-548-565	150.1±7.0	This work
$UO_2(OH)_4^{2-}$	10	13	0.1	$5 \cdot 10^{-6}$	488-500-517-534-548-563	8.3±0.3	This work
$UO_2(OH)_3^-$	10	13.5	0.3	$5 \cdot 10^{-6}$	492-505-518-529-545-561	194.9±5.0	This work
$UO_2(OH)_4^{2-}$	10	13.5	0.3	$5 \cdot 10^{-6}$	490-502-517-533-549-568	10.0±0.6	This work

[a] Approximate wavelengths.

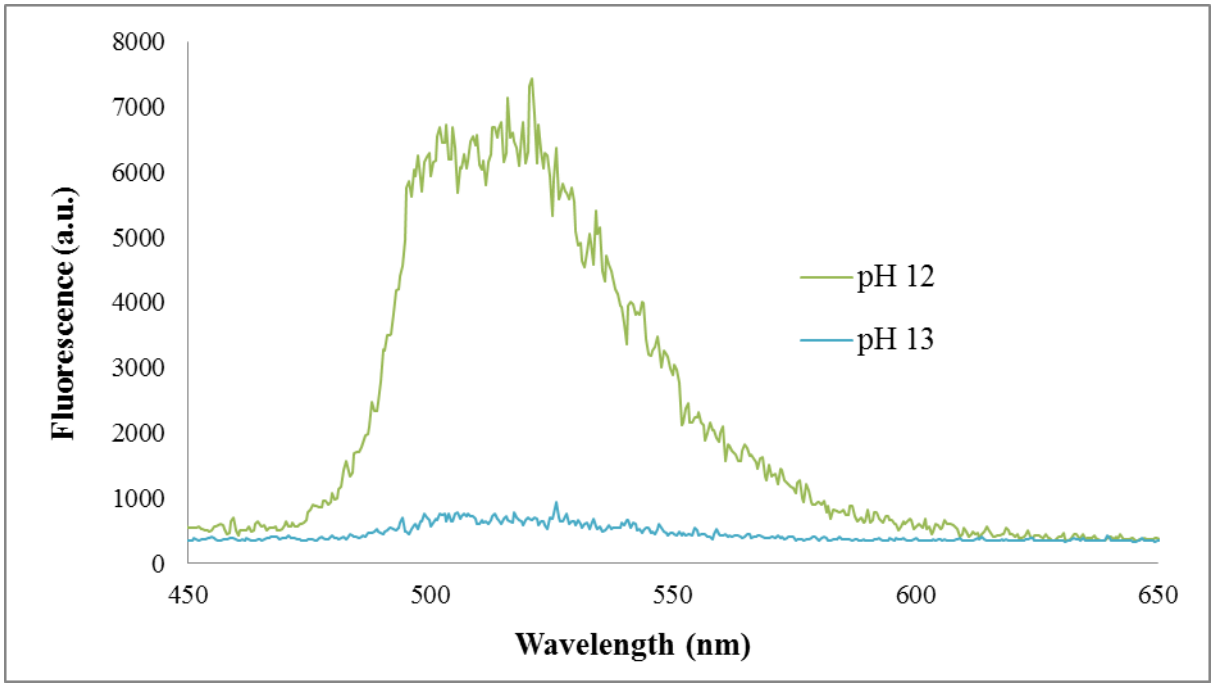

Figure 5.1. Fluorescence spectra for experiments 5 (green) and 6 (blue) at room temperature.

Solving the mass balance (Appendix A) for these two species, the results show that the species $UO_2(OH)_3^-$ makes up 58.5% of the total uranium at pH 12, 12.4% at pH 13 and 4.3% at pH 13.5. This can be seen in the fluorescence at room temperature (25 °C) (Figure 5.1). The program ORIGINPRO 8 was used to fit the spectra for samples 5–7 using Gaussian peaks. The fitting of sample 6, as an example, can be seen in Figure 5.2. There is no change in the position of the peak maxima due to changes in the pH.

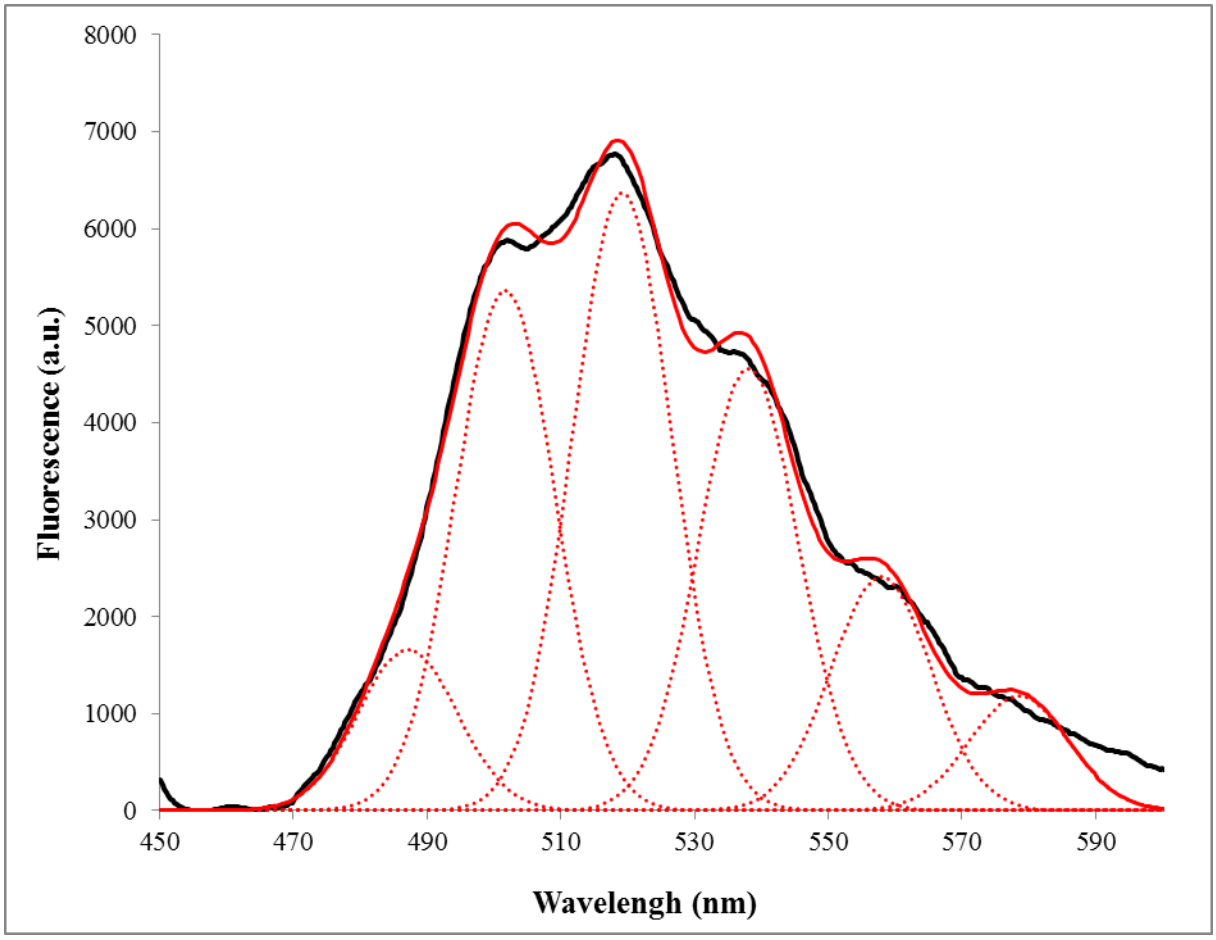

Figure 5.2. Fitting of the fluorescence spectra for experiment 6.

Bibliographic research was made in order to compare the results of this study at pH values greater than 12, but only the work of Kitamura et al. [17] was found to cover this area. The obtained positions for the maxima of the peaks are quite different from the ones found by Kitamura et al. [17] at an ionic strength of 1 mol dm^{-3}, perhaps because they worked with 5 peaks instead of 6 and the temperature used by Kitamura et al. [17] was 77 K instead of 10 K (Table 5.7). Six peaks were used instead of 5 because the fluorescence spectra seemed at first sight to have 6 peaks, and the fittings were better than when using 5 peaks (Table 5.8).

Table 5.7 Maximum peaks of measurements at low temperature (10 K).

Num.	pH	[U(VI)] ($mol \cdot dm^{-3}$)	Peak 1 (nm)	Peak 2 (nm)	Peak 3 (nm)	Peak 4 (nm)	Peak 5 (nm)	Peak 6 (nm)
5	12	$5 \cdot 10^{-6}$	489.8	504.5	519.8	533.1	548.0	566.0
6	13	$5 \cdot 10^{-6}$	488.4	500.7	517.6	535.1	551.2	569.3
7	13.5	$5 \cdot 10^{-6}$	493.7	505.8	519.9	535.0	550.6	568.5
Kitamura	12.3	10^{-5}	492	511	-	534	556	581
et al. [17][a]	14	10^{-4}	495	515	-	536	559	585

[a] Approximate wavelengths.

Table 5.8 Statistics of the spectra fitting using 5 Gaussian peaks and 6 Gaussian peaks.

Num.	pH	[U(VI)] ($mol \cdot dm^{-3}$)	Number of peaks	Reduced Chi squared	Residual sum of squares	Adjusted R squared
5	12	$5 \cdot 10^{-6}$	5	$1.45 \cdot 10^{5}$	$1.00 \cdot 10^{8}$	$9.79 \cdot 10^{-1}$
			6	$2.23 \cdot 10^{4}$	$2.24 \cdot 10^{7}$	$9.96 \cdot 10^{-1}$
6	13	$5 \cdot 10^{-6}$	5	$8.94 \cdot 10^{5}$	$6.19 \cdot 10^{8}$	$9.95 \cdot 10^{-1}$
			6	$5.27 \cdot 10^{5}$	$3.63 \cdot 10^{8}$	$9.97 \cdot 10^{-1}$
7	13.5	$5 \cdot 10^{-6}$	5	$8.35 \cdot 10^{4}$	$5.78 \cdot 10^{7}$	$9.97 \cdot 10^{-1}$
			6	$3.96 \cdot 10^{4}$	$2.73 \cdot 10^{7}$	$9.98 \cdot 10^{-1}$

Due to the short lifetime of the species $UO_2(OH)_4^{2-}$ compared to the species $UO_2(OH)_3^-$, the spectra at time 100 μs, correspond only to the spectra of the species $UO_2(OH)_3^-$. In experiment 5, the species $UO_2(OH)_4^{2-}$ has a lifetime of 11.2 ± 0.4 μs and it is the longest lifetime obtained for this species in all the experiments that were made at 10 K. Using the lifetime of the species $UO_2(OH)_3^-$, it was possible to calculate its decay curve. As a result the contribution of the species $UO_2(OH)_3^-$ at time 0 μs can be calculated:

$$F_{(\lambda,0\mu s)} = \frac{F_{(\lambda,100\mu s)} \cdot D_{UO_2(OH)_3-(0\ \mu s)}}{D_{UO_2(OH)_3-(100\ \mu s)}} \quad (1)$$

F(λ, 0μs) is the fluorescence intensity of each wavelength of the species $UO_2(OH)_3^-$ at time 0 μs, *F(λ, 100μs)* is the fluorescence intensity of each wavelength of the species $UO_2(OH)_3^-$ at time 100 μs, $D_{UO2(OH)3-}$ *(0 μs)* is the fluorescence intensity of the decay curve of the species

$UO_2(OH)_3^-$ at time 0 μs and $D_{UO2(OH)3-}$ *(100 μs)* is the fluorescence intensity of the decay curve of the species $UO_2(OH)_3^-$ at time 100 μs. Once the contribution of the species $UO_2(OH)_3^-$ is obtained, then the contribution of the species $UO_2(OH)_4^{2-}$ is the subtract of the spectra $UO_2(OH)_3^-$ from the whole spectra at time 0 μs.

Again, the spectra from samples 5–7 were fitted to Gaussian peaks using the program ORIGINPRO 8 (Tables 5.9 and 5.10). In Figure 5.3 the fitting of sample 7 can be seen as an example. The $UO_2(OH)_4^{2-}$ species has a life-time shorter than the life-time of $UO_2(OH)_3^-$, but its intensity at the beginning is bigger. No difference in the position of the peaks due to the pH increase or between the species $UO_2(OH)_3^-$ and $UO_2(OH)_4^{2-}$ was seen. The position of the peak maxima of the deconvoluted species is similar to the positions for the whole spectra and therefore quite different from the position of the peak maxima found in the literature [17].

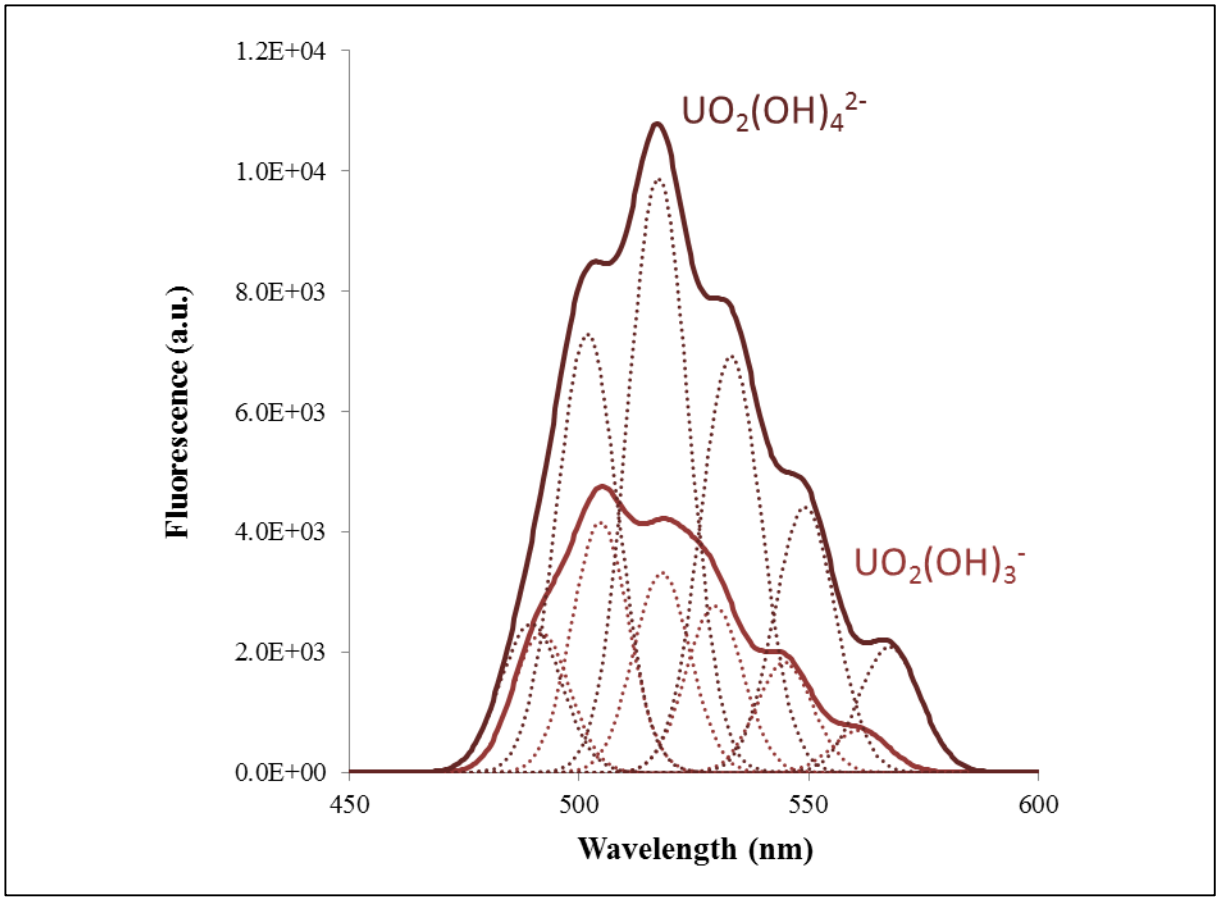

Figure 5.3. Fitting of the fluorescence spectra of a single species in experiment 7.

Table 5.9 Maximum peaks of measurements at low temperature for short-lived and long-lived species (10 K).

Num.	pH	[U(VI)] ($mol \cdot dm^{-3}$)	Species	Peak 1 (nm)	Peak 2 (nm)	Peak 3 (nm)	Peak 4 (nm)	Peak 5 (nm)	Peak 6 (nm)
5	12	$5 \cdot 10^{-6}$	$UO_2(OH)_3^-$	485.1	503.2	521.1	533.9	550	569.4
			$UO_2(OH)_4^{2-}$	488.4	503.5	518.6	532.7	548.7	569
6	13	$5 \cdot 10^{-6}$	$UO_2(OH)_3^-$	487.2	500.9	516.8	532.3	547.5	565
			$UO_2(OH)_4^{2-}$	488.2	499.9	517	533.8	548	562.5
7	13.5	$5 \cdot 10^{-6}$	$UO_2(OH)_3^-$	491.9	504.7	518	529.3	544.8	561.2
			$UO_2(OH)_4^{2-}$	489.6	501.9	517.3	533.1	549.2	567.6
Kitamura	12.3	10^{-5}		492	511	-	534	556	581
et al. [17][a]	14	10^{-4}		495	515	-	536	559	585

[a] Approximate wavelengths.

Table 5.10 Statistics of the deconvoluted spectra fitting using 5 Gaussian peaks and 6 Gaussian peaks.

Num.	pH	[U(VI)] ($mol \cdot dm^{-3}$)	Species	Number of peaks	Reduced Chi squared	Residual sum of squares	Adjusted R squared
5	12	$5 \cdot 10^{-6}$	$UO_2(OH)_3^-$	5	$5.33 \cdot 10^{3}$	$5.41 \cdot 10^{6}$	$9.69 \cdot 10^{-1}$
			$UO_2(OH)_3^-$	6	$3.91 \cdot 10^{3}$	$3.96 \cdot 10^{6}$	$9.80 \cdot 10^{-1}$
			$UO_2(OH)_4^{2-}$	5	$4.06 \cdot 10^{4}$	$4.12 \cdot 10^{7}$	$9.90 \cdot 10^{-1}$
			$UO_2(OH)_4^{2-}$	6	$2.32 \cdot 10^{4}$	$2.35 \cdot 10^{7}$	$9.94 \cdot 10^{-1}$
6	13	$5 \cdot 10^{-6}$	$UO_2(OH)_3^-$	5	$5.71 \cdot 10^{4}$	$5.79 \cdot 10^{7}$	$9.89 \cdot 10^{-1}$
			$UO_2(OH)_3^-$	6	$3.65 \cdot 10^{4}$	$3.69 \cdot 10^{7}$	$9.93 \cdot 10^{-1}$
			$UO_2(OH)_4^{2-}$	5	$5.36 \cdot 10^{5}$	$5.44 \cdot 10^{8}$	$9.94 \cdot 10^{-1}$
			$UO_2(OH)_4^{2-}$	6	$4.64 \cdot 10^{5}$	$4.69 \cdot 10^{8}$	$9.95 \cdot 10^{-1}$
7	13.5	$5 \cdot 10^{-6}$	$UO_2(OH)_3^-$	5	$7.13 \cdot 10^{3}$	$7.23 \cdot 10^{6}$	$9.96 \cdot 10^{-1}$
			$UO_2(OH)_3^-$	6	$5.87 \cdot 10^{3}$	$5.94 \cdot 10^{6}$	$9.97 \cdot 10^{-1}$
			$UO_2(OH)_4^{2-}$	5	$8.44 \cdot 10^{4}$	$8.56 \cdot 10^{7}$	$9.91 \cdot 10^{-1}$
			$UO_2(OH)_4^{2-}$	6	$6.49 \cdot 10^{4}$	$6.57 \cdot 10^{7}$	$9.93 \cdot 10^{-1}$

5.3.2. Effect of hydrogen peroxide

In the experiments that contained hydrogen peroxide the fluorescence decreased drastically compared to the experiments in the absence of H_2O_2 (this was observed at pH 11 and 12). The quenching of the fluorescence produced by the addition of hydrogen peroxide was thought to be due to the formation of a uranyl–peroxide complex in solution, which would displace the fluorescent $UO_2(OH)_3^-$ through the reaction:

$$UO_2(OH)_3^- + H_2O_2 + OH^- \rightleftarrows UO_2(O_2)(OH)_2^{2-} + 2H_2O \qquad (2)$$

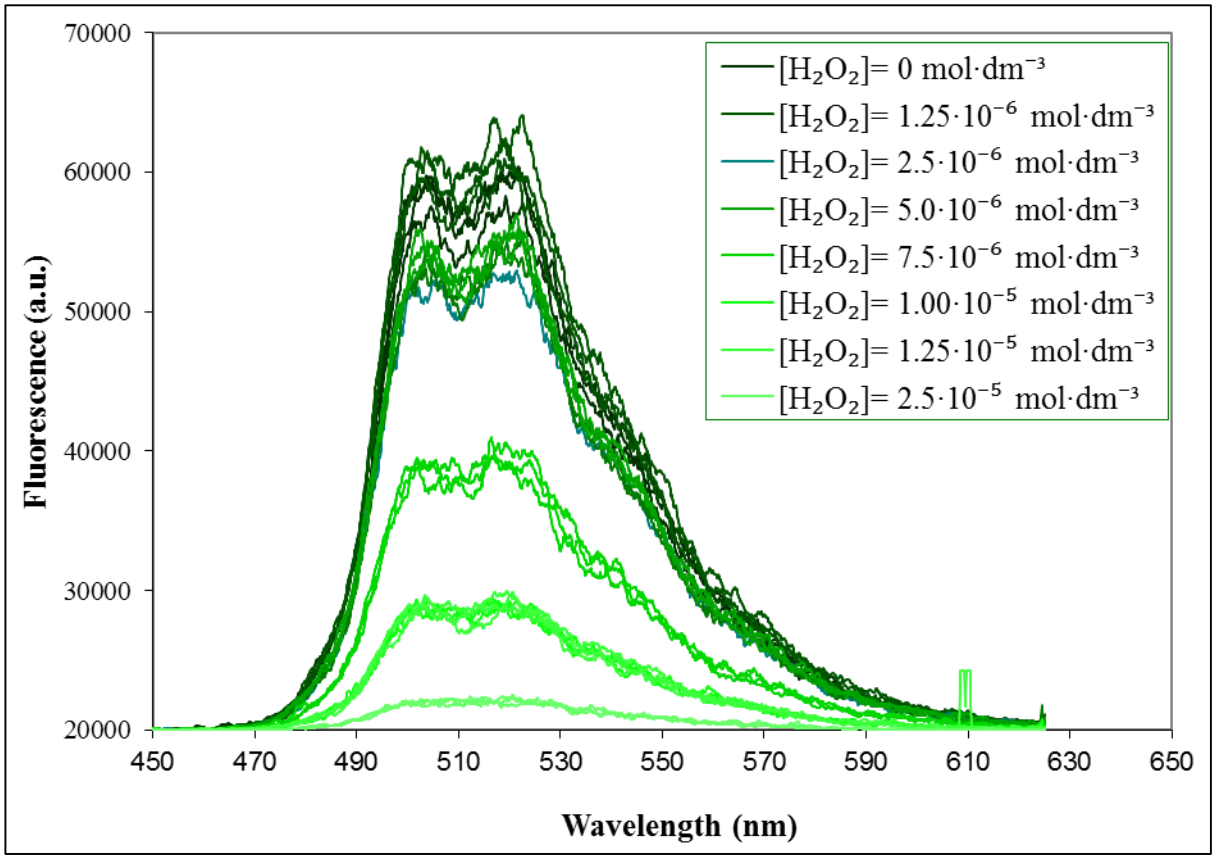

Figure 5.4. Fluorescence spectra of the samples with different hydrogen peroxide concentrations. [U(VI)] of 10^{-5} mol·dm^{-3}, pH:12, ionic strength: 0.1 mol·dm^{-3} and $[H_2O_2]$ between 0 and $2\cdot10^{-5}$ mol·dm^{-3} (fluorescence intensity diminishes as hydrogen peroxide concentration augments).

In order to study the quenching produced by the hydrogen peroxide on the uranium(VI) fluorescence, experiments where the hydrogen peroxide concentration was varied were carried out. Each experiment was repeated at a different uranium(VI) concentrations, in the range between $5 \cdot 10^{-7}$ and $1 \cdot 10^{-5}$ mol·dm^{-3}. The composition of the solutions and the acquisition parameters are shown in Tables 5.2 and 5.11, respectively. An example of the spectra obtained is shown in Figure 5.4. Experiments with two different ionic strengths (0.01 and 0.1 mol·dm^{-3} of TMACl) were prepared in order to prove that the ionic strength has no effect on the fluorescence. At these concentrations the formation of secondary phases [55] or nanoclusters [46–51] were discarded.

Table 5.11 Experiments carried out at pH = 12 to study the quenching produced by the hydrogen peroxide.

Experiment	**Ionic strength (mol·dm^{-3})**	**[U(VI)] (mol·dm^{-3})**	**$[H_2O_2]_0$ (mol·dm^{-3})**
8	0.1	$1 \cdot 10^{-6}$	$0\text{-}2.5 \cdot 10^{-6}$
9	0.1	$5 \cdot 10^{-6}$	$0\text{-}1 \cdot 10^{-5}$
10	0.1	$1 \cdot 10^{-5}$	$0\text{-}2.5 \cdot 10^{-5}$
11	0.1	$1 \cdot 10^{-5}$	$0\text{-}2.5 \cdot 10^{-5}$
12	0.1	$1 \cdot 10^{-6}$	$0\text{-}1 \cdot 10^{-5}$
13	0.1	$5 \cdot 10^{-6}$	$0\text{-}5 \cdot 10^{-5}$
14	0.1	$1 \cdot 10^{-5}$	$0\text{-}1 \cdot 10^{-4}$
15	0.01	$5 \cdot 10^{-7}$	$0\text{-}5 \cdot 10^{-6}$
16	0.01	$1 \cdot 10^{-6}$	$0\text{-}1 \cdot 10^{-5}$
17	0.01	$5 \cdot 10^{-6}$	$0\text{-}1 \cdot 10^{-5}$
18	0.01	$1 \cdot 10^{-5}$	$0\text{-}1 \cdot 10^{-4}$
19	0.01	$1 \cdot 10^{-6}$	$0\text{-}1 \cdot 10^{-5}$
20	0.01	$1 \cdot 10^{-5}$	$0\text{-}1 \cdot 10^{-4}$

In the fluorescence lifetimes studies, a monoexponential decay fitted perfectly the fluorescence decay in every case, indicating that the complex between uranium and hydrogen peroxide has no fluorescence because all the fluorescence was emitted by the remaining species, $UO_2(OH)_3^-$. As an example, see Figure 5.5.

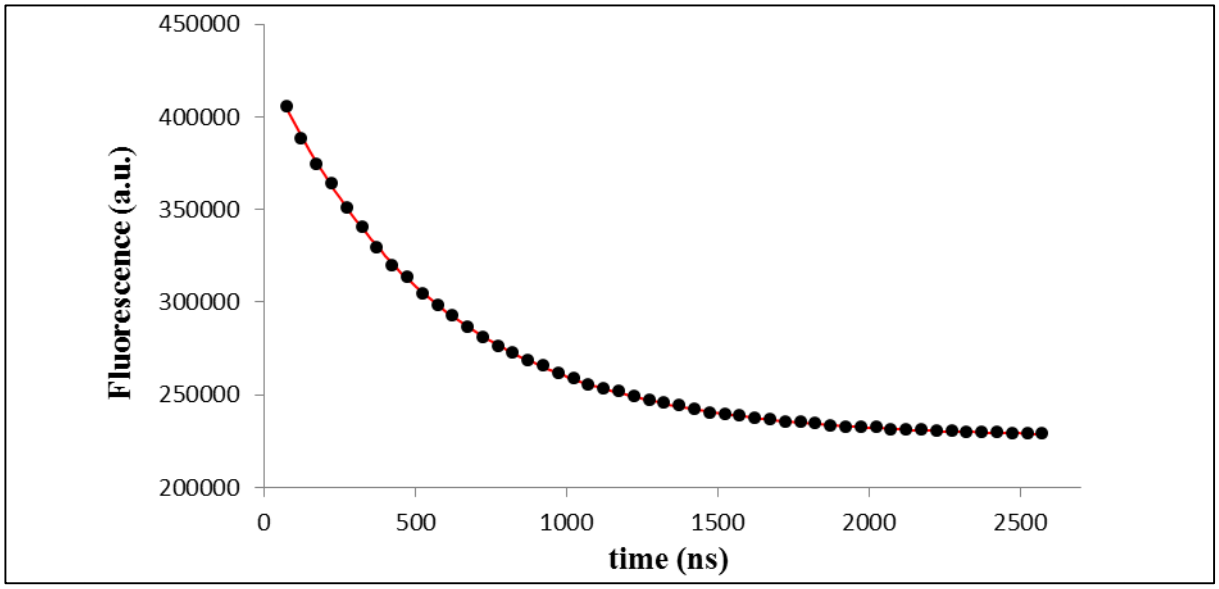

Figure 5.5. Decay curve for a uranium concentration of 10^{-5} mol·dm^{-3}, hydrogen peroxide concentration of 10^{-5} mol·dm^{-3} and an ionic strength of 0.01 mol·dm^{-3} at pH 12.

Table 5.12 Lifetime measurements for the experiments with U(VI) and H_2O_2 at room temperature (pH: 12).

Experiment	Ionic strength (mol·dm^{-3})	[U(VI)] (mol·dm^{-3})	$[H_2O_2]_0$ (mol·dm^{-3})	Lifetime (ns)
8	0.1	$1 \cdot 10^{-6}$	0-2.5 · 10^{-6}	71; 136;262;318;285;241;145
9	0.1	$5 \cdot 10^{-6}$	0-1 · 10^{-5}	239;316;361;387;415;322;519
10	0.1	$1 \cdot 10^{-5}$	0-2.5 · 10^{-5}	342;348;329;339;357;395;405;312
11	0.1	$1 \cdot 10^{-5}$	0-2.5 · 10^{-5}	293;310;268;323;323;313;292
12	0.1	$1 \cdot 10^{-6}$	0-1 · 10^{-5}	152;164;156;125;90
13	0.1	$5 \cdot 10^{-6}$	0-5 · 10^{-5}	374;363;391;379;417
14	0.1	$1 \cdot 10^{-5}$	0-1 · 10^{-4}	293;300;350;453;408
15	0.01	$5 \cdot 10^{-7}$	0-5 · 10^{-6}	515;515;501;512;527;550;520
16	0.01	$1 \cdot 10^{-6}$	0-1 · 10^{-5}	511;516;528;528;540;520
17	0.01	$5 \cdot 10^{-6}$	0-1 · 10^{-5}	411;414;414;414;418;421;432
18	0.01	$1 \cdot 10^{-5}$	0-1 · 10^{-4}	525;551;543;554;567;566;568
19	0.01	$1 \cdot 10^{-6}$	0-1 · 10^{-5}	498;515;491;474
20	0.01	$1 \cdot 10^{-5}$	0-1 · 10^{-4}	501;508;521;522

In Table 5.12 the lifetimes for each H_2O_2 concentration and for each set of experimental conditions are shown. In each set of experiments it is observed that the lifetime does not decrease when the hydrogen peroxide concentration increases. With τ_0 being the lifetime without hydrogen peroxide and τ the lifetime with hydrogen peroxide, the τ_0/τ ratio

remained constant in all the experiments. Therefore it is possible to affirm that there is static quenching affecting the fluorescence.

The decrease of the fluorescence as a function of the quencher concentration (hydrogen peroxide) was used to determine the equilibrium constant of Eq. (2). This kind of equilibrium constant determination is thoroughly described in the literature [56].

At pH = 12 and with a uranium(VI) concentration between $5 \cdot 10^{-7}$ and $1 \cdot 10^{-5}$ mol·dm^{-3}, there is another species in solution:

$$UO_2(OH)_4^{2-} + H_2O_2 \rightleftarrows UO_2(O_2)(OH)_2^{2-} + 2H_2O \quad (3)$$

Solving the mass balances (Appendix A), the percentage of $UO_2(OH)_3^-$ in solution is obtained. The percentage calculated at pH 12 implies that only the 58.5% of the total uranium is fluorescent.

Assuming that the $[UO_2(OH)_3^-]/[UO_2(OH)_4^{2-}]$ ratio would be constant during the reaction, as well as in the equilibrium, the mass balance of uranium(VI) is given by:

$$[U(VI)]_{tot} = [UO_2(OH)_3^-]_{eq} + [UO_2(OH)_4^{2-}]_{eq} + [UO_2O_2(OH)_2^{2-}]_{eq} \quad (4)$$

Combining expressions (2) and (4), Eq. (5) is obtained (Appendix A):

$$\frac{[UO_2(OH)_3^-]_0}{[UO_2(OH)_3^-]_{eq}} = 1 + a3K_1[OH^-][H_2O_2] \quad (5)$$

where $[UO_2(OH)_3^-]_0$ is the initial concentration of $UO_2(OH)_3^-$ without hydrogen peroxide, $[UO_2(OH)_3^-]_{eq}$ is the concentration of $UO_2(OH)_3^-$ with hydrogen peroxide at the equilibrium, *a3* is the percentage of $[UO_2(OH)_3^-]$ in solution (at pH 12 = 58.5%), K_1 is the equilibrium constant of reaction (3), and $[OH^-]$ and $[H_2O_2]$ are the concentrations of OH^- and H_2O_2, respectively.

Eq. (5) obtained has the form of the Stern–Volmer equation[57].

$$\frac{F_0}{F} = 1 + K_{SV}[Q] \tag{6}$$

where F_0 is the fluorescence in the absence of the quencher and F is the fluorescence in the presence of a certain concentration of the quencher Q. K_{sv} is the Stern–Volmer constant. The fluorescence decrease is proportional to the decrease in the $UO_2(OH)_3^-$ concentration. Therefore Eq. (5) can be written in the form of the Stern–Volmer equation:

$$\frac{[UO_2(OH)_3^-]_0}{[UO_2(OH)_3^-]_{eq}} = 1 + K_{SV}[H_2O_2] \tag{7}$$

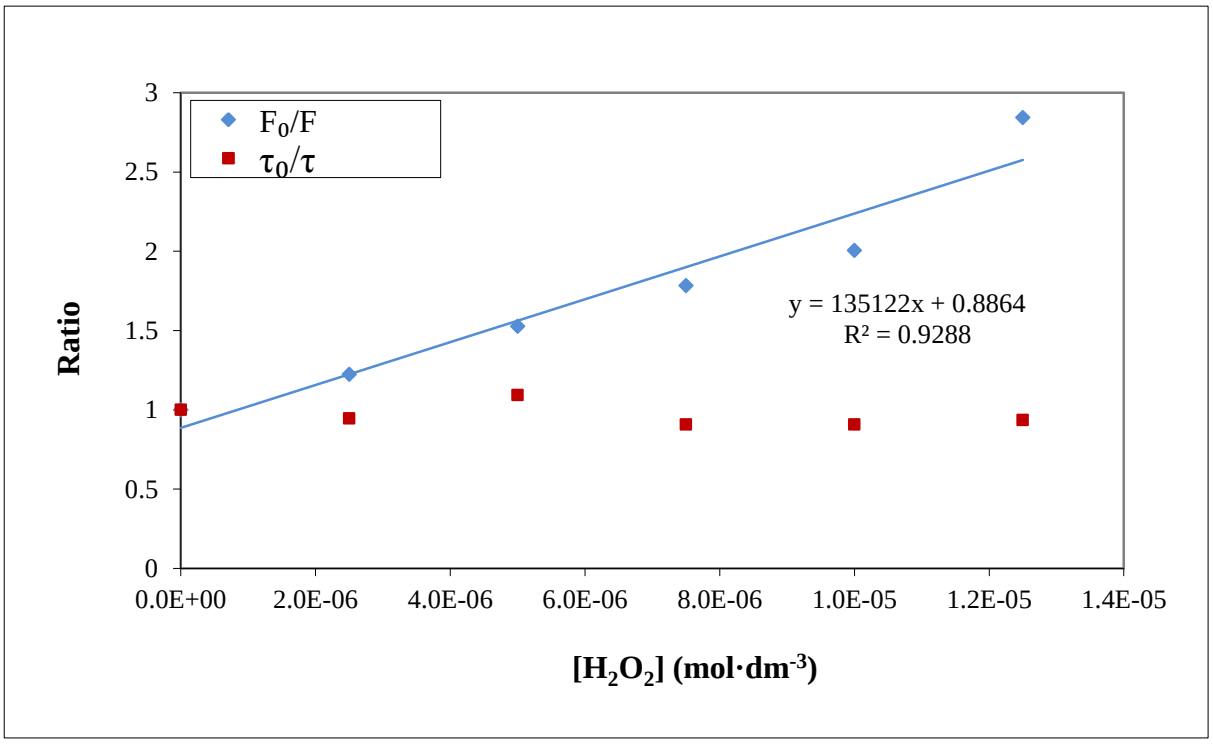

Figure 5.6. Influence of the hydrogen peroxide concentration on the fluorescence of uranium(VI). [U(VI)] = 10^{-5} mol·dm^{-3}, pH: 12, ionic strength: 0.1 mol dm^{-3} and [H_2O_2] between 0 and $2 \cdot 10^{-5}$ mol· dm^{-3}.

By using the fluorescence intensities and the half-life values determined for each experiment, the F_0/F ratio against hydrogen peroxide is represented. Hence, as an example, Figure 5.6 shows the results obtained for the data presented in Figure 5.4. In Figure 5.6, τ_0/τ is represented. It can be seen graphically that the ratio is almost constant over the whole range of hydrogen peroxide concentrations studied, indicating that the quenching is static due to the formation of a non-fluorescent complex in solution.

The lineal regression for each experiment was calculated. From the slope obtained, the equilibrium constant of reaction (2) ($\log K_1$) was found. Considering the formation constant of $UO_2(OH)_3^-$ ($\log K_3 = 21.75 \pm 0.4$) [58], the formation constant of the uranyl–peroxide complex was obtained:

$$UO_2^{2+} + H_2O_2 + 4OH^- \rightleftarrows UO_2(O_2)(OH)_2^{2-} + 2H_2O \qquad \text{K} \qquad (8)$$

Table 5.13 Set of experiments used to find the formation constant (pH: 12).

Num.	[U(VI)] (mol·dm^{-3})	[U(VI)] (mol·dm^{-3})	K_{sv} (slope)	K_1	$\log K_1$	logK	$\log K^0$
8	$1 \cdot 10^{-6}$	0-2.5 · 10^{-6}	746300	$1.3 \cdot 10^8$	8.1 ± 0.1	29.2 ± 0.4	29.6 ± 0.4
9	$5 \cdot 10^{-6}$	0-1 · 10^{-5}	232800	$4.0 \cdot 10^7$	7.6 ± 0.1	28.7 ± 0.4	29.1 ± 0.4
10	$1 \cdot 10^{-5}$	0-2.5 · 10^{-5}	307400	$5.3 \cdot 10^7$	7.7 ± 0.1	28.8 ± 0.4	29.3 ± 0.4
11	$1 \cdot 10^{-5}$	0-2.5 · 10^{-5}	135100	$2.3 \cdot 10^7$	7.4 ± 0.4	28.5 ± 0.4	28.9 ± 0.4
12	$1 \cdot 10^{-6}$	0-1 · 10^{-5}	41242	$7.0 \cdot 10^6$	6.8 ± 0.1	27.9 ± 0.4	28.4 ± 0.4
13	$5 \cdot 10^{-6}$	0-5 · 10^{-5}	25673	$4.4 \cdot 10^6$	6.6 ± 0.3	27.7 ± 0.5	28.2 ± 0.5
14	$1 \cdot 10^{-5}$	0-1 · 10^{-4}	106966	$1.8 \cdot 10^7$	7.3 ± 0.0	28.4 ± 0.4	28.8 ± 0.4
15	$5 \cdot 10^{-7}$	0-5 · 10^{-6}	58591	$1.0 \cdot 10^7$	7.0 ± 0.1	28.5 ± 0.4	28.7 ± 0.4
16	$1 \cdot 10^{-6}$	0-1 · 10^{-5}	117319	$2.0 \cdot 10^7$	7.3 ± 0.1	28.8 ± 0.4	29.0 ± 0.4
17	$5 \cdot 10^{-6}$	0-1 · 10^{-5}	69163	$1.2 \cdot 10^7$	7.1 ± 0.0	28.6 ± 0.4	28.7 ± 0.4
18	$1 \cdot 10^{-5}$	0-1 · 10^{-4}	20160	$3.4 \cdot 10^6$	6.5 ± 0.0	28.0 ± 0.4	28.2 ± 0.4
19	$1 \cdot 10^{-6}$	0-1 · 10^{-5}	17541	$3.0 \cdot 10^6$	6.5 ± 0.1	28.0 ± 0.4	28.1 ± 0.4
20	$1 \cdot 10^{-5}$	0-1 · 10^{-4}	28759	$4.9 \cdot 10^6$	6.7 ± 0.1	28.2 ± 0.4	28.4 ± 0.4
Mean							**28.7 ± 0.4**

Using the Debye–Hückel approximation [58] (Appendix B), the effect of the ionic strength of the solution was corrected, and finally from the results obtained (Table 5.13) the mean value for each parameter was calculated, giving a final value for $\log K^0$ of 28.7 ± 0.4. This constant is similar to the constant corresponding to the species $UO_2O_2(OH)_2^{2-}$, determined by UV–Visible spectrometry in the chapter 4 of the Thesis: 28.1 ± 0.1, which supports the values presented in the two works, obtained from different techniques.

Measurements at very low temperature (10 K) were made in order to see if the uranium complex with hydrogen peroxide was fluorescent at 10 K (Table 5.14). A biexponential decay was the function with the best fit in all the experiments. These results are very similar to those observed in experiments without hydrogen peroxide. The two different times obtained correspond to the species $UO_2(OH)_3^-$ and $UO_2(OH)_4^{2-}$, so the complex between U(VI) and H_2O_2 is not fluorescent, even at 10 K. This lack of emission could be due to the covalent interactions in the bond between the atom of uranium and the molecule of peroxide that stabilizes the molecule. In addition there are hints that the highest occupied molecular orbital (HOMO) is localized on the peroxy group [45,59–61]. The uranyl peroxide mineral studtite is also non-emissive at room-temperature and at 77 K [62]. Malcolm et al. postulated that the quenching occurs due to the presence of the peroxide group or due to vibrational quenching because of the coordinated water molecules.

Table 5.14 Lifetime measurements for the experiments with U(VI) and H_2O_2 at low temperature (10 K).

Experiment	**pH**	**[U(VI)] (mol·dm^{-3})**	**[H_2O_2] (mol·dm^{-3})**	τ_1 (μs)	τ_2 (μs)
21	12	$5 \cdot 10^{-6}$	10^{-5}	356.9±18.8	4.9±0.2
22	12	$5 \cdot 10^{-6}$	$2 \cdot 10^{-5}$	396.8±13.6	5.5±0.5
23	13	$5 \cdot 10^{-6}$	10^{-5}	162.9±9.3	11.2±0.8
24	13.5	$5 \cdot 10^{-6}$	10^{-5}	228.7±11.8	29.7±4.3

The addition of hydrogen peroxide does not have any particular effect on the lifetimes of the species. It was not possible to compare the different spectra as was done above in the experiments at room temperature, because the measurements were made on different days, due to the complexity of the experimental set-up.

As was done previously for the case without hydrogen peroxide, spectra from samples 21 to 24 were fitted using Gaussian peaks, considering the whole spectra and also considering the contributions of the species $UO_2(OH)_3^-$ and $UO_2(OH)_4^{2-}$ separately (Tables 5.15–18). The addition of the hydrogen peroxide does not produce any shift in the position of the peak maxima of the fluorescence spectra.

Table 5.15. Maximum peaks of measurements at low temperature (10 K).

Num.	pH	[U(VI)] ($mol \cdot dm^{-3}$)	[H_2O_2] ($mol \cdot dm^{-3}$)	Peak 1 (nm)	Peak 2 (nm)	Peak 3 (nm)	Peak 4 (nm)	Peak 5 (nm)	Peak 6 (nm)
21	12	$5 \cdot 10^{-6}$	10^{-5}	492.3	503.6	519.3	537.1	554.3	571.9
22	12	$5 \cdot 10^{-6}$	$2 \cdot 10^{-5}$	488.4	504.3	520.6	535.2	550.0	568.5
23	13	$5 \cdot 10^{-6}$	10^{-5}	490.8	502.1	517.6	532.3	546.3	562.5
24	13.5	$5 \cdot 10^{-6}$	10^{-5}	490.3	502.6	518.5	532.7	546.8	564.6
Kitamura	12.3	10^{-5}	0	492	511	-	534	556	581
et al. [17][a]	14	10^{-4}	0	495	515	-	536	559	585

[a] Approximate wavelengths.

Table 5.16. Maximum peaks of measurement at low temperature for short-lived and long-lived species (10 K).

Num.	pH	[U(VI)] ($mol \cdot dm^{-3}$)	[H_2O_2] ($mol \cdot dm^{-3}$)	Species	Peak 1 (nm)	Peak 2 (nm)	Peak 3 (nm)	Peak 4 (nm)	Peak 5 (nm)	Peak 6 (nm)
21	12	$5 \cdot 10^{-6}$	10^{-5}	$UO_2(OH)_3^-$	488.3	503.4	519.9	537.7	556.1	572.2
				$UO_2(OH)_4^{2-}$	487.1	499.6	518.3	537.0	554.9	573.7
22	12	$5 \cdot 10^{-6}$	$2 \cdot 10^{-5}$	$UO_2(OH)_3^-$	485.7	504.3	521.7	533.3	548.1	568.0
				$UO_2(OH)_4^{2-}$	486.7	502.2	519.0	534.4	549.8	569.1
23	13	$5 \cdot 10^{-6}$	10^{-5}	$UO_2(OH)_3^-$	488.3	502.3	517.4	531.3	546.4	563.7
				$UO_2(OH)_4^{2-}$	492.1	502.2	517.1	531.4	545.3	561.6
24	13.5	$5 \cdot 10^{-6}$	10^{-5}	$UO_2(OH)_3^-$	488.3	502.2	518.2	533.7	549.0	568.4
				$UO_2(OH)_4^{2-}$	491.6	503.6	519.3	534.4	549.4	567.5
Kitamura	12.3	10^{-5}	0		492	511	-	534	556	581
et al. [17][a]	14	10^{-4}	0		495	515	-	536	559	585

[a] Approximate wavelengths.

Table 5.17. Statistics of the spectra fitting using 5 Gaussian peaks and 6 Gaussian peaks.

Num.	pH	[U(VI)] ($mol \cdot dm^{-3}$)	[H_2O_2] ($mol \cdot dm^{-3}$)	Number of peaks	Reduced Chi squared	Residual sum of squares	Adjusted R squared
21	12	$5 \cdot 10^{-6}$	10^{-5}	5	$5.89 \cdot 10^{4}$	$4.08 \cdot 10^{7}$	$9.94 \cdot 10^{-1}$
				6	$3.75 \cdot 10^{4}$	$2.59 \cdot 10^{7}$	$9.96 \cdot 10^{-1}$
22	12	$5 \cdot 10^{-6}$	$2 \cdot 10^{-5}$	5	$6.45 \cdot 10^{4}$	$6.54 \cdot 10^{7}$	$9.97 \cdot 10^{-1}$
				6	$1.70 \cdot 10^{4}$	$1.74 \cdot 10^{7}$	$9.99 \cdot 10^{-1}$
23	13	$5 \cdot 10^{-6}$	10^{-5}	5	$1.28 \cdot 10^{5}$	$8.83 \cdot 10^{7}$	$9.93 \cdot 10^{-1}$
				6	$1.55 \cdot 10^{4}$	$1.07 \cdot 10^{7}$	$9.99 \cdot 10^{-1}$
24	13.5	$5 \cdot 10^{-6}$	10^{-5}	5	$9.90 \cdot 10^{4}$	$1.00 \cdot 10^{8}$	$9.93 \cdot 10^{-1}$
				6	$1.72 \cdot 10^{4}$	$1.74 \cdot 10^{7}$	$9.99 \cdot 10^{-1}$

Table 5.18. Statistics of the deconvoluted spectra fitting using 5 Gaussian peaks and 6 Gaussian peaks.

Num.	pH	[U(VI)] ($mol \cdot dm^{-3}$)	Species	Number of peaks	Reduced Chi squared	Residual sum of squares	Adjusted R squared
21	12	$5 \cdot 10^{-6}$	$UO_2(OH)_3^-$	5	$8.28 \cdot 10^{2}$	$8.39 \cdot 10^{5}$	$9.95 \cdot 10^{-1}$
			$UO_2(OH)_3^-$	6	$7.29 \cdot 10^{2}$	$7.37 \cdot 10^{5}$	$9.95 \cdot 10^{-1}$
			$UO_2(OH)_4^{2-}$	5	$6.80 \cdot 10^{4}$	$6.90 \cdot 10^{7}$	$9.88 \cdot 10^{-1}$
			$UO_2(OH)_4^{2-}$	6	$5.75 \cdot 10^{4}$	$5.82 \cdot 10^{7}$	$9.90 \cdot 10^{-1}$
22	12	$5 \cdot 10^{-6}$	$UO_2(OH)_3^-$	5	$1.16 \cdot 10^{4}$	$1.18 \cdot 10^{7}$	$9.96 \cdot 10^{-1}$
			$UO_2(OH)_3^-$	6	$1.09 \cdot 10^{4}$	$1.10 \cdot 10^{7}$	$9.96 \cdot 10^{-1}$
			$UO_2(OH)_4^{2-}$	5	$2.87 \cdot 10^{4}$	$2.92 \cdot 10^{7}$	$9.97 \cdot 10^{-1}$
			$UO_2(OH)_4^{2-}$	6	$7.31 \cdot 10^{3}$	$7.47 \cdot 10^{6}$	$9.99 \cdot 10^{-1}$
23	13	$5 \cdot 10^{-6}$	$UO_2(OH)_3^-$	5	$8.04 \cdot 10^{3}$	$8.15 \cdot 10^{6}$	$9.94 \cdot 10^{-1}$
			$UO_2(OH)_3^-$	6	$5.35 \cdot 10^{3}$	$5.47 \cdot 10^{6}$	$9.96 \cdot 10^{-1}$
			$UO_2(OH)_4^{2-}$	5	$2.27 \cdot 10^{4}$	$2.30 \cdot 10^{7}$	$9.97 \cdot 10^{-1}$
			$UO_2(OH)_4^{2-}$	6	$1.45 \cdot 10^{4}$	$1.48 \cdot 10^{7}$	$9.98 \cdot 10^{-1}$
24	13.5	$5 \cdot 10^{-6}$	$UO_2(OH)_3^-$	5	$7.65 \cdot 10^{3}$	$7.76 \cdot 10^{6}$	$9.93 \cdot 10^{-1}$
			$UO_2(OH)_3^-$	6	$6.13 \cdot 10^{3}$	$6.20 \cdot 10^{6}$	$9.95 \cdot 10^{-1}$
			$UO_2(OH)_4^{2-}$	5	$1.65 \cdot 10^{3}$	$1.67 \cdot 10^{6}$	$9.99 \cdot 10^{-1}$
			$UO_2(OH)_4^{2-}$	6	$1.19 \cdot 10^{3}$	$1.21 \cdot 10^{6}$	$9.99 \cdot 10^{-1}$

Surprisingly, it was observed (Figure 5.7) that the contribution of the long-lived species $UO_2(OH)_3^-$ to the fluorescence of the entire spectra increases when the H_2O_2 concentration increased. It seems that the short-lived species $UO_2(OH)_4^{2-}$ has a greater

affinity to form the non-fluorescent complex $UO_2O_2(OH)_2^{2-}$, despite the fact that the theoretical concentrations calculated using MEDUSA [63] show a constant relation between the concentrations of the long-lived species $UO_2(OH)_3^-$ and the short-lived species $UO_2(OH)_4^{2-}$.

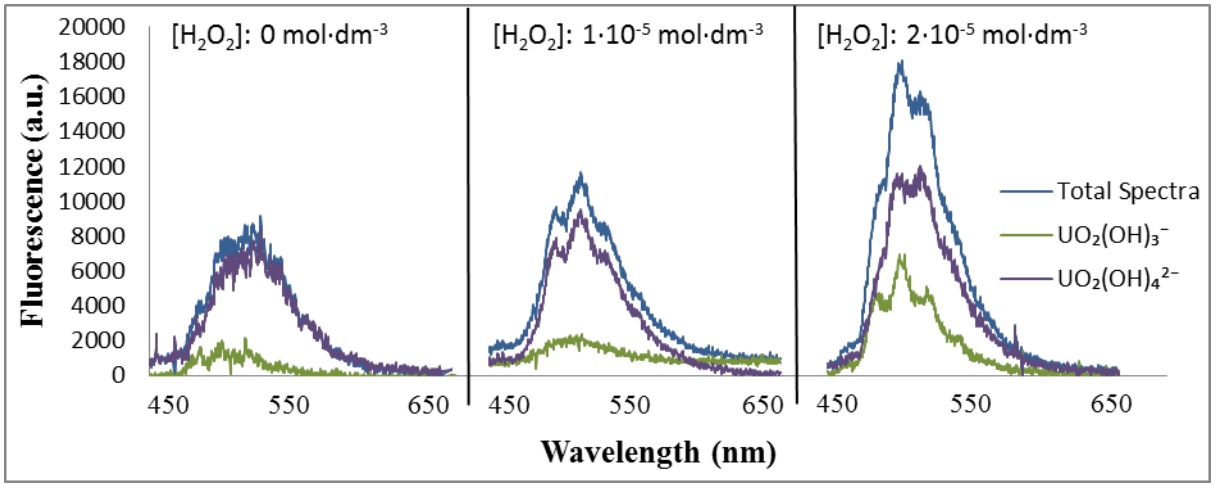

Figure 5.7. $UO_2(OH)_3^-$ and $UO_2(OH)_4^{2-}$ contribution to the total spectra for different H_2O_2 concentrations.

5.4. CONCLUSIONS

Fluorescence of U(VI) at high alkaline concentrations was studied (pH: 11–13.5). The species $UO_2(OH)_3^-$ and $(UO_2)_3(OH)_7^-$ were identified at pH 11 by TRLFS lifetimes analysis. At pH 12 only the species $UO_2(OH)_3^-$ has fluorescence and at pH 13 no fluorescence was detected, suggesting that the predominant species, $UO_2(OH)_4^{2-}$, is not fluorescent. On the other hand, two hydroxo complexes, $UO_2(OH)_3^-$ and $UO_2(OH)_4^{2-}$, were seen thanks to the use of Cryo-TRLFS techniques. Samples with a uranium concentration of $5\cdot10^{-6}$ mol· dm^{-3} at different pHs between 12 and 13.5 were analysed by Time Resolved Laser-induced Fluorescence Spectroscopy at 10 K. In all the samples two different lifetimes were observed: one with a lifetime between 150.1 ± 7.0 and 198.2 ± 7.8 μs and other with a lifetime between 8.3 ± 0.3 and 11.2 ± 0.4 μs. It was considered that the one with the longest lifetime is the species $UO_2(OH)_3^-$ which is fluorescent at room temperature, and the one with the shortest lifetime is the species $UO_2(OH)_4^{2-}$, which is non-fluorescent at room temperature.

In addition to the lifetimes, the peak distributions of the fluorescent spectra were studied too. It was seen that the position of the peaks of the different samples are quite different from the ones found in the literature [17], using different experimental conditions and fitting the fluorescence spectra with 5 Gaussian peaks instead of 6.

Thanks to the difference between lifetimes, it was possible to calculate the contribution of each species to the total fluorescence spectra. The peak distribution for each species was calculated. The position of the peaks for each species is similar to the position of the peaks for the whole spectra and therefore quite different from the data found in the literature [17].

Hydrogen peroxide produces a quenching effect that diminishes the fluorescence intensity of the uranium fluorescent species. At pH 12 and room temperature only the $UO_2(OH)_3^-$ species is fluorescent. At this pH the addition of hydrogen peroxide does not reduce the lifetime of $UO_2(OH)_3^-$, proving that there is no dynamic quenching, only static. In a previous work, the formation of uranium complexes with hydrogen peroxide at pH 12 was studied using UV–Visible spectrometry [42] and two complexes were identified, $UO_2O_2(OH)_2^{2-}$ and $UO_2(O_2)_2(OH)_2^{4-}$. Using the Stern–Volmer equation for static quenching it was possible to calculate the equilibrium formation constant of the first species, $UO_2O_2(OH)_2^{2-}$, $K^0 = 28.7 \pm 0.4$. This constant value is similar to the one determined using UV–Visible spectrometry, 28.1 ± 0.1 [42].

The addition of hydrogen peroxide does not show any particular effects to the lifetime of the species or to the peaks position of the spectra of the species.

5.5. REFERENCES

1 I. Pointeau, C. Landesman, E. Giffaut, P. Reiller. (2004). Reproducibility of the uptake of U(VI) onto degraded cement pastes and calcium silicate hydrate phases. *Radiochim. Acta*, **92**, 645.

2 S. Höglund, L. Eliason, B. Allard, K. Andersson, B. Torstenfelt. (1985). Sorption of some fission products and actinides in concrete systems. *Mater. Res. Soc. Symp. Proc.*, **50**, 683.

3 F.T. Ewart, R.M. Howse, H.P. Thomason, S.J. Williams, J.E. Cross. (1985). The solubility of actinides in the near-field. *Mater. Res. Soc.Symp. Proc.*, **50**, 701.

4 U. R. Berner. (1992). Evolution of pore water chemistry during degradation of cement in a radioactive waste repository environment. *Waste Manage.*, **12**, 201.

5 J.A. Stegemann, N.R. Buenfeld. (2002). Prediction of leachate pH for cement paste containing pure metal compounds. *J. Hazard. Mater. B*, **90**, 169.

6 B. Kienzler, P. Vejmelka, H. J. Herbert, H. Meyer and C. Altenhein-Haese. (2000). Long-Term Leaching Experiments of Full-Scale Cemented Waste Forms: Experiments and Modeling. *Nucl. Technol*., **129**, 101.

7 E. Wieland, C.A. Johnson, B. Lothenbach, F. Winnefeld. (2006). Mechanisms and Modelling of Waste/Cement Interactions – Survey of Topics Presented at the Meiringen Workshop. *Mater. Res. Soc. Symp. Proc.*, **932**, 663.

8 G. Geipel. (2006). Some aspects of actinide speciation by laser-induced spectroscopy. *Coord. Chem. Rev.*, **250**, 844.

9 T. Vercouter, P. Vitorge, B. Amekraz, C. Moulin. (2008). Stoichiometries and thermodynamic stabilities for aqueous sulfate complexes of U(VI). *Inorg. Chem.*, **47**, 2180.

10 Ch. Moulin, P. Decambox, V. Moulin, J.G. Decaillon. (1995). Uranium speciation in solution by time-resolved laser-induced fluorescence . *Anal. Chem.*, **67**, 348.

11 G. Geipel, A. Brachmann, V. Brendler, G. Bernhard, H. Nitsche. (1996). Uranium(VI) Sulfate Complexation Studied by Time-Resolved Laser-Induced Fluorescence Spectroscopy (TRLFS). *Radiochim. Acta*, **75**, 199.

12 A. Vetešnik, M. Smelova, K. Štamberg, D. Vopálka. (2008). Uranium(VI) Sulfate Complexation as a Function of Temperature and Ionic Strength Studied by TRLFS. *Uranium Min. Hydrogeol*. 623.

13 I. Bonhoure, S. Meca, V. Martí, J. de Pablo, J.L. Cortina. (2007). A new time-resolved laser-induced fluorescence spectrometry (TRLFS) data acquisition procedure applied to the uranyl-phosphate system. *Radiochim. Acta*, **95**, 165.

14 T. Arnold, S. Utsunomiya, G. Geipel, R.C. Ewing, N. Baumann, V. Brendler. (2006). Adsorbed U(VI) surface species on muscovite identified by laser fluorescence spectroscopy and transmission electron microscopy. *Environ. Sci. Technol.*, **40**, 4646.

15 N. Baumann, V. Brendler, T. Arnold, G. Geipel, G. Bernhard. (2005). Uranyl sorption onto gibbsite studied by time-resolved laser-induced fluorescence spectroscopy (TRLFS). *J. Colloid Interface Sci.*, **290**, 318.

16 V. Eliet, G. Bidoglio, N. Omonetto, L. Parma, I. Grenthe. (1995). Characterisation of hydroxide complexes of uranium(VI) by time-resolved fluorescence spectroscopy. *J. Chem. Soc., Faraday Trans.*, **91**, 2275.

17 A. Kitamura, T. Yamamura, H. Hase, T. Yamamoto, H. Moriyama. (1998). Measurement of Hydrolysis Species of U(VI) by Time-Resolved Laser Induced Fluorescence Spectroscopy. *Radiochim. Acta*, **82**, 147.

18 R. Steudtner, T. Arnold, G. Geipel, G. Bernhard. (2010). Fluorescence spectroscopic study on complexation of uranium(VI) by glucose: a comparison of room and low temperature measurements. *J. Radioanal. Nucl. Chem.*, **284**, 421.

19 K. Grossmann, T. Arnold, A. Ikeda-Ohno, R. Steudtner, G. Geipel, G. Bernhard. (2009). Fluorescence properties of a uranyl(V)-carbonate species [U(V)O(2)(CO(3))(3)](5-) at low temperature. *Spectrochim. Acta Part A*, **72**, 449.

20 Z. Wang, J.M. Zachara, J.P. McKinley, S.C. Smith. (2005). Cryogenic Laser Induced U(VI) Fluorescence Studies of a U(VI) Substituted Natural Calcite: Implications to U(VI) Speciation in Contaminated Hanford Sediments. *Environ. Sci. Technol.*, **39**, 2651.

21 T. Arnold, K. Grobmann, N. Baumann. (2010). Uranium speciation in biofilms studied by laser fluorescence techniques. *Anal. Bioanal. Chem.*, **396**, 1641.

22 S. Hayakawa, M. Hirata. (1959). Unusual Temperature Dependence of Fluorescence of Uranyl Ions Embedded in Ice. *J. Chem. Phys.*, **30**, 330.

23 D.D. Pant, D.P. Khandelwal, H.D. Bist. (1959). Temperature dependence of fluorescence bands of uranyl nitrate solutions. *Curr. Sci.*, **28**, 483.

24 Z. Wang, J.M. Zachara, W. Yantasee, P.L. Gassman, C. Liu, A.G. Joly. (2004). Cryogenic Laser Induced Fluorescence Characterization of U(VI) in Hanford Vadose Zone Pore Waters. *Environ. Sci. Technol.*, **38**, 5591.

25 Z. Wang, J.M. Zachara, P.L. Gassman, C. Liu, O. Qafoku, W. Yantasee, J.G. Catalano. (2005). Fluorescence spectroscopy of U(VI)-silicates and U(VI)-contaminated Hanford sediment. *Geochim. Cosmochim. Acta*, **6**, 1391.

26 A.F. Leung. (1982). Visible spectra and flourescence decay rates of a crystal and frozen solutions of uranyl nitrate. *J. Phys. Chem. Solids*, **43**, (5) 467.

27 J. Tits, T. Stumpf, T. Rabung, E. Wieland, T. Fanghänel. (2003). Uptake of Cm(III) and Eu(III) by calcium silicate hydrates: a solution chemistry and time-resolved laser fluorescence spectroscopy study. *Environ. Sci. Technol.*, **37**, 3568.

28 A.F. Leung, K.K. Tsang. (1979). Temperature-dependence of fluorescence decay-rates of mono-valent-cation uranyl nitrates. *J. Phys. Chem. Solids*, **40**, 1093.

29 R. Matsushima, H. Fujimori, S. Sakuraba. (1974). Quenching of the uranyl (UO_2^{2+}) emission by inorganic ions in solution. *J. Chem. Soc., Faraday Trans.*, **1**, 70, 1702.

30 C. Jégou, B. Muzeau, V. Broudic, S. Peuget, A. Poulesquen, D. Roudil, C. Corbel, J. (2005). Effect of external gamma irradiation on dissolution of the spent UO_2 fuel matrix. *Nucl. Mater.*, **341**, 62.

31 C. Corbel, G. Sattonay, S. Guilbert, F. Garrido, M. Barthe, C. Jegou, J. (2006). Addition versus radiolytic production effects of hydrogen peroxide on aqueous corrosion of UO_2. *Nucl. Mater.*, **348**, 1.

32 F. Clarens, J. Giménez, J. de Pablo, I. Casas, M. Rovira, J. Dies, J. Quiñones, A. Martínez-Esparza. (2005). Influence of beta radiation on UO_2 dissolution at different pH values. *Radiochim. Acta*, **93**, 533.

33 S. Sunder, N.H. Miller, D.W. Shoesmith. (2004). Corrosion of uranium dioxide in hydrogen peroxide solutions. *Corros. Sci.*, **46**, 1095.

34 F. Clarens, J. de Pablo, I. Casas, J. Giménez, M. Rovira, J. Merino, E. Cera, J. Bruno, J. Quiñones, A. Martínez-Esparza. (2005). The oxidative dissolution of unirradiated UO_2 by hydrogen peroxide as a function of pH. *J. Nucl. Mater.*, **345**, 225.

35 J. Merino, E. Cera, J. Bruno, J. Quiñones, I. Casas, F. Clarens, J. Giménez, J. de Pablo, M. Rovira, A. Martínez-Esparza. (2005). Radiolytic modelling of spent fuel oxidative dissolution mechanism. Calibration against UO_2 dynamic leaching experiments. *J. Nucl. Mater.*, **346**, 40.

36 I. Casas, J. de Pablo, F. Clarens, J. Giménez, J. Merino, J. Bruno, A. Martínez-Esparza. (2009). Combined Effect of H_2O_2 and HCO_3^- on UO_2 (s). Dissolution Rates under Anoxic Conditions. *Radiochim. Acta*, **97**, 485.

37 A.I. Moskvin. (1968). To the question of complex formation with hydrogen peroxide and oxalate solutions. *Radiokhim.*, **10**, (1) 13.

38 K.-W. Kim, K.-Y. Lee, D.-Y. Chung, E.-H. Lee, J.-K. Moon, D.-W. Shin. (2012). Evaluation of the stability of uranyl peroxo-carbonato complex ions in carbonate media at different temperatures. *J. Hazard. Mater.*, **233–234**, 213.

39 K.-W. Kim, Y.-H. Kim, S.-Y. Lee, J.-W. Lee, K.-S. Joe, E.-H. Lee, J.-S. Kim, K. Song, K.-C. Song. (2009). Precipitation characteristics of uranyl ions at different pHs depending on the presence of carbonate ions and hydrogen peroxide. *Environ. Sci. Technol.*, **43**, 2355.

40 K.-W. Kim, E.-C. Jung, K.-Y. Lee, H.-R. Cho, E.-H. Lee, D.-Y. Chung. (2012). Evaluation of the behavior of uranium peroxocarbonate complexes in Na-U(VI)-CO_3-OH-H_2O_2 solutions by Raman spectroscopy. *J. Phys. Chem. A*, **116**, 12024.

41 G.S. Goff, L.F. Brodnax, M.R. Cisneros, S.M. Peper, S.E. Field, B.L. Scott, W.H. Runde. (2008). First identification and thermodynamic characterization of the ternary U(VI) species, UO2(O2)(CO3)2(4-), in UO2-H2O2-K2CO3 solutions. *Inorg. Chem.*, **47**, 1984.

42 S. Meca, A. Martínez-Torrents, V. Martí, J. Giménez, I. Casas, J. de Pablo. (2011). Determination of the equilibrium formation constants of two U(VI)-peroxide complexes at alkaline pH. *Dalton Trans.*, **40**, 7976.

43 A. Meca. (2009). PhD Thesis: Processos que afecten la mobilitat de l'urani en entorns hiperalcalins oxidants i sediments contaminats. Universitat Politècnica de Catalunya.

44 L. Zanonato, P. Di Bernardo, I. Grenthe. (2012). Chemical equilibria in the binary and ternary uranyl(VI)-hydroxide-peroxide systems. *Dalton Trans.*, **41**, 3380.

45 B. Vlaisavljevich, L. Gagliardi, P.C. Burns. (2010). Understanding the structure and formation of uranyl peroxide nanoclusters by quantum chemical calculations. *J. Am. Chem. Soc.*, **132**, 14503.

46 P.C. Burns. (2012). Nuclear Fuel in a Reactor Accident. *Science*, **335**, 1184.

47 R.J. Baker. (2012). New Reactivity of the Uranyl(VI) Ion. *Chem. Eur. J.*, **18**, 16258.

48 P.C. Burns. (2011). Nanoscale uranium-based cage clusters inspired by uranium mineralogy. *Mineral. Mag.*, **75**, (1) 1.

49 G.E. Sigmon, P.C. Burns. (2011). Rapid self-assembly of uranyl polyhedra into crown clusters. *J. Am. Chem. Soc.*, **133**, 9137.

50 C.R. Armstrong, M. Nyman, T. Shvareva, G.E. Sigmon, P.C. Burns, A. Navrotsky. (2011). Uranyl peroxide enhanced nuclear fuel corrosion in seawater. *Proc. Natl. Acad. Sci. USA*, **109**, (6) 1874.

51 P.C. Burns, K.-A. Kubatko, G. Sigmon, B.J. Fryer, J.E. Gagnon, M.R. Antonio, L. Soderholm. (2005). Actinyl Peroxide Nanospheres. *Angew. Chem., Int. Ed.*, **44**, 2135.

52 A. Martínez-Torrents, S. Meca, N. Baumann, V. Martí, J. Giménez, J. de Pablo and I. Casas. (2013). Uranium speciation studies at alkaline pH and in the presence of hydrogen peroxide using time-resolved laser-induced fluorescence spectroscopy. *Polyhedron*, **55**, 92–101.

53 C.L. Clark, S.D. Conradson, R.J. Donohoe, D.W. Keogh, D.E. Morris, P.D. Palmer, R.D. Rogers, C.D. Tait. (1999). Chemical speciation of the uranyl ion under highly alkaline conditions. Synthesis, structures, and oxo ligand exchange dynamics. *Inorg. Chem.*, **38**, 1456.

54 S. Meca, J. Giménez, I. Casas, V. Martí, J. de Pablo. (2012). Uranium speciation in river sediments contaminated by phosphate ores. *Environ. Chem. Lett.*, **10**, 49.

55 F. Clarens, J. De Pablo, I. Díez-Pérez, I. Casas, J. Giménez, M. Rovira. (2004). Formation of studtite during the oxidative dissolution of UO_2 by hydrogen peroxide: A SFM study. *Environ. Sci.Technol.*, **38**, 6656.

56 Th.D. Gauthier, E.C. Shane, W.F. Guerin, W.R. Seltz, C.L. (1986). Fluorescence quenching method for determining constants for polycyclic aromatic hydrocarbons binding to dissolved humic materials. Grant, *Environ. Sci. Technol.*, **20**, 1162.

57 J.R. Lakowicz. (1999), Principles of Fluorescence Spectroscopy, Kluwer Academic/ *Plenum Publishers*.

58 I. Grenthe, J. Fuger, R.J.M. Konings, R.J. Lemire, A.B. Muller, C. Nguyen-Trung, H. Wanner, (1992) in: Wanner, Forest (Eds.), Chemical Thermodynamics, Chemical Thermodynamics of Uranium. *NEA-OECD, vol. 1, Elsevier*.

59 V. Vallet, U. Wahlgren, I. Grenthe. (2012). Probing the nature of chemical bonding in uranyl(VI) complexes with quantum chemical methods. J. Phys. Chem. A 116 12373.

60 L.C. Schuller, R.C. Ewing, U. Becker. (2010). Quantum-mechanical evaluation of Np-incorporation into studtite. *Am. Mineral.*, **95**, (8–9) 1151.

61 S. Ostanin, P. Zeller. (2007). Ab initio study of uranyl peroxides: Electronic factors behind the phase stability. *Phys. Rev. B*, **75**, (7) 073101.

62 C. Mallon, A. Walshe, R.J. Forster, T.E. Keyes, R.J. Baker. (2012). Physical characterization and reactivity of the uranyl peroxide [UO2(η(2)-O2)(H2O)2]·2H2O: implications for storage of spent nuclear fuels. *Inorg. Chem.*, **51**, 8509.

63 I. Puigdomenech. (2004). MEDUSA, Sweden . <http://www.kemi.kth.se/medusa/>, (accessed 04.12.12).

A FINDING K_1 IN TRLFS FROM STERN-VOLMER EQUATION AND MASS BALANCES

TRLFS measures consist in acquiring the fluorescence spectra of a solution in a wavelengths range and measuring the lifetime as the time that takes the solution to lose his fluorescence.

In the TRLFS experiments of this work it was noticed that solutions with hydrogen peroxide were less fluorescent than the others without. This phenomenon is known as quenching. There are two kinds of quenching. Being τ_0 the lifetime without hydrogen peroxide and τ the lifetime with hydrogen peroxide, if τ_0/τ varies for different quencher concentrations then the quenching is dynamic, but if τ_0/τ remains constant in all the experiments, then the quenching is static. That is the case in this work. Static quenching can be expressed by the following Stern-Volmer equation:

$$\frac{F_0}{F} = 1 + K_{sv} \cdot [Q] \qquad \text{(A1)}$$

Where F_0 is the fluorescence in the absence of the quencher, and F is the fluorescence in the presence of a certain concentration of quencher, $[Q]$ (mol·dm^{-3}).K_{sv} is the Stern-Volmer constant.

At pH 12 and with the presence of hydrogen peroxide the following reactions are considered:

$UO_2(OH)_3^- + H_2O_2 + OH^- \leftrightarrows UO_2(OH)_2(O_2)^{2-} + 2H_2O$ K_1 (A2)

$UO_2(OH)_4^{2-} + H_2O_2 \leftrightarrows UO_2(OH)_2(O_2)^{2-} + 2H_2O$ K_2 (A3)

$UO_2^{2+} + 3OH^- \leftrightarrows UO_2(OH)_3^-$ K_3 (A4)

$UO_2^{2+} + 4OH^- \leftrightarrows UO_2(OH)_4^{2-}$ K_4 (A5)

First of all the speciation in absence of hydrogen peroxide was studied.

$$K_3 = \frac{\left[UO_2(OH)_3^-\right]}{\left[UO_2^{2+}\right]_{eq}\left[OH^-\right]^3} \Rightarrow \left[UO_2^{2+}\right]_{eq} = \frac{\left[UO_2(OH)_3^-\right]}{K_3\left[OH^-\right]^3} \quad \text{(A6)}$$

$$K_4 = \frac{\left[UO_2(OH)_4^{2-}\right]}{\left[UO_2^{2+}\right]_{eq}\left[OH^-\right]^4} \Rightarrow \left[UO_2(OH)_4^{2-}\right] = K_4\left[UO_2^{2+}\right]_{eq}\left[OH^-\right]^4 \quad \text{(A7)}$$

Combining A6 and A7:

$$\left[UO_2(OH)_4^{2-}\right] = K_4\frac{\left[UO_2(OH)_3^-\right]}{K_3\left[OH^-\right]^3}\left[OH^-\right]^4 \quad \text{(A8)}$$

The total concentration of U(VI) can be expressed as:

$$\left[U(VI)\right]_{tot} = \left[UO_2(OH)_3^-\right] + \left[UO_2(OH)_4^{2-}\right] + \left[UO_2^{2+}\right]_{eq} \quad \text{(A9)}$$

$$\left[U(VI)\right]_{tot} = \left[UO_2(OH)_3^-\right] + K_4\frac{\left[UO_2(OH)_3^-\right]}{K_3\left[OH^-\right]^3}\left[OH^-\right]^4 + \frac{\left[UO_2(OH)_3^-\right]}{K_3\left[OH^-\right]^3} \quad \text{(A10)}$$

$$\left[U(VI)\right]_{tot} = \frac{K_3\left[OH^-\right]^3\left[UO_2(OH)_3^-\right] + K_4\left[UO_2(OH)_3^-\right]\left[OH^-\right]^4 + \left[UO_2(OH)_3^-\right]}{K_3\left[OH^-\right]^3} \quad \text{(A11)}$$

$$K_3\left[OH^-\right]^3\left[U(VI)\right]_{tot} = K_3\left[OH^-\right]^3\left[UO_2(OH)_3^-\right] + K_4\left[UO_2(OH)_3^-\right]\left[OH^-\right]^4 + \left[UO_2(OH)_3^-\right]$$

(A12)

$$K_3\left[OH^-\right]^3\left[U(VI)\right]_{tot} = \left[UO_2(OH)_3^-\right]\left(K_3\left[OH^-\right]^3 + K_4\left[OH^-\right]^4 + 1\right) \quad \text{(A13)}$$

$$\left[UO_2(OH)_3^-\right] = \frac{K_3\left[OH^-\right]^3\left[U(VI)\right]_{tot}}{K_3\left[OH^-\right]^3 + K_4\left[OH^-\right]^4 + 1} \quad \text{(A14)}$$

A new variable a3 was considered:

$$a3=\frac{K_3[OH^-]^3}{K_3[OH^-]^3+K_4[OH^-]^4+1} \quad \text{(A15)}$$

Then for a $[OH^-]$ = 0.01 mol·dm^{-3} and considering the formation constants of the $UO_2(OH)_3^-$ and $UO_2(OH)_4^{2-}$ hydroxocomplexes ($\log K_3$= 21.75±0.42; $\log K_4$= 23.60±0.68) [58], a3 = 0.585.

Studying the other hydroxocomplex:

$$[UO_2(OH)_4^{2-}]=K_4[UO_2^{2+}]_{eq}[OH^-]^4=K_4\frac{[UO_2(OH)_3^-]}{K_3[OH^-]^3}[OH^-]^4=K_4\frac{a3[U(VI)]_{tot}}{K_3[OH^-]^3}[OH^-]^4 \quad \text{(A16)}$$

A new variable a4 was considered:

$$a4=\frac{K_4[OH^-]a3}{K_3} \quad \text{(A17)}$$

Then for a $[OH^-]$ = 0.01 mol·dm^{-3}, a4=0.415.

Finally the relation between the complexes and the total U(VI) concentration is:

$[UO_2(OH)_3^-]=0.585\cdot[U(VI)]tot$ (A18)

$[UO_2(OH)_4^{2-}]=0.415\cdot[U(VI)]tot$ (A19)

As can be seen here, a3 and a4 are equivalent to the percentage of U(VI) in the form of the species $UO_2(OH)_3^-$ and $UO_2(OH)_4^{2-}$ respectively.

Now, considering the hydrogen peroxide in solution, the Stern-Volmer equation is found using mass balances.

$$K_1 = \frac{\left[UO_2(O_2)(OH)_2{}^{2-}\right]}{\left[UO_2(OH)_3{}^{-}\right]_{eq}\left[OH^-\right]\left[H_2O_2\right]_{eq}} \quad \text{(A20)}$$

$$K_2 = \frac{\left[UO_2(O_2)(OH)_2{}^{2-}\right]}{\left[UO_2(OH)_4{}^{2-}\right]_{eq}\left[H_2O_2\right]_{eq}} \quad \text{(A21)}$$

$$\left[UO_2(OH)_3{}^{-}\right]_0 + \left[UO_2(OH)_4{}^{2-}\right]_0 = \left[UO_2(OH)_3{}^{-}\right]_{eq} + \left[UO_2(OH)_4{}^{2-}\right]_{eq} + \left[UO_2(O_2)(OH)_2{}^{2-}\right] \quad \text{(A22)}$$

It was supposed:

$$\left[H_2O_2\right]_o = \left[H_2O_2\right]_{eq} \quad \text{(A23)}$$

$$\frac{\left[UO_2(OH)_3{}^{-}\right]_o}{\left[UO_2(OH)_4{}^{2-}\right]_o} = \frac{\left[UO_2(OH)_3{}^{-}\right]_{eq}}{\left[UO_2(OH)_4{}^{2-}\right]_{eq}} \quad \text{(A24)}$$

Then expression A25 could be written:

$$\left[UO_2(O_2)(OH)_2{}^{2-}\right] = K_1\left[UO_2(OH)_3{}^{-}\right]_{eq}\left[OH^-\right]\left[H_2O_2\right]_{eq} \quad \text{(A25)}$$

It is possible to rewrite A22 as:

$$\underbrace{\left[UO_2(OH)_3{}^{-}\right]_0 + \left[UO_2(OH)_4{}^{2-}\right]_0}_{[U(VI)]_{tot}} = \left[UO_2(OH)_3{}^{-}\right]_{eq} + \left[UO_2(OH)_4{}^{2-}\right]_{eq} + K_1\left[UO_2(OH)_3{}^{-}\right]_{eq}\left[OH^-\right]\left[H_2O_2\right] \quad \text{(A26)}$$

Dividing all the terms of A26 by $[UO_2(OH)_3^-]_{eq}$ and using the A24 expression, A27 is obtained:

$$\frac{\left[UO_2{}^{2+}\right]_{tot}}{\left[UO_2(OH)_3{}^{-}\right]_{eq}} = 1 + \frac{\left[UO_2(OH)_4{}^{2-}\right]_o}{\left[UO_2(OH)_3{}^{-}\right]_o} + K_1\left[OH^-\right]\left[H_2O_2\right] \quad \text{(A27)}$$

As shown before a3 is the percentage of U(VI) in the form of $[UO_2(OH)_3^-]_o$.

$$\frac{\left[UO_2(OH)_3^-\right]_o (1/a3)}{\left[UO_2(OH)_3^-\right]_{eq}} = 1 + \frac{\left[UO_2(OH)_4^{2-}\right]_o}{\left[UO_2(OH)_3^-\right]_o} + K_1\left[OH^-\right]\left[H_2O_2\right] \quad \text{(A28)}$$

$$\frac{\left[UO_2(OH)_3^-\right]_o}{\left[UO_2(OH)_3^-\right]_{eq}} = a3\left(1 + \frac{\left[UO_2(OH)_4^{2-}\right]_o}{\left[UO_2(OH)_3^-\right]_o}\right) + a3K_1\left[OH^-\right]\left[H_2O_2\right] \quad \text{(A29)}$$

Also, a4 is the percentage of U(VI) in the form of $[UO_2(OH)_4^{2-}]_o$.

$$\underbrace{\frac{\left[UO_2(OH)_3^-\right]_o}{\left[UO_2(OH)_3^-\right]_{eq}}}_{F_0/F} = \underbrace{a3 + \frac{a3a4\left[UO_2^{2+}\right]_{tot}}{a3\left[UO_2^{2+}\right]_{tot}}}_{1} + \underbrace{a3K_1\left[OH^-\right]\left[H_2O_2\right]}_{K_{sv}} \quad \text{(A30)}$$

And finally the Stern-Volmer expression was obtained:

$$\frac{F_0}{F} = 1 + K_{sv}\cdot[H_2O_2] \quad \text{(A31)}$$

B. Debye Hückel Approximations

All the constants obtained experimentally were corrected to ionic strength 0, using the Debye-Hückel approximation [58].

The following formula was used:

$$\log\beta - \Delta z^2 D = \log\beta^0 - \Delta\varepsilon I_m \quad \text{(B1)}$$

$$\Delta z^2 = (mz_M - qz_L - n)^2 + n - mz_M^2 - qz_L^2 \quad \text{(B2)}$$

$$D = \frac{0.5091\sqrt{I_m}}{1+1.5\sqrt{I_m}} \quad \text{(B3)}$$

Where $log\beta$ is the constant that needs to be corrected, z_M, z_L and n are the charges of the complex $M_mL_q(OH)_n$, being M the metal ion and L the ligand, m the stoichiometric coefficient of M, q the stoichiometric coefficient of the ligand and n the stoichiometric coefficient of OH. $\Delta\varepsilon$ is the interaction difference between the solute coefficients, I_m is the ionic strength (in molality instead of molarity) and $log\beta^0$ is the constant at ionic strength 0. Δz^2 is the squared increment of charge and D is the Debye-Hückel term.

Bibliographical constants were also corrected with this approximation, when they were used at the ionic strength of the solution.

6 Design Of A New Reactor To Work At Low Volume Liquid/Surface Solid Ratio And High Pressure And Temperature. Dissolution Rate Studies Of UO_2 Under Both Anoxic And Reducing Conditions

6 Design Of A New Reactor To Work At Low Volume Liquid/Surface Solid Ratio And High Pressure And Temperature. Dissolution Rate Studies Of UO_2 Under Both Anoxic And Reducing Conditions

6.1. INTRODUCTION

The study of the behavior of the Spent Nuclear Fuel Matrix is critical for the deep geological repository safety assessment. As an approach to the chemical behavior of the Spent Nuclear Fuel matrix, it is possible to use unirradiated UO_2 as a chemical analogue. Casas et al. [1] studied the dissolution kinetics of UO_2 under oxidizing conditions proposing a first mechanism of oxidation-dissolution of UO_2. Later the same group studied the role of pe, pH and carbonate on the solubility of UO_2 at reducing conditions [2]. The oxidative dissolution mechanism was improved by De Pablo et al. [3,4,5] adding the effect of Temperature, pH, carbonate concentration and oxygen partial pressure and a mechanism of the dissolution of UO_2 due to the uranium-carbonate complexation was proposed [5]. Due to the radiolysis of water, species like H_2, O_2 and H_2O_2 are formed. Clarens et al. [6] added the concentration of hydrogen peroxide as a new parameter to the oxidative dissolution mechanism studies and determined the effect of the pH in the dissolution of UO_2 in H_2O_2 solutions. Precipitation of the uranium peroxide Studtite was observed at different concentrations of hydrogen peroxide adding complexity to the dissolution mechanism. Casas et al. [7] added a new parameter to the dissolution experiments: pressure. They designed a reactor in order to perform experiments up to 100 bars and temperatures up to 100^{o}C. The reactor was continuously stirred and they determined UO_2(s) dissolution rates in a hydrogen peroxide and carbonate media as a function of pressure and temperature. Lately, Casas et al. [8] improved the knowledge in the effect of carbonate and hydrogen peroxide concentration in UO_2 dissolution observing and increase in the dissolution when both the concentration of carbonate and hydrogen peroxide increased.

Flow through reactors were also used to determine matrix dissolution rates of nuclear spent fuel at very different conditions. Earlier studies are collected in Gray and Wilson [9], where the effect of carbonate concentration, oxygen pressure and temperature is well documented. In Röllin et al. [10] matrix dissolution rates were determined at oxidizing, anoxic and reducing conditions. Recently, dissolution rates of high burn-up spent fuels have been determined by Serrano-Purroy et al. [11,12].

All these experiments have something in common. In all of them the leachate was far from saturation in order to avoid precipitation. These experiments were designed to study the dissolution mechanisms but not to reproduce the conditions expected in a deep geologic repository. Wronkiekicz et al. [13] take this fact in consideration and used an experimental set-up with a very low flow (leachant drops through the solid) of leaching solution during 10 years at 90ºC. They observed a decrease in the release rate after the first two years produced by a dense mat of alteration phases that trap the loose particles of UO_2. They also observed precipitation of secondary uranium phases, reducing the release rate of UO_2 in solution. Following this trend a new reactor has been designed where leachant drops pass through the solid particle at a certain flow rate. Due to the low flow rate and the low volume liquid/surface solid ratio, the concentration of UO_2 in the leachate reaches saturation. Reactor can be operated at different pressures, temperatures, atmosphere composition and leaching composition. One of the aims of this set-up is to approximate the experimental conditions to those that could be found in a deep geologic repository.

6.2. EXPERIMENTAL

6.2.1. Experimental set-up

The main idea of the experimental set-up is to have a solid in powder or in pellet in contact with drops of leachant in a very low flow. The contact would be at a controlled atmosphere, pressure and temperature. The leachate is afterwards collected at the bottom of the reactor.

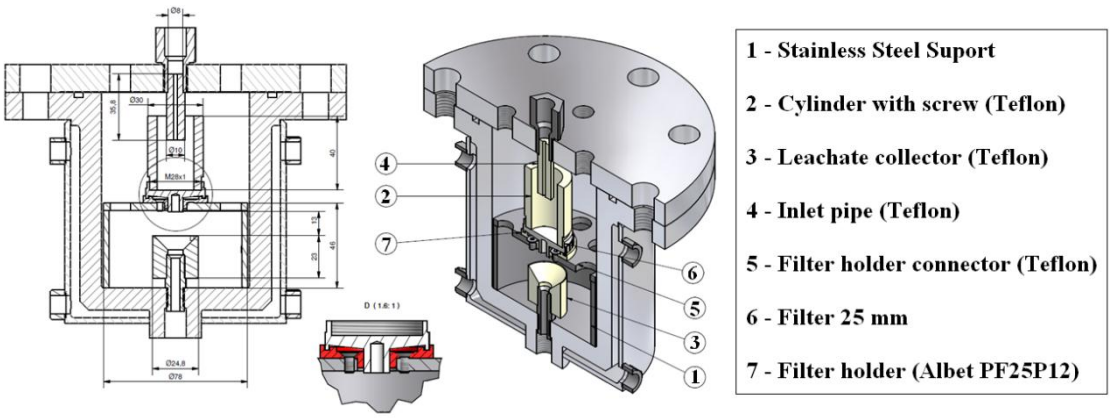

Figure 6.1. Design of the stainless steel reactor.

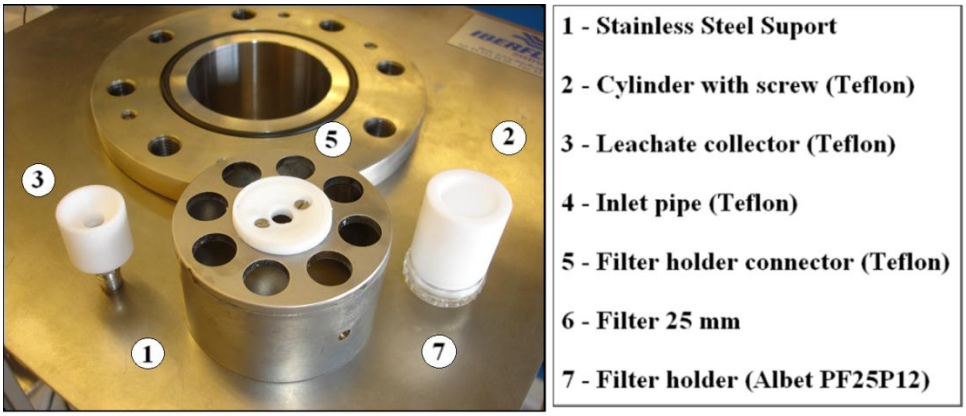

Figure 6.2. Three of the four parts of the Teflon structure inside the reactor. The absent part is the Teflon pipe that is connected to the upper part of the reactor.

In order to fulfill this idea, a stainless-steel (AISI 316) reactor was designed (Figure 6.1).This reactor allows working at inner gas pressures up to 50 bars, even with hydrogen gas. The reactor is equipped with a manometer and a thermometer to measure the pressure and the temperature inside the reactor. It also has a security valve to avoid

overpressure and two inlets, one for gas and the other for liquid. The inlet of gas connects through different valves and manometers the inside of the reactor with the selected gas cylinder. The leachant is stored in a bottle continuously purged with the selected gas. From this bottle, a chromatographic pump (Knauer, Smartline Pump 100) impulses the leachant into the reactor directly through the Teflon structure inside the reactor. The use of a chromatographic pump allows working at higher pressures and low flow. The Teflon structure (Figure 6.1 and 6.2) guides the leaching solution and stores the solid avoiding any contact of the solid with the steel. It is formed by 4 pieces. First a Teflon cylinder that guides the leachant into the inside of the reactor in order to assure that the leachant drops fall vertically into the top of the solid and from a close distance. The second Teflon piece is a larger cylinder with a screw at the end. This piece assures that all the leachant falls into the solid and it is connected to a commercial filter holder (Albet PF25P12). The filter holder contains a filter with the solid as powder or as a pellet. This second piece also contains the solid into the Teflon structure avoiding dispersion into the insides of the steel reactor, especially when venting or pressurizing the reactor. The third piece is connected with the bottom of the filter holder allowing that the leachate drops into the bottom of the reactor where the last Teflon piece recovers the leachate, and guides it into the outlet in the bottom of the steel reactor. The leachate then can be recovered using a pair of valves in a closed bottle with a septum in order to avoid air contamination. The reactor has a jacket in order to change the temperature inside the reactor by circulating some fluid at a different temperature (Figure 6.3).

Figure 6.3. Dissolution studies experimental set-up.

6.2.2. Materials and Methods

Crystalline Uranium (IV) dioxide was obtained from a UO_2 pellet supplied by ENUSA (Empresa Nacional del Uranio S.A.). X-ray powder diffraction (XRD) analysis showed the bulk of the sample to correspond to $UO_{2.01}$ [2]. For the experiments two different particles sizes were used, one with particles larger than 500 μm and the other with particles between 150 and 500 μm (surface areas of 0.005 and 0.01m^2 g^{-1}, respectively) [14,15]. The hydrogen peroxide solutions were obtained from the same initial solution (Merck) and the concentration was periodically standardized with thiosulfate (Scharlau) in H_2SO_4. Cylinders of 99.99% hydrogen gas and 99.99% nitrogen gas were provided by Abelló Linde S.A.

Two kinds of leaching solutions were prepared. One was prepared with 10^{-3} mol·dm^{-3} Na_2CO_3 and $19 \cdot 10^{-3}$ mol·dm^{-3} $NaClO_4$. The second one was prepared simulating cement pore water. Some species of the pore water solution precipitated in the small valves and tubes of the chromatographic pump, obstructing them and blocking the flow of leachant. To avoid these precipitation problems, the solution was diluted ten times. The composition after the dilution is shown in Table 6.1. The uranium composition was determined by means of a Time Resolved Laser Fluorescence Spectroscopy and adding FLURAN ® to increase Uranium (VI) fluorescence [16]. Some samples were analyzed by ICP-MS technique to assure that the concentration results were correct. Experiments were made at room temperature.

Table 6.1. Cement pore water composition (mol·dm^{-3}) used in the dissolution rate experiments.

Element	Composition
pH	12.2
[Al]	$2.6 \cdot 10^{-6}$
[K]	$1.8 \cdot 10^{-3}$
[Na]	$4.9 \cdot 10^{-3}$
[Ca]	$7.1 \cdot 10^{-3}$
[SO_4^{2-}]	$4.3 \cdot 10^{-5}$
[Si]	$5.3 \cdot 10^{-4}$

A Platinum mesh with Palladium black electrodeposition was used to catalyse the hydrogen reaction with oxygen in order to eliminate oxygen traces and assure better reducing conditions. The Platinum mesh was used to avoid the solid dispersion in the filter due to the mechanical effects of the falling drops.

Hydrogen peroxide is a very oxidant species that reacts with a lot of materials. In order to see if hydrogen peroxide reacts with any of the elements that compose the experimental set-up, an extra experiment was made. The experimental set-up was prepared like in all other experiments, but in this case without using uranium. The hydrogen peroxide concentration was measured by iodometry with standardized thiosulfate. The concentration of hydrogen peroxide did not change due to its pass throw the experimental set-up, so it is possible to say that hydrogen peroxide did not react with any of the materials of the experimental set-up.

6.3. RESULTS AND DISCUSSION

The experiments carried out in this work are collected in Table 6.2 In experiments 1 and 2, the flow rate was varied during the experiment, from $3.34 \cdot 10^{-7}$ dm^3/s to 10^{-5} dm^3/s. The concentration of Uranium in $mol \cdot dm^{-3} \cdot m^{-2}$ was plotted versus the inverse of the flow in $s \cdot dm^{-3}$. The points follow a straight line, showing that a steady state was reached. In Figure 6.4 the concentration of uranium versus the inverse of the leaching flow, in experiment 1, is shown as an example.

The dissolution rate was determined using the following equation:

$$r\ (mol\, m^{-2} s^{-1}) = \frac{[U(VI)](mol\ dm^{-3}) * Q\ (dm^3 s^{-1})}{m_{particle}(g) * A_{sup}.(\ m^2 g^{-1})} \quad (1)$$

In equation 1, r is the dissolution rate in $mol \cdot m^{-2} \cdot s^{-1}$, *[U(VI)]* is the concentration of uranium (VI) found at the steady state in the outflow solution in $mol \cdot dm^{-3}$, Q is the flow rate in $dm^3 \cdot s^{-1}$, $m_{particle}$ is the mass of the UO_2 particles in grams and A_{sup} is the specific surface area of the particles in $m^2 \cdot g^{-1}$.

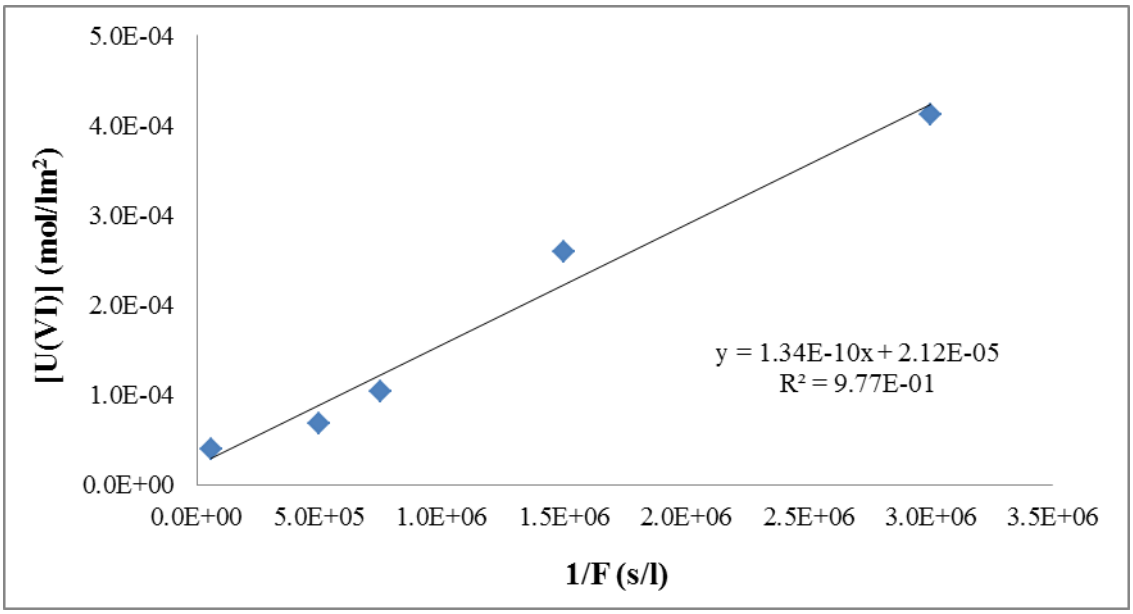

Figure 6.4. Uranium (VI) concentration (mol·dm^{-3} m^{-2}) versus the inverse of flow rate in experiment 1.

Table 6.2. Experiments performed in this work.

EXP.	LEACHANT	pH	[H_2O_2] (mol·dm^{-3})	FLOW RATE (dm^3 s^{-1})	GAS (5-7 bars)	PARTICLE SIZE (µm)	MASS (g)
1	$1\cdot10^{-3}$ mol·dm^{-3} HCO_3^- $19\cdot10^{-3}$ mol·dm^{-3} $NaClO_4$	8	10^{-3}	variable	N_2	150-500	0.2021
2	$1\cdot10^{-3}$ mol· dm^{-3} HCO_3^- $19\cdot10^{-3}$ mol· dm^{-3} $NaClO_4$	8	10^{-3}	variable	H_2	150-500	0.2021
3	$1\cdot10^{-3}$ mol· dm^{-3} HCO_3^- $19\cdot10^{-3}$ mol· dm^{-3} $NaClO_4$	8	10^{-3}	$1.67\cdot10^{-5}$	N_2	~500	0.0233
4	$1\cdot10^{-3}$ mol· dm^{-3} HCO_3^- $19\cdot10^{-3}$ mol· dm^{-3} $NaClO_4$	8	10^{-3}	$1.67\cdot10^{-5}$	H_2	~500	0.0243
5	Pore water	12.2	10^{-3}	$1.67\cdot10^{-5}$	N_2	~500	0.0243
6	Pore water	12.2	10^{-3}	$1.67\cdot10^{-5}$	H_2	~500	0.0243

The dissolution rate determined for each experiment in Table 6.2 is shown in Table 6.3 together with some dissolution rates from the literature [10,12,17-20]. The values presented in the Table 6.3 from Clarens [17], Eary et al. [18], Gimenez et al. [19]

and Shoesmith et al. [20] correspond to a concentration of hydrogen peroxide of 10^{-3} mol·dm^{-3}, like the one used in this work. In the work from Clarens [17] the influence of pH, carbonate and hydrogen peroxide concentrations on the dissolution rate of UO_2 at anoxic conditions was studied. Eary et al. [18] studied the kinetics of UO_2 dissolution at acidic conditions without carbonates. Gimenez et al. [19] studied the dissolution rates of UO_2 at a very high ionic strength. Shoesmith [20] studied the effect of hydrogen peroxide and carbonate concentration in the dissolution rate of a CANDU fuel disk. The value in Table 6.3 corresponds to a solution without carbonates. Serrano-Purroy et al. [12] studied the dissolution rates of spent fuel, considering two different zones: The center and the periphery of the pellet. Powder from each fraction was obtained, milled and sieved. The average particle size was 90±40 μm in the center fraction and 140±50 μm in the periphery fraction. The leaching solution used in their experiments had the same composition as the carbonate solution used in this work ($1\cdot10^{-3}$ mol·dm^{-3} HCO_3^-; $19\cdot10^{-3}$ mol·dm^{-3} $NaClO_4$) but without hydrogen peroxide. Röllin et al. [10] investigated the dissolution rates of spent fuel under different pH and RedOx conditions in carbonate solutions without the addition of hydrogen peroxide. The oxidant in the work of Serrano-Purroy et al. [12] and Röllin et al. [10] is mainly oxygen.

In Table 6.3 the experiments at variable flow rate, a particle size of 150-500 μm and 0.2021 g of UO_2 are shown. Once the steady state was demonstrated experiments at only one flow rate were used. In these experiments another particle size was used with 10 times less mass. At these high flow rate ($1.67\cdot10^{-5}$ mol·dm^{-3}) the concentrations of uranium obtained are in the range between 10^{-9} and $5\cdot10^{-9}$ mol·dm^{-3}. These low concentrations are near the detection limit of the technique and therefore the error in the measurements is high. It is possible to observe that experiments 1 and 2 are one order magnitude lower than experiments 3 and 4. This difference could be due to the experimental error mentioned before, but also to the uncertainties in the surface area. Also during the first two experiments a plastic spacer was used in order to improve the distribution of leachant. It was not used in the following experiments since the Pd mesh was already distributing the leachant. Perhaps the spacer, created favored paths for the leachant or it is even possible that absorbs part of the uranium in solution.

Table 6.3. Dissolution rates (BIC: $1 \cdot 10^{-3}$ mol·dm^{-3} HCO_3^-; $19 \cdot 10^{-3}$ mol·dm^{-3} $NaClO_4$).

EXP.	LEACHANT	pH	FLOW RATE ($dm^3\ s^{-1}$)	GAS (5-7 bars)	PART. SIZE (μm)	MASS (g)	RATE (mol $s^{-1}m^{-2}$)
1	BIC	8	variable	N_2	150-500	0.2021	$(1.5\pm0.2)\cdot10^{-10}$
2	BIC	8	variable	H_2	150-500	0.2021	$(5.3\pm3.4)\cdot10^{-11}$
3	BIC	8	$1.67\cdot10^{-5}$	N_2	~500	0.0233	$(1.3\pm0.9)\cdot10^{-9}$
4	BIC	8	$1.67\cdot10^{-5}$	H_2	~500	0.0243	$(4.6\pm2.7)\cdot10^{-10}$
5	Pore water	12.2	$1.67\cdot10^{-5}$	N_2	~500	0.0243	$(7.4\pm3.9)\cdot10^{-10}$
6	Pore water	12.2	$1.67\cdot10^{-5}$	H_2	~500	0.0243	$(2.4\pm1.8)\cdot10^{-10}$
a	0.1 mol·dm^{-3} $NaClO_4$	7	$(3\text{-}3.5)\cdot10^{-6}$	N_2	100-320	1	$(8.3\pm3.2)\cdot10^{-11}$
a	0.1 mol·dm^{-3} $NaClO_4$	9	$(3\text{-}3.5)\cdot10^{-6}$	N_2	100-320	1	$(2.7\pm1.0)\cdot10^{-10}$
a	0.1 mol·dm^{-3} $NaClO_4$	10.5	$(3\text{-}3.5)\cdot10^{-6}$	N_2	100-320	1	$(3.3\pm1.1)\cdot10^{-10}$
a	$2\cdot10^{-3}$ mol·dm^{-3} HCO_3^-	8	$(3\text{-}3.5)\cdot10^{-6}$	N_2	100-320	1	$(2.0\pm0.7)\cdot10^{-9}$
b	0.03 mol·dm^{-3} HCl	1.5	-	N_2	250-1190	25	$(8.4\pm5.5)\cdot10^{-7}$
c	5 mol·dm^{-3} NaCl	8	-	N_2	10-50	-	$9.0\cdot10^{-11}$
d	0.1 mol·dm^{-3} $NaClO_4$	9.5	-	Air	CANDU fuel disk		$(2.5\pm1.5)\cdot10^{-11}$
e	BIC	7.6	$2.1\cdot10^{-7}$	Air	90±40	0.9973	$(1.0\pm0.5)\cdot10^{-10}$
e	BIC	7.6	$2.1\cdot10^{-7}$	Air	140±50	1.0495	$(3.8\pm1.8)\cdot10^{-11}$
f	0.01 mol·dm^{-3} HCO_3^-	8.4	-	Air	250-500	0.5	$(7.7\pm0.4)\cdot10^{-11}$
f	0.01 mol·dm^{-3} HCO_3^-	9.3	-	Air	250-500	0.5	$(1.2\pm0.1)\cdot10^{-10}$
f	0.01 mol·dm^{-3} HCO_3^-	8.4	-	H_2	250-500	0.5	$(7.3\pm1.3)\cdot10^{-13}$
f	0.01 mol·dm^{-3} HCO_3^-	9.3	-	H_2	250-500	0.5	$(7.7\pm1.7)\cdot10^{-14}$

[a] Clarens [17] ; [b] Eary et al. [18] ; [c] Giménez et al. [19] ; [d] Shoesmith et al. [20];
[e] Serrano et al. [12] ; [f] Röllin et al. [10].

Nevertheless, in general, it is clear that the dissolution rates are slower in hydrogen than in nitrogen. The decrease on the dissolution rate due to the presence of hydrogen instead of nitrogen is of about one third in all the experiments of this work. This decrease could be attributed to the scavenging of oxidants, due to the reaction of hydrogen peroxide with hydrogen [21-25] and also to the competition between hydrogen peroxide and hydrogen to oxidize or reduce uranium respectively [10,24,25]. The decomposition of H_2 due to the catalytic effect of UO_2 produces hydrogen radicals

that are capable to reduce the UO_2 surface. In addition the presence of palladium could catalyze the reaction of hydrogen peroxide with hydrogen [23].

First of all the scavenging effect of hydrogen was considered. The reaction of hydrogen peroxide with hydrogen has a kinetic constant of 0.029±0.009 $dm^3\ mol^{-1}s^{-1}$ [21,22].

$$r\ (mol\ dm^{-3}\ s^{-1}) = k \cdot [H_2O_2] \cdot [H_2] \qquad (2)$$

In all the experiments of this work, the concentration of hydrogen peroxide was 10^{-3} $mol \cdot dm^{-3}$ and the concentration of hydrogen taking into account the Henry's law (($7.8 \cdot 10^{-4}$ $mol \cdot dm^{-3} \cdot atm^{-1}$, at 298K)) was approximately $5 \cdot 10^{-3}$ $mol \cdot dm^{-3}$. So the rate of the reaction is $1.5 \cdot 10^{-7}$ $mol \cdot dm^{-3} s^{-1}$, too slow to produce any effect on the hydrogen peroxide concentration in the leaching solution. However the palladium mesh can catalyze this reaction [23]. Calculations were made using extrapolations from the data presented in Nilsson et al. [23] and estimating the contact time and S/V ratio between the leaching solution and the Pd mesh. These calculations showed that only for very low flows (between 10^{-7} and 10^{-6} $dm^3 s^{-1}$), Pd could have a detectable catalytic effect. However if some of the initial hydrogen peroxide would have reacted due to this catalyzed reaction, a decrease in the concentration of uranium would have been observed in very low flows when representing the concentration of uranium versus the inverse of the leaching flow, and it was not the case.

If the reaction between hydrogen and hydrogen peroxide is not the responsible on the decrease of the uranium dissolution, even when the catalyzing effect of Pd is considered, then another process must occur. H_2 can react with the U(VI) dissolved in solution reducing it to U(IV), but this reaction is very slow and it can be neglected [25]. Röllin et al. [10] suggested a catalytic effect of the surface of UO_2 to decompose the hydrogen molecule into hydrogen radicals that would reduce the surface of UO_2 creating a protective effect against corrosion. Some years later Broczkowski et al. [24,25] concluded that this catalytic effect was not due to the catalytic effect of the UO_2 surface but to the catalytic effect of the ε particles present in the spent fuel. In the experiment carried out in this work, crystalline UO_2 without ε particles was used. However the UO_2 particles were in contact with the Pd mesh that could act as catalyzer. It is possible that

the decrease in the UO_2 dissolution rate in the presence of H_2 is mainly due to the protective effect of H_2 against UO_2 corrosion. Nevertheless a small H_2O_2 scavenging effect could also contribute to the UO_2 dissolution rate decrease.

Dissolution rates are higher when bicarbonate is present in the solution in both nitrogen and hydrogen atmospheres. The pore water contains several ions in solution (Table 6.1) that can precipitate in the form of secondary phases of uranium like calcium uranates. Therefore the concentration of uranium in the leachate would be lower and the dissolution rate calculated would be also lower. Scanning Electron Microscopy (SEM) observations made after the experiments showed no uranium secondary phases formation. Hence, the lower dissolution rate in pore water is not likely to be due to the precipitation of secondary phases. The difference between the dissolution rates should be then, due to the presence of bicarbonate, a strong complexing agent that enhances the dissolution of UO_2 [17,26].

When comparing the results of this work with the literature, the dissolution rate of Clarens [17] with $2 \cdot 10^{-3}$ $mol \cdot dm^{-3}$ HCO_3^- is very similar to the dissolution rate of experiment 3 in similar conditions, but one order of magnitude higher than the dissolution rate of experiment 1. That seems to corroborate that the dissolution rates of experiment 1 and 2 should be higher. Looking at the dissolution rates from Clarens [17] without carbonates, the dissolution rate increases when the pH also increases, from neutral to alkaline pH. So the dissolution rate of experiment 5 is consistent with this trend, it is higher than the ones in Clarens [17] because the pH is also higher. When the experiments of this work were performed under 5-7 bars of hydrogen, the dissolution rates decreased, but they were still several orders of magnitude higher than the ones from Röllin et al. [10] with hydrogen atmosphere and carbonates but without hydrogen peroxide. This means that although hydrogen is affecting the release of uranium, the presence of hydrogen peroxide still enhances the dissolution rate of uranium with or without carbonates.

Summarizing the result of this work and the literature, the highest dissolution rates are obtained at very low pH [18]. The effect of pH is explained in Clarens [17] and Clarens et al. [6]. The dissolution rate increases for extreme pH, at very acidic or very alkaline conditions. At similar pH, the dissolution rate of uranium is higher when it is in

contact with hydrogen peroxide rather than with oxygen [10,12,17-20]. When both oxygen and hydrogen peroxide are present, oxygen increases the rate of decomposition of hydrogen peroxide [20] diminishing the effect of hydrogen peroxide in the dissolution of uranium. Either with hydrogen peroxide or with oxygen, the presence of carbonates increases the dissolution rate of uranium [10,12,17-20]. On the contrary, the dissolution rate of uranium decreases with the presence of hydrogen.

6.3.1 Future Studies: The reactor as a multipurpose tool

This reactor can also be used to study:

- Secondary phase formation in long-term experiments.
- RedOx studies on solid surfaces.
- Sorption research.
- Experiments where three different phases solid-liquid-gas interact.
- Studies on the effect of high pressure and temperature above 298K.

6.4. CONCLUSIONS

A flow-through experimental reactor has been designed in order to perform studies at both high pressure and high temperature conditions. A chromatographic pump is used to impulse the leachant throughout the reactor in order to work at very low flows but high pressures. Therefore, high surface solid to volume leachant ratios, similar to the ones predicted in the final repository, can be obtained. The reactor allows working at different atmospheres at pressures up to 50 bars. The temperature inside the reactor can be set using a jacket.

The reactor was constructed and successfully tested in a series of experiments with very complex leachants like cement pore water, very oxidant leachants like hydrogen peroxide, anoxic and reducing conditions, different flow rates and different pressures.

Using this new reactor the evolution of uranium concentrations released from an UO_2 sample was studied at different conditions.

Two conclusions were obtained from the results. First, the dissolution rates are higher in the solution with $1 \cdot 10^{-3}$ mol·dm^{-3} HCO_3^- and $19 \cdot 10^{-3}$ mol·dm^{-3} $NaClO_4$ than with pore water, due to the effect of carbonates. Second, at hydrogen pressures between 5 and 7 bars, hydrogen is only capable to partially reduce the effect of hydrogen peroxide on the dissolution rate of uranium. It was concluded that, under hydrogen atmosphere, the presence of hydrogen peroxide increases the dissolution rate of uranium by several orders of magnitude with or without carbonates.

The new reactor designed has proven to be a very useful tool to perform dissolution rate experiments at different conditions and it could be used in the future for a great variety of studies.

6.5. REFERENCES

1 I. Casas, J. Giménez, V. Martí, M.E. Torrero and J. de Pablo. (1994). Kinetic studies of unirradiated UO_2 dissolution under oxidizing conditions in batch and flow through experiments. *Radiochim.Acta*, **66/67**, 23-27.

2 I. Casas, J. de Pablo, J. Giménez, M.E. Torrero, J. Bruno, E. Cera, R.J. Finch and R.C. Ewing. (1998). The role of pe, pH, and carbonate on the solubility of UO2 and uraninite under nominally reducing conditions. *Geochim. Cosmochim. Acta*, **62**, 13 2223-2231.

3 J. de Pablo, I. Casas, J. Giménez, M. Molera, M. Rovira, L. Duro and J. Bruno. (1999). The oxidative dissolution mechanism of uranium dioxide. I. The effect of temperature in hydrogen carbonate medium. *Geochim. Cosmochim. Acta*, **63**, 19/20 3097-3103.

4 J. de Pablo, I. Casas, J. Giménez, F. Clarens, L. Duro and J. Bruno. (2003). The Oxidative Dissolution Mechanism of Uranium Dioxide. The Effect of pH and Oxygen Partial Pressure. *MRS Proceed.*, **807**, 83.

5 J. Giménez, F.Clarens, I. Casas, M. Rovira, J. de Pablo and J. Bruno. (2005). Oxidation and dissolution of UO_2 in bicarbonate media: Implications for the spent nuclear fuel oxidative dissolution mechanism. *J. Nucl. Mater.*, **345**, 232-238.

6 F. Clarens, J. de Pablo, I. Casas, J. Giménez, M. Rovira, J. Merino, E. Cera, J. Bruno, J. Quiñones and A. Martínez-Esparza. (2005). The oxidative dissolution of unirradiated UO_2 by hydrogen peroxide as a function of pH. *J. Nucl. Mater.*, **345**, 225-231.

7 I. Casas, M. Borrell, L. Sánchez, J. de Pablo, J. Giménez and F. Clarens. (2008). Determination of UO_2(s) dissolution rates in a hydrogen peroxide medium as a function of pressure and temperature. *J. Nucl. Mater.*, **375**, 151-156.

8 I. Casas, J. de Pablo, F. Clarens, J. Gimenez, J. Merino, J. Bruno and A. Martinez-Esparza. (2009). Combined Effect of H_2O_2 and HCO_3^- on UO_2(s) Dissolution Rates under Anoxic Conditions. *Radiochim. Acta*, **97**, 9, 485-490.

9 Gray W. J. and Wilson C. N. (1995) Spent fuel dissolution studies: FY1991 to 1994. *Report PNL-10540 (USA).*

10 S.Röllin, K.Spahiu and U.-B. Eklund. (2001). Determination of dissolution rates of spent fuel in carbonate solutions under different redox conditions with a flow-through experiment. *J. Nucl. Mater.*, **297**, 231-243.

11 D. Serrano-Purroy, F. Clarens, J.-P- Glatz, B. Christiansen, J. de Pablo, J. Giménez, I. Casas, A. Martínez-Esparza. (2009). Leaching of 53 MW/d kg U spent nuclear fuel in a flow-through reactor. *Radiochim.Acta*, **97**, 491-496.

12 D. Serrano-Purroy, I. Casas, E. González-Robles, J.P. Glatz, D.H. Wegen, F. Clarens, J. Giménez, J. de Pablo, A. Martínez-Esparza. (2013). Dynamic leaching studies of 48 MWd/kgU $U0_2$ commercial spent nuclear fuel under oxic conditions. *J. Nucl. Mater.*, **434**, 451-460.

13 D.J. Wronkiewicz, J.K. Bates, S.F. Wolf and E.C. Buck. (1996). Ten-year results from unsaturated drip tests with UO_2 at 90° C: implications for the corrosion of spent nuclear fuel. *J. Nucl. Mater.*, **238**, (1) 78-95.

14 J.de Pablo, I. Casas, F. Clarens, J. Giménez, and M. Rovira. (2003). Contribución experimental y modelización de procesos básicos para el desarrollo del modelo de alteración de la matriz del combustible irradiado. Vol.1. *Publicaciones técnicas, ENRESA, SPAIN*.

15 E. Iglesias, J. Quiñones, S. Pérez de Andrés, J. M. Cobo and J. Alcaide. (2005). Influencia del área superficial específica en la alteración del combustible nuclear irradiado. Estado del arte. *DFN/RR-02/SP-05, Ciemat*.

16 K.W. Jung, J.M. Kim, C.J. Kim and J.M. Lee. (1987). Trace Analysis of Uranium in Aqueous Samples by Laser-induced Fluorescence Spectroscopy. *J. Korean Nucl. Soc.*, **19**, 4, 242-248.

17 F. Clarens. (2004). PhD Thesis: Efecto de la radiólisis y de los productos radiolíticos en la disolución del UO_2: Aplicación al modelo de alteración de la matriz del combustible nuclear gastado. *Universitat Politècnica de Catalunya*.

18 L.E. Eary and L.M. Cathles. (1983). A kinetic model of UO_2 dissolution in acid, H_2O_2 solutions that includes uranium peroxide hydrate precipitation. *Metall. Trans. B.*, **14**, 325-334.

19 J. Giménez, E. Baraj, M.E. Torrero, I. Casas and J. de Pablo. (1996). Effect of H_2O_2, NaClO and Fe on the dissolution of unirradiated UO_2 in NaCl 5 mol kg^{-1}. Comparison with spent fuel dissolution experiments. *J. Nucl. Mater.*, **238**, 64-69.

20 D.W. Shoesmith and S. Sunder. (1992). The prediction of nuclear fuel (UO_2) dissolution rates under waste disposal conditions. *J. Nucl. Mater.*, **190**, 20-35.

21 J. Giménez, I. Casas, R. Sureda and J. de Pablo. (2012). Kinetics of hydrogen peroxide consumption in aqueous phase at different hydrogen partial pressures. *Radiochim. Acta*, **100**, 445-448.

22 R. Sureda. (2011). PhD Thesis: Disolución del combustible nuclear gastado en un almacenamiento geológico profundo. Efecto de los productos radiolíticos y de formación de fases secundarias. *Universitat Politècnica de Catalunya*.

23 S. Nilsson and M. Jonsson. (2008). On the catalytic effects of UO_2(s) and Pd(s) on the reaction between H_2O_2 and H_2 in aqueous solution. *J. Nucl. Mater.*, **372**, 160-163.

24 M.E. Broczkowski, J.J. Noël and D.W. Shoesmith. (2005). The inhibiting effects of hydrogen on the corrosion of uranium dioxide under nuclear waste disposal conditions. *J. Nucl. Mater.*, **346**, 16-23.

25 L. Wu, Z. Qin, D.W. Shoesmith. (2014). Improved model for corrosion of used nuclear fuel under permanent disposal conditions inside a failed waste. Container. *Corros. Sci.*, **84**, 85-95.

26 J. de Pablo, I. Casas, J. Gimenez, M. Molera, M. Rovira, L. Duro and J. Bruno. (1999). The oxidative dissolution mechanism of uranium dioxide. I. The effect of temperature in hydrogen carbonate medium. *Geochim. Cosmochim. Acta.,* **63**, 19-20, 3097-3103.

7 α-Radiolysis Under Alkaline Conditions In Both 0.05 And 5.0 Molar NaCl

7 α-Radiolysis Under Alkaline Conditions In Both 0.05 And 5.0 Molar NaCl

7.1. INTRODUCTION

Most of the developed countries use nuclear power to obtain energy. The waste that nuclear power produces is very difficult to manage and the final solution for it, according to the consensus of the scientific community, is the deep geological repository. However, only few countries have a clear project about how their repository should be. In most cases is not yet chosen how will be the lithology that will host the repository, how will be constructed this repository or which protections the waste will have. In addition, the production of fuels has evolved over the years, making the composition of those quite varied. Due to that, in every prediction of the behavior of the fuel in the repository is necessary to take into account several factors, such as pH, dose rate (alpha, beta , gamma), inventory of radionuclides, composition of the groundwater and the geological site, ionic strength, etc. ... For example, depending on the lithology chosen ionic strength might vary from 0.1 to 15 $mol \cdot dm^{-3}$ [1, 2]. In the case of pH, it may vary from neutral or slightly alkaline values to highly alkaline because of the use of cement in structural and protective elements.

A conservative hypothesis used in the safety assessment of a deep geological repository is that water might get in contact with the spent fuel earlier than expected due to a failure in the container barrier. A very conservative but still reasonable assumption considers this to occur after the first 1000 years, when most effects due to beta and gamma radiation have become negligible [3]. This is why many studies are solely focused on alpha radiation. Moreover, in some cases, as in the WIPP (Waste Isolation Pilot Plant) [4,5] , the high-level waste stored is composed by Transuranium Elements, which mainly emit alpha radiation.

One of the effects of alpha radiation is the production of water radiolytic products: radicals like e^-_{aq}, $H^\bullet$, $OH^\bullet$ and molecules like H_2 and H_2O_2. The radicals $H^\bullet$, $OH^\bullet$ and e^-_{aq} are very reactive and can produce secondary radicals like $HO_2^\bullet$ and $O_2^{-\bullet}$. The most stable species formed are H_2 and H_2O_2 in aqueous solutions of low chloride

concentration. In salt brines H_2 and oxo halogenides such as HClO or HBrO (depending on the brine composition) are the species formed [3,6-8]. The oxidants formed increase the rate of oxidation and the rate of dissolution of the fuel matrix [9 and references therein]. These effects in alkaline pHs and high ionic strength were studied by Kelm et al. [10] and Kelm and Bohnert [11].

The effects of radiolyis on the fuel matrix have been studied in different ways. One option used by many authors is to add the radiolysis product directly to the solution. In this case it is possible to work in non-rad laboratories. Many authors have used this method in various studies to analyze the effect of pH and ionic strength on the dissolution of UO_2 [12-16].

Another option is to dissolve in the solution radiation emitting species like ^{241}Am [17] or ^{211}At [18]. The last one has the advantage of being a short-lived isotope and therefore, after some time, the activity of the samples is reduced so the solution can be analyzed in conventional environments.

In other cases cyclotron radiation has been used to study the effects of radiolysis. This system is more costly, but has the advantage that it is not necessary to introduce any species in the system in order to obtain radiation [19,20].

Finally it is possible to use pellets doped with a radioactive element. In this case the radiation is generated from the pellet. However, in the case of alpha and beta radiation only the solution within a short distance from the pellet is affected by the emitting radiation, in contrast to previous methods where the radiation affects the whole solution.

Muzeau et al. [21] and Cui et al. [22] use this method to conclude that the key factors in the dissolution of the matrix are: the alpha activity, the hydrogen concentration and the bromide concentration (in salt brines the concentration of bromide could be very high). Under static conditions the radiolysis redox balance at the UO_2/water interface creates locally oxidizing conditions of a magnitude depending on the sample alpha activity. A higher solution redox potential results in increased uranium solubility and modifies the solid phase at equilibrium with solution. Under anoxic

conditions uranium has a low solubility limit (10^{-10} to 10^{-8} mol·dm^{-3}). Low activities don't significantly increase the solution potential and the dissolution is then controlled by the uranium solubility. In the case of higher activities alpha radiolysis significantly increases the solution redox potential and thus the uranium solubility limit. The uranium release continues to increase limited only by the kinetics of UO_2 oxidation by oxidants generated by water radiolysis, given the presence of carbonates in solution. Under anoxic conditions (O_2 < 1ppm) in a carbonate solution (10^{-3} mol·dm^{-3}) lies an alpha-activity threshold between 18 and 33 MBq·$g_{UO_2}^{-1}$. Alpha activity values below the threshold do not change the redox potential sufficiently and the uranium release is controlled by the solubility. Above the threshold the alpha activity produces an increase in the redox potential and the uranium release is controlled by the kinetics of the radiolytic oxidation. However if 1 bar of hydrogen pressure is added to the system, the threshold is located above 385 MBq·$g_{UO_2}^{-1}$. Nevertheless, recent studies [23-25] have observed that the presence of bromide in solution mitigates the effect of hydrogen on the alpha-activity threshold, leading to high concentrations of uranium in solution. Curiously if the energy radiation is high enough, the effect of bromide disappears [20].

The main objective of the present work is to determine the effect on the SNF matrix dissolution of alpha-radiolysis under alkaline conditions. In this sense, alpha-radiolysis under alkaline conditions will be studied at different dose rates, different ionic strength as well as varying the location of the alpha-emitters (either into the pellets or dissolved in solution). The effects of alpha-radiolysis will be determined, on one hand, through the generation of radiolytic products: H_2, O_2, HClO and H_2O_2, and on the other hand from the dissolution of both U and Pu.

7.2. MATERIALS AND METHODS

7.2.1. Description of the system

Ten different experiments were performed (Table 7.1). In all of them a pellet was in contact with 0.02 dm^3 of solution in a glass vessel. They were carried out in a glove box in argon atmosphere. In 5 of the 10 experiments (1a, 2a, 3a, 4a, 6a) a gas sampling device was connected to the vessels as shown in Kelm and Bohnert [11]. The gas sampling devices were changed at different times to analyze their composition. The volume of the whole set-up was approximately 0.05 dm^3. The solution was analyzed only at the end of the experiment. In the other five experiments (1b , 2b , 3b , 4b , 6b) solution aliquots were taken at different times to be analyzed. Each of the five experiments "a" has its replica in terms of initial parameters in the experiments "b". In experiments 1a and 1b, a depleted UO_2 (s) pellet doped with 10% ^{238}Pu was used. In the case of experiments 2a and 2b the pellet was doped with 0.1 % ^{238}Pu. The solution for the experiments with doped pellets was NaCl 5 $mol \cdot dm^{-3}$. In experiments 3a and 3b, depleted uranium pellets were used but in this case in the solution of NaCl 5 $mol \cdot dm^{-3}$, ^{238}Pu was dissolved. Experiments 4a and 4b had the same casuistry that 3a and 3b but in this case the concentration of NaCl was 0.05 $mol \cdot dm^{-3}$. Finally experiments 6a and 6b were used as blanks. A pellet of depleted uranium with a solution of NaCl 5 $mol \cdot dm^{-3}$ was used.

Table 7.1: Summary of the experiments performed.

Experiment	Solid	Pu in solution	NaCl
1a	$Pu_{0.10}U_{0.90}O_2$ [10%]	0	5 $mol \cdot dm^{-3}$
2a	$Pu_{0.001}U_{0.999}O_2$ [0.1%]	0	5 $mol \cdot dm^{-3}$
3a	Pellet UO_2 depleted	2.7 GBq/dm^3	5 $mol \cdot dm^{-3}$
4a	Pellet UO_2 depleted	2.7 GBq/dm^3	0.05 $mol \cdot dm^{-3}$
6a	Pellet UO_2 depleted	0	5 $mol \cdot dm^{-3}$
1b	$Pu_{0.10}U_{0.90}O_2$ [10%]	0	5 $mol \cdot dm^{-3}$
2b	$Pu_{0.001}U_{0.999}O_2$ [0.1%]	0	5 $mol \cdot dm^{-3}$
3b	Pellet UO_2 depleted	2.7 GBq/dm^3	5 $mol \cdot dm^{-3}$
4b	Pellet UO_2 depleted	2.7 GBq/dm^3	0.05 $mol \cdot dm^{-3}$
6b	Pellet UO_2 depleted	0	5 $mol \cdot dm^{-3}$

7.2.2. Preparation of pellets of UO_2 (s)

The pellets of depleted UO_2(s) were annealed at 1100 °C in atmosphere at Ar/H_2. The UO_2 pellets (s) were pretreated before starting the experiments. To clean and remove any impurities on the surface, the pellets were submerged in HCl 0.001 $mol \cdot dm^{-3}$ for one day. Depending on the time that the pellets were stored; an oxidized layer could be formed on the surface [21]. In order to remove completely any oxidized layer on the surface of the pellet, the pellets were submerged in a solution of 10^{-3} $mol \cdot dm^{-3}$ $NaHCO_3$ for one day.

7.2.3. Preparation of solutions

All solutions were prepared in a glovebox under Ar atmosphere. The water used in the solutions was ultrapure water (Milli Q, 18.2 MΩ • cm). For experiments 3a, 3b, 4a, 4b a solution of ^{238}Pu, with a specific activity of 2.7 GBq/dm^{-3}, was prepared. A stock of 10.8 mg of PuO_2 with a specific activity of $6.3 \cdot 10^{11}$ Bq/g was used to prepare the solution. The solutions of 5 $mol \cdot dm^{-3}$ and 0.05 $mol \cdot dm^{-3}$ NaCl were prepared from recrystallized NaCl according to the procedure described in Kelm and Bohnert [8]. The pH of the experiments was adjusted to a pHc = 12, using a 0.01 $mol \cdot dm^{-3}$ NaOH solution.

7.2.4. Sample analysis

7.2.4.1. Determination of U and Pu

U and Pu concentrations in solution were measured by ICP-MS (ELAN 6100, Perkin Elmer Inc, Waltham, USA) and α - spectroscopy analysis using an analysis chamber with a S100 field channel analysator (^{238}Pu, $^{239/240}Pu$) and passivated implanted planar silicon (PIPS) detectors (Canberra 74/01, Canberra Industries Inc, Meriden, USA).

7.2.4.2 Determination of H_2O_2

The concentration of H_2O_2 was measured using a compact photometer PF-12 Macherey-Nagel, the photometric determination of hydrogen peroxide was by catalytic oxidation of an indicator using peroxidase.

7.2.4.3 Determination of ClO^-

The ClO^- concentration in solution was measured by UV-visible spectrometry (Cary 50 ; Varian, Inc. ; Agilent Technologies).

7.2.4.4 Determination of H_2 and O_2

The gas sampling devices used in experiments 1a, 2a, 3a, 4a, 6a were filled with neon at a known concentration and were connected to the sample vessels inside the glove box. Before connecting the gas sampling devices, the sample vessels were purged with a stream of argon . The gas composition is determined by a Quadropole Gas Mass Spectrometer (GAM400, In Process Instruments, Bremen, Germany) provided with Faraday and SEV detectors and a batch inlet system. The calibration was performed in the same pressure range as the sample measurements. The measurements were performed with the SEV-detector. The gas samples were measured 10 times and the mean value was specified.

7.3. RESULTS AND DISCUSSION

7.3.1 . Calculating the dose due to alpha activity

7.3.1.1 . Calculation of doses in experiments 1a, 1b, 2a, 2b

It was considered a pellet of 3mm radius and 1.5 mm thick, in a volume of 0.02 dm^3 of 5 $mol \cdot dm^{-3}$ NaCl [26]. Alpha-particles with an energy of 5.5 MeV, have a path cell in UO_2 of 11.8 μm. So it can be considered a region of 11.8 μm thick on the surface of the pellet where the emitted particles can reach the solution. More inside the pellet, the particles emitted cannot exit the pellet. It is considered that 18.8 % of the radiation released is dissipated homogeneously in the solution [11]. The pellets are doped with 10 % of ^{238}Pu in experiments 1a, 1b and 0.1 % of the same isotope in experiments 2a, 2b. The alpha activity of the 10 % doped pellet is comparable to the alpha activity of one recently disposed MOX fuel (Mixed OXide fuel) and the alpha activity of the 0.1 % doped pellet is of the same order of magnitude of a PWR fuel (Pressurized Water Reactor fuel) ten years after discharge or a MOX fuel up to 1000 years of storage and not high burn-up.

The maximum range of α radiation in brine is 45 μm. It was taken into account that the density of the solution may vary depending on the concentration of NaCl . The dose rate obtained is 10.4 Gy/h for experiments 1a, 1b and 0.1 Gy/h for experiments 2a, 2b.

7.3.1.2 . Calculation of doses in experiments 3a, 3b, 4a, 4b

The activity for the experiments 3a, 3b, 4a, 4b where ^{238}Pu oxide is dissolved in solution was determined by alpha spectroscopy. The dose rate was 7.2 Gy/h for experiments 3a, 3b and 8.6 Gy/h for experiments 4a, 4b. The difference is due to the different concentration of NaCl in solution that leads to a change in the density of the solution.

7.3.1.3 . Calculation of doses in experiments 6a , 6b

The dose of depleted UO_2 pellets was calculated in a similar way to the one used in the calculation for experiments 1a, 1b , 2a, 2b . In this case the size and weight of the pellets were known. It was considered a specific activity of $2.43 \cdot 10^4$ Bq/g . The dose rate for depleted UO_2 is $2.4 \cdot 10^{-4}$ Gy/h for experiment 6a and $2.6 \cdot 10^{-4}$ Gy/h for Experiment 6b.

7.3.2. Radiolytic products analyzed in the gas phase: H_2, O_2

In figures 7.1 and 7.2 it can be seen the H_2 and O_2 concentrations measured in moles per kg of solvent , depending on the dose rate in kGy . The concentrations are measured from experiments 1a, 2a, 3a, 4a, 6a. The data is consistent with those obtained in Kelm and Bohnert [11] , but this study is focused in the lower dose range. It can be seen that the ionic strength does not seem to affect the formation of H_2 and O_2. If this is true, then the formation of radiolytic H_2 and O_2 would not be a factor while selecting lithologies with varying ionic charge in order to store the nuclear waste. No difference was appreciated between experiments where radiation was generated in the pellet and where it was generated in solution. This information may allow in the future studying the formation of radiolytic H_2 and O_2, using pellets doped with alpha emitters or with alpha emitters dissolved in solution, according to the needs of the experiment. For example if the solution must be analyzed, then the minimum possible activity will be needed and doped pellets will be used, whereas if our interest is focused on the solid, it will be more useful to dissolve an alpha emitter in solution and work with depleted UO_2 pellets.

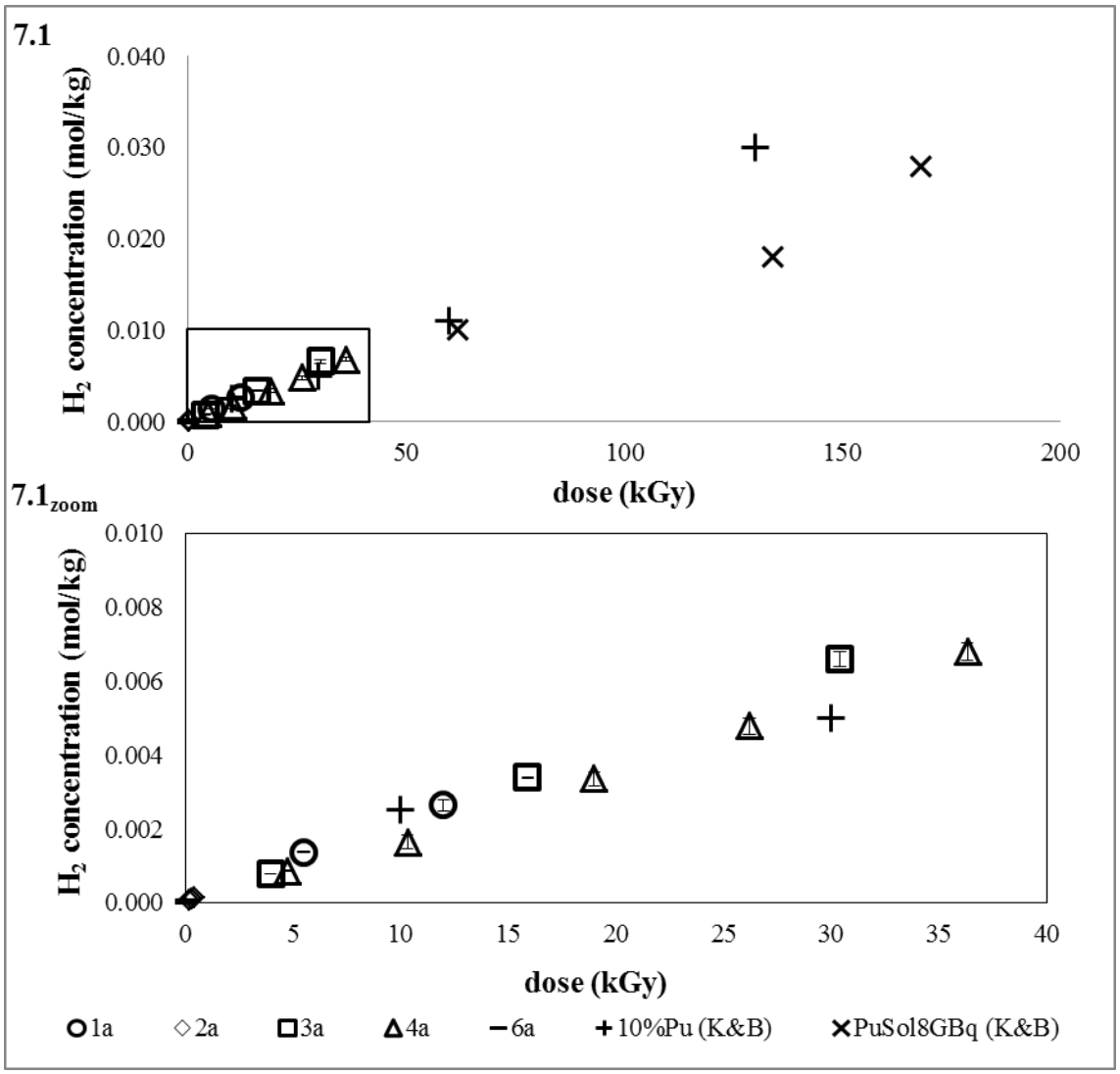

Figure 7.1. H_2 production. (K&B : Kelm and Bohnert [11]).The range between 0 and 40 kGy can be seen in detail in 7.1_{zoom}.

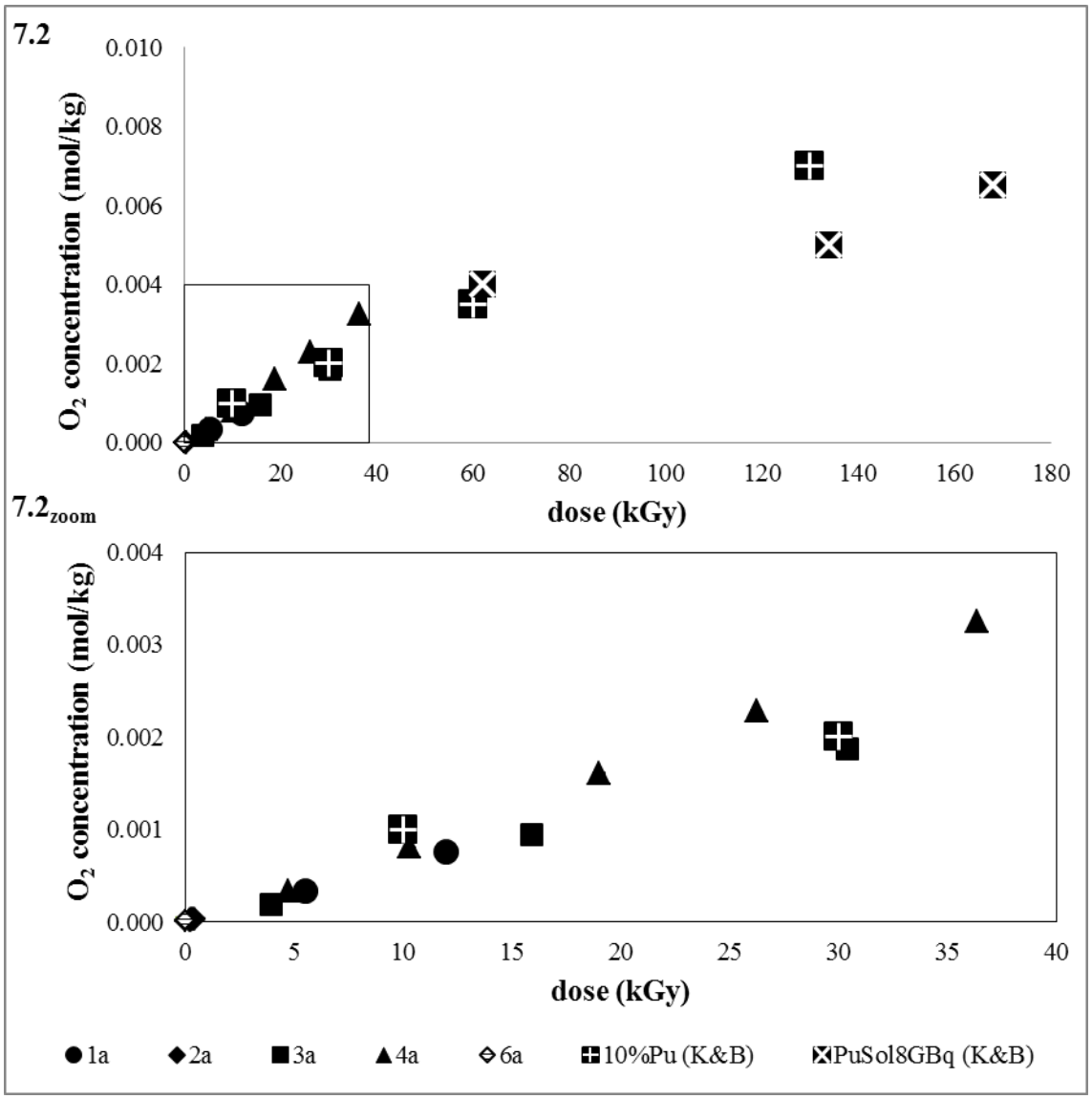

Figure 7.2. O_2 production. (K&B : Kelm and Bohnert [11]). The range between 0 and 40 kGy can be seen in detail in 7.2_{zoom}

7.3.3 . Radiolytic products analyzed in the liquid phase: H_2O_2 , ClO^-

In experiments 1a, 1b, 3a, 3b, ClO^- was detected at very similar concentrations in function of the dose rate. In this case it also seems that the origin of the radiation, inside or outside the pellets, doesn't affect the formation of radiolysis products. In experiments 2a, 2b, 6a, 6b, ClO^- was not detected due to the low dose rate. In experiments 4a and 4b, ClO^- was also not detected but in this case because the concentration of Cl^- was too low: 0.05 mol·dm^{-3} NaCl.

On the other hand, in experiments 4a, 4b the presence of H_2O_2 instead of ClO^- is observed. In experiments 2a, 2b, 6a, 6b, H_2O_2 is not detected due to low dose rate, and in 1a, 1b, 3a, 3b is not detected because of the high concentration of NaCl (5 $mol \cdot dm^{-3}$). As expected [8], in the solutions with more concentration of NaCl, ClO^- is formed mainly by alpha- radiolysis whereas in solutions with low concentration of NaCl, H_2O_2 is formed as a main product of alpha radiolysis.

7.3.4. Effects of alpha- radiolysis in the concentration of uranium and plutonium in solution

The filtered samples of uranium and plutonium have lower concentrations of both elements than in unfiltered samples, probably due to the formation of colloids or even precipitation. For this reason it is very difficult to quantify the concentration of U and Pu in the experiments.

In the experiment 1b the variation of the U concentration was between $1 \cdot 10^{-6}$ and $5 \cdot 10^{-5}$ $mol \cdot dm^{-3}$ in a range between 2.5 and 20 kGy. In the experiment 1a the concentration of uranium at the end of the experiment was $5 \pm 4 \cdot 10^{-7}$ $mol \cdot dm^{-3}$ for 74 kGy. In the experiment of Kelm and Bohnert [11] the U concentration was approximately $3 \cdot 10^{-7}$ $mol \cdot dm^{-3}$ for 10 kGy, $2 \cdot 10^{-8}$ $mol \cdot dm^{-3}$ for 65 kGy and $3 \cdot 10^{-5}$ $mol \cdot dm^{-3}$ for 130 kGy. Therefore, the uranium concentration of experiment 1a has the same order of magnitude as the ones from Kelm and Bohnert [11].

In addition to the possible formation of colloids, in the experiments 3 and 4 is very difficult to quantify the uranium and plutonium dissolved from the pellet, due to the PuO_2 dissolved in solution. It seems that the experiment 4 has a higher concentration of U and Pu than in the experiment 3, but due to experimental problems explained above, it is not possible to consider it as certain.

However, it is possible to observe qualitatively that experiments 1, 3 and 4 have a higher concentration of U and Pu that experiments 2 and 6. As expected, experiments with high dose rate also have higher concentrations of U and Pu.

7.3.5. Modeling of the experimental data using the software Macksima-Chemist

The experimental data obtained in this work was modelled using the software Macksima-Chemist [27]. This software needs data about the experimental conditions like dose and concentrations and also needs the equations that will constitute the kinetic system. These equations are mainly kinetic equations of the species in solution. It also requires the kinetic rate constants and the G-values. The G-value, also known as primary radiolytic yield, is the number of species formed per 100 eV of absorbed energy. It is proportional to the dose and has a very high dependence on the linear energy transfer (LET).

The equations and the corresponding rate constants used in the modelling were obtained from the bibliography (Table 7.2).

Table 7.2: Reactions and rate constants at zero ionic strength (Elements written with a negative sign and followed by "*(C)"* act as a catalyst).

Eq. number	Reaction	Rate constant	Ref.
1	$OH^{\bullet} + OH^{\bullet} = H_2O_2$	$5.50 \cdot 10^9$	28,29
2	$OH^{\bullet} + e^- = OH^-$	$3.00 \cdot 10^{10}$	29,30
3	$OH^{\bullet} + H^{\bullet} = H_2O$	$9.70 \cdot 10^9$	31,32
4	$OH^{\bullet} + HO_2^{\bullet} = H_2O + O_2$	$7.00 \cdot 10^9$	32
5	$OH^{\bullet} + O_2^{-\bullet} = O_2 + OH^-$	$1.00 \cdot 10^{10}$	29
6	$OH^{\bullet} + H_2O_2 = HO_2^{\bullet} + H_2O$	$2.70 \cdot 10^7$	29,33
7	$OH^{\bullet} + H_2 = H^{\bullet} + H_2O$	$3.40 \cdot 10^7$	29,33
8	$OH^{\bullet} + OH^- = H_2O + O^{-\bullet}$	$1.30 \cdot 10^{10}$	34
9	$OH^{\bullet} + HO_2^- = HO_2^{\bullet} + OH^-$	$7.50 \cdot 10^9$	29
10	$O^{-\bullet} + H_2O = OH^{\bullet} + OH^-$	$1.80 \cdot 10^6$	29,34
11	$e^- + e^- = H_2 + OH^- + OH^-$	$5.50 \cdot 10^9$	29,30
12	$e^- + H^{\bullet} = H_2 + OH^-$	$2.50 \cdot 10^{10}$	29,30
13	$e^- + O_2^{-\bullet} = HO_2^- + OH^-$	$1.30 \cdot 10^{10}$	29
14	$e^- + HO_2^{\bullet} = HO_2^-$	$2.00 \cdot 10^{10}$	29
15	$e^- + H_2O_2 = OH^{\bullet} + OH^-$	$1.10 \cdot 10^{10}$	29,35
16	$e^- + O_2 = O_2^{-\bullet}$	$1.90 \cdot 10^{10}$	29
17	$e^- + H^+ = H^{\bullet}$	$2.30 \cdot 10^{10}$	29,36
18	$e^- + H_2O = H^{\bullet} + OH^-$	$1.90 \cdot 10^1$	29,35
19	$e^- + HO_2^- = O^{-\bullet} + OH^-$	$3.50 \cdot 10^9$	29
20	$O_2^{-\bullet} + O_2^{-\bullet} = HO_2^- + O_2 - H^+$	$1.00 \cdot 10^9$	29
21	$H^{\bullet} + H^{\bullet} = H_2$	$5.00 \cdot 10^9$	37
22	$H^{\bullet} + O_2^{-\bullet} = HO_2^-$	$2.00 \cdot 10^{10}$	29

23	$H^{\bullet} + HO_2 = H_2O_2$	$8.50 \cdot 10^{9}$	32
24	$H^{\bullet} + H_2O_2 = H_2O + OH^{\bullet}$	$4.20 \cdot 10^{7}$	32,38
25	$H^{\bullet} + O_2 = HO_2^{\bullet}$	$2.10 \cdot 10^{10}$	29
26	$H^{\bullet} + OH^{-} = E^{-} + H_2O$	$2.20 \cdot 10^{7}$	29,35
27	$HO_2^{\bullet} + HO_2^{\bullet} = H_2O_2 + O_2^{\bullet}$	$8.40 \cdot 10^{5}$	29
28	$HO_2^{\bullet} + O_2^{-\bullet} = O_2^{\bullet} + HO_2^{-}$	$9.60 \cdot 10^{7}$	29
29	$HO_2^{\bullet} = H^{+} + O_2^{-}$	$8.00 \cdot 10^{5}$	29
30	$H^{+} + O_2^{-\bullet} = HO_2^{\bullet}$	$5.00 \cdot 10^{10}$	29
31	$H_2O_2 = H^{+} + HO_2^{-}$	$3.56 \cdot 10^{2-}$	29
32	$H^{+} + HO_2^{-} = H_2O_2$	$2.00 \cdot 10^{10}$	29
33	$H_2O^{\bullet} = H^{+} + OH^{-}$	$2.60 \cdot 10^{5-}$	29,39
34	$H^{+} + OH^{-} = H_2O^{\bullet}$	$1.43 \cdot 10^{11}$	29,40
35	$O_2 = O_2D$	$1.00 \cdot 10^{6}$	29
36	$H_2 = H_2D$	$1.00 \cdot 10^{6}$	29
37	$OH^{\bullet} + Cl^{-} = ClOH^{-}$	$4.30 \cdot 10^{9}$	29,41
38	$OH^{\bullet} + HClO = ClO + H_2O$	$9.00 \cdot 10^{9}$	29
39	$OH^{\bullet} + ClO_2^{-} = ClO_2 + H_2O - H^{+}$ *(C)*	$6.30 \cdot 10^{9}$	29
40	$e^{-} + Cl = Cl^{-} + H_2O$	$1.00 \cdot 10^{10}$	29
41	$e^{-} + Cl_2^{-} = Cl^{-} + Cl^{-} + H_2O$	$1.00 \cdot 10^{10}$	29
42	$e^{-} + ClOH^{-} = Cl^{-} + OH^{-} + H_2O$	$1.00 \cdot 10^{10}$	29
43	$e^{-} + HClO = ClOH^{-}$	$5.30 \cdot 10^{10}$	29
44	$e^{-} + Cl_2 = Cl_2^{-}$	$1.00 \cdot 10^{10}$	29
45	$e^{-} + Cl_3^{-} = Cl_2^{-} + Cl^{-}$	$1.00 \cdot 10^{10}$	29
46	$e^{-} + ClO_2^{-} = ClO + OH^{-} - H^{+}$ *(C)*	$4.50 \cdot 10^{10}$	29
47	$e^{-} + ClO_3^{-} = ClO_2 + OH^{-} - H^{+}$ *(C)*	$0.00 \cdot 10^{0}$	29
48	$H^{\bullet} + Cl = Cl^{-} + H^{+}$	$1.00 \cdot 10^{10}$	29
49	$H^{\bullet} + Cl_2^{-} = Cl^{-} + Cl^{-} + H^{+}$	$8.00 \cdot 10^{9}$	29,42
50	$H^{\bullet} + ClOH^{-} = Cl^{-} + H_2O$	$1.00 \cdot 10^{10}$	29
51	$H^{\bullet} + Cl_2 = Cl_2^{-} + H^{+}$	$7.00 \cdot 10^{9}$	29,43
52	$H^{\bullet} + HClO = ClOH^{-} + H^{+}$	$1.00 \cdot 10^{10}$	29
53	$H^{\bullet} + Cl_3^{-} = Cl_2^{-} + Cl^{-} + H^{+}$	$6.00 \cdot 10^{10}$	44
54	$HO_2^{\bullet} + Cl_2^{-} = Cl^{-} + HCl + O_2$	$4.00 \cdot 10^{9}$	29
55	$HCl = Cl^{-} + H^{+}$	$5.00 \cdot 10^{5}$	29
56	$HO_2^{\bullet} + Cl_2 = Cl_2^{-} + H^{+} + O_2$	$1.00 \cdot 10^{9}$	29
57	$HO_2^{\bullet} + Cl_3^{-} = Cl_2^{-} + HCl + O_2$	$1.00 \cdot 10^{9}$	29
58	$O_2^{-\bullet} + Cl_2^{-} = Cl^{-} + Cl^{-} + O_2$	$1.20 \cdot 10^{10}$	29
59	$O_2^{-\bullet} + HClO = ClOH^{-} + O_2$	$7.50 \cdot 10^{6}$	29
60	$H_2O_2 + Cl_2^{-} = HCl + HCl + O_2^{-\bullet}$	$1.40 \cdot 10^{5}$	29,45
61	$H_2O_2 + Cl_2 = HO_2^{\bullet} + Cl_2^{-} + H^{+}$	$1.90 \cdot 10^{2}$	29
62	$H_2O_2 + HClO = HCl + H_2O + O_2$	$1.70 \cdot 10^{5}$	29
63	$OH^{-} + Cl_2^{-} = ClOH^{-} + Cl^{-}$	$9.04 \cdot 10^{6}$	46
64	$OH^{-} + Cl_2 = HClO + Cl^{-}$	$6.00 \cdot 10^{8}$	47
65	$H^{+} + ClOH^{-} = Cl^{\bullet} + H_2O$	$6.80 \cdot 10^{10}$	41
66	$H_2O + Cl_2O_2 = HClO + ClO_2^{-} + H^{+}$	$2.00 \cdot 10^{2}$	29

67	$H_2O + Cl_2O_2 = O_2 + HClO + HCl$	$0.00 \cdot 10^{0}$	29
68	$H_2O + Cl_2O = HClO + HClO$	$1.00 \cdot 10^{2}$	29
69	$H_2O + Cl_2O_4 = ClO_2^- + ClO_3^- + H^+ + H^+$	$1.00 \cdot 10^{2}$	29
70	$H_2O + Cl_2O_4 = HClO + HCl + O_4$	$1.00 \cdot 10^{2}$	29
71	$O_4 = O_2 + O_2$	$1.00 \cdot 10^{5}$	29
72	$Cl^- + Cl^\bullet = Cl_2^{-\bullet}$	$2.10 \cdot 10^{10}$	29,41
73	$Cl^- + ClOH^- = Cl_2^- + OH^-$	$2.93 \cdot 10^{3}$	46
74	$Cl^- + HClO = Cl_2 + OH^-$	$3.60 \cdot 10^{3-}$	48
75	$Cl^- + Cl_2 = Cl_3^-$	$2.00 \cdot 10^{4}$	49
76	$ClOH^- = OH + Cl^-$	$6.10 \cdot 10^{9}$	29,41
77	$Cl_2^{-\bullet} = Cl^\bullet + Cl^-$	$1.10 \cdot 10^{5}$	29,41
78	$Cl_2^{-\bullet} + Cl_2^{-\bullet} = Cl_3^- + Cl^-$	$5.15 \cdot 10^{8}$	50
79	$Cl_3^- = Cl_2 + Cl^-$	$1.10 \cdot 10^{5}$	49
80	$ClO + ClO = Cl_2O_2$	$1.50 \cdot 10^{10}$	29
81	$ClO_2 + ClO_2 = Cl_2O_4$	$1.00 \cdot 10^{2}$	29
82	$Cl_2O_2 + ClO_2^- = ClO_3^- + Cl_2O$	$1.00 \cdot 10^{2}$	29
83	$e^- + ClO_3^- = ClO_3^{2-}$	$1.60 \cdot 10^{5}$	51
84	$ClO_3^{2-} + OH^\bullet = OH^- + ClO_3^-$	$1.00 \cdot 10^{10}$	51
85	$ClO_3^{2-} + O^{-\bullet} = OH^- + ClO_3^- - H^+$ *(C)*	$1.20 \cdot 10^{9}$	51
86	$HClO + HClO = Cl^- + ClO_2^- + H^+ + H^+$	$6.00 \cdot 10^{9-}$	52,53
87	$ClO_2^- + HClO = Cl^- + ClO_3^- + H^+$	$9.00 \cdot 10^{7-}$	52,53
88	$HClO + HClO = O_2 + HCl + HCl$	$3.00 \cdot 10^{10-}$	54
89	$H_2D = H_2$	$1.33 \cdot 10^{3}$	*
90	$O_2D = O_2$	$1.09 \cdot 10^{3}$	*
91	$HClO + Cl^- = Cl_2 + H_2O - H^+$	$9.00 \cdot 10^{3}$	55
92	$Cl_2 = HClO + Cl^- + H^+ - H_2O$ *(C)*	$1.50 \cdot 10^{1}$	55
93	$Cl_2^- + H_2 = H^\bullet + HCl + Cl^-$	$4.30 \cdot 10^{5}$	11

** Kinetic rates for desorbed H_2 (H_2D) and O_2 (O_2D) (from the solution to the gas phase), are obtained from Henry's law.*

Despite the use of gas sampling devices, the experimental system is considered as an open system. The gas sampling devices were changed for new ones in every sampling, avoiding an accumulation of the gas and overpressure in the system. Therefore the species desorbed from the solution H_2D and O_2D will not interact with any chemical reaction.

The experiments were performed at two different ionic strength 0.05 and 5 mol·dm^{-3} NaCl. For each ionic strength the constants in table 7.2 were corrected using the Brönsted-Bjerrum equation[56-59]:

$$\log k = \log k_0 + 1.02 \times z_A \times z_B \times \frac{\sqrt{S}}{1+\sqrt{S}} \quad (1)$$

Where k is the rate constant (dm^3·mol^{-1}·s^{-1}), k_0 is the rate constant at zero ionic strength (dm^3·mol^{-1}·s^{-1}), z_A and z_B are the charge number of the ions involved and S the ionic strength in mol·dm^{-3}.

The formation rate of primary radiolytic species or G-value is also depending on the ionic strength of the media. In our experiments the ionic strength has been set using NaCl. The cation Na^+ is quite radiation chemically inactive but the anion Cl^- reacts with the radicals, oxidizing them.

Most of the data related to the G-values come from experiments with gamma radiation. G-values coming from alpha-hydrolysis experiments are difficult to find and must be deduced. The G-values used in the model are in table 7.3.

Table 7.3. Alpha radiation chemical primary yields (G-values) used in the model.

Species	**0.05 mol·dm^{-3} NaCl**	**5 mol·dm^{-3} NaCl**
H_2O_2	0.98	0.23
HO_2	0.22	0.05
H_2	1.30	1.52
$H^{\bullet}$	0.21	0.26
e^-_{aq}	0.06	0.06
$OH^{\bullet}$	0.25	0.06
OH^-	0	1.01
H^+	0.06	0
Cl^-	0	-1.62
$Cl_2^{-\bullet}$	0	0
$ClOH^-$	0	0.55
HClO	0	1.07
H_2O	-2.65	-3.25

Several simulations were run changing the values of the kinetic constants and the G-values, and the concentration of species O_2, H_2, O_2D and H_2D, was compared. The effect of multiplying the kinetic constants for 0.1 and 10 respectively is negligible for the majority of reactions. Of course it implies a change of more than 10% for the reactions 35, 36, 89 and 90, but apart from those only in reactions 46 and 52 a change between 0.5% and 5% was reported. Regarding the G-values a change of more than 10% is reported when multiplying the G-values of species H_2O_2, H_2, $H^{\bullet}$, $OH^{\bullet}$, $HO_2^{\bullet}$ and HClO for 0.1 and 10 respectively.

Using the values of kinetic constants in table 7.2 and varying the G-value of the species $OH^{\bullet}$, from 0.05 to 0.4 and 1.5, the model was compared with the experimental values (Figures 7.3 to 7.6). As can be seen in figures 7.3-7.6, the model produces a good simulation of what happened experimentally. Depending on the G-value of the species $OH^{\bullet}$, the model fits better for the experiments in the lower dose range or for the experiments with doses higher than 40 kGy.

Being the production of hydrolysis gas, a safety concern in the spent fuel storage, this model can be used to predict possible overpressures in closed systems, avoiding accidents.

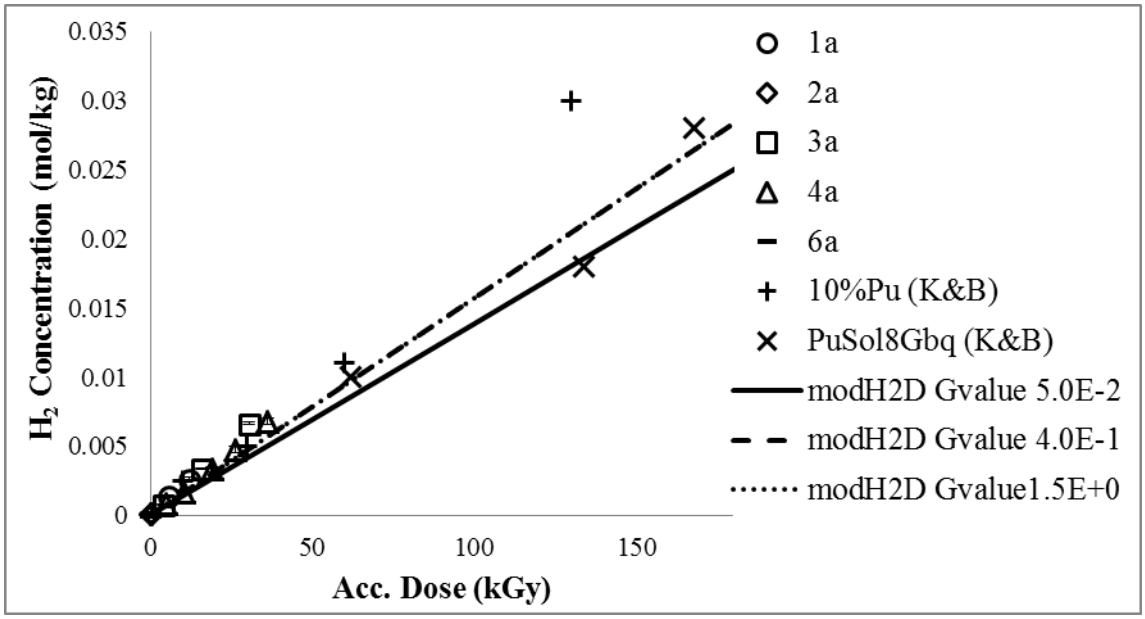

Figure 7.3. H_2 production. (K&B : Kelm and Bohnert [11]). $OH^{\bullet}$ g-value varies from 0.05 to 1.5.

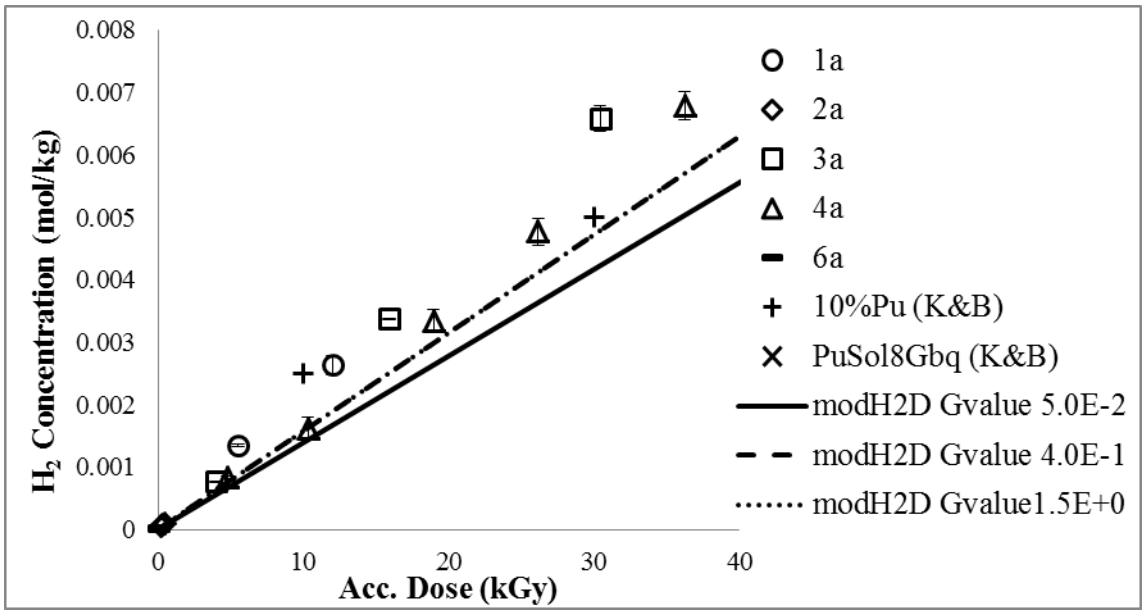

Figure 7.4. H_2 production. (K&B : Kelm and Bohnert [11]). $OH^{\bullet}$ g-value varies from 0.05 to 1.5.

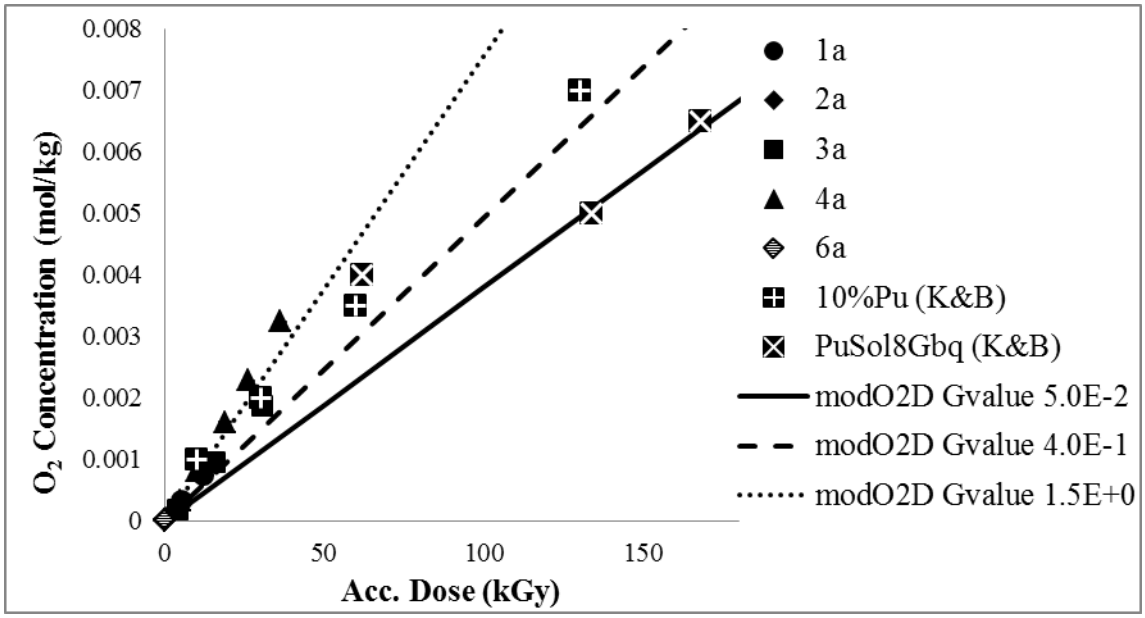

Figure 7.5. O_2 production. (K&B : Kelm and Bohnert [11]). $OH^{\bullet}$ g-value varies from 0.05 to 1.5.

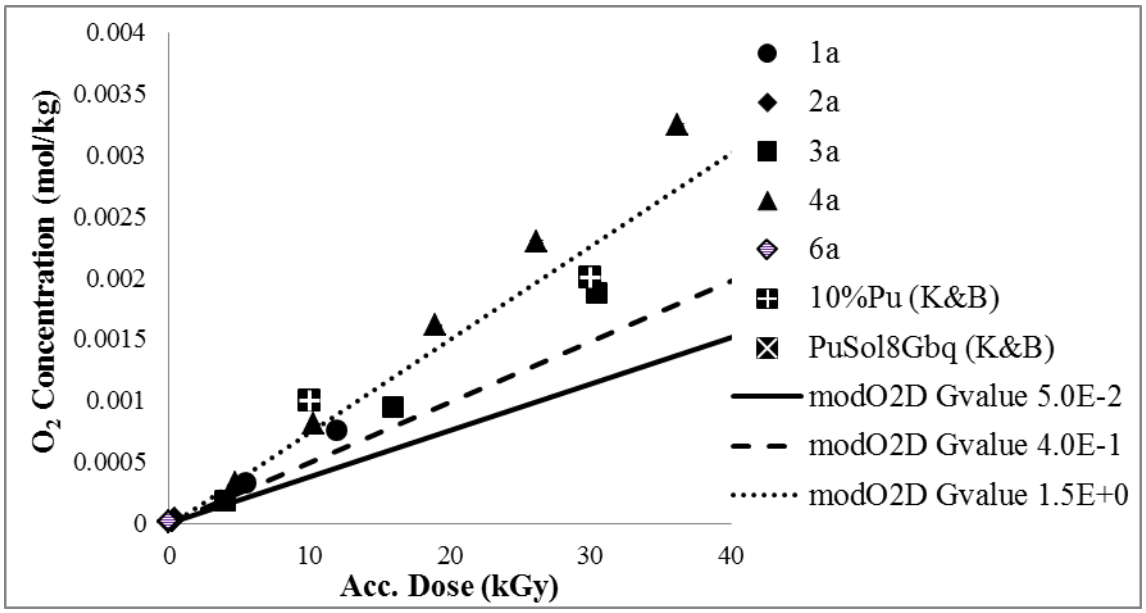

Figure 7.6. O_2 production. (K&B : Kelm and Bohnert [11]). $OH^{\bullet}$ g-value varies from 0.05 to 1.5.

7.4. CONCLUSIONS

Ten different radiolysis experiments were carried out with different sampling systems, alpha-doping and ionic strength with the objective of observing the effect of different experimental conditions on the radiolysis products formation and the dissolution of U and Pu.

The results obtained on H_2 and O_2 formation, at a dose rate below 40 KGy, for different ionic strengths, are in well agreement with those achieved by Kelm and Bohnert [11].

The situation of the alpha-emitters (inside the pellet or in solution) doesn't affect the gas production under the experimental conditions.

The production of H_2 and O_2 in the experiment with an ionic strength of 0.05 $mol \cdot dm^{-3}$ NaCl is similar to those obtained with an ionic strength of 5 $mol \cdot dm^{-3}$ NaCl.

Production of HClO is observed in experiments with 5 $mol \cdot dm^{-3}$ NaCl ionic strength and H_2O_2 generation is seen in experiments with 0.05 $mol \cdot dm^{-3}$ NaCl.

Due to low dose rate in experiments 2a, 2b, 6a and 6b the radiolysis products formation is also very low.

Uranium release becomes higher when the dose rate is increased.

The software Macksima-Chemist was used to model the experimental data, obtaining a good simulation in the studied accumulated dose range in the formation of O_2, an especially at accumulated doses higher than 40 kGy in the formation of H_2. The model was proved, on one hand, to be robust when changing the values of the kinetic constants but, on the other hand, sensitive to the changes of most of the G-values.

7.5. REFERENCES

1 P. Carbol, D.H. Wegen, T. Wiss and P. Fors. (2012). Spent Fuel as Waste Material. IN: (Konings, R. J. M., ed.) Comprehensive Nuclear Materials. **5** 389-420 *Elsevier, Amsterdam, Netherlands*.

2 V. Metz, B. Kienzler and W. Schüßler. (2003). Geochemical evaluation of different groundwater–host rock systems for radioactive waste disposal. *Journal of Contaminant Hydrology*, **61**, 265-279.

3 V. Metz, H. Geckeis, E. González-Robles, A. Loida, C. Bube and B. Kienzler. (2012). Radionuclide behaviour in the near-field of a geological repository for spent nuclear fuel. *Radiochimica Acta*, **100**, 699-713.

4 J.F. Lucchini, M. Borkowski, J. Swanson, D. Cleveland, M.K. Richmann and D.T. Reed. (2013). Salt Formations, a Safe Place for Transuranic Waste Disposal. *Transactions of the American Nuclear Society*, **108**, 16-20, 149-150.

5 J.F. Lucchini, M. Borkowski, M.K. Richmann, S. Ballard and D.T. Reed. (2007). Solubility of Nd^{3+} and UO_2^{2+} in WIPP brine as oxidation-state invariant analogs for plutonium. *Journal of Alloys and Compounds* **444-445** 506-511.

6 H.A. Schwarz. (1981). Free radicals generated by radiolysis of aqueous solutions. *Journal of Chemical Education*. **58**, 2, 101.

7 T.A. Hu. (2012). Improved Model for Hydrogen Generation Rate of Radioactive Waste at the Hanford Site. *Nuclear Technology*, **178** (1), 39-54.

8 M. Kelm. and E. Bohnert. (2004). A kinetic model for the radiolysis of chloride brine, its sensitivity against model parameters and a comparison with experiments. *Forschungszentrum Karlsruhe Wissenschaftliche Berichte FZKA*, 6977, 60.

9 T.E. Eriksen, D.W. Shoesmith and M. Jonsson. (2012). Radiation induced dissolution of UO_2 based nuclear fuel—a critical review of predictive modelling approaches. *Journal of Nuclear Materials*, **420**, 409-423.

10 M. Kelm, I. Pashalidis. and J.I. Kim. (1999). Spectroscopic investigation on the formation of hypochlorite by alpha radiolysis in concentrated NaCl solutions. *Applied Radiation and Isotopes*, **51**, 637-642.

11 M. Kelm and E. Bohnert. (2002). Radiolysis and corrosion of ^{238}Pu-doped UO_2 pellets in chloride brine. *Proc. Indian Acad. Sci. (Chem. Sci.)*, **114**, 697-704.

12 M.M. Hossain and M. Jonsson. (2008). Effects of ionic strength on the kinetics for UO_2 oxidation. *Journal of Nuclear Materials*, **373**, 190-193.

13 O. Roth, H. Hasselberg and M. Jonsson. (2009). Radiation chemical synthesis and characterization of UO_2 nanoparticles. *Journal of Nuclear Materials*, **383**, 231-236.

14 J. Giménez, E. Baraj, M.E. Torrero, I. Casas and J. de Pablo. (1996). Effect of H_2O_2, NaClO and Fe on the dissolution of unirradiated UO_2 in NaCl 5 mol kg^{-1}. Comparison with spent fuel dissolution experiments. *Journal of Nuclear Materials*, **238**, 64-69.

15 F. Clarens, J. de Pablo, I. Casas, J. Giménez, M. Rovira, J. Merino, E. Cera, J. Bruno, J. Quiñones and A. Martínez-Esparza. (2005). The oxidative dissolution of unirradiated UO_2 by hydrogen peroxide as a function of pH. *Journal of Nuclear Materials*, **345**, 225-231.

16 I. Casas, J. de Pablo, F. Clarens, J. Giménez, J. Merino, J. Bruno and A. Martínez-Esparza. (2009). Combined effect of H_2O_2 and HCO_3^- on UO_2(s) dissolution rates under anoxic conditions. *Radiochimica Acta*, **97**, 485-490.

17 F.N. Smith, S.I. Sinkov, C.Z. Soderquist, R.S. Wittman, A.R. Geanes, B.K. McNamara and E.C. Buck. (2013). Spectroscopic Detection of Hydrogen Peroxide Generated by Alpha Radiolysis in Solution. *14th International High-Level Radioactive Waste Management Conference, IHLRWMC 2013: Integrating Storage, Transportation, and Disposal*, 2, 679-684.

18 C. Ekberg, E. Aneheim, A. Fermvik and G. Skarnemark. (2010). Using ^{211}At as internal alpha radiolysis source allowing for simple detection of radiolysis products. *Radiation Physics and Chemistry* **79** 454-456.

19 G. Guimbretière, A. Cañizares, P. Simon, Y. A. Tobon-Correa, M.R. Ammar, C. Corbel and M.F. Barthe. (2011). In-Situ Raman Observation of the First Step of Uranium Dioxide Weathering Exposed to Water Radiolysis. *Spectroscopy Letters*, **44** (7-8) 570-573.

20 F. Crumière, J. Vandenborre, R. Essehli, G. Blain, J. Barbet and M. Fattahi. (2013). LET effects on the hydrogen production induced by the radiolysis of pure water. *Radiation Physics and Chemistry* **82** 74-79.

21 B. Muzeau, C. Jégou, F. Delaunay, V. Broudic, A. Brevet, H. Catalette, E. Simoni and C. Corbel. (2009). Radiolytic oxidation of UO_2 pellets doped with alpha-emitters ($^{238/239}$Pu). *Journal of Alloys and Compounds*, **467**, 578-589.

22 D. Cui, E. Ekeroth, P. Fors and K. Spahiu. (2008). Surface Mediated Processes in the Interaction of Spent Fuel or alpha-doped UO_2 with H_2. *Materials Research Society Symposium Proceedings*, **1104**, 112-124.

23 M. Kelm. and E. Bohnert. (2005). Gamma radiolysis of NaCl brine: Effect of dissolved radiolysis gases on the radiolytic yield of long-lived products. *Journal of Nuclear Materials*, **346**, 1-4.

24 V. Metz, E. Bohnert, M. Kelm, D. Schild, J. Reinhardt, B. Kienzler and M.R. Buchmeiser. (2007). γ-Radiolysis of NaCl Brine in the Presence of UO_2(s): Effects of Hydrogen and Bromide. *Materials Research Society Symposium Proceedings* **985** 33-40.

25 V. Metz, A. Loida, E. Bohnert, D. Schild and K. Dardenne. (2008). Effects of hydrogen and bromide on the corrosion of spent nuclear fuel and γ-irradiated UO_2(s) in NaCl brine. *Radiochimica Acta* **96** (9-11) 637-648.

26 V.V. Rondinella, H. Matzke, J. Cobos and T. Wiss. (1999). α-Radiolysis and α-Radiation Damage Effects on UO_2 Dissolution Under Spent Fuel Storage Conditions. *Materials Research Society Symposium Proceedings*, **556**, 447.

27 M. Carver, D. Hanley, N. Ross and C. Austin. (1979), MACKSIMA-CHEMIST, Mass Action Chemical Kinetics Simulation – Automatic Chemical Equation Manipulation and Integration Using Stiff, Sparse Techniques, AECL – 6413. Revised by J. Paquette (1987).

28 Thomas, J.K. (1965), The nature of the reducing species in the radiolysis of acidic aqueous solutions at high intensities. *The International Journal Of Applied Radiation And Isotopes*, **16**, 8, 451-456.

29 S. Sunder, H. Christensen. (1993), Gamma Radiolysis of Water Solutions Relevant to the Nuclear Fuel Waste Management Program. *Nuclear Technology*, **104**, 3, 403-417,.

30 Matheson, M. S. & Rabani, J. (1965), Pulse Radiolysis of Aqueous Hydrogen Solutions .I. Rate Constants for Reaction of Eaq- with Itself and Other Transients. 2. Interconvertibility of Eaq- and H. *J. Phys. Chem*. **69**, 1324.

31 T. Lundström, H. Christensen and K. Sehested. (2002), The reaction of OH with H at elevated temperatures. *Radiation Physics and Chemistry*, **64** 1, 29-33.

32 T. Lundström. (2003), radiation chemistry of aquous solutions related to nuclear reactor systems and spent fuel management. *PhD thesis Linköping University, Sweden*.

33 H. Christensen and K Sehestedt. (1983), Reaction of hydroxyl radicals with hydrogen at elevated temperatures. Determination of the activation energy. *Journal of Physical Chemistry*, **87**, 1 118-120.

34 D. Zehavi and J. Rabani. (1971), Pulse radiolytic investigation of Oaq- radical ions. *The Journal of Physical Chemistry*. **75**, 11, 1738-1744.

35 Buxton G.V.; Greenstock C.L.; Helman W.P. and Ross A.B. (1988), Critical-Review of Rate Constants for Reactions of Hydrated Electrons, Hydrogen-Atoms and Hydroxyl Radicals (•OH/•O–). *Aqueous-Solution Journal of Physical and Chemical Reference Data*, **17**, 513-886.

36 Jha, K.N., Bolton, G.L. and Freeman, G.R. (1972), Temperature shifts in the optical spectra of solvated electrons in methanol and ethanol. *Journal of Physical Chemistry*, **76**, 25, 3876-3883.

37 Sehested, K., Christensen, H. (1990), The rate constant of the biomolecular reaction of hydrogen atoms at elevated temperatures. *Radiation Physics and Chemistry*. **36**, 3, 499-500.

38 B.G. Ershov, A.V. Gordeev, M. Kelm, E. Janata. (2003), Rate constant for the reaction of the H atom with H_2O_2 in aqueous solution. *Radiat. Phys Chem*. **67**, 613-616.

39 Eigen, M. and de Maeyer, L. (1955), Die Geschwindigkeit der Neutralisationsreaktion. *Die Naturwissenschaften*. **42**, 14, 413-414.

40 Buxton, G.V., Sellers, R.M. (1987), Reactivity of the hydrated electron and the hydroxyl radical with boric acid in aqueous solutions. *Radiation Physics and Chemistry*, **29**, 2, 137-140.

41 G.G. Jayson, B.J. Parsons and A.J. Swallow. (1973), Some Simple, Highly Reactive, Inorganic Chlorine Derivatives in Aqueous Solution. *J. Chem. Soc., Faraday Trans*. **1**, 69, 1597-1607.

42 Lierse, C., Sullivan, J.C., Schmidt, K.H. (1987), Rates of oxidation of selected actinides by Cl_2^-. *Inorganic Chemistry*, **26**, 9, 1408-1410.

43 Navaratnam, S., Parsons, B.J., Swallow, A.J. (1980), Some reactions of the dichloride anion radical. *Radiation Physics and Chemistry*, **15**, 2-3, 159-161.

44 Gogolev, A.V.; Makarov, I.E.; Pikaev, A.K. (1984), Pulsed radiolysis of concentrated hydrochloric acid. *High Energy Chem*. **18**(6): 390-5.

45 Hasegawa, K. and Neta, P. (1978), Rate constants and mechanisms of reaction of Cl2- radicals. *J. Phys. Chem*. **82**(8): 854-7.

46 Grigorev, A.E.; Makarov, I.E. and Pikaev, A.K. (1987), Formation of Cl_2^- in the bulk solution during the radiolysis of concentrated aqueous solutions of chlorides. *High Energy Chem*. **21**(2): 99-102.

47 J.T. Jayne, C.E. Kolb. (2002), Rate Constant for the Reaction of Cl_2(aq) with OH-. *J.Phys.Chem.A*, **106**, 7748-7754.

48 M. Gershenzon, P. Davidovits, J. T. Jayne, C. E. Kolb, and D. R. Worsnop. (2002), Rate Constant for the Reaction of Cl_2(aq) with OH-.*J. Phys. Chem. A*, **106**, 7748-7754.

49 Ershov, B.G., Kelm, M. , Janata, E., Gordeev, A.V., Bohnert, E. (2002) Radiation-chemical effects in the near-field of a final disposal site: Role of bromine on the radiolytic processes in NaCl-solutions. *Radiochimica Acta*. **90**, 9-11, 617-622.

50 Kelm, M., Metz, V. , Bohnert, E., Janata, E. and Bube, C. (2011), Interaction of hydrogen with radiolysis products in NaCl solution - comparing pulse radiolysis experiments with simulations. *Radiation Physics and Chemistry*. **80**, 3, 426-434.

51 Ershov, B.G., Kelm, M., Janata, E. (2000), Pulse radiolysis studies of the reactions of e(aq)- and .OH with ClO_3^- ions in aqueous solution. *Radiation Physics and Chemistry*. **59**, 3, 1, Pages 309-312.

52 M.W.Lister. (1956), Decomposition of Sodium Hypochlorite: The Uncatalyzed Reaction. *Can. J. Chem*. **34**, 465-478.

53 M.W.Lister. (1956), Decomposition of Sodium Hypochlorite: The catalyzed Reaction. *Can. J. Chem*. **34**, 479-488.

54 M.W. Lister, R.C. Petterson. (1962), Oxygen Evolution from Sodium Hypochlorite Solutions. *Can. J. Chem*. **40**, 729-733.

55 T.X. Wang, D.W. Margerum, (1994). Kinetics of reversible Chlorine Hydrolysis: Temperature Dependence and General - Acid/Base - Assisted Mechanism. *Inorg. Chem*. **33**, 1050-1055.

56 Brönsted, J.N. (1922). Zur Theorie der chemischen Reaktionsgeschwindigkeit. *Z. Phys. Chem.* **102**, 169.

57 Brönsted, J.N. (1925). Zur Theorie der chemischen Reaktionsgeschwindigkeit II. *Z. Phys. Chem.* **115**, 337.

58 Bjerrum, N. (1924). Zur Theorie der chemischen Reaktionsgeschwindigkeit. *Z. Phys. Chem.* **108**, 82.

59 Bjerrum, N. (1926). Zur Theorie der chemischen Reaktionsgeschwindigkeit II. *Z. Phys. Chem.* **118**, 251.

8 Incorporation of Selenium(IV) and Selenium(VI) on Uranyl Peroxide Studtite and Determination of its Point of Zero Charge

8 Incorporation of Selenium(IV) and Selenium(VI) on Uranyl Peroxide Studtite and Determination of its Point of Zero Charge

8.1. INTRODUCTION

The uranyl peroxides studtite ($UO_2O_2 \cdot 4H_2O$) and metastudtite ($UO_2O_2 \cdot 2H_2O$) are the only peroxide minerals in nature [1] and might be formed as secondary solid phases during the oxidative dissolution of the UO_2 spent nuclear fuel (SNF) [2,3].

In addition, in the accident at Fukushima Daiichi in Japan large amounts of seawater got in contact with irradiated fuel. The intense radiation field of the fuel (including α-, β-decay and γ radiation) might cause changes in water composition, forming radiolytic species (O_2, H_2O_2, H_2, $OH^{\cdot}$, O_2^{-}, $HO_2^{\cdot}$, e^{-}, $H^{\cdot}$) [4,5] being hydrogen peroxide one of the main oxidant species [6]. Under these conditions, high uranium(VI) and high local hydrogen peroxide concentrations in solution, uranium peroxide clusters [7,8], as well as the uranyl peroxide solids could be formed [9]. These clusters might precipitate in the presence of alkali ions or remain in solution during months even in the absence of a source of hydrogen peroxide [10].

The formation of the uranyl peroxides on the SNF surface could become an effective barrier from retarding its corrosion process [5,11]. Studtite and metastudtite might have the capacity to incorporate transuranics and fission products into their structure, retarding their migration through the environment [12-15]. Studtite has shown an important sorption capacity for strontium [16] and cesium [17]. In both cases, sorption was higher at alkaline pH, due to both the predominance of the cationic form (Sr^{2+} or Cs^{+}) in solution and the pH_{pzc} of the studtite. Preliminary results showed that, on the contrary, selenium(VI) sorption is higher at acidic pH, which is likely due to the predominance of the SeO_4^{2-} anion in solution [18].

Selenium is an element of special concern in the nuclear fuel cycle, and it is one of the main radionuclides considered in the safety analysis of a High Level Nuclear Waste (HLNW) repository, because of the long half-life ^{79}Se isotope, which is chemically and radiologically toxic [19,20]. In addition to the toxicity of the ^{79}Se isotope, selenium is a highly mobile

element in oxidizing geochemical environments and may have a high impact on the cumulative radioactive dose if there is not a mechanism that might retard its transport through the geosphere [21].

The most probable mechanism for selenium retention in a HLNW repository is the sorption onto mineral phases formed onto the spent nuclear fuel (SNF) or mineral phases surrounding the repository [22-24]. In this sense, different studies have been carried out in order to evaluate the selenium sorption in different sorbents such as iron oxides, which might be formed as a product of the container corrosion. However, the possible retention of selenium onto the solid phases which might be formed in the near-field of the nuclear waste (in particular, the uranyl secondary solid phases formed on the surface of the SNF) has almost not been addressed, yet. Only Chen et al. [19] studied the possible incorporation of ^{79}Se into the structures of different uranium phases such as uranyl oxide hydrates, uranyl silicates, uranyl phosphates, and uranyl carbonates, based on their crystal chemistry.

In the present work the point of zero charge of Studtite has been determined. This parameter is very useful to reveal the sorption mechanism and it is also decisive in chemical phenomena like for example coagulation, interaction between particles in colloidal suspensions and electrochemical phenomena [25, 26].

It is also an important objective of this work to determine the studtite sorption capacity for selenium(IV) and selenium(VI) by means of kinetic and equilibrium experiments. According to the results obtained, the actual role of uranyl peroxides sorption capacity on the selenium released from the spent nuclear fuel will be evaluated.

8.2. EXPERIMENTAL

8.2.1. Solid phase

$UO_2O_2 \cdot 4H_2O(s)$ was precipitated by mixing a uranyl nitrate solution with a hydrogen peroxide solution according to the experimental methodology previously developed [16], based on the reaction:

$$UO_2^{2+} + H_2O_2 + 4\ H_2O \leftrightarrows UO_2O_2 \cdot 4H_2O(s) + 2\ H^+ \qquad K = 7.7 \cdot 10^2 \qquad (1)$$

The yellow powdered solid obtained was dried and characterized as pure studtite by X-ray diffraction spectroscopy (XRD, Bruker D5005). The surface area of the solid was determined by the BET method using a Micromeritics Flowsorb II 2300 instrument. The value obtained was $13.43 \pm 0.01\ m^2/g$.

The solid was also characterized by XRD at the end of the experiments because of the possible transformation of studtite to metastudite ($UO_2O_2 \cdot 2H_2O$) or schoepite ($UO_2(OH)_2 \cdot xH_2O$) [16,17]. The results showed that studtite was stable and no significant phase transformation took place during the experiments.

8.2.2. Point of zero charge determination methodology

For the determination of the point of zero charge of the studtite the immersion methodology was used [25,26]. Eleven solutions with different initial pH (adjusted with either $HClO_4$ or NaOH carbonate-free) and 0.1 $mol \cdot dm^{-3}$ $NaClO_4$ ionic strength were prepared. 0.05 g of studtite were added to each solution and the suspensions obtained were stirred during 24 h. The pH of the solutions was measured using a digital pHmeter Crison GLP22 calibrated with three different standards. Experiments were carried out in a glovebox with inert gas atmosphere.

8.2.3. Sorption experiments methodology

The study was carried out in batch experiments at 25.0±0.1 °C in a glovebox under nitrogen gas. A known amount of the solid (~0.05 g) was put in contact with 20 cm^3 of selenium solution in stoppered polystyrene tubes. The ionic medium was $NaClO_4$ 0.01 $mol \cdot dm^{-3}$. The tubes were continuously stirred in an end-over-end agitator. At different times samples were taken and filtered through 0.20 µm MICROPORE pore size filters. Selenium and uranium concentrations in solution were determined by ICP-MS (Agilent 7500 cx). The pH of the samples was measured before the contact with the solid and at equilibrium, by using a CRISON pH Meter GLP22. The initial pH was adjusted by addition of $HClO_4$ or NaOH when necessary.

The concentration of selenium attached to the solid in moles of Se per m^2 of dry solid, $\{Se\}_s$, was calculated by subtracting the final metal concentration, $[Se]_{eq}$ in $mol \cdot dm^{-3}$, to the initial concentration of metal added to the solution, $[Se]_0$ in $mol \cdot dm^{-3}$, and normalising with the surface area (SA) to volume (V) ratio:

$$\{Se\}_s = \left([Se]_0 - [Se]_{eq}\right) \cdot \frac{V}{SA} \qquad (2)$$

Three different series of experiments were carried out, with the objective to study sorption kinetics, sorption isotherms, and sorption variation with pH.

8.3. RESULTS AND DISCUSSION

8.3.1. Point of zero charge determination

The difference between the initial pH and the pH at equilibrium in each experiment allows the determination of the point of zero charge of the studtite. Both initial and equilibrium pH are shown in Table 8.1 and are represented as a function of initial pH in Figure 8.1. At pH lower than 4, the variation of the pH from the start of the experiment to the equilibrium is very low. However, from pH near 4, the variation of the pH during the experiment is much higher and increases with increasing pH. Because of this, Figure 8.1 is

presented as two different figures to facilitate its visualization. The immersion methodology establishes that the pH at which this difference of behavior occurs is the point of zero charge. According to this, from the experiments carried out in this work, and considering the linear fitting equations presented in Figure 8.1, the value of the pH_{pzc} obtained was 4.0±0.2, which is much more lower than the pH_{pzc} values of the different uranium oxides: UO_2 pH_{pzc}=7.7±0.4; U_3O_8 pH_{pzc}=7.8±0.5 [27] and for Schoepite pH_{pzc}= 6.5-7.1 [28]. A plausible hypothesis to explain this behavior could be that the protons bond to the peroxo-group are more easily released (more acid) than those bond to the oxo-group, as it is deduced from the different acidity of water ($Ka=10^{-14}$) and hydrogen peroxide ($Ka=10^{-11.3}$).

Table 8.1. pH values (±0.001) determined following the immersion methodology.

Initial pH	Equilibrium pH	|ΔpH|
2.056	2.083	0.027
2.429	2.447	0.018
3.032	3.050	0.018
3.560	3.564	0.004
3.971	4.027	0.056
4.083	3.947	0.136
4.837	4.489	0.348
4.872	4.196	0.676
6.077	4.279	1.798
8.529	4.345	4.184
9.169	4.887	4.282

The pH_{pzc} of studtite determined in the present work can be used to explain the sorption properties observed for this solid. In Figure 8.2, the sorption of cesium and strontium as a function of pH is shown together with the value of the pH_{pzc}. In both cases, sorption was deduced to be based on electrostatic interactions between the surface of the solid and the chemical species in solution. Cesium and strontium are found in solution only as the cation Cs^+ or Sr^{2+} and they would be preferentially sorbed on anionic surfaces. As it can be seen in Figure 8.2, their sorption increases from the value of the pH_{pzc}, due to the fact that at these pH values the surface of the studtite is negatively charged ($pH>pH_{pzc}$).

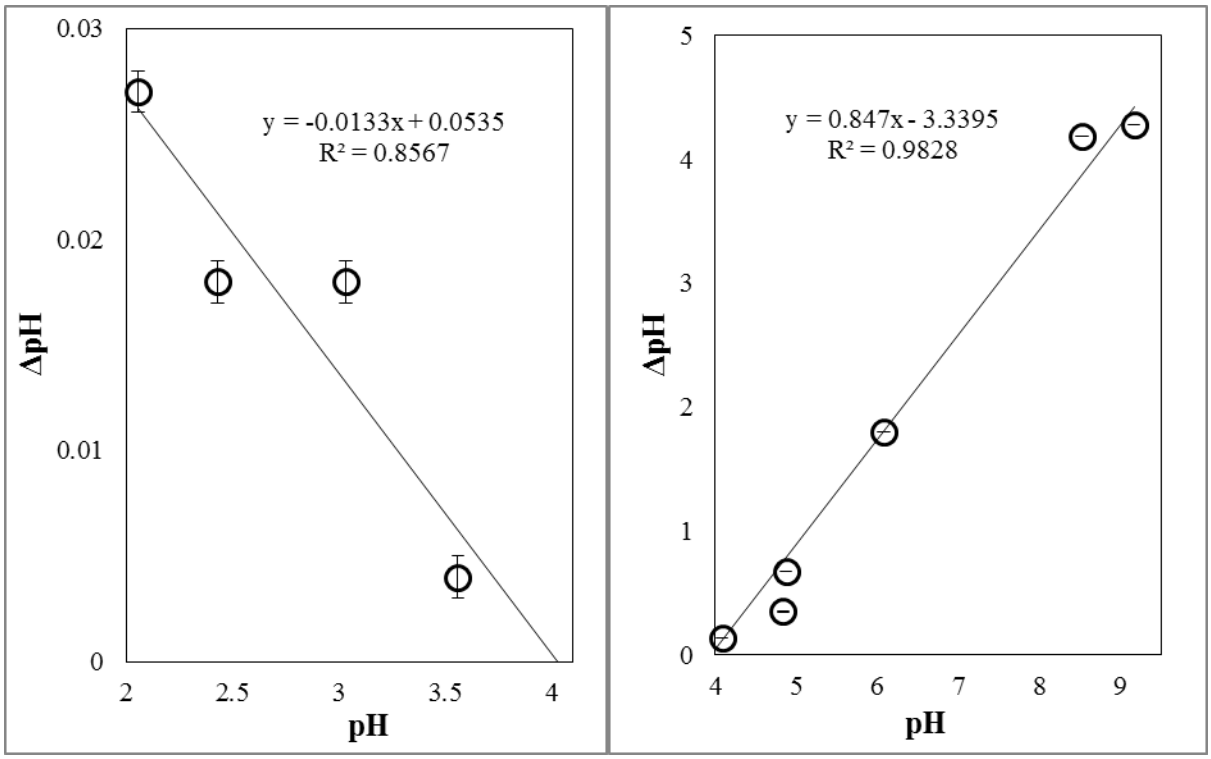

Figure 8.1.Variation of the pH in solution after the addition of 0.05 g of studtite.

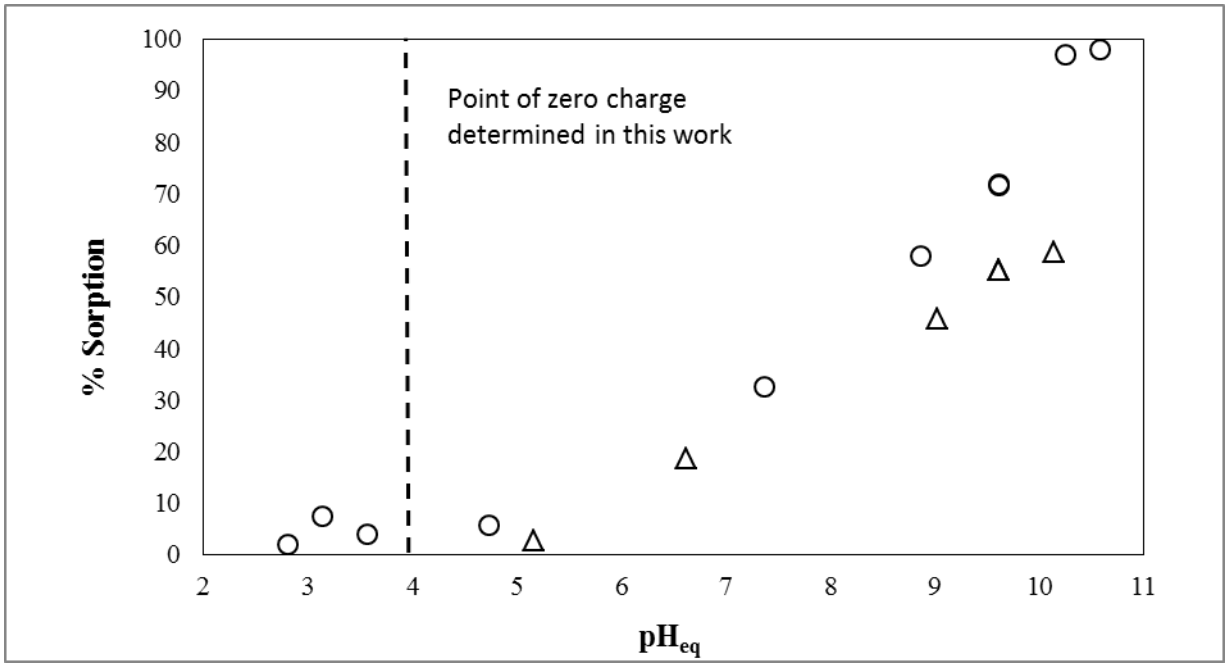

Figure 8.2. Studtite sorption capacity as a function of pH showing the value of the pH_{pzc} determined in this work. ○Strontium [16] ; △Cesium [17].

8.3.2. Selenium sorption as a function of time

The variation of Se(IV) and Se(VI) sorption as a function of time is shown in Figure 8.3, where it can be seen that after 20 h equilibrium is already reached for either Se(IV) and Se(VI). The percentage of sorption (as $100 \cdot [Se]_s/[Se]_0$) is relatively high (≈ 80%) for selenite and lower for selenate (≈ 20%).

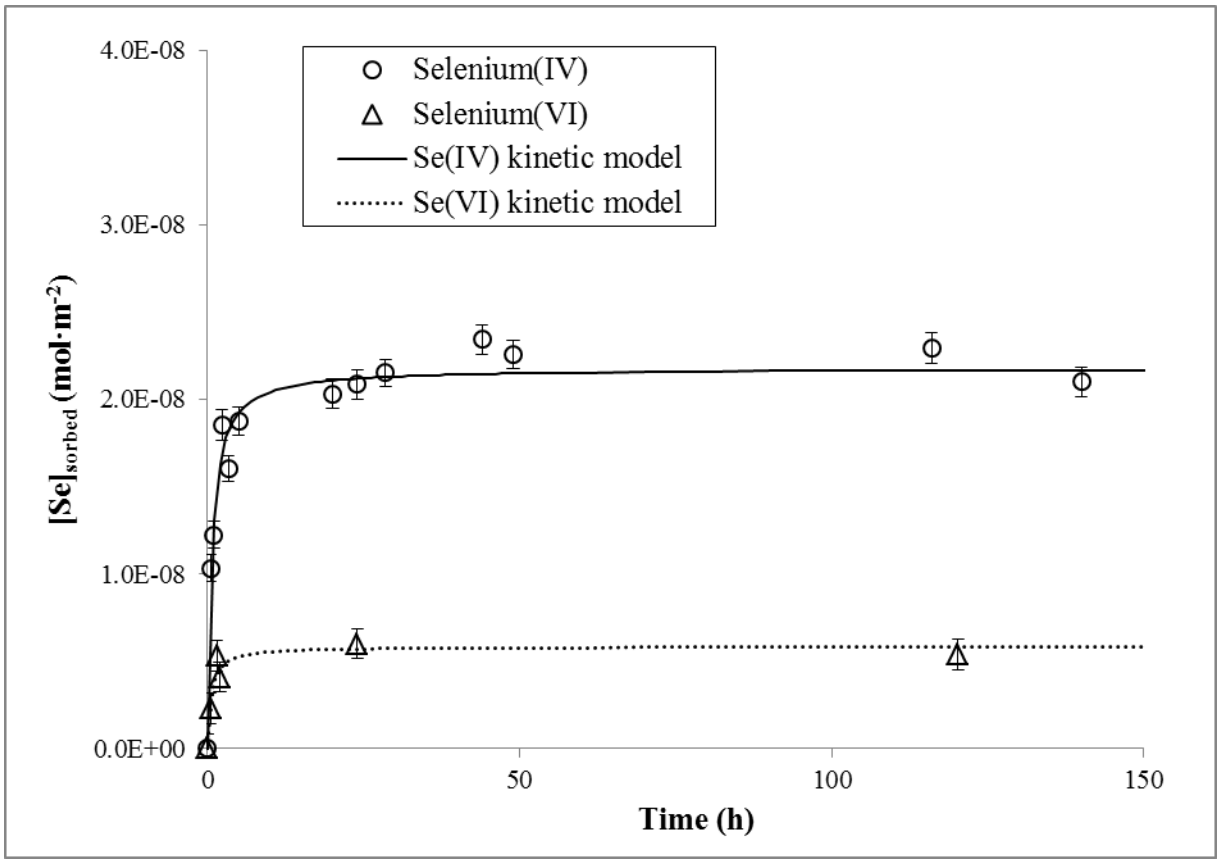

Figure 8.3. Variation of selenium(IV) and selenium(VI) sorbed onto studtite with time. The lines represent the fitting of the pseudo-second order reaction model to the experimental data. Experiments carried out with 0.05 g of studtite, $[Se(IV)]_0 = 9 \cdot 10^{-7}$ mol·dm^{-3}, and $[Se(VI)]_0 = 1.2 \cdot 10^{-6}$ mol·dm^{-3} in the presence of 0.01 mol·dm^{-3} $NaClO_4$ at pH=3.

The best fitting of the kinetic data has been obtained using a pseudo-second order rate equation [29], which has been widely used to describe metal or semimetal sorption on different sorbents [29,30]. The pseudo-second order kinetic rate equation is:

$$\frac{t}{\{Se\}_s} = \frac{1}{k \cdot \{Se\}_{s,eq}^2} + \frac{1}{\{Se\}_{s,eq}} t \qquad (3)$$

where $\{Se\}_{s,eq}$ is the amount of selenium sorbed at equilibrium (in $mol \cdot m^{-2}$), k is the rate constant of sorption (in $m^2 \cdot mol^{-1} \cdot s^{-1}$) and $\{Se\}_s$ is the amount of selenium sorbed on the surface of the solid (in $mol \cdot m^{-2}$) at any contact time, t (in s).

When the experimental data from Figure 8.3 were introduced into the equation 2, straight lines were obtained by plotting $t/\{Se\}_s$ against t, indicating that the process follows the pseudo-second order rate equation. The amount of selenium sorbed at equilibrium is 2.3 $(\pm 0.0) \cdot 10^{-8}$ $mol \cdot m^{-2}$ for selenite and 6.2 $(\pm 0.1) \cdot 10^{-9}$ $mol \cdot m^{-2}$ for selenate while the sorption rate constants are 9.2 $(\pm 3.5) \cdot 10^{3}$ $m^2 \cdot mol^{-1} \cdot s^{-1}$ and 6.4 $(\pm 2.3) \cdot 10^{4}$ $m^2 \cdot mol^{-1} \cdot s^{-1}$ for selenite and selenate, respectively (linear regression with R^2=0.9992 and R^2=0.9991 for selenium(IV) and selenium(VI), respectively).

Information about the sorption mechanism might be also deduced from the kinetic data. A simple intraparticle diffusion model was developed by Weber and Morris [31] and it could be used as a first approach for the description of the sorption processes on the studtite. The dependence of $\{Se\}_s$ with time is given by the following equation [32]:

$$\{Se\}_s = k_d \cdot \sqrt{t} + A \qquad (4)$$

where k_d is the intraparticle diffusion rate constant (in $mol \cdot m^{-2} \cdot s^{-1}$) and A (in $mol \cdot m^{-2}$) is a constant related to the thickness of the boundary layer. If the Weber–Morris plot of $\{Sr\}_s$ versus $\sqrt{t}$ gives a straight line, this means that the sorption process is only controlled by intraparticle diffusion. As it can be seen in Figure 8.4, the data exhibit two linear plots for both selenium(IV) and selenium(VI), what would indicate that two or more processes influence the sorption process and a possible diffusion in micropores of the studtite should not be discarded in addition to the intra-particle diffusion [33].

a)

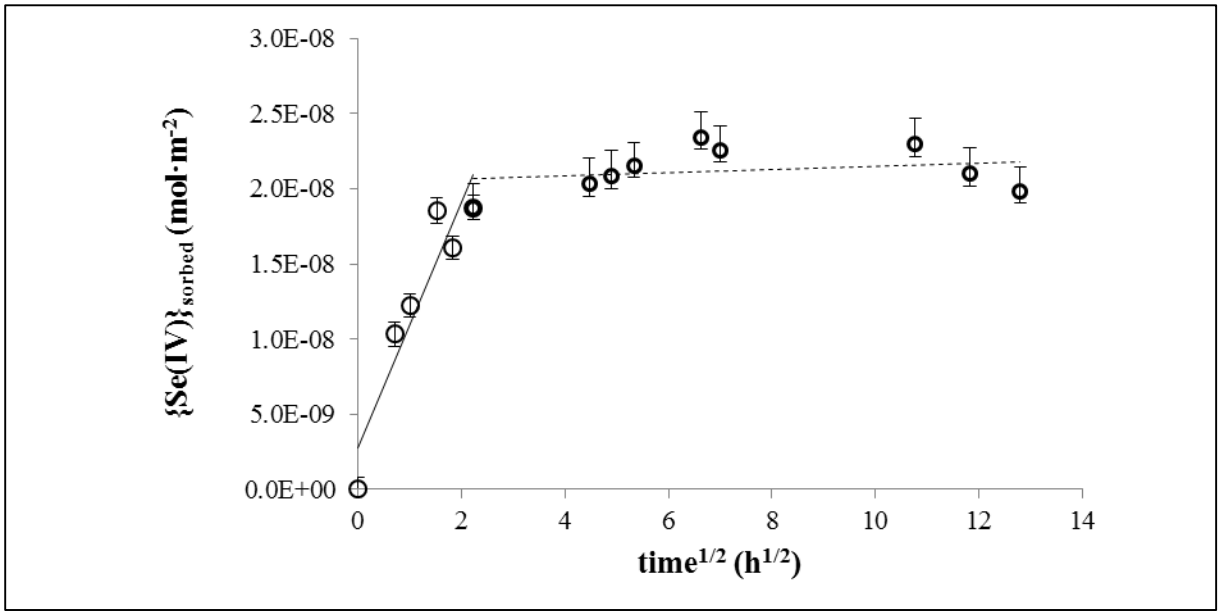

b)

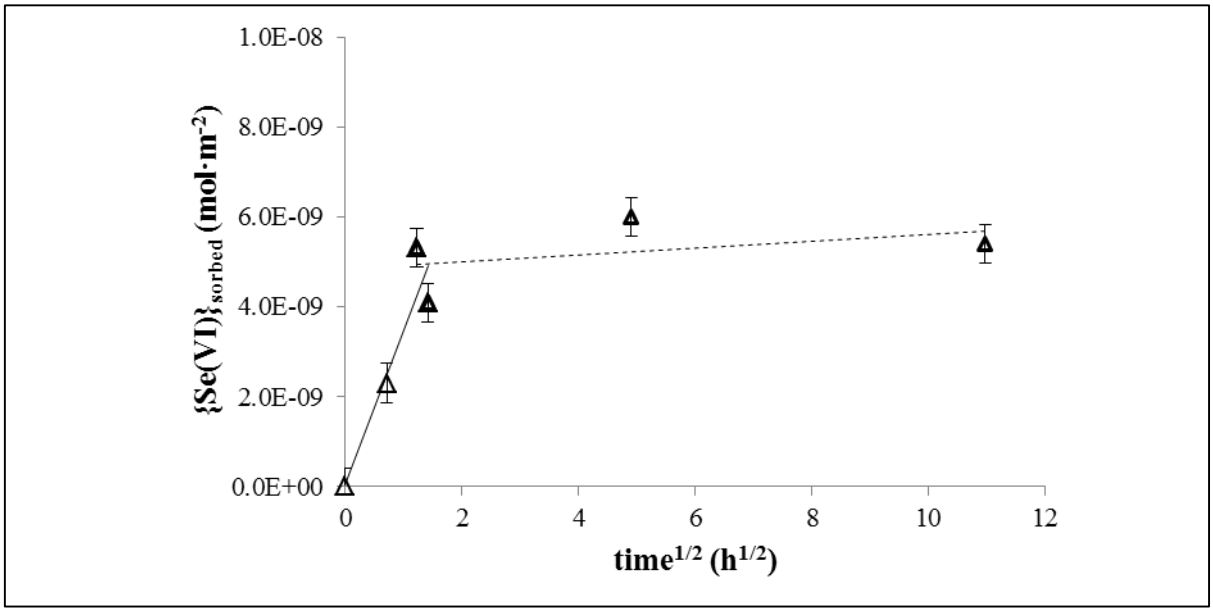

Figure 8.4. Fitting of the Weber and Morris model to the experimental data obtained for (a) Selenium(IV), and (b) selenium(VI).

As it can be seen in Figure 8.3, sorption is relatively fast under the experimental conditions; equilibrium is reached in approximately 1 day, which will be the time used for equilibration in the subsequent experiments. In addition, the low time needed for equilibration indicates that the sorption of selenium released from the spent nuclear fuel would not be retarded by the kinetics of the process.

8.3.3. Isotherms of selenium sorption on studtite

In order to determine the maximum sorption capacity of the solid as well as to have information on the mechanism of selenium interaction with the solid, the variation of the selenium sorbed on studtite as a function of the selenium equilibrium concentration in solution has been determined. The results obtained for Se(IV) and Se(VI) at 0.01 $mol \cdot dm^{-3}$ ionic strength are shown in Figure 8.5. As it can be seen, in both cases the selenium sorbed on studtite increases with selenium in solution until a certain value, which indicates that all the active sites on the solid surface are occupied. At even higher selenium concentrations in solution there is not an increase of the sorption because of the lack of available active sites on the solid.

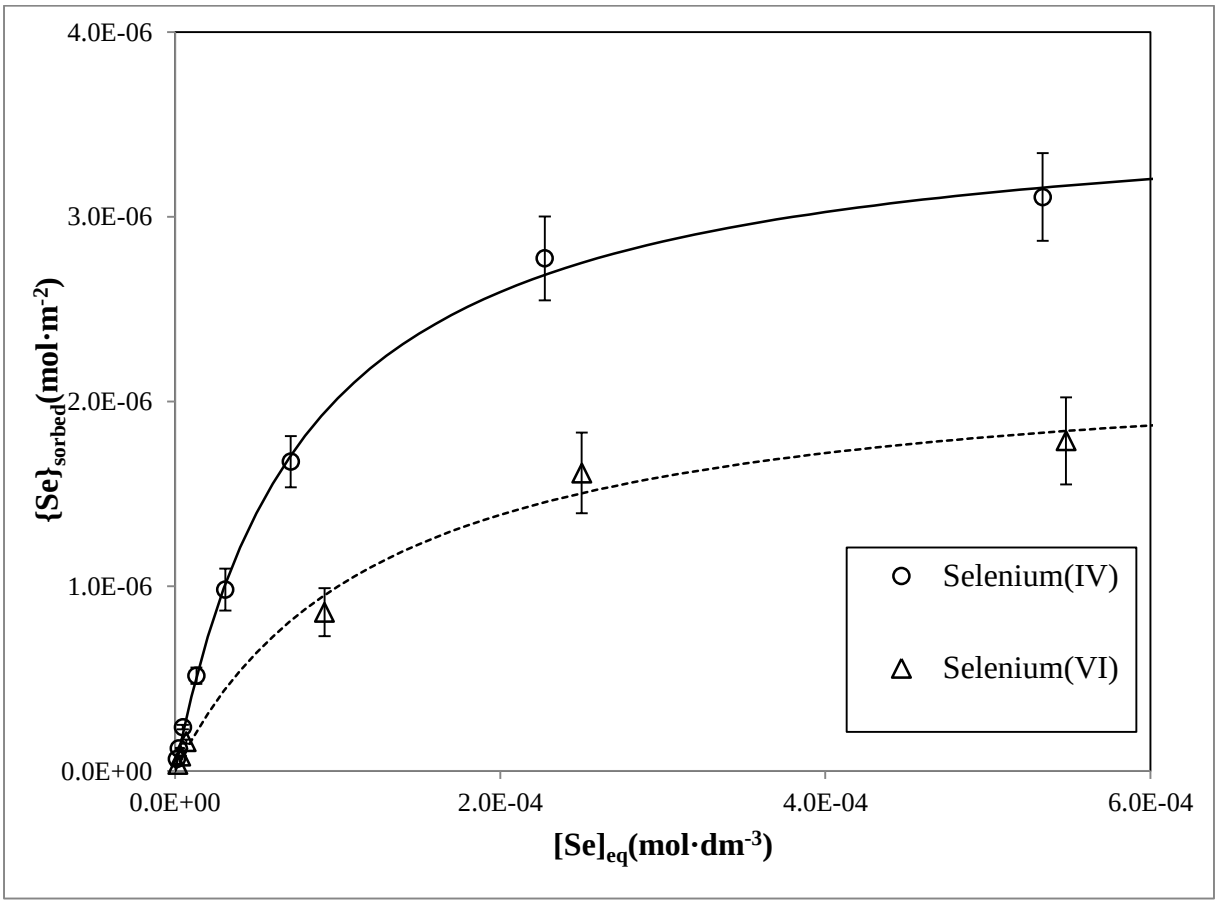

Figure 8.5. Variation of selenium(IV) and selenium(VI) sorbed onto studtite as a function of equilibrium selenium concentration in solution. The lines represent the fitting of the Langmuir model to the experimental data. Experiments carried out with 0.05 g of studtite, at 0.01 $mol \cdot dm^{-3}$ ionic strength and pH=3.

The data have been fitted with a non-competitive Langmuir isotherm, based on the following sorption equilibrium:

$$Se + >S \Leftrightarrow >S\text{-}Se$$

$$K_L = \frac{\{S-Se\}}{\{S\}\cdot[Se]} \quad (5)$$

where K_L is the Langmuir constant ($dm^3 \cdot mol^{-1}$), *{S-Se}* stands for the concentration of occupied surface sites and *{S}* for the free surface sites.

We can define the parameter gamma, Γ, as the selenium concentration sorbed on the studtite at equilibrium ($mol \cdot m^{-2}$):

$$\Gamma = \frac{\{S\text{-}Se\}}{\text{surface area}} \quad (6)$$

and, therefore:

$$\Gamma_{max} = \frac{\{S\}_{tot}}{\text{surface area}} \quad (7)$$

where Γ_{max} is the maximum selenium sorption ($mol \cdot m^{-2}$) and $\{S\}_{tot}$ stands for the total concentration of surface sites:

$$\{S\}_{tot} = \{S\} + \{S\text{-}Se\} \quad (8)$$

From equations 4-7, it is possible to derive the following expression:

$$\Gamma = \Gamma_{max}\frac{K_L\cdot[Se]}{1+K_L\cdot[Se]} \quad (9)$$

The fitting to the Langmuir isotherm is shown in Figure 8.5 together with the experimental values, the parameters obtained in the fitting are shown in Table 8.2. A good fitting of the Langmuir isotherm to the experimental data is observed. The good fitting corroborates monolayer coverage on the studtite surface.

Table 8.2. Results of the fitting of the Langmuir model to the experimental data.

Species	**Γ_{max} (mol·m^{-2})**	**K_L (dm^3·mol^{-1})**
Selenium(IV)	3.60 (±0.02)·10^{-6}	1.2 (±0.1)·10^4
Selenium(VI)	2.30 (±0.05)·10^{-6}	7.9 (±0.1)·10^3

On the other hand, the strength of the sorption might be deduced from the so-called separation factor, R_L:

$$R_L = \frac{1}{1+K_L \times [Se]_0} \quad (10)$$

If the value of R_L is 0 the sorption is irreversible; a value between 0 and 1 indicates that the sorption is favorable; R_L=1 indicates that the sorption is linear and, finally, if the value is higher than 1, the sorption is unfavorable. The R_L values calculated in this work are 0.99-0.13 for selenite and 0.99-0.19 for selenate, indicating in all the cases that the sorption process is favorable.

Although ionic strengths higher than 0.01 mol·dm^{-3} are not likely in natural waters, the sorption of selenium(IV) and selenium(VI) onto studtite has also been determined in this work at 0.1 mol·dm^{-3} in order to know if there might be competition processes on the sorption of selenium. As it can be seen in Figure 8.6, the sorption capacity for both selenium(IV) and selenium(VI) at 0.1 mol·dm^{-3} ionic strength is always lower than at 0.01 mol·dm^{-3}, indicating that at such high ionic strength there are competition processes for the active sites of the solid surface.

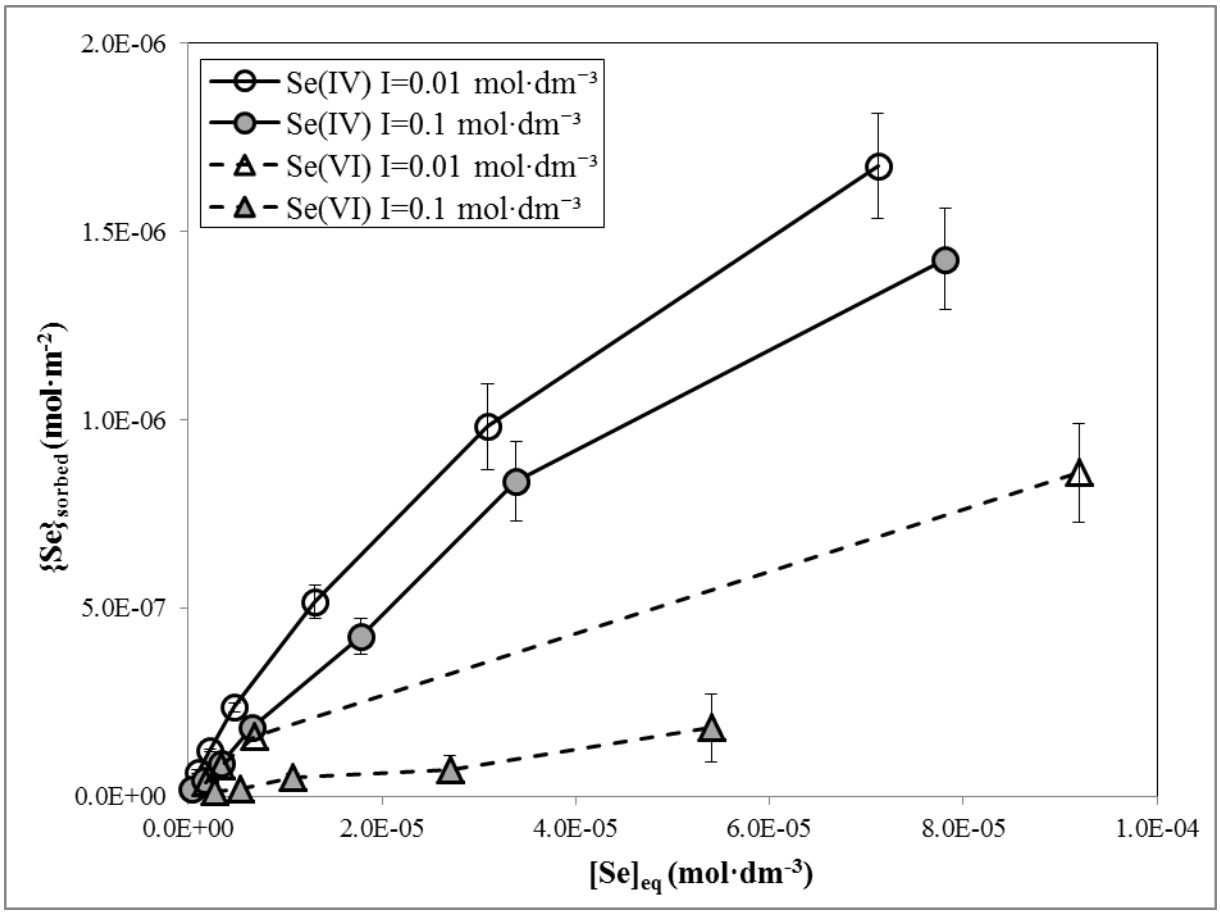

Figure 8.6. Influence of ionic strength on the selenium(IV) and selenium(VI) sorption on studtite. Experiments carried out with 0.05 g of studtite and pH=3. The lines do not represent any model.

8.3.4. Influence of pH on the sorption of Se(IV) and Se(VI) on studtite

Figure 8.7 shows the variation of the selenium(IV) and selenium(VI) sorption as a function of equilibrium pH. As it can be seen, the main trend is that sorption is higher at acidic pH than at alkaline pH. This behaviour is consistent with the chemical speciation of selenium in solution together with the acid-base properties of the solid.

The acid-base equilibria for Se(IV) and Se(VI) in solution are:

$H_2SeO_3(aq) \leftrightarrows HSeO_3^- + H^+$ $pK_{a1}= 2,53$ (11)

$HSeO_3^- \leftrightarrows SeO_3^{2-} + H^+$ $pK_{a2}= 10,59$ (12)

$HSeO_4^- \leftrightarrows SeO_4^{2-} + H^+$ $pK_{a1}= 1,8$ (13)

indicating that even at acidic pH Se(IV) and Se(VI) are in the form of negatively charged species. In this work the pH_{pzc} for studtite has been determined to be 4.0±0.2. Considering the selenium chemical speciation in solution together with the charge of the solid surface, at pH higher than the pH_{pzc}, the surface of the solid is negatively charged and $HSeO_3^-$, SeO_3^{2-} and SeO_4^{2-} predominate in solution, hence, the interaction of a negatively charged solid surface and anionic species in solution is expected not to be favored, resulting in very low sorption. However, at $pH<pH_{pzc}$, studtite surface is positively charged while the selenium predominant species are anions, the interaction of the species in solution and the surface of the solid is expected to be more favored than at alkaline pH and a higher sorption is observed.

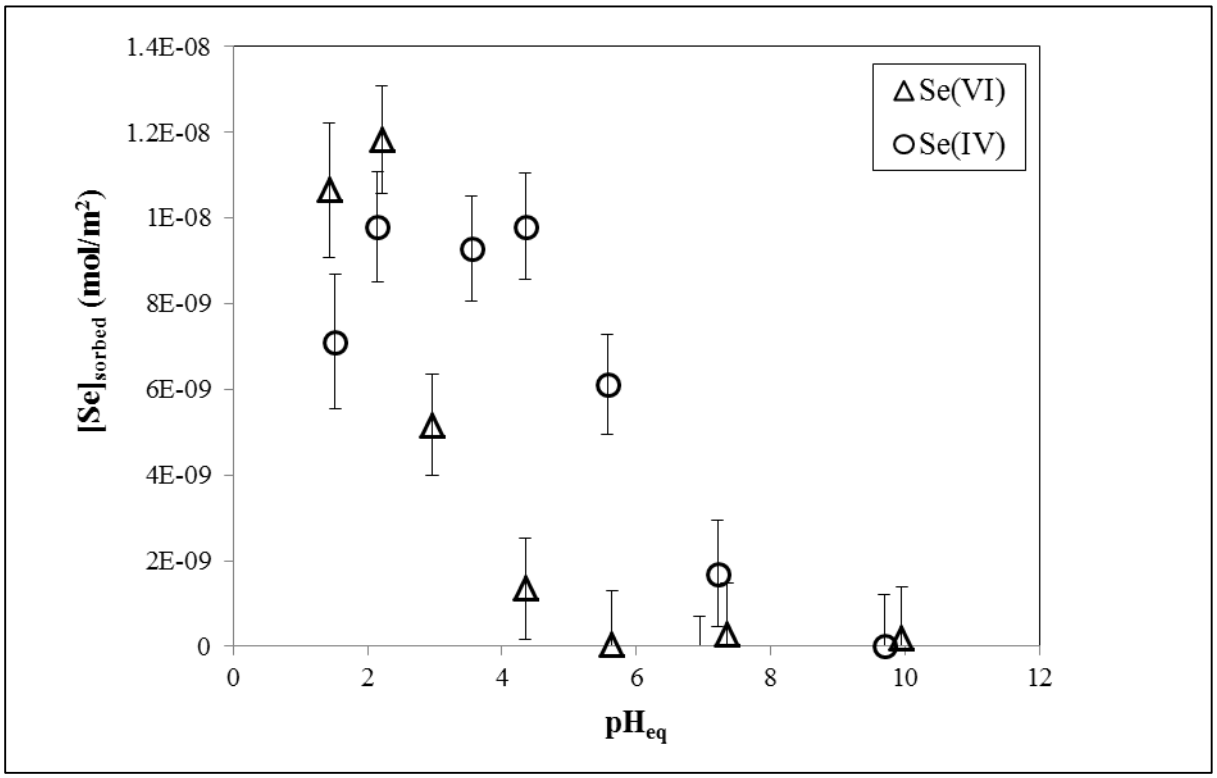

Figure 8.7. Variation of selenium(IV) and selenium(VI) sorbed onto studtite as a function of equilibrium pH. Experiments carried out with 0.05 g of studtite, $[Se(IV)]_0= 1.3\cdot10^{-6}$ mol·dm^{-3}, and $[Se(VI)]_0= 1.2\cdot10^{-6}$ mol·dm^{-3} in the presence of 0.01 mol·dm^{-3} $NaClO_4$.

This pH-dependence of sorption based on the chemical speciation of selenium and on the electrical charge of the solid surface could be clearer seen in Figure 8.8, which shows a combination of the experimental sorption data as a function of equilibrium pH together with fraction diagrams of selenium species in solution. As it can be seen, in the case of selenium(IV), sorption is very high at very acidic pH (due to the predominance of H_2SeO_3 in solution and a solid surface positively charged) and increases with the increase of the

percentage of the $HSeO_3^-$ species, until the change of the charge of the solid surface. In the case of selenium (VI), in the acidic pH range, it seems that the sorption is higher when $HSeO_4^-$ predominates, which could indicate that the selenium sorbed species on the solid would be the hydrogenselenate ion.

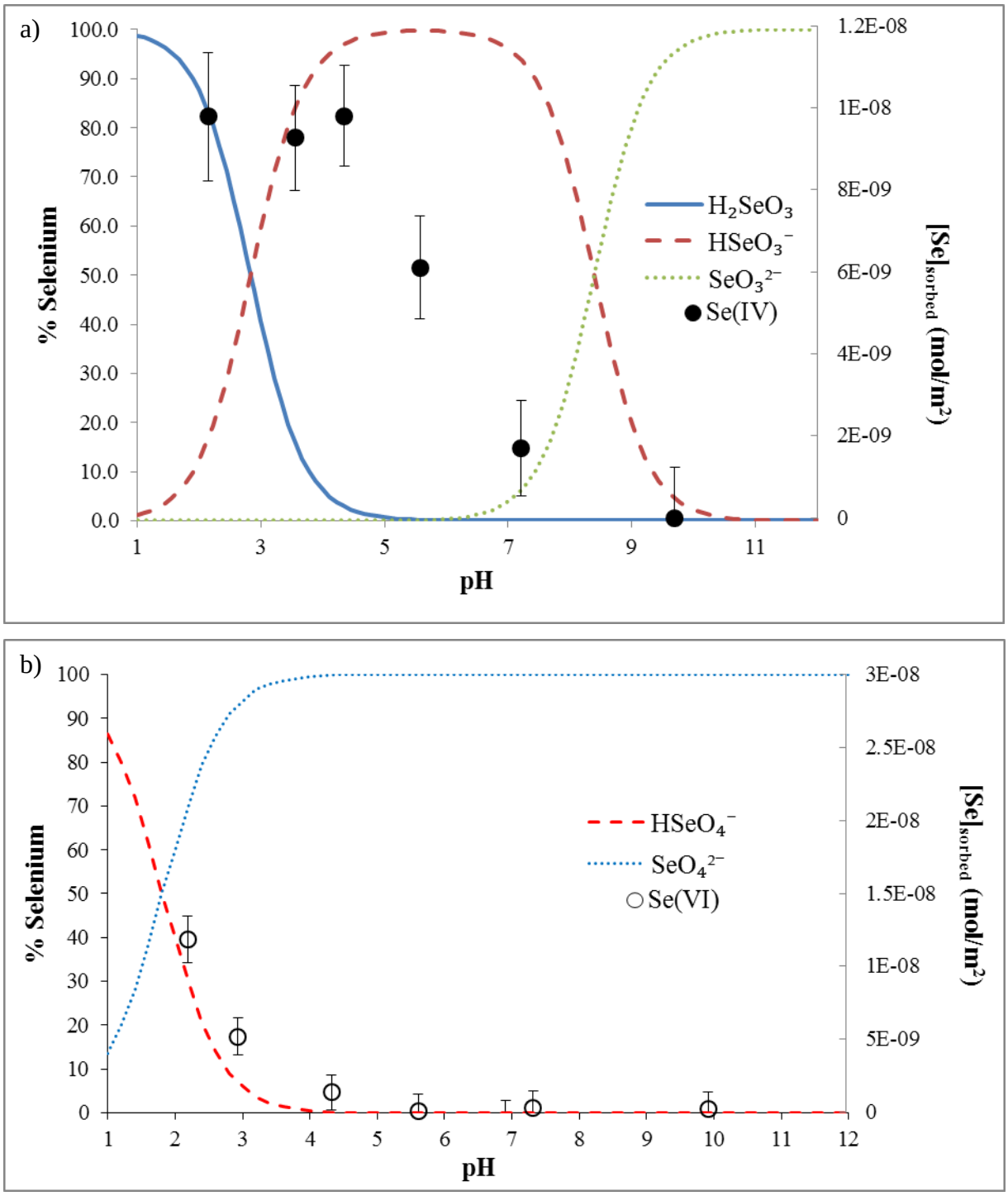

Figure 8.8. Comparison between experimental sorption data on (a) selenium(IV) and (b) selenium(VI) with selenium fraction diagrams.

8.4. CONCLUSIONS

In this work, new data on the uranyl peroxide studtite are presented. The value of the pH_{pzc} of the studtite have been determined for the first time. This data is critical for the knowledge of the chemical behavior of the studtite in the environment. The pH_{pzc} has been determined to be 4.0±0.2 by using the so-called 'immersion methodology'. This value of the point of zero charge fits with the sorption envelopes determined for different species in solution such as Cs^{+} and Sr^{2+}.

The main objective of the studies on sorption of radionuclides on studtite is the definition of the actual effect of the solid on the migration of radionuclides released by the nuclear fuel or spent nuclear fuel after the contact with water. This effect would be especially important for radionuclides which are not retarded through other processes such as precipitation or co-precipitation, e.g. cesium, strontium and selenium. The results obtained in the present study together with previous results on the sorption of cesium and strontium show that uranium peroxide solids might have an important influence on retention of such radionuclides. However, in the case of selenium, the maximum sorption occurs at pH values more acidic than the ones expected at the waters that can contact the fuel.

The sorption of selenium(IV) and selenium(VI) is relatively fast, indicating that selenium released from the nuclear fuel could actually be incorporated to the studtite, retarding its migration through the groundwaters. Selenium sorption into studtite can be explained by a two-step mechanism, the first step where the main characteristic is macropore diffusion and a second step where the diffusion is through micropores. The pseudo-second order model, is the model that best fits the experimental data. The sorption rate constants are 9.2 $(\pm 3.5)\cdot 10^{3}$ $m^{2}\cdot mol^{-1}\cdot s^{-1}$ and 6.4 $(\pm 2.3)\cdot 10^{4}$ $m^{2}\cdot mol^{-1}\cdot s^{-1}$ for selenite and selenate, respectively.

Selenium is sorbed onto studtite following a monolayer coverage, with maximum sorption capacities of 3.6 (±0.02)·10^{-6} mol·m^{-2} and 2.3 (±0.05)·10^{-6} mol·m^{-2} for selenium(IV) and selenium(VI), respectively. Sorption is always higher for selenium(IV) than for selenium(VI) in the concentrations range studied. Selenium species are mostly anions and therefore they are sorbed predominantly in the pH range in which the surface of the studtite is positively charged. For selenium(VI), the results seem to indicate that the selenium sorbed species on the solid would be the $HSeO_4^-$ ion. For selenium(IV), sorption is higher when the H_2SeO_3 and $HSeO_3^-$ species predominate.

8.5. REFERENCES

1 K.-A. Hughes Kubatko, K.B. Helean, A. Navrotsky and P.C. Burns. (2003). Stability of peroxide-containing uranyl minerals. *Science*, **302**, 1191-1193.

2 B. McNamara, E.C. Buck, B. Hanson. (2003). Observation of studtite and metastudtite on spent fuel. *Mater. Res. Soc. Symp. Proc.*, **757**, 401-406.

3 B. McNamara, B. Hanson, E.C. Buck, C.Z. Soderquist. (2004). A radiochemical analysis of metastudtite and leachates from spent fuel. *Mater. Res. Soc. Symp. Proc.* , **824**, 139-144.

4 D.W. Shoesmith, S. Sunder. (1992). Prediction of nuclear fuel (UO_2) dissolution under waste disposal conditions. *J. Nucl. Mater.*, **190**, 20-35.

5 D.W. Shoesmith. (2000). Fuel corrosion processes under waste disposal conditions. *J. Nucl. Mater.*, **282**, 1-31.

6 J. Bruno, E. Cera, M. Grivé, U.B. Eklund, T. Eriksen. (1999). Experimental determination and chemical modeling of radiolytic processes at spent fuel/water interface. *Report SKB TR-99-26, SKB, Stockholm, Sweden*.

7 B. Vlaisavljevich, L. Gagliardi, L., P.C. Burns. (2010). Understanding the structure and formation of uranyl peroxide nanoclusters by quantum chemical calculations. *J. Am. Chem. Soc.*, **132**, 14503-14508.

8 P.C. Burns. (2011). Nanoscale uranium-based cage clusters inspired by uranium mineralogy. *Mineral. Mag.*, **75**, 1–25.

9 P.C. Burns, R.C. Ewing, A. Navrotsky. (2012). Nuclear fuel in a reactor accident. *Science*, **335**, 1184-1188.

10 Armstrong, C.R., Nyman, M., Shvareva, T., Sigmon, G.E., Burns, P.C., Navrotsky, A. (2012). Uranyl peroxide enhanced nuclear fuel corrosion in seawater. *P. Natl. Acad. Sci. USA*, **109**, 1874-1877.

11 Sunder, S., Miller, N.H., Shoesmith, D.W. (2004). Corrosion of uranium dioxide in hydrogen peroxide solutions. *Corros. Sci.*, **46**, 1095-1111.

12 Douglas, M., Clark, S.B., Friese, J.I., Arey, B.W., Buck, E.C., Hanson, B. (2005). Neptunium(V) partitioning to uranium(VI) oxide and peroxide solids. *Environ. Sci. Technol.*, **39**, 4117-4124.

13 P.C. Burns, R.C. Ewing, M.L. Miller. (1997). Incorporating mechanisms of actinide elements into the structures of U^{6+} phases formed during the oxidation of spent nuclear fuel. *J. Nucl. Mater.*, **245**, 1-9.

14 P.C. Burns, P.C., A.L. Klingensmith. (2006). Uranium mineralogy and neptunium mobility. *Elements*, **2**, 351-356.

15 A.L. Klingensmith, K.M. Deely, W.S. Kinman, V. Kelly, P.C. Burns. (2007). Neptunium incorporation in sodium-substituted metaschoepite. *Am. Mineral.*, **92**, 662-669.

16 R. Sureda, X. Martínez-Lladó, M. Rovira, J. de Pablo, I. Casas, J. Giménez. (2010). Sorption of strontium on uranyl peroxide: Implications for a high-level nuclear waste repository. *J. Hazard. Mater.*, **181**, 881-885.

17 J. Giménez, X. Martínez-Lladó, M. Rovira, J. de Pablo, I. Casas, R. Sureda, A. Martínez-Esparza. (2010). Cesium sorption on studtite ($UO_2O_2 \cdot 4H_2O$). *Radiochim. Acta.*, **98**, 479-483.

18 J. Giménez, R. Sureda, J. de Pablo, I. Casas, X. Martínez-Lladó, M. Rovira, A. Martínez-Esparza. (2009). The role of uranium peroxide studtite on the retention of Cs, Sr and Se(VI). *Mater. Res. Soc. Symp. Proc.*, **1193**, 621-626.

19 F. Chen, P.C. Burns, R.C. Ewing. (1999). ^{79}Se: geochemical and crystallo-chemical retardation mechanisms. *J. Nucl. Mater.*, **275**, 81-94.

20 ENRESA. (1997). Evaluación del comportamiento y la seguridad de un almacenamiento profundo en granito. Documento de Síntesis. *Report 48-1P-M-OOG-21, Madrid, Spain*.

21 F. Séby, M. Potin-Gautier, E. Giffaut, O. Donard. (1998). Assessing the speciation and the biogeochemical processes affecting the mobility of selenium from a geological repository of radioactive wastes to the biosphere. *Analysis*. **26**, 193-198.

22 X. Wang, X. Liu. (2005). Sorption and desorption of radioselenium on calcareous soil and its solid components studied by batch and column experiments. *Appl. Radiat. Isot.*, **62**, 1-9.

23 D.I. Kaplan and R. J. Serne. (1995). Distribution coefficient values describing Iodine, Neptunium, Selenium, Technetium, and Uranium sorption to Hanford sediments. *U.S. D.O.E.*

24 T. Missana, U. Alonso, M. García-Gutierrez. (2009). Experimental study and modelling of selenite sorption onto illite and smectite clays. *J. Colloid. Interf. Sci.*, **334**, 132-138.

25 Fiol, N. and Villaescusa, I. (2009). Determination of sorbent point zero charge: usefulness in sorption studies. *Environmental Chemistry Letters*, **7**, 79-84.

26 Bourikas, K., Vakros, J., Kordulis, C. and Lycourghiotis, A. (2003). Potentiometric Mass Titrations: Experimental and Theoretical Establishment of a New Technique for Determining the Point of Zero Charge (PZC) of Metal (Hydr)Oxides. *J.Phys. Chem. B*, **107**, 9441-9451.

27 Clarens F. (2004). Efecto de la radiólisis y de los productos radiolíticos en la disolución del UO_2: Aplicación al modelo de alteración de la matriz del combustible nuclear gastado. *Universitat Politécnica de Catalunya*.

28 Schindler, M., Mutter, A., Hawthorne, F.C. and Putnis, A. (2004). Prediction of crystal morphology of complex uranyl-sheet minerals II. *Observation. Can. Mineral.*, **42**, 1651-1666.

29 Y.S. Ho, G. McKay. (1999). Pseudo second-order model for sorption processes, P*rocess Biochem.*, **34**, 451-465.

30 M. Martínez, N. Miralles, S. Hidalgo, N. Fiol, I. Villaescusa, J. Poch. (2006). Removal of lead(II) and cadmium(II) from aqueous solutions using grape stalk waste. *J. Hazard. Mater. B*, **133**, 203-211.

31 W.J. Weber, J.C. Morris. (1963). Kinetics of adsorption on carbon solution. *J. San. Eng. Div. ASCE*, **89**, 31-59.

32 C. Valderrama, X. Gamisans, X. de las Heras, A. Farran, J.L. Cortina. (2008). Sorption kinetics of polycyclic aromatic hydrocarbons removal using granular activated carbon: intraparticle diffusion coefficients. *J. Hazard. Mater.*, **157**, 386-396.

33 C. Valderrama, J.I. Barios, M. Caetano, A. Farran, J.L. Cortina. (2010). Kinetic evaluation of phenol/aniline mixtures adsorption from aqueous solutions onto activated carbon and hypercrosslinked polymeric resin (MN200). *React. Funct. Polym.*, **70**, 142-150.

9. Conclusions

9. Conclusions

1. The speciation of uranium(VI) in the presence of hydrogen peroxide was studied in alkaline conditions and in the absence of carbonates. Two UO_2^{2+}–H_2O_2–OH^- complexes were considered at pH12 according to UV-vis spectrophotometric data on uranium solutions titrated with H_2O_2. The proposed formation reactions are:

$$UO_2^{2+} + H_2O_2 + 4OH^- \leftrightarrows UO_2(O_2)(OH)_2^{2-} + 2H_2O: \beta^\circ_{1,1,4}$$

$$UO_2^{2+} + 2H_2O_2 + 6OH^- \leftrightarrows UO_2(O_2)_2(OH)_2^{4-} + 4H_2O: \beta^\circ_{1,2,6}$$

The equilibrium constants for both reactions were determined by using the STAR program: $\log \beta^\circ_{1,1,4} = 28.1 \pm 0.1$ and $\log \beta^\circ_{1,2,6}=36.8 \pm 0.2$.

2. Hydrogen peroxide produces a static quenching effect that diminishes the fluorescence intensity of the uranium fluorescent species. Using the Stern–Volmer equation for static quenching it was possible to calculate the equilibrium formation constant of the first species, $UO_2O_2(OH)_2^{2-}$, $K^0 = 28.7 \pm 0.4$. A similar value to the one determined using UV–Visible spectrophotometry.

3. Fluorescence of U(VI) at high alkaline concentrations was studied (pH: 11–13.5). The species $UO_2(OH)_3^-$ and $(UO_2)_3(OH)_7^-$ were identified at pH 11 by Time Resolved Laser-induced Fluorescence Spectroscopy (TRLFS) lifetimes analysis. At pH 12 and room temperature, only the species $UO_2(OH)_3^-$ has fluorescence and at pH 13 no fluorescence was detected, suggesting that the predominant species, $UO_2(OH)_4^{2-}$, is not fluorescent. On the other hand, two hydroxo complexes, $UO_2(OH)_3^-$ and $UO_2(OH)_4^{2-}$, were seen thanks to the use of Cryo-TRLFS techniques. Two different lifetimes were observed at 10K: one with a lifetime between 150.1 ± 7.0 and 198.2 ± 7.8 μs and other with a lifetime between 8.3 ± 0.3 and 11.2 ± 0.4 μs. It was considered that the one with the longest lifetime is the species $UO_2(OH)_3^-$ which is fluorescent at room temperature, and the one with the shortest lifetime is the species $UO_2(OH)_4^{2-}$, which is non-fluorescent at room temperature. Thanks to the difference between lifetimes, it was possible to calculate the contribution of each species to the total fluorescence spectra.

4. A flow-through experimental reactor has been designed in order to perform studies at both high pressure and high temperature conditions. It was constructed and successfully tested in a series of experiments with very complex leachants like cement pore water, very oxidant leachants like hydrogen peroxide, anoxic and reducing conditions, different flow rates and different pressures.

Using this new reactor the kinetics of uranium dissolution was studied at different conditions using hydrogen peroxide as an oxidant. As a result of this work, two species proved to have an effect in the dissolution rate of uranium: hydrogen and carbonate. Combining hydrogen peroxide and carbonates the uranium dissolution rate increases. On the contrary, the uranium dissolution rate with hydrogen peroxide decreases under hydrogen atmosphere. However it is still several orders of magnitude higher than the uranium dissolution rates found in the literature under hydrogen gas without hydrogen peroxide.

5. Ten different radiolysis experiments were carried out with different sampling systems, alpha-doping and ionic strength with the objective of observing the effect of different experimental conditions on the radiolysis products formation and the dissolution of U and Pu. The experiments were performed at pH 12.

The results obtained on H_2 and O_2 formation, at a dose rate below 40 KGy, for different ionic strengths, are in good agreement with those in the bibliography. The situation of the alpha-emitters (inside the pellet or in solution) doesn't affect the gas production under the experimental conditions. The production of H_2 and O_2 in the experiment with an ionic strength of 0.05 $mol \cdot dm^{-3}$ NaCl is similar to those obtained with an ionic strength of 5 $mol \cdot dm^{-3}$ NaCl.

Production of HClO is observed in experiments with 5 $mol \cdot dm^{-3}$ NaCl ionic strength and H_2O_2 generation is seen in experiments with 0.05 $mol \cdot dm^{-3}$ NaCl. Uranium release becomes higher when the dose rate is increased.

The software Macksima-Chemist was used to model the experimental data, obtaining a good simulation in the studied accumulated dose range in the formation of O_2, and especially at accumulated doses higher than 40 kGy in the formation of H_2. The model was proved, on one hand, to be robust when changing the values of the kinetic constants but, on the other hand, sensitive to the changes of most of the G-values.

6. The value of the pHpzc of the studtite has been determined for the first time. This data is critical for the knowledge of the chemical behavior of the studtite in the environment. The pH_{pzc} has been determined to be 4.0±0.2 by using the so-called 'immersion methodology'. This value of the point of zero charge fits with the sorption envelopes determined for different cationic and anionic species in solution such as Cs^+, Sr^{2+}, and $HSeO_4^-$.

7. The sorption of selenium(IV) and selenium(VI) is relatively fast, indicating that selenium released from the nuclear fuel could actually be incorporated to the studtite, retarding its migration through the groundwaters. Selenium sorption into studtite can be explained by a two-step mechanism, the first step where the main characteristic is macropore diffusion and a second step where the diffusion is through micropores. The pseudo-second order model, is the model that best fits the experimental data. The sorption rate constants are $9 \cdot 10^3$ $m^2 \cdot mol^{-1} \cdot s^{-1}$ and $6.4 \cdot 10^4$ $m^2 \cdot mol^{-1} \cdot s^{-1}$ for selenite and selenate, respectively.

Selenium is sorbed onto studtite following a monolayer coverage, with maximum sorption capacities of $3.6 \cdot 10^{-6}$ $mol \cdot m^{-2}$ and $2.3 \cdot 10^{-6}$ $mol \cdot m^{-2}$ for selenium(IV) and selenium(VI), respectively. Sorption is always higher for selenium(IV) than for selenium(VI) in the concentrations range studied. Selenium species are mostly anions and therefore they are sorbed predominantly in the pH range in which the surface of the studtite is positively charged. For selenium(VI), the results seem to indicate that the selenium sorbed species on the solid would be the $HSeO_4^-$ ion. For selenium(IV), sorption is higher when the H_2SeO_3 and $HSeO_3^-$ species predominate.

10 Annex: Publications

10 Annex: Publications

Peer reviewed publications:

- S. Meca, A. Martínez-Torrents, V. Martí, J. Giménez, I. Casas, J. de Pablo. (2011). Determination of the equilibrium formation constants of two U(VI)-peroxide complexes at alkaline pH. *Dalton Trans*. **40**, 7976-7982.

- A. Martínez-Torrents, S. Meca, N. Baumann, V. Martí, J. Giménez, J. de Pablo, I. Casas. (2013). Uranium speciation studies at alkaline pH and in presence of Hydrogen Peroxide using Time-Resolved Laser-induced Fluorescence Spectroscopy. *Polyhedron,* **55,** 92–101

- A. Martínez-Torrents, J. Giménez, I. Casas, J. de Pablo. (2014). Design of a new Reactor to work at low volume Liquid/Surface solid ratio and High Pressure and Temperature. Dissolution Rate Studies of UO_2 under both anoxic and reducing conditions. Materials Research Society Proceedings - *Scientific Basis for Nuclear Waste Management XXXVII*. Volume 1665, Symposium NW, 37-p53.

- A. Martínez-Torrents, J. Giménez, X. Martínez-Lladó, J. de Pablo, I. Casas. Incorporation of Selenium(IV) and Selenium(VI) on Uranyl Peroxide. *Journal of Radioanalytical & Nuclear Chemistry*. DOI 10.1007/s10967-014-3323-7.

- J. Giménez, J. de Pablo, I. Casas, X. Martínez-Lladó, M. Rovira, A. Martínez Torrents. (2014). Solubility study and point of zero charge of studtite (UO_2O_2•$4H_2O$). *Applied Geochemistry*, **49**, 42-45.

- A. Martínez-Torrents, E. González-Robles, E. Bohnert, I. Casas, J. de Pablo, V. Metz. α-Radiolysis under alkaline conditions in 0.05 and 5.0 molar NaCl. Proceedings of the International Workshop ABC-Salt III (In Print).